Mathematical modelling of geophysical melt drainage

Ian Hewitt

Trinity College

University of Oxford

A thesis submitted for the degree of

Doctor of Philosophy

Trinity Term 2009

Acknowledgements

This thesis owes a great deal to the support and encouragement of many people, without whom it would never have materialised:

My supervisor, Andrew Fowler, who has been a constant source of inspiration, ideas and advice, and has always been incredibly generous with his time. He has enthused me with a wide interest in science as a whole, and the role an applied mathematician can play in its advancement.

My fellow students and other faculty members in OCIAM, especially those on the third floor corridor, who have motivated and encouraged me. Also, a number of other scientists who I have met around the world, at Woods Hole in particular, whose enthusiasm for searching to understand the world around us has had a strong influence on me.

Trinity College, which has provided me with a 'home' in Oxford for the last seven years.

EPSRC, which funded my studentship.

My friends and family, whose support and humour through the highs and lows of the past three years has been truly invaluable, and for which I am eternally grateful.

Mathematical modelling of geophysical melt drainage

Ian Hewitt

Trinity College
University of Oxford

A thesis submitted for the degree of Doctor of Philosophy

Trinity Term 2009

Fluid flows involving transport of a liquid phase in close proximity with its solid phase involve continuous transfer of mass and heat, which can influence the nature of the drainage that occurs. We consider mathematical models for two such situations; magma flow in the mantle and water flow beneath glaciers. In part I, we derive a model for porous flow within a partially molten column of mantle undergoing decompression melting. By ignoring composition effects, and by scaling the equations appropriately, approximate analytical solutions can be found for one-dimensional upwelling, which allow the region and extent of melting to be determined. We study the dynamics of open channels of melt flow in the same situation, and find that such channels would have low pressure compared to the surrounding porous flow, and therefore draw in melt from a region of the size of a compaction length. We suggest that such channels could form through the unstable effects of melting caused by heat transfer by the upwelling melt. We emphasise the similarity with channels of meltwater that are known to exist beneath ice. In part II we pose a generalised model for subglacial water flow, which is described as an effective porous medium, the pore space being determined from an evolution equation. This is used to investigate the flow into a channel, which is found to be drawn from a surrounding region whose size, we suggest, determines the spacing between major drainage channels beneath ice sheets. These are compared to the observed spacing of eskers. A critical condition on the discharge necessary to sustain a channel is found, which may provide a criteria to decide where and when channelised drainage occurs. Lastly, a simple drainage model is used to explain seasonal variations in the velocity of a valley glacier.

Contents

Preface

There are a number of naturally occurring situations in which a polycrystalline material undergoes melting, and the resulting melt drains from the remaining solid due to buoyancy. This thesis considers mathematical models for two such situations, namely the extraction of magma from the mantle, and the drainage of water from beneath glaciers and ice sheets.

These apparently different applications in fact have many similarities, which become evident in the mathematical modelling. In the mantle, magma is produced as upwelling rock undergoes *decompression* melting; at the base of glaciers water is produced due to frictional and geothermal heating. Whatever the cause of melting, the liquid melt and the residual solid can move relative to one another, and the resulting flow tends to have feedbacks on the rate of melting.

In both settings there is a major distinction between porous-like flows, in which melt is distributed over a large area, and channel-like flows, in which melt is localised in relatively fast-flowing streams. This thesis is broadly concerned with the interaction between these two different types of melt flow, and we aim to transfer previously developed ideas from each application to provide insights into the other.

The most well developed theory for subglacial water flow is that of Röthlisberger channels - open channels of water incised into the ice at the bed (see chapter 4) - and we will make use of those ideas to construct equivalent models for channels of magma in the mantle; though the ultimate cause of melting is different there are similarities that will be seen in chapter 3. On the other hand, the standard models for the melting regions of the mantle treat it as a deforming porous medium that *compacts* as the melt is drained from it; we will use this as an analogy for a model for generalised porous flow beneath ice sheets in chapter 5. In this case we can transfer the concept of a *compaction* length - the length over which deformation of the drainage space accommodates pressure perturbations - to gain insight into how water moves in the vicinity of a subglacial channel.

The thesis is divided into two largely self contained parts, the first concerning magma migration and the second concerning subglacial water. Each part has its own introduction, which aims to provide some background and motivation for the mathematical modelling, to review some of the relevant previous work, and to highlight some of the more standard modelling ideas. There are then two chapters of new work for each application.

Chapter 2 studies one-dimensional solutions for a simple physical model of upwelling rock, using conservation principles to determine the region that melts and the amount of melt produced. Chapter 3 looks at models for channels of magma and how these would be fed by flow from a surrounding compacting matrix. It also shows how such channels could potentially form from two-dimensional perturbations in the model of chapter 2.

Chapter 5 considers an equivalent description of subglacial drainage, based on a compacting porous flow feeding into channels, and looks at the implications for water pressure variations beneath an ice sheet. Chapter 6 attempts to use some of these ideas to explain some observed variations in the sliding rate of a glacier driven by changes in the subglacial water pressure. It forms a slight aside to the rest of the thesis, but demonstrates how some of the ideas concerning meltwater flow might be put to practical use.

Part I

Magma migration in the mantle

Chapter 1

Introduction

1.1 Mantle convection and magma production

1.1.1 Magmatism

Magma is molten rock, which is produced at high temperatures in the Earth's mantle. It tends to be less dense than the surrounding solid rock and therefore moves upwards, potentially bursting through the crust to result in volcanism, or solidifying beneath the surface to create new crust. This part of this thesis will be concerned with understanding certain aspects of the melting that produces magma and the first stages of its ascent towards the surface.

The mantle is the largely solid part of the Earth which occupies the region beneath the crust down to a depth of around 2970 km. The crust varies in thickness between around 5 km and 70 km, with oceanic crust much thinner than continental crust; it is formed by the solidification of molten rocks that ascend from within the mantle, and, due to the way in which the rocks melt and solidifiy, is chemically distinct from the mantle.

Despite the mantle being predominantly solid, the temperatures and pressures are such that large parts of it deform by creeping in a viscous manner. This plastic region of the mantle is called the *asthenosphere*, and typically begins at around 100 km depth. The shallower parts of the mantle that are more rigid, together with the crust, make up the *lithosphere*. The temperature of the mantle increases with depth to around 4000 K at the boundary with the outer core. The lithosphere may be viewed as a thermal boundary layer due to the cold (atmospheric $\sim$ 300 K) temperatures at the Earth's surface.

The large temperature differences and the fact that the rock can deform plastically cause the mantle to convect, with hot rock rising and cooling in some regions, and

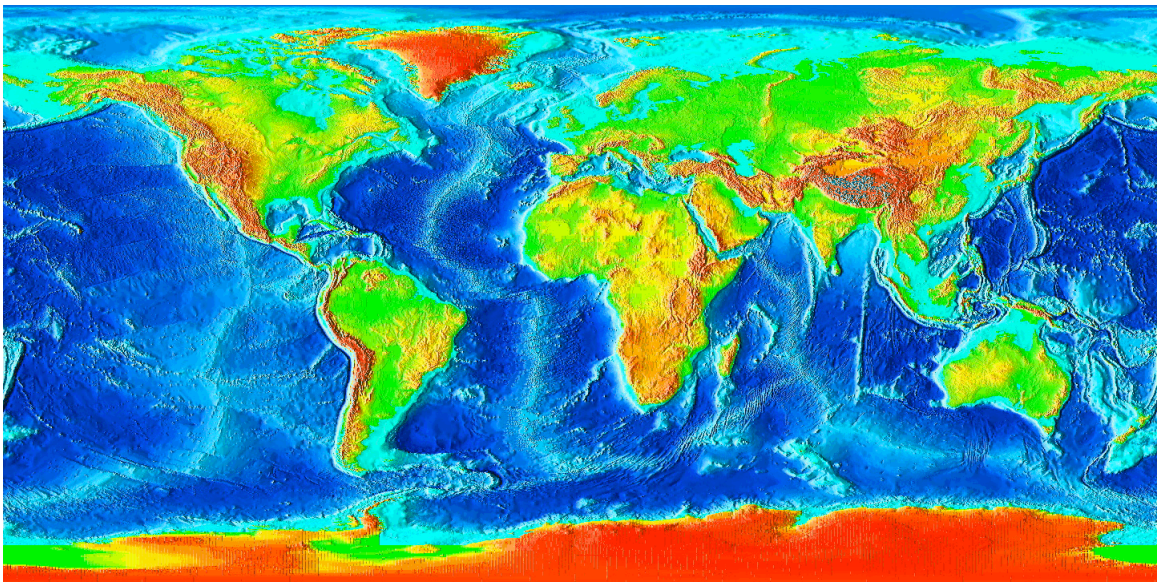

Figure 1.1: Height of the Earth's surface, showing mid-ocean ridges as elevated (light blue) linear features in the deep ocean.

cooler rock descending in others. This convection drives, and is affected by, the motion of the overlying lithosphere, which is broken up into *tectonic plates*.

The rocks in the upper mantle are typically composed of minerals such as olivine, pyroxene and spinel. They have a melting temperature of around 1500 K under atmospheric conditions, but the melting temperature increases substantially with increasing pressure, so at the elevated pressures in the mantle the rocks are for the most part solid despite the high temperatures. In some places where hot rock is ascending however, it is caused to melt, or partially melt, to produce magma, and it is to these places that we turn our attention.

A common place for this to happen is beneath *mid-ocean ridges* (figure 1.1), where two tectonic plates diverge from one another and new oceanic crust is formed in between. As a first approximation, the mantle flow in such regions can be considered two dimensional (figure 1.2), rising upwards and spreading sideways beneath the plates; the ascending rock melts, and the magma which rises beneath the spreading axis solidifies to produce the new crust along the ridge. The large supply of heat carried by the upwelling rock means the lithosphere becomes very thin in these regions and rises to within a few kilometres of the surface. Most such ridges occur below the ocean, though there are some places - notably Iceland - where the ridge rises above sea level and forms volcanic islands.

Magma production also occurs in isolated mantle plumes - hot spots occurring

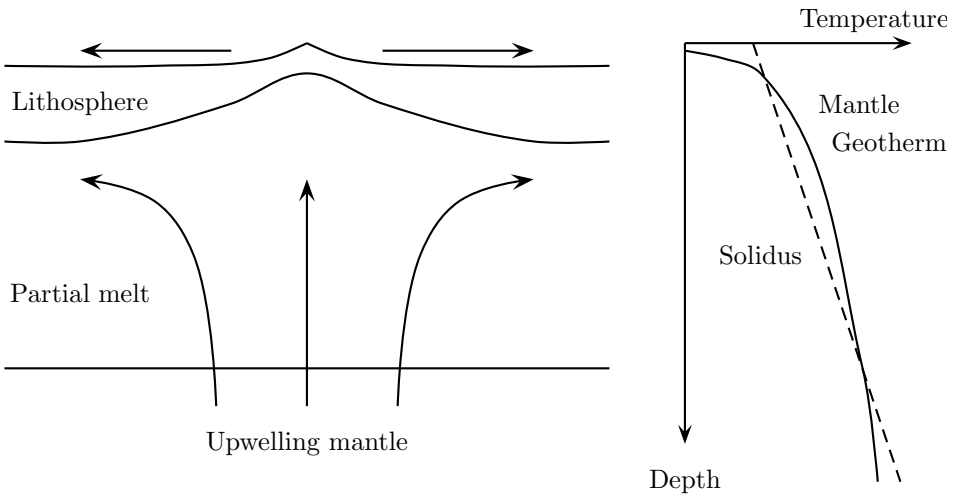

Figure 1.2: The situation at a mid-oceanic ridge where tectonic plates are diverging. On the right is a schematic illustration of the mantle geotherm that would exist if the mantle were not to partially melt, and the solidus temperature at the ridge axis.

away from tectonic plate boundaries - and in subduction zones, where plates come together and one sinks beneath the other, but we concentrate mainly on the situation beneath mid-ocean ridges. We are interested in how magma is produced, how it then moves through the residual mantle rock, and how (or if) it can rise through the lithosphere to the surface.

1.1.2 Partial melting

As the mantle rock rises it cools adiabatically. The melting temperature (the *solidus*) at large depths is higher than the mantle temperature, but decreases with decreasing pressure towards the surface (see figure 1.2). If the gradient of the solidus with depth is large enough then the adiabatic temperature profile intersects the solidus and the solid rock must start to melt. The temperature is then constrained to the solidus as it continues to rise; and since the solidus decreases with decreasing pressure, the ascending rock contains excess heat, which is consumed as latent heat and drives continual melting. This process is known as *decompression* melting, and results in a region of *partial melt*. Eventually, near the surface, the temperature must drop significantly to reach the cold temperature at the surface, and at this point it falls below the solidus again.

The melt forms preferentially at the intersections of individual grains that can be expected to form an interconnected network, even at low porosity (McKenzie, 1984). The melt is therefore able to move through the porous solid matrix and, being

less dense, will rise buoyantly. This separation of melt from the matrix results in a compensating motion of the matrix - the matrix is said to *compact*.

When ascending melt reaches the base of the relatively cold lithosphere it may solidify (addition of material to the base of the lithosphere in this way is termed *underplating*), or it may find a way to continue its rise through the lithosphere, perhaps to reach a magma chamber or to erupt directly at the surface. Such continued transport may occur through a pre-existing conduit, or may require *magma-fracturing* of the lithosphere.

1.2 Mathematical models

1.2.1 Porous flow

Many authors have set out model equations for partially molten material (Turcotte and Ahern, 1978; Ahern and Turcotte, 1979; McKenzie, 1984; Ribe, 1985a; Fowler, 1985, 1990a,b; Spiegelman, 1993a); the context is one of two-phase flow, with mass exchange between the solid and liquid phases. The formulations differ in some specifics, but have the same general form, and have been put to a variety of uses. In particular, there are a number of reasons to believe that porous flow is not the only means of magma ascent, and various instabilities of the porous flow have been investigated; these will be discussed further shortly.

In the asthenosphere, both the solid rock and the liquid magma behave as viscous fluids. The general approach to modelling partial melting is to assume that at least some aspects of the solid motion are externally prescribed by the larger scale mantle convection and the spreading plates. The focus is then on how the melt moves through the solid matrix. The situation is simplified somewhat by the vast difference in viscosity of the melt and solid, and the observation (or at least inference) that the porosity is small.

It is therefore appropriate to describe the melt flow using Darcy's law. More complicated equations giving a systematic description of two-phase flow are possible in which many extra surface effects can be included (Drew, 1983; Fowler, 1985, 1990a; Bercovici et al., 2001; Šrámek et al., 2007). However, these require making various assumptions concerning interactive drag coefficients and partitioning of surface forces, and for most practical applications they are reduced to Darcy's law. We do not intend to concern ourselves too much with the details and point the interested reader towards the work of Bercovici et al. (2001).

1.2.2 Compaction

The first attempts to model partial melting were by Turcotte and Ahern (1978). One of the principle assumptions they made is that the pressure in the melt and solid are the same, stating that viscous deformation of the grains will readily occur over short length scales (less than 100 m) to quickly equalize pressures. Effectively this allows the matrix to freely compact as the melt migrates upwards through it.

It is now realised that this compaction is in fact *due* to the difference in pressure between the phases, which must therefore be accounted for in any model of the process, as is generally the case for other two-phase flows and particularly, for example, in soil mechanics. Following the widely used form of the equations suggested by McKenzie (1984), this pressure difference has commonly been parameterized in terms of a *bulk viscosity* ζ, related in some way to the intrinsic shear viscosity η_s. Compaction then occurs according to the law

$$-\zeta \nabla \cdot \mathbf{V} = p_s - p_l, \tag{1.1}$$

in which $\mathbf{V}$ is the velocity of the matrix, and p_s and p_l are the pressure in the solid and melt respectively. The bulk viscosity essentially describes how easily a two-phase material can be squeezed to extract the melt and, in the context of melt generation, will depend strongly on the melt fraction ϕ. A number of arguments based on microscopic models, suggest that $\zeta \sim \eta_s/\phi$ (Batchelor, 1967; Fowler, 1985; Sleep, 1988; Bercovici et al., 2001), so that the matrix becomes incompressible at zero melt fraction. The dependence of the bulk viscosity on porosity has been treated in different ways by different authors, with much of the early work regarding ζ as a constant, and more recently using alternative porosity-dependent definitions.

1.2.3 Thermodynamics

Much of the work following McKenzie's original equations has neglected the melting process and concentrated on the melt migration and the matrix motion when melt is somehow already *in situ* (Spiegelman and McKenzie, 1987; Spiegelman, 1993a; Spiegelman et al., 2001). Feedbacks of the melt flow on the melt fraction have been included by accounting for dissolution reactions, in which the concentrations of different minerals in each phase are prescribed to evolve towards given chemical equilibria, which typically vary with pressure and therefore depth (Aharonov et al., 1995). If the underlying decompression melting is included at all, it is usually prescribed at a

given rate in order to match the total *degree of melting*; that is, the fraction of an original lump of rock that has melted (Spiegelman et al., 2001).

An energy equation has therefore been neglected in many studies and, perhaps because of this, there has been surprisingly little attempt to describe the onset of partial melting and to place it within the wider context of mantle circulation. The partial melt occupies only part of the ascending mantle and its position should be found by considering the thermodynamics; the boundaries are 'free boundaries', in the sense that their location is unknown *a priori* and must be found as part of the solution. Accounting for the thermodynamics *within* the partially molten region is also necessary in order to consistently determine the melting rate.

It is common to assume that the partially molten region is in a local thermodynamic equilibrium, since on the scale of the pores the exchange of material between the solid and liquid phases is virtually instantaneous and causes the temperature to quickly adjust to reach equilibrium (Ahern and Turcotte, 1979; McKenzie, 1984; Fowler, 1990a; Šrámek et al., 2007; Katz, 2008).

For a given composition $\mathbf{c}_s$ and pressure p, the temperature at which the rock melts is the solidus T_S, which can be written

$$T_S = T_S(p, \mathbf{c}_s). \tag{1.2}$$

$\mathbf{c}_s$ is a (potentially long) vector containing the concentrations of each different chemical component in the rock. Certain chemical components are less, or more, *compatible*, so as the rock starts to melt they preferentially transfer to the melt or remain in the solid phase. The compositions $\mathbf{c}_s$ of the solid and $\mathbf{c}_l$ of the liquid are therefore different, and gradually change as the rock undergoes continual melting. This preferential melting is what causes the erupted magma (and consequently the solidified crust) to have a different chemical structure to the parent mantle.

In order to fully determine the melting rate, one needs to model the advection and diffusion of each component in each phase, and the advection and diffusion of heat, or enthalpy, together with equilibrium relationships for the chemical compositions, pressure and temperature.

1.2.4 Summary of previous work

The early work of Turcotte and Ahern (1978; Ahern and Turcotte, 1979), assumed Darcy flow through a matrix with (effectively) zero bulk viscosity. They solved an energy equation, assuming an empirical relationship between temperature, pressure and melt fraction, and identified the free boundary nature of the problem, locating

the depth at which melting begins by considering the surrounding temperature field and ensuring continuity of temperature gradients. Capping of the melt fraction at the top of the region removed the need to consider a thermal boundary layer there.

Ribe (1985a) included compaction, but did not include temperature as a variable, rather prescribing a melting distribution that decays exponentially with distance above the onset of meting. The conclusion was that compaction is relatively unimportant in determining the behaviour beneath mid-ocean ridges.

Spiegelman and McKenzie (1987) ignored the melting process and concentrated on determining the direction of melt flow in a compacting matrix undergoing the two dimensional 'corner' flow typical of a mid-ocean ridge.

Scott and Stevenson (1984, 1986) investigated the possibility for solitary waves in the melt fraction, which they termed 'magmons' on account of their soliton-like properties (see also Spiegelman, 1993a). When melt production is included however (Scott and Stevenson, 1989), they suggest such waves are unlikely since the 'background' profile of increasing melt fraction inhibits their growth. They point out the importance of consistently modelling the melting process (Stevenson and Scott, 1991).

Fowler (1985, 1989) suggests a model that incorporates temperature as a principal variable and includes equations for the surrounding subsolidus rock. For a one-dimensional situation, a procedure is outlined to uncouple the free boundary location from the interesting dynamics that all occur within the partially molten region, a method that we will later employ.

There has been no comparable attempt to solve the partial melt problem in its wider context until the recent work by Šrámek et al. (2007). Based on the two-phase formalism of Bercovici et al. (2001), they consider the total melting of an ascending column of rock, correctly noting the free boundary at which melting starts, although attempting to determine its position without suitable jump conditions.

All of these works treat the mantle as a one-component rock, so chemical effects do not come into play. A related body of work has treated two-component rocks (and occasionally more), and examined the effects of dissolution reactions (Ortoleva et al., 1987b; Aharonov et al., 1995; Asimow and Stolper, 1999). This typically does not include temperature as a primary variable, and assumes either that melt is already present, or prescribes a background melting rate. Katz (2008) has shown how to incorporate both chemical and thermal effects to consistently determine the melting rate using an enthalpy method.

1.2.5 Outlook

In chapter 2 we review a simple model for a partially molten region, including temperature as a principal variable, and we discuss appropriate boundary conditions to apply to the partial melting that occurs beneath a mid-ocean ridge. Our emphasis is on physics rather than chemistry, so we treat the rock as a single component. This is in line with many previous models; it is a vast simplification of the real mantle, in which the rock composition plays a major role, but we believe the insights that can be gained are useful.

Having established a sensible model, we provide solutions for a one-dimensional upwelling column of mantle such as might be appropriate directly beneath the ridge. The situation differs from that considered by Šrámek et al. (2007), in that we apply thermal boundary conditions at the Earth's surface that acts as a 'lid' on the partially molten region below. This causes a solidified boundary layer (the lithosphere) to form and its position, just as the onset of melting, must be determined by conserving energy across the boundary. The requisite dynamical boundary condition to apply to the partially molten region at this upper boundary has previously been addressed only by Fowler (1989, 1990a) and is not entirely obvious; we suggest later that the requirement that the boundary itself is in thermodynamic equilibrium necessitates that the pressures in the solid and the melt be equal there.

Given a prescribed mantle ascent rate (we consider this to be externally driven by the large-scale mantle circulation) and the temperature of the upwelling rock, the results will allow for the full determination of where and how much partial melting occurs.

1.3 Flow localisation

1.3.1 Melt focussing

At mid-ocean ridges, partial melting occurs over a wide area of upwelling mantle, and yet volcanic activity and new crust generation is confined to a relatively narrow region at the ridge axis. This suggests there is a focussing of magma flow towards the ridge from where it is produced, despite the host matrix spreading away. Spiegelman and McKenzie (1987) showed that the viscous stress gradients due to the 'corner flow' of the matrix naturally focus melt flow from a wider region in to the spreading centre.

Spiegelman (1993a,b) also suggested that ascending magma that reaches the base of the lithosphere without solidifying will spontaneously form into high porosity melt

channels as a result of the rigid overlying lid, and since the lithosphere base slopes upwards towards the ridge axis, these channels provide an efficient route to transport melt to the ridge centre. A similar high porosity boundary layer, or *decompaction* layer was also suggested by Sparks and Parmentier (1991).

However there are various reasons to believe that more substantial focussing of melt occurs within the porous flow (Kelemen et al., 1997). Principally, the chemical composition of erupted melt is inconsistent with ascent purely by porous flow, and is thought to require chemically isolated transport along high porosity or open pathways. Similar evidence comes from radioactive decay rates, which provide constraints on how fast melt has ascended.

1.3.2 Geochemical observations

Chemical analyses of igneous rocks that have been produced from partial melting provide some constraints on the processes involved in their generation and migration. A rock's composition is determined by the complex pattern of melting and solidification through which it has passed; different compositions suggest a different temperature and pressure path to the surface.

The composition of mid-ocean ridge basalt (MORB) collected from spreading ridges is compared to that of residual mantle rock that is dredged from deep ocean rifts (*abyssal* peridotite), or found in mantle *ophiolites* (old sections of mantle that have been lifted and emplaced in the continental crust). It is observed that MORB is undersaturated in the mineral orthopyroxene (Opx) at the pressures typical of the top of the mantle (O'Hara, 1965); the melt from which it solidified is therefore inferred to have travelled from lower in the mantle, where it *was* saturated, without equilibrating with the surrounding rock. Since Opx should quickly dissolve in undersaturated melt this is thought to be inconsistent with porous flow (Spiegelman and Kenyon, 1992; Kelemen et al., 1997).

Evidence for isolated transport also comes from examining trace element concentrations. Highly incompatible elements such as light rare earth elements are preferentially melted near the base of the partial melting zone. Abyssal peridotites are strongly depleted in these elements and are a long way from equilibrium with the melt that formed MORB (Johnson et al., 1990), again suggesting that the melt moved through the upper mantle in chemical isolation (otherwise the supply of enriched melt from below would return trace elements to the depleted peridotite and return them to equilibrium).

There is some heterogeneity in these observations however, and not all melts parental to MORB are thought to be derived from deep in the mantle. Thus MORB represents a mixture of melts derived from different depths, which may be mixed as they ascend, but remain cehmically isolated from the surrounding source rock (Kelemen et al., 1997).

These inferences have led to many conceptual 'two-porosity' models of melt extraction termed *fractional* or *near-fractional* melting - the idea being that melt is produced in the pores in equilibrium with the surrounding matrix, but is then instantaneously, or near-instantaneously, extracted to the surface so that its chemical signature is preserved (Asimow and Stolper, 1999; McKenzie, 1985; Iwamori, 1993).

1.3.3 Geophysical observations

Mantle peridotites in ophiolites also contain evidence for localised flow. These are *dunites*; composed of a very high fraction of olivine, they form elongated lenses and are interpreted as the solidified remains of high porosity melt channels. Their low fraction of pyroxene and large concentration of olivine is thought to be due to dissolution of pyroxene and precipitation of olivine as would be expected during the flow of olivine rich melt. Dunites are found in many locations in a large range of sizes, but are typically tens of metres wide and kilometres long; the largest observed dunites are in Oman (Kelemen et al., 1997).

Besides what can be inferred from observations, continued transport through the lithosphere must occur through some form of dikes or conduits, and in order to avoid freezing this must occur at a sufficiently fast rate; there must therefore be a large supply of magma to the base of the lithosphere, which requires some form of localisation in the asthenosphere below.

1.3.4 Focussing mechanisms

The inference that porous flow may not be the main extraction mechanism from the partially molten region has led to various suggested mechanisms that would cause more localised flow.

One obvious such mechanism is if the matrix fractures (Nicolas, 1986; Sleep, 1988; Ito and Martel, 2002; Maaloe, 2003). There is some debate over whether fracture in the usual (elastic) sense can occur at depth within the mantle, because the rock is sufficiently ductile that large stresses are relieved by plastic deformation. High melt pressures would certainly facilitate the magma-fracturing process, and Nicolas (1986)

found evidence for fracture-like dikes in ophiolites. If fractures do occur, they may migrate upwards and coalesce (Ito and Martel, 2002), and if there are sufficiently many they may connect and form a network for melt transport (Maaloe, 2003). Sleep (1988) showed how low melt pressure within a dike can draw in melt from the surrounding porous rock and this would enable an initially small fracture to grow and transport considerable quantities of melt.

An instability introduced by Stevenson (1989) involves a positive feedback between porosity and solid deformation (Buck and Su, 1989; Richardson, 1998). In a viscously deforming medium it is expected that the presence of melt weakens the matrix so that regions of higher porosity are weaker. Under shearing conditions this causes the pressure there to be decreased; melt is therefore drawn from the stronger regions to the weaker regions, which are thus further weakened. This can lead to the formation of high porosity 'melt bands' (Spiegelman, 2003; Katz et al., 2006).

A rather different type of instability, and currently perhaps the favoured explanation for focussed flow, is the reactive infiltration instability (RII) (Ortoleva et al., 1987b,a; Kelemen et al., 1995; Aharonov et al., 1995; Spiegelman et al., 2001; Spiegelman and Kelemen, 2003). This relies on a feedback between dissolution and melt flux, and will occur if the solubility of some mineral, such as pyroxene, increases with decreasing pressure and therefore depth. Unsaturated flow from lower in the partially molten region causes dissolution and areas of larger than average porosity with a large melt flow therefore undergo more dissolution; this further increases the porosity and a positive feedback develops. Stabilizing mechanisms include diffusion of solute in the melt, and compaction of the matrix, and these lead to strongly preferred wavelength selection (Spiegelman et al., 2001), with a channel spacing smaller than the *compaction length*, which will be seen in chapter 2 to be the length over which differential pressures cause compaction of the matrix.

Essentially the same instability can occur without the need for dissolution, even for a one-component rock, when the solidus is pressure dependent; this type of *melting* instability was suggested by Sleep (1988) and Fowler (1990b), but has not been fully explored. The rate of decompression melting is determined by how fast the upwelling material decompresses, and therefore transfers its sensible heat to latent heat. In regions of large melt fraction, the *melt*, rather than the matrix, provides the dominant vertical heat transport, so the regions of larger melt fraction undergo more melting and a positive feedback ensues. In chapter 3 we demonstrate this instability using the simple model of chapter 2.

1.3.5 Channelised flow

Either fracturing or reactive instabilities may allow for the possibility of open channels of melt in the mantle. If a fracture forms it would likely be planar in shape, and magma would flow in a narrow walled crack. Viscous closure of the crack walls, and non-uniform melting, might however be expected to cause it to gradually evolve into a series of more cylindrical conduits, similar to the flow in fissures described by Bruce and Huppert (1989; Huppert and Bruce, 1990).

Some studies of open conduits in the mantle have been made in the past; experiments have been conducted by injecting light viscous fluids into more viscous one and comparing the observations with theory for flow in deformable tubes (Scott et al., 1986; Olson and Christensen, 1986; Helfrich and Whitehead, 1990). Much of the interest has been with the solitary waves that travel up such conduits and for which the experiments and theory are in good agreement.

Richardson et al. (1996) considered conduit flow within a viscous porous medium, and studied the flow into and out of the conduit during the passage of a solitary wave.

Little attention has however been paid to how melt gets into a supposed conduit from the surrounding partial melt, and it is evidently crucial that this is possible, as supplying a lumped influx at the bottom of a conduit in the mantle seems unrealistic. As mentioned above, Sleep (1988) considered how melt can be drawn into a low pressure inclusion and found that this is possible over distances comparable to the compaction length.

1.3.6 Outlook

In chapter 3 we study the dynamics of open magma channels in the mantle, and we consider the flow into such a channel from the surrounding partial melt. Importantly, we consider the effects of decompression melting as a result of the magma flow. This effect has not been included in previous models but, if such fractures or conduits do exist within the mantle, we will see that it plays an important role in determining how they behave.

The situation we find is very similar to that which is well known for channels of melt water beneath glaciers (Röthlisberger, 1972; Nye, 1976), with the size of the channel largely governed by a balance between melting and viscous closure of the walls. In the subglacial case the melting is driven by viscous dissipation of the turbulent water flow, whereas in this case it is driven by laminar advection down

the solidus gradient; both these situations have the effect of providing a melting rate which is proportional to flow rate.

Using the model of chapter 2, we examine how an open channel can evolve from a perturbation to the porous flow in the partially molten region as a result of the runaway melting instability outlined above. We find that melt is drawn into a channel from a distance on the order of the compaction length, and suggest that adjacent channels might be spaced at this distance.

Chapter 2

Partial melting in upwelling mantle

2.1 Mathematical model

2.1.1 Model setup

The situation we consider is shown in figure 2.1; larger scale plate motion and mantle convection cause upwelling and spreading of the mantle rock. Decompression causes a region D to become partially molten, and this is separated from the subsolidus (solid) region D^+ by an unknown boundary ∂D. The model consists of equations to describe the dynamics within D and D^+, together with boundary conditions across ∂D, at the fixed Earth surface and in the deep mantle.

When we come to find solutions we consider the case of a one-dimensional upwelling column, and therefore neglect the 'corner flow' of the matrix near the surface. In this case the matrix unrealistically (but necessarily) continues to move vertically 'through' the surface of the Earth. In reality it would turn sideways and move away with the spreading plates, but we hope that the one dimensional solutions give a reasonable approximation to the situation directly beneath the ridge.

2.1.2 Partially molten rock

The equations we use to model the partially molten region are based on conservation of mass, momentum and energy over representative volumes of the porous medium, supplemented by constitutive laws which parameterise the finer scale physics.

Balance laws

It may be helpful later to have recourse to the integral form of the conservation laws, so we start from these. For an arbitrary volume of the partially molten region V with

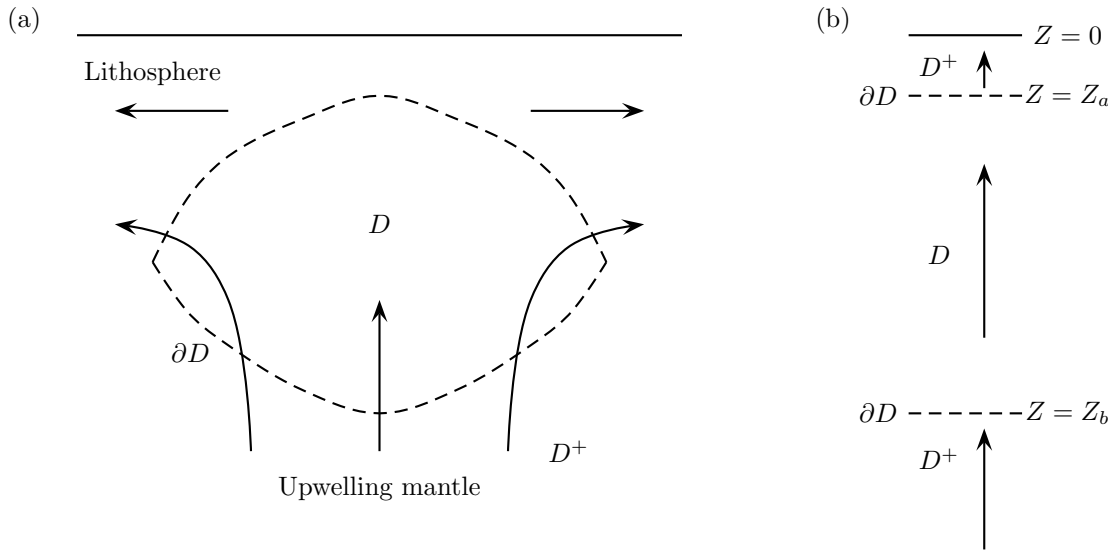

Figure 2.1: (a) Schematic of the model region considered in section 2.1. The partially molten region D is bounded by ∂D from the subsolidus regions D^+. Arrows show the direction of matrix motion at a mid-ocean ridge. (b) The one-dimensional set-up, with Z measured vertically upwards from the surface and the partial melt occupying the region $Z_b < Z < Z_a$.

boundary ∂V having outward pointing normal $\mathbf{n}$, conservation of mass for each phase is expressed by

$$\frac{d}{dt}\int_V \rho_l \phi \ \mathrm{d}V = -\int_{\partial V} \rho_l \phi \mathbf{u}\cdot\mathbf{n} \ \mathrm{d}S + \int_V m \ \mathrm{d}V, \tag{2.1}$$

$$\frac{d}{dt}\int_V \rho_s (1-\phi) \ \mathrm{d}V = -\int_{\partial V} \rho_s (1-\phi)\mathbf{V}\cdot\mathbf{n} \ \mathrm{d}S - \int_V m \ \mathrm{d}V, \tag{2.2}$$

in which $\mathbf{u}$ and $\mathbf{V}$ are the velocities of melt and solid, respectively; ρ_s and ρ_l are the densities of melt and solid, respectively; and m (kg m^{-3} s^{-1}) is the melt rate converting solid into melt.

Inertia is negligible so conservation of overall momentum is expressed by the force balance

$$\int_{\partial V} \phi\boldsymbol{\sigma}_l\cdot\mathbf{n} + (1-\phi)\boldsymbol{\sigma}_s\cdot\mathbf{n} \ \mathrm{d}S + \int_V \rho_l\phi\mathbf{g} + \rho_s(1-\phi)\mathbf{g} \ \mathrm{d}V = 0, \tag{2.3}$$

in which $\boldsymbol{\sigma}_l$ and $\boldsymbol{\sigma}_s$ are the stress tensors in the melt and matrix, respectively, and $\mathbf{g} = -g\mathbf{k}$ is the gravitational acceleration, in the vertical direction.

Conservation of energy requires

$$\begin{aligned}\frac{d}{dt}\int_V \rho_l\phi e_l + \rho_s(1-\phi)e_s \ \mathrm{d}V = &-\int_{\partial V} [\rho_l\phi e_l\mathbf{u} + \rho_s(1-\phi)e_s\mathbf{V}]\cdot\mathbf{n} \ \mathrm{d}S + \int_{\partial V} k\nabla T\cdot\mathbf{n} \ \mathrm{d}S \\ &+ \int_{\partial V} \phi\mathbf{u}\cdot\boldsymbol{\sigma}_l\cdot\mathbf{n} + (1-\phi)\mathbf{V}\cdot\boldsymbol{\sigma}_s\cdot\mathbf{n} \ \mathrm{d}S + \int_V \rho_l\phi\mathbf{g}\cdot\mathbf{u} + \rho_s(1-\phi)\mathbf{g}\cdot\mathbf{V} \ \mathrm{d}V,\end{aligned} \tag{2.4}$$

in which e_l and e_s are the specific internal energy (i.e. energy per unit mass) of the melt and solid phases, T is the temperature, which is assumed to be the same in each phase, and k is the thermal conductivity, which for simplicity we also assume to be the same in each phase.

Darcy's law

Separately conserving momentum of each phase in (2.3) requires consideration of local interfacial forces and surface effects; we gloss over these details and assume from the outset that the local force balance is described by Darcy's law for the relative motion between the phases,

$$\phi(\mathbf{u} - \mathbf{V}) = \frac{k_\phi}{\eta_l}(-\nabla p_l + \rho_l \mathbf{g}), \tag{2.5}$$

Here p_l is the pressure in the melt, η_l is the melt viscosity, and the permeability k_ϕ depends on the porosity,

$$k_\phi = \frac{a^2\phi^2}{b}, \tag{2.6}$$

with a being a typical grain size in the rock, and b a tortuosity factor.

Rheology

Having accounted for the melt's viscosity in Darcy's law we now recognise that compared to the matrix, the melt supports negligible deviatoric stress. It is therefore sensible to assume the following constitutive laws for the stress tensors in (2.3);

$$\boldsymbol{\sigma}_l = -p_l \boldsymbol{\delta}, \tag{2.7}$$

$$\boldsymbol{\sigma}_s = -p_s \boldsymbol{\delta} + \boldsymbol{\tau}, \quad \boldsymbol{\tau} = \eta_s \left(\nabla \mathbf{V} + \nabla \mathbf{V}^T - \frac{2}{3}\boldsymbol{\delta} \nabla \cdot \mathbf{V} \right), \tag{2.8}$$

where p_l and p_s are the pressure in melt and solid, respectively, $\boldsymbol{\tau}$ is the deviatoric stress tensor, and η_s is the viscosity of the solid rock.

Conservation equations

Assuming the variables are smooth, the integral equations (2.1) and (2.2), are expressed by the differential equations

$$\frac{\partial}{\partial t}(\phi \rho_l) + \nabla . (\phi \rho_l \mathbf{u}) = m, \tag{2.9}$$

$$\frac{\partial}{\partial t}((1-\phi)\rho_s) + \nabla . ((1-\phi)\, \rho_s \mathbf{V}) = -m, \tag{2.10}$$

the force balance (2.3) is

$$0 = -\nabla p_s + \nabla(\phi(p_s - p_l)) + \rho_s \mathbf{g} - \phi(\rho_s - \rho_l)\mathbf{g} + \nabla \cdot (1-\phi)\boldsymbol{\tau}, \tag{2.11}$$

and the energy equation (2.4) becomes

$$\frac{\partial}{\partial t}\left((1-\phi)\rho_s e_s + \phi\rho_l e_l\right) + \nabla.\left((1-\phi)\rho_s e_s \mathbf{V} + \phi\rho_l e_l \mathbf{u}\right) = \nabla.\left(k\nabla T\right) + \Psi, \tag{2.12}$$

where Ψ is the work done against viscous and gravitational forces,

$$\Psi = \nabla \cdot ((1-\phi)\mathbf{V} \cdot \boldsymbol{\sigma}_s) + \nabla \cdot (\phi \mathbf{u} \cdot \boldsymbol{\sigma}_l) + (1-\phi)\rho_s \mathbf{g} \cdot \mathbf{V} + \phi\rho_l \mathbf{g} \cdot \mathbf{u}. \tag{2.13}$$

After repeated use of (2.9)-(2.11), and with the definition of latent heat

$$L = \Delta e + p_l \Delta v = e_l - e_s + p_l\left(v_l - v_s\right), \tag{2.14}$$

($v = 1/\rho$ is the specific volume), we can write (2.12) as

$$\begin{aligned} &mL + (1-\phi)\rho_s c\left(\frac{\partial T}{\partial t} + \mathbf{V} \cdot \nabla T\right) + \phi\rho_l c\left(\frac{\partial T}{\partial t} + \mathbf{u} \cdot \nabla T\right) \\ &- (1-\phi)\beta T\left(\frac{\partial p_s}{\partial t} + \mathbf{V} \cdot \nabla p_s\right) - \phi\beta T\left(\frac{\partial p_l}{\partial t} + \mathbf{u} \cdot \nabla p_l\right) = \nabla \cdot (k\nabla T) + \Phi. \end{aligned} \tag{2.15}$$

Here c is the specific heat capacity, β is the thermal expansion coefficient (both assumed equal in each phase), and Φ is the viscous dissipation, given by

$$\Phi = (1-\phi)\boldsymbol{\tau} : \nabla\mathbf{V} - (1-\phi)\frac{p_s - p_l}{\rho_s}\left(\frac{\partial \rho_s}{\partial t} + \nabla \cdot (\rho_s \mathbf{V})\right) + \phi(\mathbf{u} - \mathbf{V}) \cdot (-\nabla p_l + \rho_l \mathbf{g}). \tag{2.16}$$

Local thermodynamic equilibrium

We make the assumption that the partially molten region is in local thermodynamic equilibrium - that is, we assume that the flow of heat across the solid-melt interface is virtually instantaneous and given the local stress field the interfacial temperature will quickly reach equilibrium. Our assumptions concerning the pressure difference $p_s - p_l \neq 0$ mean that the stresses do not equilibrate so readily, so local thermodynamic equilibrium means that the temperature will depend on the interfacial stress which, since $\eta_l \ll \eta_s$, is the liquid pressure p_l (Kamb, 1961).

Thermodynamic equilibrium requires the continuity of free energy across the interface, thus we require

$$\Delta G = \Delta h - T\Delta S = 0, \tag{2.17}$$

where $\Delta G = G_l - G_s$ is the difference in specific Gibbs free energy, $\Delta h = \Delta e + p_l \Delta v$ is the specific enthalpy difference and $\Delta S = S_l - S_s$ is the specific entropy difference. By considering variations in the pressure p_l and melting temperature T_S from reference values p_m, T_m, this gives the equilibrium Clapeyron condition

$$T_S = T_m + \Gamma(p_l - p_m). \tag{2.18}$$

in which Γ is the Clapeyron slope. The subscript S here refers to the *solidus* temperature; more generally this will also depend on the composition of the rock, but we consider only one component for simplicity, so that the solidus depends only on pressure.

Compaction

As in any two-phase flow model, we must close the problem by prescribing a relationship between the pressures of the phases. This is commonly done using a bulk viscosity (1.1), but this expression should more properly be viewed as the *definition* of the bulk viscosity, which we should therefore derive. One way of doing this is to consider the deformation of individual 'tubules' in the porous matrix (Nye, 1953; Sleep, 1988); if we consider these as cylinders of radius a, contained in representative areas A^2 of the matrix, the walls of the cylinder will enlarge by melting at a rate $m_* = mA^2$ and close down by viscous creep at a rate $\pi a^2(p_s - p_l)/\eta_s$, thus

$$2\pi a \frac{da}{dt} = \frac{m_*}{\rho_s} - \frac{\pi a^2}{\eta_s}(p_s - p_l). \tag{2.19}$$

Associating the area of these tubules with the porosity, so that $\pi a^2 = \phi A^2$, we have

$$\frac{\phi}{\eta_s}(p_s - p_l) = \frac{m}{\rho_s} - \frac{d\phi}{dt}, \tag{2.20}$$

and now combining with mass conservation (2.10), assuming ρ_s is constant, and ignoring the small term proportional to ϕ (this argument is only appropriate with the assumption of small porosity), gives (1.1) in the form

$$p_s - p_l = -\frac{\eta_s}{\phi} \nabla \cdot \mathbf{V}. \tag{2.21}$$

Similar expressions can be derived from alternative microscopic models; Batchelor (1967) derives the same expression for the bulk viscosity by considering energy dissipation when a two phase material is compressed, and Šrámek et al. (2007) also recover (2.21) with a more in depth discussion of the interface thermodynamics.

Summary

The equations proposed to model the partially molten region are conservation of mass for each phase (2.9) and (2.10), overall force balance (2.11), and conservation of energy (2.15). The melt flow is governed by Darcy's law (2.5), and the divergence (or otherwise) of the matrix by the compaction law (2.21). The temperature is constrained to the solidus (2.18), which closes the problem, providing 7 equations for the 7 unknowns (in one-dimension) ϕ, $\mathbf{u}$, $\mathbf{V}$, p_s, p_l, m and T.

Having allowed for the variation in density due to pressure changes in deriving (2.15), and therefore accounted for cooling due to adiabatic decompression, we will subsequently assume that the density of each phase is constant, with $\rho_l < \rho_s$. We also treat the other material properties in the problem as constants; this is a simplification, since the viscosity of the matrix, in particular, should vary considerably with temperature and pressure. Indeed it is the large increase in viscosity as the rock cools near the surface that determines where the asthenosphere merges with the lithosphere. The mantle deforms by viscous creep and would probably also be modelled better using a power law rheology, for which the *effective* viscosity depends on the state of stress.

2.1.3 Subsolidus rock

In the subsolidus region the equations are much simpler. We include the same physical mechanisms and assume the same solid rheology and material properties, so the equations can be read off from the previous section taking $\phi = 0$. The continuity and momentum equations are the standard Navier Stokes equations for an incompressible viscous fluid at zero Reynolds number, with velocity $\mathbf{V}$ and pressure p,

$$\nabla \cdot \mathbf{V} = 0, \tag{2.22}$$

$$0 = -\nabla p + \rho_s \mathbf{g} + \eta_s \nabla^2 \mathbf{V}, \tag{2.23}$$

The energy equation takes the form

$$\rho_s c \left(\frac{\partial T}{\partial t} + \mathbf{V} \cdot \nabla T \right) - \beta T \left(\frac{\partial p}{\partial t} + \mathbf{V} \cdot \nabla p \right) = \nabla \cdot (k \nabla T) + \Phi, \tag{2.24}$$

and since the temperature is no longer constrained to the solidus, this determines T.

2.1.4 Boundary conditions

Two types of boundary conditions are required to consider the problem set out in figure 2.1; prescribed conditions at the 'fixed' boundaries - the surface and the deep mantle - and conservation laws across the interface ∂D between the subsolidus and partially molten rock. The first of these, the conditions at the fixed boundaries, depend rather on the particular solution one wants to look for; we expect to prescribe the temperature at the surface and of the upwelling rock, as well as suitable conditions on the subsolidus flow. In particular we expect to prescribe the upwelling rate $\mathbf{V} = W\mathbf{k}$ deep beneath the axis. We leave further discussion of these conditions until the next section, and concentrate on the conditions on ∂D.

Jump conditions

At the boundary between melting and solid regions, the same physical principles of mass, momentum and energy conservation must apply. Working from the integral forms in (2.1)-(2.4) we derive the following Rankine-Hugoniot 'jump' conditions between values on either side of the boundary:

$$(\rho_l\phi + \rho_s(1-\phi) - \rho_s)\,\mathbf{v}\cdot\mathbf{n} = \rho_l\phi\mathbf{u}\cdot\mathbf{n} + \rho_s(1-\phi)\mathbf{V}\cdot\mathbf{n} - \rho_s\mathbf{V}^+\cdot\mathbf{n}, \tag{2.25}$$

$$\phi\boldsymbol{\sigma}_l\cdot\mathbf{n} + (1-\phi)\boldsymbol{\sigma}_s\cdot\mathbf{n} = \boldsymbol{\sigma}^+\cdot\mathbf{n}, \tag{2.26}$$

$$\begin{aligned}\left(\rho_l\phi e_l + \rho_s(1-\phi)e_s - \rho_s e_s^+\right)\mathbf{v}\cdot\mathbf{n} = &\left(\rho_l\phi e_l\mathbf{u}\cdot\mathbf{n} + \rho_s(1-\phi)e_s\mathbf{V}\cdot\mathbf{n} - \rho_s e_s^+\mathbf{V}^+\cdot\mathbf{n}\right)\\ &+ \left[k\frac{\partial T}{\partial n}\right]_-^+ - \left(\phi\mathbf{u}\cdot\boldsymbol{\sigma}_l\cdot\mathbf{n} + (1-\phi)\mathbf{V}\cdot\boldsymbol{\sigma}_s\cdot\mathbf{n} - \mathbf{V}^+\cdot\boldsymbol{\sigma}^+\cdot\mathbf{n}\right)\end{aligned} \tag{2.27}$$

Here $^+$ refers to subsolidus variables, while the subscripts s and l refer to values in the partially molten region; $\mathbf{n}$ is the outward pointing (towards the subsolidus side) normal to the boundary; and $\mathbf{v}$ is the velocity of the boundary, which will be zero in a steady state. $[]_-^+$ denotes the jump in the quantity from partially molten to subsolidus regions. Ignoring the small deviatoric stress in (2.26), these can be rearranged to give the following conditions:

$$\rho_l\phi(\mathbf{u}-\mathbf{v})\cdot\mathbf{n} - \rho_s\phi(\mathbf{V}-\mathbf{v})\cdot\mathbf{n} = \rho_s(\mathbf{V}^+-\mathbf{V})\cdot\mathbf{n}, \tag{2.28}$$

$$\phi p_l + (1-\phi)p_s = p^+, \tag{2.29}$$

$$\rho_l L\phi(\mathbf{u}-\mathbf{v})\cdot\mathbf{n} = \left[-k\frac{\partial T}{\partial n}\right]_-^+ + \phi(1-\phi)(p_s-p_l)\left(\frac{\rho_l}{\rho_s}(\mathbf{u}-\mathbf{v})\cdot\mathbf{n} - (\mathbf{V}-\mathbf{v})\cdot\mathbf{n}\right). \tag{2.30}$$

We must also require the continuity of temperature across the boundary,

$$[T]_-^+ = 0. \tag{2.31}$$

Thermodynamic equilibrium of the boundaries

Conditions (2.28)-(2.31) tell us something about the velocity, temperature and pressures at ∂D, but are not sufficient to close the problem; (2.29) can provide only one condition on the pressures p_s and p_l and since these are different we still need another condition to relate them. We also need a condition on the melt fraction ϕ; it seems intuitive to assume that the melt fraction at the onset of melting is zero so that the necessary condition is $\phi = 0$ on the lower part of ∂D (this may be defined specifically as that part of ∂D where $\mathbf{V} \cdot \mathbf{n} < 0$).

We can in fact derive this condition, and the extra condition on the pressure, by the requirement that the boundary itself is in thermodynamic equilibrium; we have previously assumed a local thermodynamic equilibrium within the partially molten region in order to derive the Clapeyron relationship (2.18); at the boundary ∂D we also suppose that macroscopic thermodynamic equilibrium must be achieved between the partially molten region and the subsolidus region, by ensuring the continuity of the average Gibbs free energy across the boundary.

We can write the average free energy on either side of the boundary (see Fowler, 1990a) as

$$G^+ = h_s^+ - TS_s \quad G^- = (h_s - TS_s) + \phi(\Delta h - T\Delta S). \tag{2.32}$$

In the reference state in which $p_s = p_l = p^+$, $h_s = h_s^+$, so continuity requires

$$[G]_-^+ = -\phi(\Delta h - T\Delta S) = 0, \tag{2.33}$$

which is the local equilibrium condition. Perturbations δp_s, δp_l, δp^+, δT and $\delta\phi$ to pressures, temperature and melt fraction must maintain this equilibrium and, noting that $\delta[\phi(\Delta h - T\Delta S)] = 0$ for local equilibrium, we therefore require

$$[\delta G]_-^+ = (v_s \delta p^+ - S_s \delta T) - (v_s \delta p_s - S_s \delta T) = 0. \tag{2.34}$$

Since in the reference state $p_s = p^+$, we find the thermodynamic condition $p_s = p^+$. From (2.29), this provides the extra condition on ∂D,

$$\phi(p_s - p_l) = 0. \tag{2.35}$$

Notice that this condition requires *either* that the melt fraction ϕ is zero *or* the pressure difference $p_s - p_l$ is zero. In practice, we expect the former to apply to the lower part of ∂D where the melting begins and the latter to apply to the upper boundary. From (2.30), this implies a continuous temperature gradient at the lower boundary, but solidification and a jump in temperature gradient at the upper boundary.

We are forced to assume here that melt will solidify at the upper boundary of the partial melting region. That this is not necessarily the case is manifestly true; magma erupts from the surface and is known to be emplaced in magma chambers within the lithosphere. However the processes which allow this to happen are not entirely clear; certainly it seems that magmafracturing and transport up preexisting conduits within the lithosphere play a major part, but how these are connected to the partial melt zone below is very much open to debate.

In the absence of any definite idea of what precisely does happen at the top of the partial melting region, we look for the simplest thermodynamically viable solution, and therefore make the naïve assumption that all the melt solidifies.

2.2 Non-dimensionalisation and simplification

2.2.1 Coordinate system

The model for the partially molten region in the previous section is a reasonably complicated set of non-linear partial differential equations, and it is helpful to scale all the variables with typical values in order to determine which are the dominant terms. Our solutions in the next section will focus on the one-dimensional upwelling column directly beneath the ridge, so it may be helpful to have the situation in figure 2.1(b) in mind.

The surface of the Earth is labelled $Z = 0$, with Z being the vertical coordinate, measured upwards. If no partial melting occurred, the mantle would rise steadily and the pressure profile would be *lithostatic*,

$$p_s = p_m + \rho_s g(Z_m - Z), \tag{2.36}$$

with reference pressure p_m at depth Z_m. The melting temperature in this case would be given instead of (2.18), by the *lithostatic solidus*

$$T_{LS} = T_m + \Gamma \rho_s g(Z_m - Z), \tag{2.37}$$

with reference melting temperature T_m at the reference depth Z_m, which we now define.

The adiabatic geotherm that the ascending rock would follow (if melting were ignored) would in some places be above the lithostatic solidus (figure 1.2) and this is (approximately) the region that must therefore undergo partial melting. We therefore choose the reference depth Z_m to be the depth at which the lithostatic solidus and

adiabatic geotherm first intersect - this should be near to (though as we shall see, not exactly) the depth at which melting starts. We take this depth to be known, and since in theory we might expect to know what the lithostatic solidus is as a function of depth, prescribing this depth effectively means prescribing the temperature of the upwelling rock.

Somewhere close to Z_m partial melting begins, and somewhere close to the surface $Z = 0$, the cold surface temperature is noticed and the partial melting region ends. We label these positions Z_b and Z_a, respectively, as shown in figure 2.1. As discussed previously the exact positions of these boundaries must form part of the solution, being found from the conservation laws in section 2.1.4.

However, the interesting dynamics are all contained *within* the partially molten region, which therefore attracts the majority of our attention; for this reason, we define another vertical coordinate $z = Z - Z_b$, so that the partial melt occupies $0 < z < l \equiv Z_a - Z_b$. By taking a good guess for this depth l, we can find the solution for the partial melting region assuming we knew it, and then use the jump conditions at Z_b and Z_a to precisely locate these boundaries, which then define the actual depth l. In this way, we can effectively separate out the solution within the partial melting region and the determination of the free boundaries. A similar procedure was outlined by Fowler (1989).

2.2.2 Scaling

We choose to scale all lengths using the depth of the partially molten region l; as discussed above, *a priori* we have only a guess at exactly what it should be, but it can be revised later. In fact, for much of this chapter, and all of chapter 3, we will assume l is known, and in section 2.3.5 we use the jump conditions on the boundaries to determine it.

We expect the pressure to be approximately given by (2.36); we therefore define a dimensionless pressure deviation p_s^* from the reference state p_m, by

$$p_s = p_m + \rho_s g l p_s^*. \tag{2.38}$$

We also expect the melt pressure p_l to follow a similar scale, but in fact it is the pressure *difference*, or *effective* pressure,

$$N = p_s - p_l, \tag{2.39}$$

which is crucial to the compaction dynamics, and we therefore use it as a primary variable in favour of p_l.

The temperature within the partially molten region follows the solidus, which will be given approximately by (2.37); it is therefore appropriate to scale the temperature according to

$$T - T_m \sim \Gamma \rho_s g l \tag{2.40}$$

Taking the mantle velocity scale V_0 to be prescribed, we then choose sensible scales for the remaining variables by balancing terms in the partial melt equations (2.5), (2.21), (2.9)-(2.11), (2.15) and (2.18). The melting scale follows from balancing the advection up the Clapeyron slope with the latent heat consumption in (2.15). The melt velocity is determined principally by buoyancy in Darcy's law (2.5), and the melt fraction then follows from balancing the divergence with melt production in (2.9). The scale for the effective pressure is then determined by balancing terms in the compaction relation (2.21). We therefore scale according to

$$mL \sim \rho_s c \Gamma \rho_s g V_0, \quad \phi u \sim \frac{k_\phi}{\eta_l} \Delta\rho g \sim \frac{ml}{\rho_l}, \quad N \sim \frac{\eta_s}{\phi} \frac{\phi u}{l}. \tag{2.41}$$

These balances are achieved by writing $z = lz^*$, $\mathbf{V} = V_0 \mathbf{V}^*$, $T = T_m + T_0 T^*$, $m = m_0 m^*$, $\phi = \phi_0 \phi^*$, $\mathbf{u} = u_0 \mathbf{u}^*$, $N = N_0 N^*$ and $t = t_0 t^*$, and choosing the scales (with subscript 0) to be:

$$T_0 = \Gamma \rho_s g l, \tag{2.42}$$

$$m_0 = \frac{c \Gamma \rho_s^2 g V_0}{L}, \tag{2.43}$$

$$\phi_0 = \left[\frac{b \eta_l c \Gamma \rho_s^2 V_0 l}{a^2 L \rho_l \Delta\rho} \right]^{1/2}, \tag{2.44}$$

$$u_0 = \frac{a^2 \Delta\rho g}{b \eta_l} \phi_0, \tag{2.45}$$

$$N_0 = \frac{\eta_s a^2 \phi_0 \Delta\rho g}{b \eta_l l}, \tag{2.46}$$

$$t_0 = \frac{l}{V_0} \tag{2.47}$$

Scaled partial melt equations

With these definitions we can rewrite the partial melt equations in non-dimensional form, dropping the asterisks but understanding that all the variables are now scaled as above. The mass conservation equations (2.9) and (2.10) can be rewritten

$$\varepsilon \frac{\partial \phi}{\partial t} + \varepsilon \nabla \cdot (\phi \mathbf{V}) + \nabla \cdot [\phi(\mathbf{u} - \varepsilon \mathbf{V})] = m, \tag{2.48}$$

$$r\nabla\cdot[\phi(\mathbf{u}-\varepsilon\mathbf{V})]+St\nabla\cdot\mathbf{V}=(r-1)m, \tag{2.49}$$

the momentum equation (2.11) becomes

$$0=-\nabla p_s-\mathbf{k}+\delta_s^2\varepsilon\nabla\cdot((1-\phi_0\phi)\boldsymbol{\tau})+\frac{r-1}{r}\phi_0\left(\delta^2\nabla\left(\phi N\right)+\phi\mathbf{k}\right). \tag{2.50}$$

Using this, Darcy's law (2.5) can be written

$$\phi\left(\mathbf{u}-\varepsilon\mathbf{V}\right)=\phi^2\left((1-\phi_0\phi)\mathbf{k}+\delta^2\nabla(1-\phi_0\phi)N-\delta^2\varepsilon\nabla\cdot((1-\phi_0\phi)\boldsymbol{\tau})\right). \tag{2.51}$$

The compaction relation (2.21) is

$$r\phi N=-St\nabla.\mathbf{V}, \tag{2.52}$$

and the energy equation (2.15) is

$$\begin{aligned}&m+\frac{1}{St}\phi\left[\left(\varepsilon\frac{\partial}{\partial t}+\mathbf{u}\cdot\nabla\right)T-\lambda r(1+\hat{\mu}T)\left(\varepsilon\frac{\partial}{\partial t}+\mathbf{u}\cdot\nabla\right)\left(p_s-\delta_s^2N\right)\right]\\&+(1-\phi_0\phi)\left[\left(\frac{\partial}{\partial t}+\mathbf{V}\cdot\nabla\right)T-\lambda\left(1+\hat{\mu}T\right)\left(\frac{\partial}{\partial t}+\mathbf{V}\cdot\nabla\right)p_s\right]=\frac{1}{Pe}\nabla^2T+\nu\,\Phi.\end{aligned} \tag{2.53}$$

with the dimensionless dissipation given by

$$\Phi=\frac{r-1}{St}(\mathbf{u}-\varepsilon\mathbf{V})\cdot(\mathbf{u}-\varepsilon\mathbf{V})+\frac{r-1}{r}\delta^2\varepsilon(1-\phi_0\phi)\boldsymbol{\tau}:\nabla\mathbf{V}-\frac{r-1}{r}\delta^2(1-\phi_0\phi)N\nabla\cdot\mathbf{V}, \tag{2.54}$$

and the matrix stress tensor by

$$\boldsymbol{\tau}=\nabla\mathbf{V}+\nabla\mathbf{V}^T-\frac{2}{3}\boldsymbol{\delta}\nabla\cdot\mathbf{V}. \tag{2.55}$$

The solidus (2.18), to which the temperature is confined, is given by

$$T=p_s-\delta_s^2N. \tag{2.56}$$

Non-dimensional parameters

Several new non-dimensional parameters have been defined:

$$r=\frac{\rho_s}{\rho_l}, \tag{2.57}$$

$$\lambda=\frac{\beta T_m}{\rho_s c\Gamma}, \tag{2.58}$$

$$\hat{\mu}=\frac{T_0}{T_m}, \tag{2.59}$$

Parameter	Value	Parameter	Value
g	10 m s^{-2}	β	3×10^{-5} K^{-1}
ρ_s	3×10^3 kg m^{-3}	b	1000
ρ_l	2.5×10^3 kg m^{-3}	a	2×10^{-3} m
Γ	10^{-7} K Pa^{-1}	η_l	10 Pa s
c	10^3 J kg^{-1} K^{-1}	η_s	10^{19} Pa s
k	2.5 J K^{-1} m^{-1} s^{-1}	T_m	1500 K
L	3×10^5 J kg^{-1}	T_s	300 K

Table 2.1: Values of constants used in chapter 2.

$$Pe = \frac{\rho_s c V_0 l}{k}, \tag{2.60}$$

$$\nu = \frac{gl}{c\Gamma\rho_s gl}, \tag{2.61}$$

$$St = \frac{L}{c\Gamma\rho_s gl}, \tag{2.62}$$

$$\varepsilon = \frac{V_0}{u_0} = \left[\frac{b\eta_l\rho_l L V_0}{a^2\Delta\rho\rho_s^2 g^2 c\Gamma l}\right]^{1/2}, \tag{2.63}$$

$$\delta^2 = \frac{N_0}{\Delta\rho gl} = \frac{k_{\phi 0}\eta_s}{\eta_l\phi_0 l^2}, \tag{2.64}$$

$$\delta_s^2 = \frac{N_0}{\rho_s gl}; \tag{2.65}$$

r is the density ratio; λ is the ratio of adiabatic to solidus temperature gradients; $\hat{\mu}$ is the ratio of temperature variation across the partially molten region to absolute temperature; Pe is the usual Péclet number; ν the ratio of gravitational potential energy to sensible heat. St is the usual Stefan number, the ratio of latent to sensible heat; ε is the ratio of typical velocities of solid and melt; δ^2 is the ratio of effective pressure gradients to buoyancy; and δ_s^2 is the ratio of effective pressure gradients to the lithostatic pressure gradient.[1]

Note that ϕ_0 is also a non-dimensional parameter, but it is related to the others by $\phi_0 = \varepsilon r/St$, and δ_s^2 is also not independent of δ^2 and r. We nevertheless use them here, for notational convenience, and to aid interpretation.

Typical values of parameters

Table 2.1 shows typical values of the various constants, which we use to estimate the size of the scales and the non-dimensional parameters. Typical estimates of the rate

[1]Note these definitions of δ and δ_s are the square roots of those used in Hewitt and Fowler (2008a) - the usage here is intended to be more consistent with other authors and with Hewitt and Fowler (2009); δ will be the dimensionless compaction length.

of mid-ocean ridge spreading suggest that new crust is generated at a rate between 1 and 10 cm a^{-1}. We take the mantle velocity scale $V_0 = 10^{-9}$ m $s^{-1} \approx 3$ cm a^{-1} consistent with this range. The depth l of the partial melting region is yet to be found exactly but will be given approximately by the reference depth $-Z_m$, for which we take the nominal value 50 km. With the values given in table 2.1, we find

$$m_0 \sim 3 \times 10^{-11} \text{ kg m}^{-3} \text{ s}^{-1}, \tag{2.66}$$

$$\phi_0 \sim 0.02, \tag{2.67}$$

$$u_0 \sim 3.5 \times 10^{-8} \text{ m s}^{-1}, \tag{2.68}$$

$$N_0 \sim 7 \times 10^{6} \text{ Pa}, \tag{2.69}$$

$$T_0 \sim 150 \text{ K}, \tag{2.70}$$

$$t_0 \sim 5 \times 10^{13} \text{ s } (\sim 1.5 \text{ My}), \tag{2.71}$$

and the parameters are

$$r \sim 1.2, \tag{2.72}$$

$$\lambda \sim 0.15, \tag{2.73}$$

$$\hat{\mu} \sim 0.1, \tag{2.74}$$

$$Pe \sim 50, \tag{2.75}$$

$$\nu \sim 3, \tag{2.76}$$

$$St \sim 2, \tag{2.77}$$

$$\varepsilon \sim 0.03, \tag{2.78}$$

$$\delta^2 \sim 0.03, \tag{2.79}$$

$$\delta_s^2 \sim 0.005 \tag{2.80}$$

There is a certain degree of uncertainty and variability in many of the parameters used here. Properties of the mantle and melt such as density and viscosity depend considerably on composition; rhyolitic magma is many orders of magnitude more viscous than basaltic magma for example, but somewhere between 1 Pa s and 100 Pa s is probably an average value for basalt (Ahern and Turcotte, 1979). Density and viscosity also vary with temperature (this is what causes mantle convection in the first place), but such effects have been ignored for the purposes of this study. We take the values in (2.80) to be representative of typical mantle conditions, but bear in mind that there may be significant variations from these.

Many of the parameters are small, which will allow for some simplifications. Before considering these, we complete the non-dimensionalisation.

Scaled subsolidus equations

In the subsolidus region the same scalings give rise to the following non-dimensional equations:

$$\nabla \cdot \mathbf{V} = 0, \tag{2.81}$$

$$0 = -\nabla p - \mathbf{k} + \delta_s^2 \varepsilon \nabla^2 \mathbf{V}, \tag{2.82}$$

$$\left(\frac{\partial}{\partial t} + \mathbf{V}\cdot\nabla\right) T - \lambda(1+\hat{\mu}T)\left(\frac{\partial}{\partial t} + \mathbf{V}\cdot\nabla\right) p = \frac{1}{Pe}\nabla^2 T + \nu\Phi. \tag{2.83}$$

Scaled boundary conditions

The thermodynamic condition (2.35) on ∂D becomes

$$\phi N = 0, \tag{2.84}$$

the continuity of temperature (2.31) is

$$[T]_-^+ = 0, \tag{2.85}$$

and the jump conditions (2.28)-(2.30) become

$$\frac{1}{St}\phi\left(u_n - \varepsilon v_n\right) - \phi_0 \phi\left(V_n - v_n\right) = \left(V_n^+ - V_n\right), \tag{2.86}$$

$$p_s - \delta_s^2 \phi_0 \phi N = p^+, \tag{2.87}$$

$$\phi\left(u_n - \varepsilon v_n\right) = -\frac{1}{Pe}\left[\frac{\partial T}{\partial n}\right]_-^+. \tag{2.88}$$

We also now consider the boundary conditions for the whole problem, for the one-dimensional case that we consider in the next section. We prescribe a limiting vertical velocity

$$\mathbf{V}\cdot\mathbf{k} \to W_0 \quad \text{as} \quad Z \to -\infty, \tag{2.89}$$

which we assume is externally determined; we will often refer to this velocity as the *upwelling rate*.

Noticing that $\hat{\mu}$ and $1/Pe$ in (2.83) are small, and that from (2.82), $\nabla p \sim -\mathbf{k}$, the adiabatic temperature profile in the *absence* of any melting would satisfy

$$W_0 \frac{\partial T}{\partial Z} \sim -\lambda W_0; \tag{2.90}$$

thus

$$T \sim \lambda(Z_m - Z), \tag{2.91}$$

the constant of integration being chosen since Z_m is, by definition, the depth at which the adiabatic geotherm intersects the lithostatic solidus, given in the dimensionless variables by

$$T_{LS} = Z_m - Z. \tag{2.92}$$

We would like the temperature profile deep in the upwelling column to be as it would be in the absence of melting (2.91), so the boundary condition we apply is therefore

$$T \to \lambda(Z_m - Z) \quad \text{as} \quad Z \to -\infty. \tag{2.93}$$

The temperature at the surface is also assumed known, and we therefore apply

$$T = T_s \quad \text{at} \quad Z = 0. \tag{2.94}$$

Remember that this dimensionless temperature is measured with respect to the reference temperature T_m at depth Z_m; the dimensionless T is therefore expected to be negative above Z_m, and in particular T_s will be large and negative.

2.2.3 Simplification

To summarize our model, (2.48)-(2.56) provide the equations for the partially molten region D, (2.81)-(2.83) provide the equations for the solid regions D^+, (2.84)-(2.88) provide the conditions across the boundary ∂D, and (2.89), (2.93) and (2.94) provide the fixed boundary conditions. The equations for the partial melt region are essentially the same as those proposed by Fowler (1985) and also by McKenzie (1984), when the porosity dependence of the bulk viscosity is realized. In comparing with McKenzie's original formulation, note that the *compaction length* is given here by

$$\delta l = \sqrt{\frac{k_{\phi_0}\zeta_0}{\eta_l}}, \tag{2.95}$$

where $\zeta_0 = \eta_s/\phi_0$ is the typical scale for the bulk viscosity. Our partial melt equations also contain the same information as those used by Šrámek et al. (2007), but are written in terms of the effective pressure N rather than melt pressure p_l. Our subsequent analysis will be slightly different to theirs because we make use of the fact that the melt fraction is small to neglect terms of order ϕ_0.

As is stands the model is still rather complicated, and before going on to look for solutions, we will make some additional simplifications. These are based on the size of the dimensionless parameters (2.72)-(2.80), and on which effects we want to include.

The simplifications we make are to ignore terms in $r-1$, λ and ϕ_0. r is the density ratio, and neglecting terms of size $r-1$ is a form of the Boussinesq approximation (we are not setting $\Delta\rho = 0$, as taking $r = 1$ literally implies, since we have still accounted for the density difference in the buoyancy term, which gives the dominant force in Darcy's law (2.51)). Neglecting terms in λ means ignoring the adiabatic effects; we do not expect these to play a crucial role in the dynamics of the partially molten region, where the fact that λ is reasonably small in (2.73) indicates the adiabatic gradient is small compared to the solidus.

From the non-dimensionalisation we have found a typical value for the melt fraction ϕ_0 which is small, and in agreement with inferences from seismography (Kelemen et al., 1997). It therefore seems a sensible simplification to ignore terms of order ϕ_0 relative to 1, since these will have only a small effect on the behaviour.

With these simplifications our simplified model is: for the partial melt region D;

$$\varepsilon\frac{\partial\phi}{\partial t} + \varepsilon\nabla\cdot(\phi\mathbf{V}) + \nabla\cdot[\phi(\mathbf{u}-\varepsilon\mathbf{V})] = m, \tag{2.96}$$

$$\nabla\cdot[\phi(\mathbf{u}-\varepsilon\mathbf{V})] + St\nabla\cdot\mathbf{V} = 0, \tag{2.97}$$

$$0 = -\nabla p_s - \mathbf{k} + \delta_s^2\varepsilon\nabla\cdot\boldsymbol{\tau}, \tag{2.98}$$

$$\phi\left(\mathbf{u}-\varepsilon\mathbf{V}\right) = \phi^2\left(\mathbf{k} + \delta^2\nabla N - \delta^2\varepsilon\nabla\cdot\boldsymbol{\tau}\right), \tag{2.99}$$

$$\phi N = -St\nabla.\mathbf{V}, \tag{2.100}$$

$$m + \frac{\partial T}{\partial t} + \frac{1}{St}\phi\left(\mathbf{u}-\varepsilon\mathbf{V}\right)\cdot\nabla T + \mathbf{V}\cdot\nabla T = \frac{1}{Pe}\nabla^2 T, \tag{2.101}$$

$$T = p_s - \delta_s^2 N; \tag{2.102}$$

for the subsolidus region D^+;

$$\nabla\cdot\mathbf{V} = 0, \tag{2.103}$$

$$0 = -\nabla p - \mathbf{k} + \delta_s^2\varepsilon\nabla\cdot\boldsymbol{\tau}, \tag{2.104}$$

$$\frac{\partial T}{\partial t} + \mathbf{V}\cdot\nabla T = \frac{1}{Pe}\nabla^2 T; \tag{2.105}$$

on the boundary ∂D;

$$\phi N = 0, \tag{2.106}$$

$$[T]_-^+ = 0, \tag{2.107}$$

$$\frac{1}{St}\phi\left(u_n - \varepsilon v_n\right) = \left(V_n^+ - V_n\right), \tag{2.108}$$

$$p_s = p^+, \tag{2.109}$$

$$\phi\,(u_n - \varepsilon v_n) = -\frac{1}{Pe}\left[\frac{\partial T}{\partial n}\right]^{+}_{-}; \tag{2.110}$$

in the deep mantle;

$$\mathbf{V}\cdot\mathbf{k} \to W_0 \quad \text{as} \quad Z \to -\infty, \tag{2.111}$$

$$T \to 0 \quad \text{as} \quad Z \to -\infty; \tag{2.112}$$

and at the surface;

$$T = T_s \quad \text{at} \quad Z = 0. \tag{2.113}$$

The typical values of the remaining parameters are

$$St \sim 2, \quad \varepsilon \sim 0.03, \quad \delta^2 \sim 0.03, \quad \delta_s^2 \sim 0.005, \quad Pe \sim 50, \tag{2.114}$$

though it is possible there could be considerable variation in these. In the next section we will additionally ignore the quadratically small terms $\delta_s^2\varepsilon\nabla\cdot\boldsymbol{\tau}$ and $\delta^2\varepsilon\nabla\cdot\boldsymbol{\tau}$ in (2.98) and (2.99), and therefore ignore the deviatoric stresses set up by the matrix flow. This is appropriate because the bulk viscosity $\zeta = \eta_s/\phi$ is considerably larger than shear viscosity when the melt fraction is small; the matrix stress gradients in (2.99) are therefore less important than effective pressure gradients by a factor ε. This highlights the dynamical importance of the effective pressure and justifies Fowler's earlier assumption (Fowler, 1985, 1989, 1990b) that the solid pressure (from (2.98)) is approximately lithostatic (Šrámek et al., 2007).

We will then look for approximate analytical solutions based on the idea that ε and δ are small. Remember that ε is the ratio of matrix to melt velocities, and δ is the ratio of compaction length to depth of the partial melt region, which also measures the ratio of effective pressure to buoyancy force.

The Stefan number St is the ratio of latent to sensible heat (i.e. the heat available due to changing solidus). In this problem it also turns out to give the ratio of solid mass flux to melt mass flux

$$St = \frac{\rho_s V_0}{\rho_s \phi_0 u_0}, \tag{2.115}$$

and its reciprocal also represents the fraction of rock which has melted by the time it reaches the top of the partially molten region (see section 2.4.4). A smaller Stefan number thus corresponds to a larger *degree of melting*. With the parameter values in table 2.1 we find $St = 2$, corresponding to 50% melting; in many cases, however, St will be larger, and for some of our analysis in chapter 3 we will treat St as a relatively large parameter.

2.3 Steady one-dimensional solutions

2.3.1 One-dimensional equations

In one dimension $\mathbf{V} = W\mathbf{k}$ and $\mathbf{u} = w\mathbf{k}$. Ignoring the matrix stresses, the equations are, for $Z_b < Z < Z_a$;

$$\varepsilon\phi_t + \varepsilon(\phi W)_Z + [\phi(w - \varepsilon W)]_Z = m, \tag{2.116}$$

$$W_Z + \frac{1}{St}[\phi(w - \varepsilon W)]_Z = 0, \tag{2.117}$$

$$\phi(w - \varepsilon W) = \phi^2(1 + \delta^2 N_Z), \tag{2.118}$$

$$\phi N = [\phi(w - \varepsilon W)]_Z, \tag{2.119}$$

$$m + T_t + WT_Z + \frac{1}{St}\phi(w - \varepsilon W)T_Z = \frac{1}{Pe}T_{ZZ}, \tag{2.120}$$

$$T = Z_m - Z - \delta_s^2 N. \tag{2.121}$$

For $Z < Z_b$ and $Z > Z_a$;

$$W_Z = 0, \tag{2.122}$$

$$T_t + WT_Z = \frac{1}{Pe}T_{ZZ}. \tag{2.123}$$

At the surface;

$$T = T_s \quad \text{at} \quad Z = 0, \tag{2.124}$$

and in the deep mantle;

$$T \to 0 \quad \text{as} \quad Z \to -\infty, \tag{2.125}$$

$$W \to W_0 \quad \text{as} \quad Z \to -\infty. \tag{2.126}$$

At the interfaces Z_a ($z = 0$) and Z_b ($z = 1$);

$$\phi N = 0, \tag{2.127}$$

$$[T]_-^+ = 0, \tag{2.128}$$

$$W^+ = W + \frac{1}{St}\phi(w - \varepsilon v_n), \tag{2.129}$$

$$-\frac{1}{Pe}\left[\frac{\partial T}{\partial Z}\right]_-^+ = \phi(w - \varepsilon v_n). \tag{2.130}$$

The steady state will have $v_n = 0$, and we have already made use of the momentum equations (2.98) and (2.104) and condition (2.109) to say that the matrix pressure is lithostatic

$$p_s = Z_m - Z. \tag{2.131}$$

These equations and boundary conditions are sufficient to solve for the variables and for the positions of the boundaries Z_a and Z_b. Since, by choice of the length scale, $Z_a = Z_b + 1$, finding the position of both effectively determines the length scale l.

Firstly however, we concentrate on the partially molten region $Z_b < Z < Z_a$, or equivalently $0 < z < 1$. After finding the solutions in this region, we go on to determine its position in section 2.3.5. The equations for $0 < z < 1$ are (2.116)-(2.120), and we attempt to apply (2.127) with

$$\phi = 0 \quad \text{at} \quad z = 0, \tag{2.132}$$

$$N = 0 \quad \text{at} \quad z = 1. \tag{2.133}$$

From (2.117), (2.118), (2.122), (2.126) and (2.129), we find immediately that

$$W = W_0 - \frac{1}{St}\phi^2(1 + \delta^2 N_z). \tag{2.134}$$

Then noting that $\varepsilon/St = \phi_0/r$ and we are neglecting terms of order ϕ_0, the remaining equations (2.116), (2.118), (2.119) and (2.121) combine to give

$$\varepsilon\phi_t + \varepsilon W_0\phi_z + \phi N = W_0 - \delta^4 P N_{zz}, \tag{2.135}$$

$$\phi N = [\phi^2(1 + \delta^2 N_z)]_z. \tag{2.136}$$

We have for simplicity ignored the $O(\delta_s^2)$ contribution to the temperature in (2.121), except in the conduction term, on the basis that the diffusive effects may be important near the boundaries; the new parameter P has been defined:

$$P = \delta_s^2/\delta^4 Pe, \tag{2.137}$$

and with our typical values $P \sim 0.1$.

(2.136) is the compaction relation, and states that melt divergence (which is equal and opposite to matrix divergence from (2.117)) is caused by compaction pressure N. (2.135) is mass conservation for the melt, in which the melt divergence has been rewritten using (2.136) and the right hand side is the melting rate m, from (2.120).

Together, this is a somewhat unusual pair of partial differential equations. In this section we will only be interested in steady states, but it is worth noticing that the coupled equations have only one characteristic with a finite slope. The degeneracy of the diffusion coefficient in (2.136) when $\phi = 0$ means that we do not expect to require a boundary condition for N at $z = 0$, and therefore the two boundary conditions (2.132) and (2.133) will, perhaps surprisingly, be sufficient to find a solution.

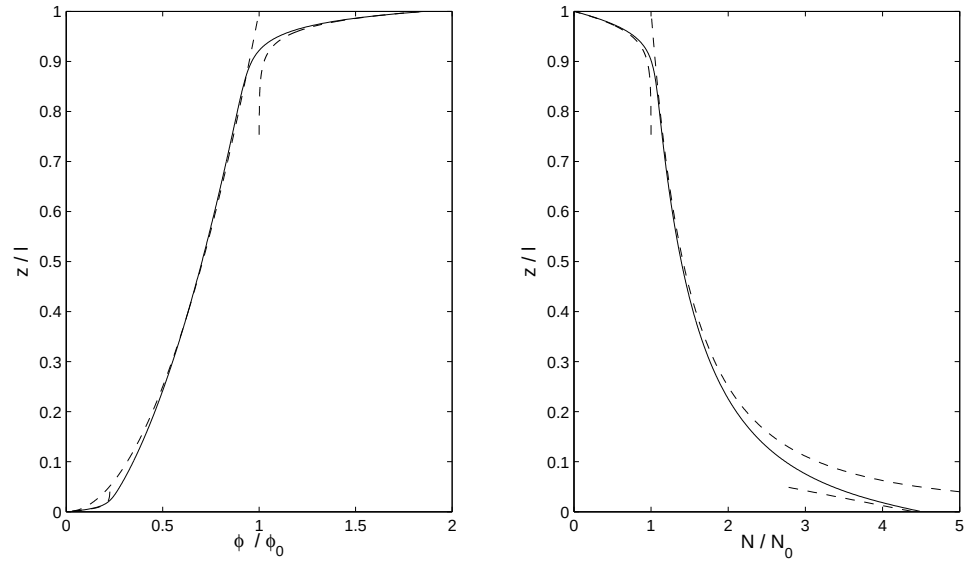

Figure 2.2: Steady solutions for melt fraction ϕ and effective pressure N in the partially molten region, with $\varepsilon = 0.03$, $\delta^2 = 0.03$, $P = 0.1$ and $W_0 = 1$. Solid lines show the numerical solutions to equations (2.135) and (2.136). Dashed lines show the analytical boundary layer approximations; the outer solution given by (2.139), the inner boundary layer of width $\varepsilon\delta^{2/3}$ at $z = 0$ given by (2.148), and the boundary layer of width δ^2 at $z = 1$ given by the solution to (2.154). The outer part of the boundary layer at $z = 0$ is not shown to avoid losing clarity.

2.3.2 Analytical boundary layer solutions

Outer solution

We treat ε and δ as small, and P as $O(1)$, and look for asymptotic solutions to (2.135) and (2.136). The steady outer solution obtained by taking $\varepsilon, \delta \to 0$ satisfies

$$[\phi^2]_z = \phi N = W_0. \tag{2.138}$$

It turns out that in order to find a sensible boundary-layer solution we should choose this outer solution to satisfy the condition $\phi = 0$ at $z = 0$, although we will still require a boundary layer there since this suggests $N \to \infty$ as $z \to 0$. The outer solutions are therefore

$$\phi = W_0^{1/2} z^{1/2}, \quad N = \frac{W_0^{1/2}}{z^{1/2}}. \tag{2.139}$$

Šrámek et al. (2007) describe this as the 'Darcy solution', since the buoyancy force is balanced by viscous drag. The effective pressure is able to freely adjust to allow the necessary compaction of the matrix, which balances the melt divergence - the

melt flow is essentially decoupled from the matrix deformation, and exactly the same behaviour for ϕ is therefore found in Ahern and Turcotte's (1979) results. Near the boundaries, however, the effective pressure cannot adjust in the same way and the relation between melt and matrix flow is less straightforward.

Boundary layer at $z = 0$

Near $z = 0$, guided by the outer solution (2.139), we write

$$z = \delta^{4/3}\hat{z}, \quad N = \delta^{-2/3}\hat{N}, \quad \phi = \delta^{2/3}\hat{\phi}. \tag{2.140}$$

Then

$$\frac{\varepsilon}{\delta^{2/3}} W_0 \hat{\phi}_{\hat{z}} + \hat{\phi}\hat{N} = W_0 - \delta^{2/3} P \hat{N}_{\hat{z}\hat{z}}, \tag{2.141}$$

$$\hat{\phi}\hat{N} = [\hat{\phi}^2(1 + \hat{N}_{\hat{z}})]_{\hat{z}}, \tag{2.142}$$

with the boundary conditions and matching conditions,

$$\hat{\phi} = 0 \quad \text{at} \quad \hat{z} = 0, \qquad \hat{\phi} \sim W_0^{1/2}\hat{z}^{1/2} \quad \text{and} \quad \hat{N} \sim \frac{W_0^{1/2}}{\hat{z}^{1/2}} \quad \text{as} \quad \hat{z} \to \infty. \tag{2.143}$$

Assuming $\delta^{2/3}P \ll 1$ and $\varepsilon \ll \delta^{2/3}$, $\hat{\phi} = W_0/\hat{N}$ and we have the single ordinary differential equation for $\hat{N}$,

$$\hat{N}_{\hat{z}} = \frac{\hat{z}\hat{N}^2}{W_0} - 1. \tag{2.144}$$

It is clear that depending on the value of $\hat{N}$ at $\hat{z} = 0$ solutions to this equation may either blow up at finite $\hat{z}$ (if $\hat{N}(0)$ is large enough) or decrease to 0 at finite $\hat{z}$ (if $\hat{N}(0)$ is small enough). The behaviour varies monotonically with the value of $\hat{N}(0)$ between these extremes and there must be a unique value, $\hat{N}_0$, such that the solution matches up with the outer solution as $\hat{z} \to \infty$. In Hewitt and Fowler (2008a) we found this value numerically; in fact (2.144) is a Ricatti equation and can be solved analytically in terms of modified Bessel functions. The solution with the correct behaviour at infinity is (see appendix A),

$$\hat{N} = \frac{W_0^{1/2}}{\hat{z}^{1/2}} \frac{K_{1/3}\left(2\hat{z}^{3/2}/3W_0^{1/2}\right)}{K_{2/3}\left(2\hat{z}^{3/2}/3W_0^{1/2}\right)}, \tag{2.145}$$

where K_ν is the modified Bessel function of order ν which is bounded at ∞. Using the known behaviour of K_ν for small argument, the value at $\hat{z} = 0$ is

$$\hat{N}_0 = \frac{W_0^{1/3}}{3^{1/3}} \frac{\Gamma(1/3)}{\Gamma(2/3)} \approx 1.37 W_0^{1/3}, \tag{2.146}$$

where $\Gamma(\nu)$ is the Gamma function.

With this initial value for N we no longer satisfy $\phi = 0$ at $z = 0$, but have $\hat{\phi}(0) = W_0/\hat{N}_0$. As suggested by the first term in (2.141) we need to rescale z again to find the smaller inner boundary region in which ϕ goes to 0. Writing $\hat{z} = \varepsilon\delta^{-2/3}\bar{z}$, the equations become

$$W_0\hat{\phi}_{\bar{z}} + \hat{\phi}\hat{N} = W_0, \quad \hat{N} = \hat{N}_0 + O\left(\varepsilon\delta^{-2/3}\right), \tag{2.147}$$

with $\hat{\phi} \to \hat{N}_0/W_0$ as $\bar{z} \to \infty$. The solution is straightforward;

$$\hat{\phi} = \frac{W_0}{\hat{N}_0}\left(1 - e^{-\hat{N}_0\bar{z}/W_0}\right). \tag{2.148}$$

In earlier work on this problem, the boundary layer at the bottom of the melt region has been called the *compaction layer* (McKenzie, 1984; Fowler, 1985; Ribe, 1985a), a somewhat misleading name since compaction occurs everywhere within the region and is actually restricted in this bottom layer by the large bulk viscosity; the melt pressure here is almost hydrostatic and melt production balances the convective derivative of ϕ in (2.116). This corresponds to Šrámek et al.'s (2007) 'viscogravitational equilibrium'.

Boundary layer at $z = 1$

At $z = 1$ there must be another boundary layer in which to satisfy $N = 0$. We write

$$z = 1 - \delta^2\tilde{z}, \tag{2.149}$$

and defining

$$E = \varepsilon W_0/\delta^2, \tag{2.150}$$

rewrite the equations as

$$-E\phi_{\tilde{z}} + \phi N = W_0 - PN_{\tilde{z}\tilde{z}}, \tag{2.151}$$

$$\delta^2\phi N = -\left[\phi^2\left(1 - N_{\tilde{z}}\right)\right]_{\tilde{z}}, \tag{2.152}$$

with matching conditions

$$\phi \to W_0^{1/2}, \quad N \to W_0^{1/2} \quad \text{as} \quad \tilde{z} \to \infty. \tag{2.153}$$

Now by taking $\delta^2 \to 0$ a first integral of (2.152) produces the coupled set of first order ordinary differential equations,

$$N_{\tilde{z}} = 1 - \frac{W_0}{\phi^2} \equiv K(\phi), \quad \phi_{\tilde{z}} = \frac{W_0 - \phi N}{\frac{2W_0P}{\phi^3} - E} \equiv \frac{G(\phi, N)}{V(\phi)}, \tag{2.154}$$

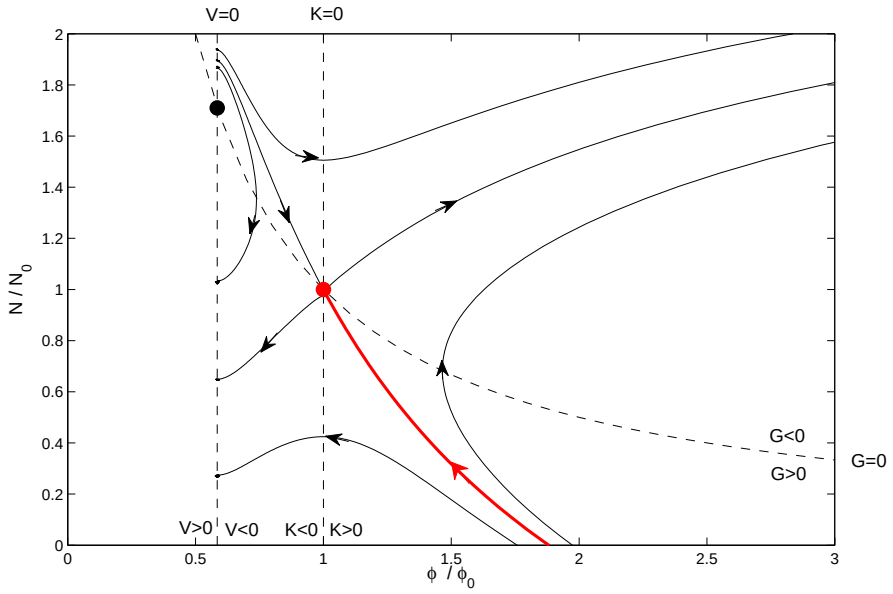

Figure 2.3: Phase plane for the system (2.154) when $E = 1$, $P = 0.1$ and $W_0 = 1$, so $2P < EW_0^{1/2}$. The dashed lines are the nullclines $G = 0$ and $K = 0$, and the line $V = 0$ on which $\phi_{\tilde{z}}$ is infinite. The fixed point at $(W_0^{1/2}, W_0^{1/2})$ is a saddle point, and there is a unique trajectory (shown in red) which reaches it from $N = 0$.

for which we are required to find a trajectory joining $N = 0$ to $\phi = W_0^{1/2}$, $N = W_0^{1/2}$ as $\tilde{z}$ goes from 0 to ∞.

Represented on a phase plane these equations are shown in figure 2.3, where we define the nullclines $K = 0$ and $G = 0$ and the line $V = 0$ on which $\phi_{\tilde{z}}$ becomes infinite. Provided $2P < EW_0^{1/2}$, we find that the fixed point $(W_0^{1/2}, W_0^{1/2})$ is a saddle point and there is one unique trajectory which reaches it from $N = 0$, with ϕ and N varying monotonically. The implications when $2P > EW_0^{1/2}$ will be discussed in section 2.4.3.

2.3.3 Numerical solutions

The simplified equations (2.135) and (2.136) with boundary conditions (2.132) and (2.133) have also been solved numerically, and the steady state solutions are shown in figure 2.2, where they are compared with the boundary layer approximations made above.

The steady state is found be solving the time-dependent version of (2.135) and allowing it to evolve to a steady state. Equation (2.136) is treated as a quadrature for N given the current value of ϕ, and this is then used to step the solution for ϕ

forward in time using (2.135). We use a uniform grid, on which (2.136) is discretised to second order accuracy. The advection term for ϕ in (2.135) is included implicitly, but the compaction and diffusion terms involving N are explicit.

In figure 2.2 we can clearly see the general parabolic profile of the melt fraction and its inverse relation with the effective pressure (2.139), the boundary layer at $z = 1$ of width $1 - z \sim \delta^2$ and the inner boundary layer at $z = 0$ of width $z \sim \varepsilon\delta^{2/3}$. Less obvious is the outer part of this boundary layer of width $z \sim \delta^{4/3}$, although the limiting values $N \to \delta^{-2/3}\hat{N}_0 \approx 4.4$ and $\phi \to \delta^{2/3}W_0/\hat{N}_0 \approx 0.23$ can be seen.

2.3.4 Some alternative parameter regimes

We briefly consider steady solutions to (2.135) and (2.136) when one or other of ε and δ is not small. The typical choices of the physical parameters suggest that both ε and δ should be quite small, so these solutions may not be directly relevant; nevertheless it is interesting to see how the solutions behave and, if nothing else, they provide a useful test of the numerical solution.

Larger values of ε correspond to the melt ascending less fast relative to the matrix; this may be the case if the rock is quite impermeable, or if the melt is very viscous. Larger values of δ correspond to a longer compaction length, and would mean that pressure differences are spread over larger areas; in particular it means that the effects of boundaries are felt over a greater distance.

The case $\varepsilon = O(1)$, $\delta \ll 1$

In this case the outer solution satisfies

$$\varepsilon W_0\phi_z + \phi N = W_0, \quad \phi N = [\phi^2]_z, \tag{2.155}$$

and the solution satisfying $\phi = 0$ at $z = 0$ is

$$\phi = \left(W_0 z + \frac{\varepsilon^2 W_0^2}{4}\right)^{1/2} - \frac{\varepsilon W_0}{2}, \quad N = \frac{W_0}{\left(W_0 z + \frac{\varepsilon^2 W_0^2}{4}\right)^{1/2}}. \tag{2.156}$$

N_z is order 1 as z goes to 0 in this case, so there is no need for a boundary layer at $z = 0$. At $z = 1$ we still need to satisfy $N = 0$, so rescaling

$$z = 1 - \delta\tilde{z}, \tag{2.157}$$

gives rise to the equations

$$-\varepsilon W_0\phi_{\tilde{z}} + \delta\phi N = \delta W_0 - \delta^3 P N_{\tilde{z}\tilde{z}}, \tag{2.158}$$

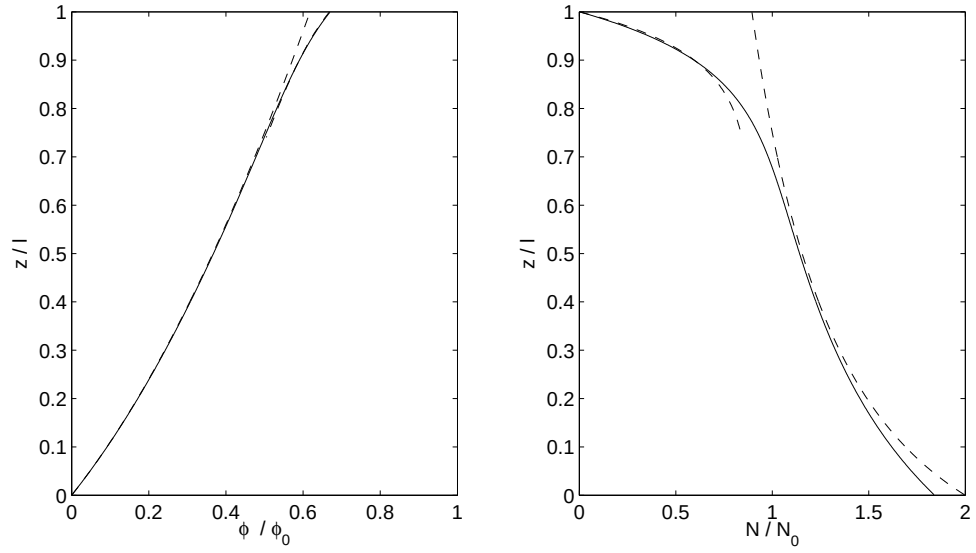

Figure 2.4: Steady solutions for melt fraction ϕ and effective pressure N to (2.135) and (2.136) for $\varepsilon = 1$, $\delta^2 = 0.03$, $P = 0.1$ and $W_0 = 1$. Solid lines show the numerical solutions. Dashed lines show the analytical approximations; an outer solution given by (2.156) and a boundary layer of width δ at $z = 1$ given by (2.162).

$$\delta\phi N = -[\phi^2(1 - \delta N_{\tilde{z}})]_{\tilde{z}}, \tag{2.159}$$

which must match with the leading order behaviour of the outer solution

$$\phi \to \phi_1 \equiv \left(W_0 + \frac{\varepsilon^2 W_0^2}{4}\right)^{1/2} - \frac{\varepsilon W_0}{2}, \quad N \to N_1 \equiv \frac{W_0}{\left(W_0 + \frac{\varepsilon^2 W_0^2}{4}\right)^{1/2}}, \quad \text{as} \quad \tilde{z} \to \infty. \tag{2.160}$$

Taking the leading order terms in δ gives $\phi_{\tilde{z}} = 0$, so $\phi = \phi_1$, and substituting this in gives the leading order equation for N,

$$\frac{\varepsilon\phi_1 N_1}{2} N_{\tilde{z}\tilde{z}} - N = -N_1, \tag{2.161}$$

with solution satisfying $N = 0$ at $\tilde{z} = 0$,

$$N = N_1 \left(1 - e^{-(2/\varepsilon\phi_1 N_1)^{1/2}\tilde{z}}\right). \tag{2.162}$$

Figure 2.4 shows the approximate outer solution given by (2.156) and the boundary layer solution given by (2.162), and compares them with the numerical solution.

The case $\delta = O(1)$, $\varepsilon \ll 1$

If δ is order 1 it is clear from the definition of $P = \delta_s^2/\delta^4 Pe$ and the fact that Pe is large, that it is inconsistent in this case to treat P as $O(1)$; we therefore neglect P

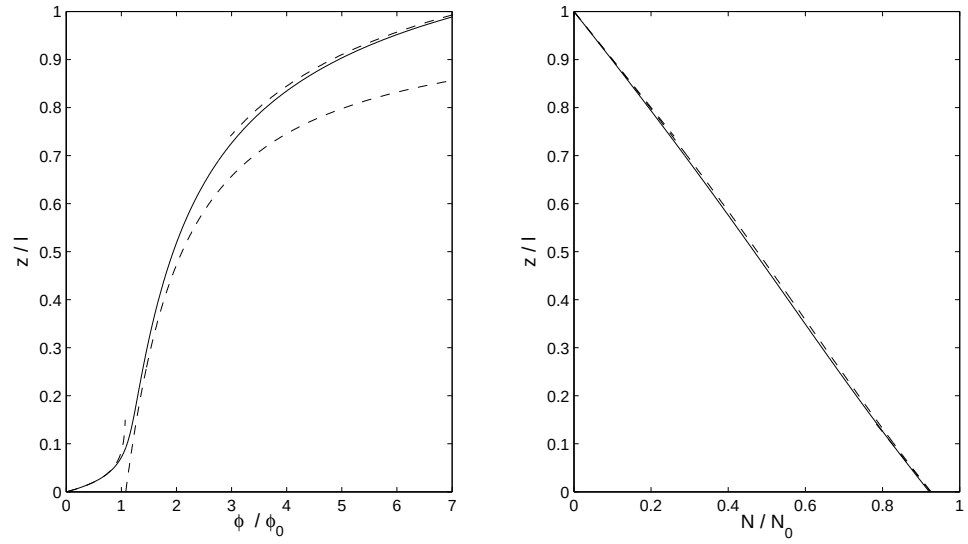

Figure 2.5: Steady solutions for melt fraction ϕ and effective pressure N to (2.135) and (2.136) for $\varepsilon = 0.03$, $\delta^2 = 1$, $P = 0.1$ and $W_0 = 1$. Solid lines show the numerical solutions. Dashed lines show the analytical approximations; an outer solution given by (2.172) and (2.170), a boundary layer of width ε at $z = 0$ given by (2.171), and a boundary layer of width $\varepsilon^{1/2}$ at $z = 1$ given by (2.176) and (2.178).

for this section. In this case the outer solution satisfies

$$\phi N = W_0 = [\phi^2(1 + \delta^2 N_z)]_z. \tag{2.163}$$

The outer solution here is very similar to the situation in the lower boundary layer when $\delta \ll 1$; we will obtain a first order equation for N from a first integral of (2.163). The constant of integration must be found by matching across the required boundary layer at $z = 0$. This boundary layer is needed in order to allow ϕ to reach 0 there, and is very similar to the inner boundary layer in (2.148); we write

$$z = \varepsilon \hat{z}, \tag{2.164}$$

and the equations are

$$W_0 \phi_{\hat{z}} + \phi N = W_0, \tag{2.165}$$

$$\varepsilon^2 \phi N = [\phi^2(\varepsilon + \delta^2 N_{\hat{z}})]_{\hat{z}}. \tag{2.166}$$

From (2.166), and using $\phi = 0$ at $\hat{z} = 0$, we see that

$$\phi^2(1 + \delta^2 N_z) = O(\varepsilon), \tag{2.167}$$

within this boundary layer, and therefore the matching behaviour for the outer solution is

$$\phi^2(1+\delta^2 N_z)=0 \quad \text{at} \quad z=0. \tag{2.168}$$

Hence, from (2.163), the outer solution satisfies $\phi = W_0/N$, and

$$\delta^2 W_0 N_z = zN^2 - W_0. \tag{2.169}$$

This last equation is essentially the same as (2.144), and since we require $N=0$ at $z=1$, the solution is (see appendix A),

$$N = \frac{W_0^{1/2}}{z^{1/2}} \frac{I_{-1/3}(\alpha)\, K_{1/3}\left(\alpha z^{3/2}\right) - K_{1/3}(\alpha)\, I_{-1/3}\left(\alpha z^{3/2}\right)}{I_{-1/3}(\alpha)\, K_{2/3}\left(\alpha z^{3/2}\right) + K_{1/3}(\alpha)\, I_{2/3}\left(\alpha z^{3/2}\right)}, \tag{2.170}$$

where $\alpha = 2/3\delta^2 W_0^{1/2}$.

Having found this outer solution, we can then go back to the boundary layer at $z=0$; from (2.166) N is approximately constant within this layer, and therefore equal to the value $N(0)$ of N from the outer solution (2.170) at $z=0$. (2.165) then has solution, as in (2.148),

$$\phi = \frac{W_0}{N(0)}\left(1 - e^{-N(0)\hat{z}/W_0}\right). \tag{2.171}$$

Since $\phi = W_0/N$ and $N \to 0$ at $z=1$, the outer solution has $\phi \to \infty$ there. The advective ϕ_z in (2.135) must become important and prevent this from happening; to find a better approximation there, we notice that $N \sim (1-z)$ and $\phi \sim 1/(1-z)$ in the outer solution and therefore scale

$$z = 1 - \varepsilon^{1/2}\tilde{z}, \quad N \sim \varepsilon^{1/2}\tilde{N}, \quad \phi \sim \varepsilon^{-1/2}\tilde{\phi}. \tag{2.172}$$

The equations become

$$-W_0\tilde{\phi}_{\tilde{z}} + \tilde{\phi}\tilde{N} = W_0, \tag{2.173}$$

$$\varepsilon^{3/2}\tilde{\phi}\tilde{N} = -[\tilde{\phi}^2(1-\delta^2\tilde{N}_{\tilde{z}})]_{\tilde{z}}, \tag{2.174}$$

and the matching conditions are

$$\tilde{N} \sim \frac{\tilde{z}}{\delta^2}, \quad \tilde{\phi} \sim \frac{\delta^2 W_0}{\tilde{z}} \quad \text{as} \quad \tilde{z} \to \infty. \tag{2.175}$$

The leading order behaviour of (2.174) is simply

$$\tilde{N} = \frac{\tilde{z}}{\delta^2}, \tag{2.176}$$

and therefore (2.173) becomes

$$-\delta^2 W_0 \tilde{\phi}_{\tilde{z}} + \tilde{\phi}\tilde{z} = \delta^2 W_0, \tag{2.177}$$

which can be solved using an integrating factor to give

$$\tilde{\phi} = \int_{\tilde{z}}^{\infty} e^{(\tilde{z}^2-\tilde{\zeta}^2)/2\delta^2 W_0}\ \mathrm{d}\tilde{\zeta} = \delta\sqrt{\frac{\pi W_0}{2}} e^{\tilde{z}^2/2\delta^2 W_0} \mathrm{erfc}\left(\tilde{z}/\delta\sqrt{2W_0}\right). \tag{2.178}$$

The outer solution given by (2.170), the boundary layer solution at $z = 0$ given by (2.171), and the boundary layer solution at $z = 1$ given by (2.178) are shown in figure 2.5, where they are compared to the numerical solution.

2.3.5 Free boundary location

So far we have found steady solutions for the melt fraction and effective pressure (and therefore also matrix velocity (2.134), melt velocity (2.118) and temperature (2.121)) within the partially molten region, *assuming* that we knew the size of this region. As has already been discussed, its position and size (and indeed whether partial melting occurs at all) must now be found by considering the temperature of the surrounding rock.

Solutions for subsolidus rock

It is straightforward to see from the continuity equation (2.122) and the jump conditions (2.129) that the matrix velocity in the subsolidus regions is constant $W = W_0$. Thus we have only to solve the temperature problem in these regions; for $Z < Z_b$ this satisfies the energy equation (2.123), with boundary conditions (2.125) as $Z \to -\infty$ and (2.128) and (2.130) at $Z = Z_b$; and for $Z > Z_a$ it satisfies (2.123) with condition (2.125) at $Z = 0$ and (2.128) and (2.130) at $Z = Z_a$. Using the known solutions for $\phi(z)$ and $N(z)$ for $Z_b < Z < Z_a$, these are

$$W_0 T_Z = \frac{1}{Pe} T_{ZZ}, \tag{2.179}$$

$$T \to 0 \quad \text{as} \quad Z \to -\infty, \tag{2.180}$$

$$T = Z_m - Z_b - \delta_s^2 N(0), \quad \text{at} \quad Z = Z_b, \tag{2.181}$$

$$T_Z = -1 - \delta_s^2 N_z(0) \quad \text{at} \quad Z = Z_b, \tag{2.182}$$

$$T = T_s \quad \text{at} \quad Z = 0, \tag{2.183}$$

$$T = Z_m - Z_a, \quad \text{at} \quad Z = Z_a, \tag{2.184}$$

$$T_Z = -1 - \delta_s^2 N_z(1) - Pe\phi(1)w(1) \quad \text{at} \quad Z = Z_a. \tag{2.185}$$

From the analytical solutions in section 2.3.2, the required information from the partial melt region is

$$N(0) \approx \delta^{-2/3}\hat{N}_0, \quad N_z(0) \approx -\frac{1}{\delta^2}, \tag{2.186}$$

$$\delta_s^2 N_z(1) + Pe\phi(1)w(1) = W_0 Pe + \delta_s^2 N_z(0). \tag{2.187}$$

The fact that there are 6 boundary conditions for two second order equations allows (or rather, requires) the positions of Z_a and Z_b to be determined too.

Using the conditions (2.181) and (2.182) at Z_b, the temperature in $Z < Z_b$ is

$$T = Z_m - Z_b - \delta_s^2 N(0) - \frac{1 + \delta_s^2 N_z(0)}{W_0 Pe}\left(e^{W_0 Pe(Z-Z_b)} - 1\right), \tag{2.188}$$

and using the conditions (2.184) and (2.185) at Z_a, the temperature in $Z > Z_a$ is

$$T = Z_m - Z_a - \frac{1 + W_0 Pe + \delta_s^2 N_z(0)}{W_0 Pe}\left(e^{W_0 Pe(Z-Z_a)} - 1\right). \tag{2.189}$$

Locating Z_b and Z_a

The remaining conditions (2.180) and (2.183) require

$$W_0 Pe\left(Z_m - Z_b - \delta_s^2 N(0)\right) + 1 + \delta_s^2 N_z(0) = 0. \tag{2.190}$$

$$W_0 Pe\left(T_s - Z_m + Z_a\right) + \left(1 + \delta_s^2 N_z(0) + W_0 Pe\right)\left(e^{-W_0 Pe Z_a} - 1\right) = 0, \tag{2.191}$$

The parameters and the scalings for the variables in (2.190) and (2.191) are themselves dependent on the unknown length scale l, and, since $Z_a = Z_b + 1$, these two equations may be rewritten as one nonlinear equation for l. Once l is known, the depth of the bottom of the partial melt region Z_b follows directly from (2.190).

The procedure we adopt is as follows: we take a guess l^* at the depth of the partial melt region and define the non-dimensional parameters δ^*, δ_s^*, Pe^* and ε^* and variable scales as in (2.42)-(2.47) using this length scale. With these values, we find the solutions $\phi^*(z)$ and $N^*(z)$ numerically or analytically, as above (note that * is being used in a different sense to that when non-dimensionalising in section 2.2). Then writing $X = l/l^*$, so that

$$Z = Z^* X^{-1}, \quad T_s = T_S^* X^{-1}, \quad \phi = \phi^* X^{-1/2}, \quad N = N^* X^{1/2},$$

$$Pe = Pe^* X, \quad \varepsilon = \varepsilon^* X^{-1/2}, \quad \delta^2 = \delta^{*2} X^{-3/2}, \quad \delta_s^2 = \delta_s^{*2} X^{-3/2}, \tag{2.192}$$

(2.190) and (2.191) combine to give an equation for X,

$$\left(e^{-W_0 Pe^*(X + Z_m^* - \delta_s^{*2} N^*(0)) - (1 + \delta_s^{*2} N_z^*(0))} - 1\right)\left(1 + \delta_s^{*2} N_z^*(0) + W_0 Pe^* X\right)$$
$$+ W_0 Pe^*\left(T_s^* + X - \delta_s^{*2} N^*(0)\right) + 1 + \delta_s^{*2} N_z^*(0) = 0, \tag{2.193}$$

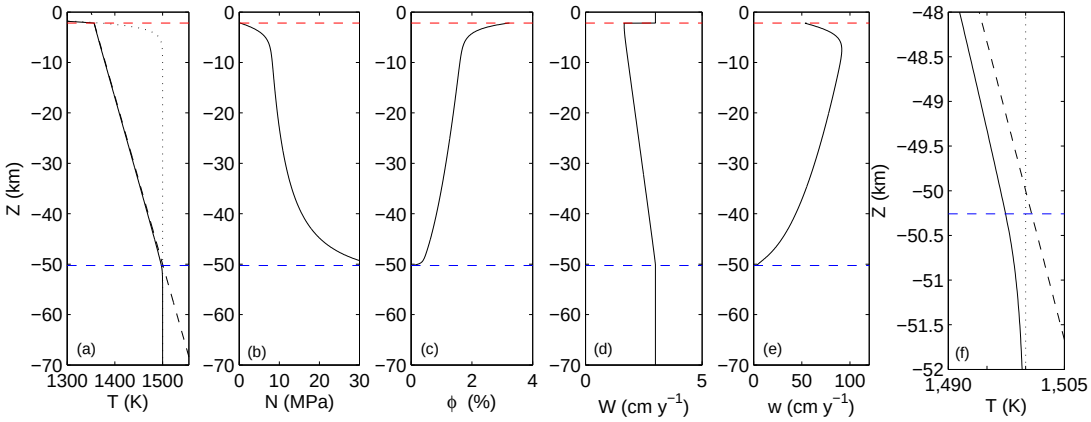

Figure 2.6: Steady state solutions for (a) temperature, (b) effective pressure, (c) melt fraction, (d) matrix velocity and (e) melt velocity in the upper 70 km of an ascending column with the values given in table 2.1, $Z_m = -50$ km and $V_0 = 3$ cm y^{-1}. Horizontal dashed lines show the boundaries of the partially molten region. Between them the temperature closely follows the lithostatic solidus (shown by the diagonal dashed line) but is slightly depressed from it by the effective pressure. An enlarged view of the temperature close to the onset of melting is shown (f), with the position Z_b of the partial melting boundary slightly below the intersection at $Z_m = -50$ km of the lithostatic solidus and mantle geotherm in the absence of partial melt (dotted line). The continuity of temperature gradient at Z_b causes a precursive decrease in the temperature of the subsolidus rock below. The jump in matrix velocity at Z_a is necessary to ensure the total mass flux is continuous there, as all the ascending melt solidifies; this also causes a discontinuity in the temperature gradient there.

in which all the * variables are known. This can be solved for X and therefore the true depth scale l. Provided our original estimate of the length scale was good, the solutions within the partially molten region still hold, with the true non-dimensional solutions being given by

$$\phi(Z) = X^{-1/2}\phi^*(Z - Z_b), \quad N(Z) = X^{1/2}N^*(Z - Z_b). \tag{2.194}$$

With the length scale known, the depth at which melting starts comes from (2.190), with the values of $N_z(0)$ and $N(0)$ coming from (2.186);

$$Z_b = Z_m + \frac{1}{rW_0Pe} - \frac{\delta_s^2}{\delta^{2/3}}\hat{N}_0. \tag{2.195}$$

Z_m is the depth we would guess partial melting starts at, based on where the adiabatic geotherm intersects the lithostatic solidus; we see here that melting may actually start at a slightly shallower depth due to heat conduction in the rock below (which acts to smooth out the change in temperature gradient) or at a greater depth due to

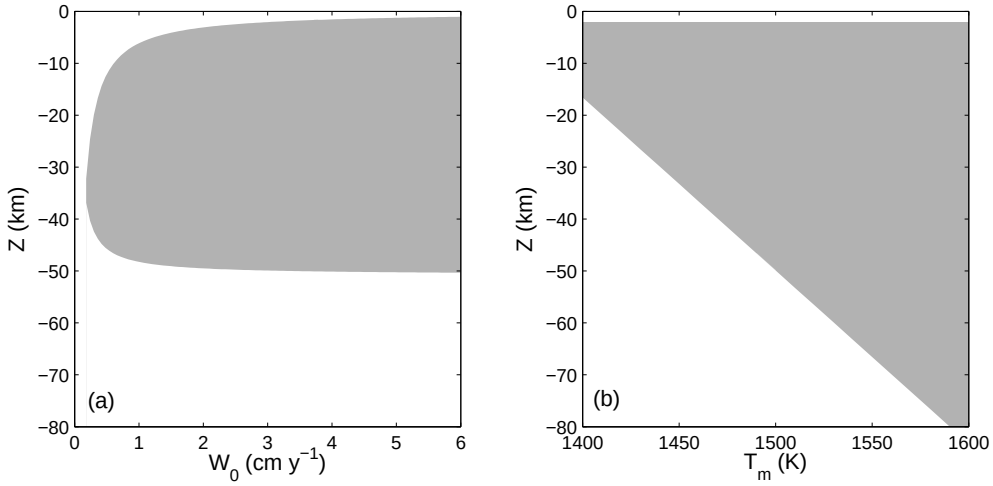

Figure 2.7: (a) The predicted region of partial melting from (2.193) as a function of upwelling rate W_0, with deep mantle temperature $T_m = 1500$ K intersecting the lithostatic solidus at $Z_m = -50$ km. For W_0 larger than 1 cm y^{-1}, the onset of melting is very close to Z_m. (b) The predicted region of partial melting as a function of deep mantle temperature T_m, when $W_0 = 3$ cm y^{-1} and the lithostatic solidus is 1500 K at 50 km depth; the onset of melting is again very close to where T_m intersects the solidus. Profiles when $T_m = 1450$ K, 1500 K and 1550 K are shown in figures 2.8, 2.6 and 2.9.

the depression of the solidus temperature from its lithostatic value as a result of the effective pressure. In fact these two terms may have counterbalancing effects - with the parameter values in (2.114), the effect of the solidus depression is larger and $Z_b < Z_m$. In any case, since Pe is large and $\delta_s^2 \ll \delta^{2/3}$, both these effects are small and the bottom of the partial melt region is well approximated by Z_m.

The full solutions for the temperature of the ascending mantle column and the behaviour of the partial melt region are shown in figure 2.6.

2.4 Discussion

2.4.1 Region of partial melting

Figure 2.7 shows the predicted region of partial melting for different parameters; as the the mantle ascent rate W_0 is reduced the size of the partial melting region decreases until, if W_0 is too small, there is no partial melting at all. The temperature of the ascending rock, which determines where it intersects the solidus, also influences the size of the partially molten region; naturally the hotter the rock the deeper it intersects the solidus and the more melting it undergoes.

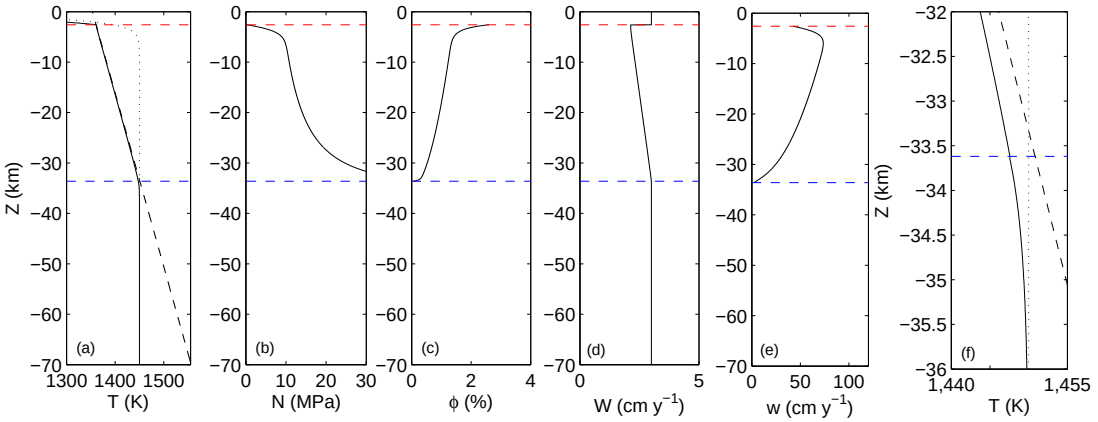

Figure 2.8: Similar to figure 2.6, showing profiles of (a) temperature, (b) effective pressure, (c) melt fraction, (d) matrix velocity and (e) melt velocity in the upper 70 km of an ascending column; (f) Close up of the temperature near to the onset of melting at Z_b, shown by the dashed horizontal line. The only difference from figure 2.6 is that the temperature of the ascending rock is 50 K cooler at 1450 K. Melting therefore begins at a shallower depth and the amount of melt produced is less.

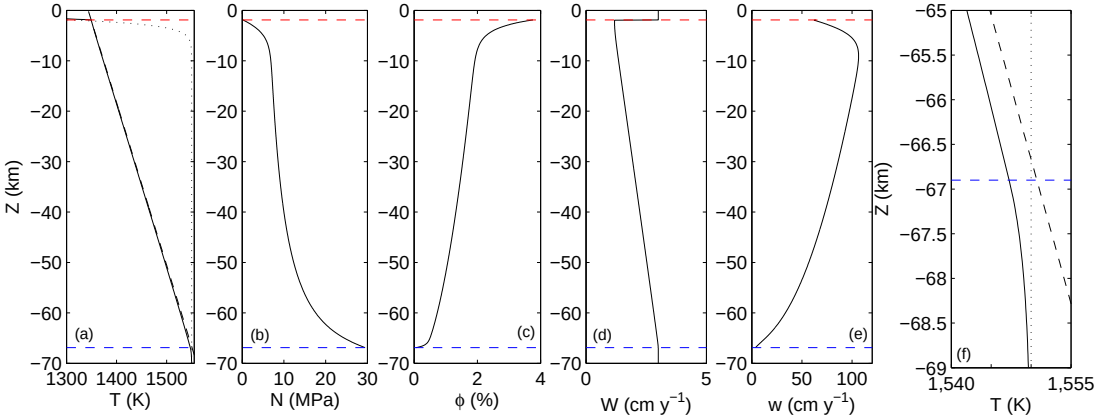

Figure 2.9: Similar to figures 2.6 and 2.8, showing profiles of (a) temperature, (b) effective pressure, (c) melt fraction, (d) matrix velocity and (e) melt velocity in the upper 70 km of an ascending column; (f) Close up of the temperature near to the onset of melting at Z_b, shown by the dashed horizontal line. The difference from figure 2.6 is that the temperature of the ascending rock is 50 K warmer at 1550 K. Melting therefore begins at a greater depth and the rock undergoes more melting.

Figures 2.8 and 2.9 show the solutions when the temperature of the ascending mantle is 1450 K and 1550 K rather than 1500 K in figure 2.6. The lithostatic solidus is the same in each figure, so the hotter rock intersects it and starts melting at a deeper level than the colder rock; this means that the rock undergoes more melting when it is hotter and the amount of melt produced is larger.

The predicted thickness of the solidified lithosphere in figure 2.6 is approximately 2 km, considerably less than the estimated thickness beneath mid-ocean ridges. This results from the one-dimensional assumption that the rock continues to ascend all the way to the surface, whereas in reality the cold rigid lithosphere will move sideways, driven by the convective motion of the overlying plate. Conduction would then allow the cold temperature at the surface to penetrate deeper into the rock and increase the size of the lithosphere.

An idea of this effect can be found by supposing that the lithosphere has no vertical motion; given the one-dimensional assumptions this violates the mass conservation condition (2.129) at the boundary between partially molten region and lithosphere, but it may provide a more realistic approximation to the temperature profile in the lithosphere, and therefore its depth. If this were the case, the temperature in $Z > Z_a$ satisfies

$$T_{ZZ} = 0, \tag{2.196}$$

with boundary conditions (2.183), (2.184) and (2.185). The temperature is therefore linear (rather than exponential as in (2.189));

$$T = Z_m - Z_a - \left(1 + \delta_s^2 N_z(0) + W_0 Pe\right)(Z - Z_a), \tag{2.197}$$

and condition (2.191) is instead

$$T_s - Z_m - \left(\delta_s^2 N_z(0) + W_0 Pe\right) Z_a = 0. \tag{2.198}$$

The equation analogous to (2.193) for X is then

$$\left(\delta_s^{*2} N_z^*(0) + W_0 Pe^* X\right)\left(W_0 Pe^*(X + Z_m^* - \delta_s^{*2} N^*(0)) + (1 + \delta_s^{*2} N_z^*(0))\right) = W_0 Pe^*(T_s^* - Z_m^*). \tag{2.199}$$

The depth l is found from this, and once it is known Z_b is given, as before, by (2.195), and Z_a is given from (2.198) by

$$Z_a = \frac{T_s - Z_m}{\delta_s^2 N_z(0) + W_0 Pe}. \tag{2.200}$$

The solutions in this case are shown in figure 2.10. As expected, the conductive boundary layer extends further down and the melt is caused to solidify at greater depth. The predicted thickness of the lithosphere is closer to 10 km.

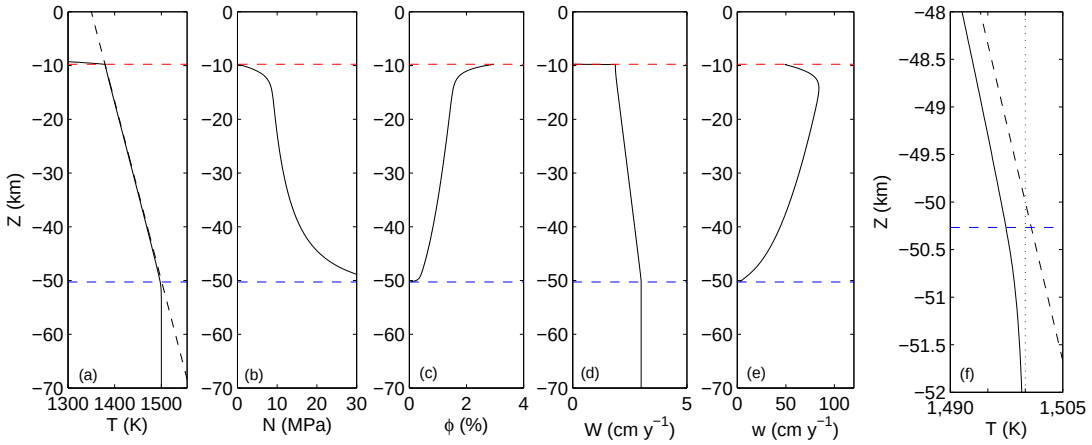

Figure 2.10: Similar to figure 2.6, showing profiles of (a) temperature, (b) effective pressure, (c) melt fraction, (d) matrix velocity and (e) melt velocity in the upper 70 km of an ascending column; (f) Close up of the temperature near to the onset of melting at Z_b, shown by the dashed horizontal line. The difference from figure 2.6 is that here the lithosphere has been prescribed to have no vertical motion and acts as a stagnant lid; hence the jump in matrix velocity at Z_a. The solutions are very similar to those in figure 2.6 except that the temperature profile in the lithosphere is different and causes partial melting to stop at a greater depth.

Solidification

Note that in this one dimensional model the lithosphere and the crust effectively have the same thickness, since the melt is assumed to solidify when it reaches the lithosphere and this is the only way in which new crust is generated. In reality of course this is not the case; melt is focussed from a wider melting region towards a ridge centre so that it is not only the melt generated directly beneath it which reaches the lithosphere there. More importantly, not all the melt solidfies; at least some, and possibly most, carries on through the lithosphere to enter magma chambers and dikes.

The amount of melt solidifying at the base of the lithosphere is important in determining its position since, by the Stefan condition (2.130), the latent heat released during solidification is what sets the temperature gradient. We should therefore not read too much into any conclusions concerning the depth of the lithosphere that arise from our solutions, except perhaps to say that the order of magnitude is consistent with observations.

It is not clear how to more adequately account for the solidification or otherwise of melt at the base of the lithosphere; it requires a more detailed prescription of what precisely occurs there to enable continued transport.

2.4.2 Fracture initiation

Transport through the lithosphere most likely involves magmafracturing (Spence et al., 1987; Lister and Kerr, 1991; Roper and Lister, 2005), aided by the supply of large quantities of melt from below. This presumably requires a highly localised source of melt *from* the partially molten region, such as has been discussed in chapter 1, else there will not be enough magma to drive the fracturing, or the flow within the dike will not be sufficient to prevent it from solidifying. Another possibility is that fracture could occur *within* the partially molten region and draw in melt from the surroundings to establish an interconnected network of veins or dykes (Nicolas, 1986; Sleep, 1988; Ito and Martel, 2002). In either case, something must cause these fractures to be initiated.

The Griffith criterion suggests such fracture should occur when the stored elastic energy becomes larger than the surface energy which is created when individual grains are pulled apart. The stored energy has size $\sim \sigma^2 a^3/E$ and the surface energy is $\sim \gamma a^2$, where a is the typical grain size, γ the surface energy, E the Young's modulus, and σ is the applied stress. Fracture therefore occurs if

$$\sigma > \Sigma \equiv \left(\frac{E\gamma}{a}\right)^{1/2}, \tag{2.201}$$

with typical values of Σ on the order of 1 MPa (Sleep, 1988; Fowler, 1990b). If τ_1 is the largest principal deviatoric stress, the largest effective stress is $\sigma = p_l - p_s + \tau_1$, giving the condition

$$N < \tau_1 - \Sigma. \tag{2.202}$$

This suggests that the matrix will fracture if the effective pressure becomes small enough. At a spreading ridge a rough estimate of deviatoric stress is $\tau_1 \sim \eta_s V_0/l \sim$ 0.2 MPa using our previously given values, but this does not take account of the temperature dependent viscosity; as the rock cools towards the surface the viscosity will increase significantly from the 10^{19} Pa used above and stresses of several MPa or more are likely there. In this case $\tau_1 > \Sigma$, and since the upper boundary condition on the partial melting region requires N to reduce towards zero there, the conditions for fracture initiation may well be met.

Fractures would occur normal to the largest extensional deviatoric stress τ_1; beneath spreading ridges this is horizontal, so fractures will be vertical and allow for efficient transport of melt.

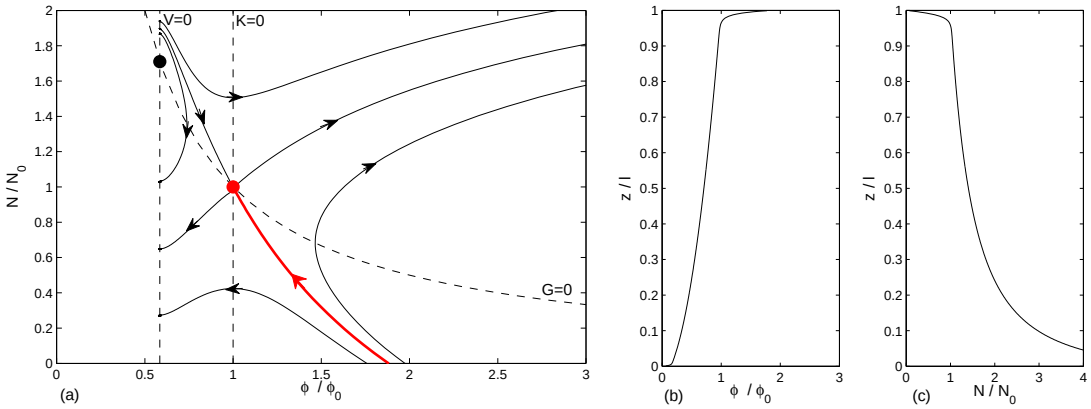

Figure 2.11: (a) Phase plane for the system in (2.203) when $E = 1$, $P = 0.1$ and $W_0 = 1$, so $2P < EW_0^{1/2}$. The line $V = 0$ is to the left of $K = 0$, the fixed point $(W_0^{1/2}, W_0^{1/2})$ is a saddle and there is a unique trajectory reaching it from $N = 0$ (shown in red). (b) and (c) show the steady-state numerical solution of (2.135), (2.136) for the same parameter values; the phase plane corresponds to the boundary layer at $z = 1$.

2.4.3 Thermodynamic boundary layer

Oscillatory solutions

The condition $N = 0$ at the upper boundary of the partial melting region required a boundary layer in which the pressure has to adjust rapidly. This was described by the phase plane in (2.154) and figure 2.3, which admits a unique solution to match with the outer region provided $2P < EW_0^{1/2}$. With the chosen parameters this is indeed the case, but it is not inconceivable for it not to be so, and in this section we examine the solutions when, conversely, $2P > EW_0^{1/2}$.

In terms of the scaled variable $\tilde{z} = (1 - z)/\delta^2$, the equations were

$$N_{\tilde{z}} = 1 - \frac{W_0}{\phi^2} \equiv K(\phi), \quad \phi_{\tilde{z}} = \frac{W_0 - \phi N}{\frac{2W_0 P}{\phi^3} - E} \equiv \frac{G(\phi, N)}{V(\phi)}, \tag{2.203}$$

and we were required to find a trajectory joining $N = 0$ to the fixed point $(\phi, N) = (W_0^{1/2}, W_0^{1/2})$ as $\tilde{z}$ goes from 0 to ∞.

Phase planes for different values of the parameters are shown in figures 2.11, 2.12, 2.13, 2.14 and 2.15. When $2P - EW_0^{1/2} < 0$ the fixed point is a saddle point and there was a unique suitable trajectory; when $0 < 2P - EW_0^{1/2} < W_0^{3/2}/8$ it is a stable node and when $2P - EW_0^{1/2} > W_0^{3/2}/8$ it is a stable spiral.

This transition from a saddle point is associated with the lines $K(\phi) = 0$ and $V(\phi) = 0$ crossing each other, so that, when $2P > EW_0^{1/2}$, the trajectory from $N = 0$

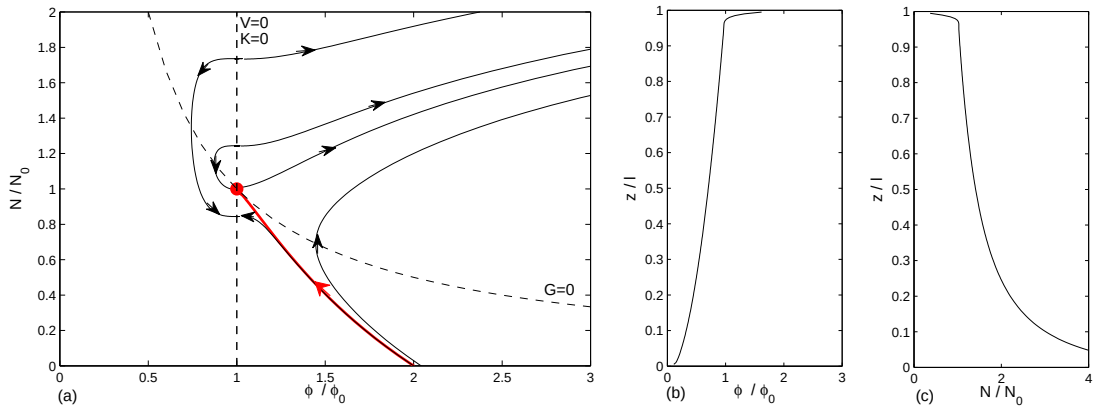

Figure 2.12: Phase plane for the system in (2.203) when $E = 1$, $P = 0.5$ and $W_0 = 1$, so $2P = EW_0^{1/2}$. The lines $V = 0$ and $K = 0$ are collinear, the fixed point $(W_0^{1/2}, W_0^{1/2})$ is a saddle/node and there is a unique trajectory reaching it from $N = 0$ (shown in red). (b) and (c) show the steady-state numerical solution of (2.135), (2.136) for the same parameter values.

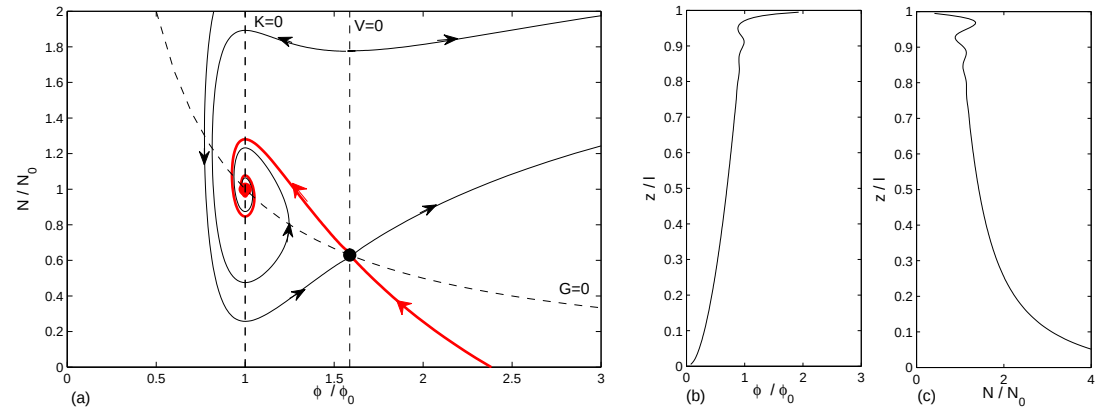

Figure 2.13: Phase plane for the system in (2.203) when $E = 1$, $P = 2$ and $W_0 = 1$, so $2P > EW_0^{1/2}$. The line $V = 0$ is to the right of $K = 0$, the fixed point $(W_0^{1/2}, W_0^{1/2})$ is a spiral but there is a unique trajectory reaching it from $N = 0$ (shown in red). (b) and (c) show the steady-state numerical solution of (2.135), (2.136) for the same parameter values.

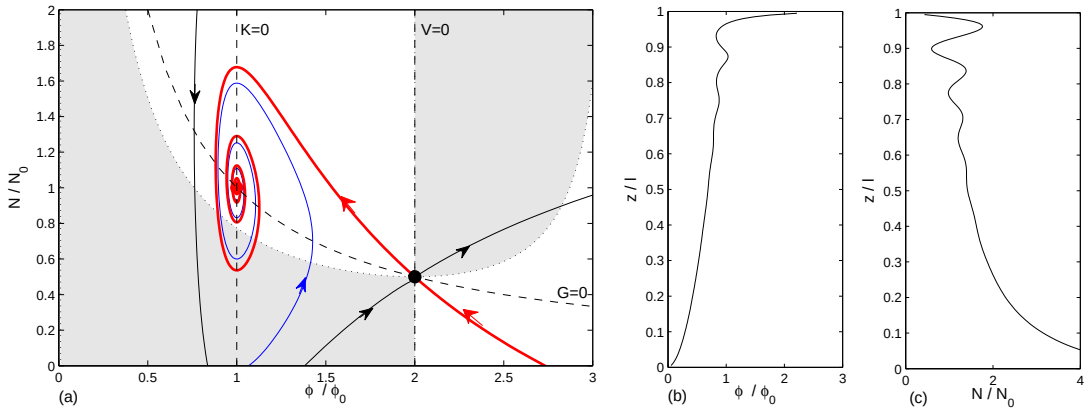

Figure 2.14: Phase plane for the system in (2.203) when $E = 1$, $P = 4$ and $W_0 = 1$, so $2P > EW_0^{1/2}$. The line $V = 0$ is to the right of $K = 0$, the fixed point $(W_0^{1/2}, W_0^{1/2})$ is a spiral and there is a trajectory reaching it from $N = 0$ (shown in red). There are infinitely many other trajectories from $N = 0$ to the fixed point (such as the one shown in blue), but we suggest these are unstable. The shaded region is where $\Re e\ \sigma > 0$ from (2.210). (b) and (c) show the steady-state numerical solution of (2.135), (2.136) for the same parameter values.

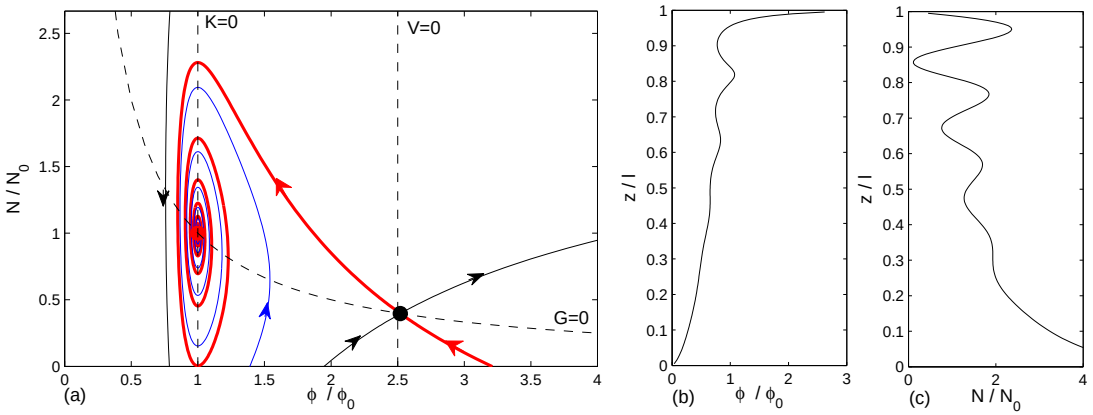

Figure 2.15: Phase plane for the system in (2.203) when $E = 1$, $P = 8$ and $W_0 = 1$, so $2P > EW_0^{1/2}$. The line $V = 0$ is to the right of $K = 0$, the fixed point $(W_0^{1/2}, W_0^{1/2})$ is a spiral but there is a unique trajectory reaching it from $N = 0$, $V < 0$ (shown in red). (b) and (c) show the steady-state numerical solution of (2.135), (2.136) for the same parameter values.

must cross the line $V = 0$. Since $N_{\tilde{z}}$ is infinite on $V = 0$, this is only possible by passing through the point $G = V = 0$, which looks like a degenerate saddle point in the phase plane. Thus although there are many trajectories that terminate at the fixed point, there is still a unique trajectory which leaves $N = 0$ and passes through this degenerate saddle point. As evident when comparing figures 2.11 and 2.13, this trajectory is the continuation of the unique solution when the fixed point is a saddle. When the fixed point is a spiral, this naturally produces solutions in which ϕ and N show oscillatory decay away from the boundary.

Alongside the phase planes in figures 2.11, 2.12, 2.13, 2.14 and 2.15 are the corresponding steady state numerical solutions to the full equations (2.135) and (2.136). As the value of $2P - EW_0^{1/2}$ is increased, the boundary layer becomes oscillatory, and the oscillations grow with the size of $2P - EW_0^{1/2}$. When P is large the boundary layer also becomes larger so that the oscillations penetrate further down into the interior of the partially molten region. In figure 2.15 the oscillations are nearly so large that N reaches zero, and for still larger values of P, N becomes negative.

As discussed in section 2.4.2 above, low values of N mean the matrix is liable to fracture, and indeed if N becomes negative fracture is all the more likely. Thus the potential for oscillatory solutions in this boundary layer offers the intriguing possibility that the fracture criterion (2.202) be met *within* the partially molten region; this would enable the newly initiated fracture to grow by drawing in melt from the surroundings.

Characteristics

The somewhat intriguing behaviour in this boundary layer can be related to the characteristics of the equations; including the time dependence in the boundary layer equations gives

$$\varepsilon\phi_t + V(\phi)\phi_{\tilde{z}} = G(\phi, N), \quad N_{\tilde{z}} = K(\phi), \tag{2.204}$$

were $V(\phi)$, $K(\phi)$ and $G(\phi, N)$ are as in (2.203). There is one real characteristic with speed V/ε. When $2P < EW_0^{1/2}$, the solution has $V < 0$, corresponding to the characteristics entering the boundary layer from below. When $2P > EW_0^{1/2}$, however, the characteristic must change direction within the boundary layer, and point outwards towards the outer solution. This is slightly surprising, since the advection of both melt and matrix is upwards and we would naïvely expect the equations to propagate information upwards. For the full equations (2.135) and (2.136), this one

characteristic is given by

$$\frac{dz}{dt} = W_0 - \frac{2W_0 P}{E}\frac{(1+\delta^2 N_z)}{\phi}, \tag{2.205}$$

which has the same property that it may be positive or negative. However the leading order equation in the outer region is

$$\varepsilon\phi_t + 2\phi\phi_z = W_0, \tag{2.206}$$

which has characteristic speed $2\phi/\varepsilon$, which is always positive. This appears to be completely unrelated to the *actual* characteristic (2.205); the singular approximation produces a new characteristic speed which is not in the full problem. It might be called a *subcharacteristic*, although that term is usually used when a singular approximation reduces the number of characteristics or changes the type of the system (e.g. from elliptic to hyperbolic).

The reason for the characteristics changing direction is the term in P; that is, heat conduction. If P is small enough the situation is as in figure 2.11 and conduction has very little effect. Since the temperature is constrained to the solidus (2.121), heat conducts *up* gradients in N and therefore downwards in the partial melting region. As P is increased the importance of this downwards information propagation increases and changes the direction of the characteristic (2.205).

The origin of the oscillatory structure is therefore in the unusual thermodynamics; the effective pressure controls the temperature, the matrix compaction *and* the melt movement. These last two dynamical roles for the effective pressure require that near the boundary of the partially molten region there must be a very sudden change in pressure, but the fact that this produces large temperature gradients, which heat conduction would attempt to smooth out, seems to force the steady solutions to have the unusual oscillatory profile.

There does not appear to be any clearer physical meaning attached to the condition $2P < EW_0^{1/2}$, other than a certain combination of physical properties; being a scaled inverse Péclet number, larger values of P imply greater relative importance of heat conduction to matrix advection. An exploration of parameter values suggests that very significant oscillations in which the effective pressure approaches zero are probably unlikely, but they may be possible if the ascent rate is less than approximately 1 cm y^{-1}. It is not at all clear how these effects will manifest themselves in the two-dimensional case or when more thermodynamic components are considered, so we do not intend to draw too many conclusions from them; we note however that the role of heat conduction when the solidus is pressure dependent may have some unexpected effects.

Stability

If P is large enough, it is clear from figures 2.14 and 2.15 that there may be more than one trajectory that starts at $N = 0$ and spirals in to the fixed point, so there appear to be infinitely many solutions to the boundary layer problem. This leads us to consider whether they are stable and could realistically exist. Note that there is still one unique trajectory passing through the degenerate saddle from $V < 0$ and any others, if they exist, have $V > 0$ everywhere.

We consider a local stability analysis; supposing $(\tilde{\phi}(\tilde{z}), \tilde{N}(\tilde{z}))$ is a steady solution to (2.203), we write $\phi = \tilde{\phi} + \phi'$, $N = \tilde{N} + N'$ and linearise the time-dependent version (2.204):

$$\varepsilon\phi'_t + V(\tilde{\phi})\phi'_{\tilde{z}} + \frac{G(\tilde{\phi}, \tilde{N})V_\phi(\tilde{\phi})}{V(\tilde{\phi})}\phi' = G_\phi(\tilde{\phi}, \tilde{N})\phi' + G_N(\tilde{\phi}, \tilde{N})N', \tag{2.207}$$

$$N'_{\tilde{z}} = K_\phi(\tilde{\phi})\phi'. \tag{2.208}$$

Treating all the coefficients here as constants, we consider solutions of the form $\phi', N' \propto e^{\sigma t/\varepsilon + ikz}$. The resulting dispersion relation is

$$\sigma = G_\phi - \frac{GV_\phi}{V} - \left(V + \frac{K_\phi G_N}{k^2}\right) ik, \tag{2.209}$$

and the real part is

$$\Re e\ \sigma = \frac{G_\phi V - GV_\phi}{V} = \frac{(E\tilde{\phi}^3 - 8PW_0)\tilde{\phi}\tilde{N} + 6PW_0^2}{\tilde{\phi}(2PW_0 - E\tilde{\phi}^3)}. \tag{2.210}$$

The local perturbation grows if this is positive. We are particularly interested in the behaviour of solutions near to the boundary, where N approaches zero. As $N \to 0$ the growth rate has the same sign as V, so the solutions will be unstable if $V > 0$. Thus any of the spiralling trajectories that approach $N = 0$ with $V > 0$ (i.e. with characteristics coming *out* of the boundary) are apparently unstable, and we can conclude they are unlikely to exist physically. The only solution that is possible is therefore the one that passes through the degenerate saddle to $V < 0$ (for which the characteristics eventually propagate *into* the boundary).

The region where $\Re e\ \sigma$ in (2.210) is positive is shown in figure 2.14, which also shows one of the possible alternative characteristics that is unstable. A further problem appears to arise in that the solution trajectory that passes through the degenerate saddle later passes into the unstable region; if this solution were also unstable there would be no steady boundary layer solution at all.

Numerically, however, we do find a stable steady solution, and it seems likely that the results of the local linear stability argument may be misleading when applied to points further from the boundary. If it works at all, we expect it to be near the boundary where N approaches zero, and it is on this ground that we suggest the alternative solutions would be unstable. Numerical experimentation also failed to find any steady solutions with $V > 0$ at the boundary, which agrees with this assertion (they would look quite different from the solution shown in figure 2.14(b) since ϕ would be decreasing towards the boundary).

2.4.4 Degree of melting

For many geological studies it is important to know how much melting a rock has undergone; this is usually called the *extent* or *degree of melting*. Sometimes it is rather confusingly referred to as the 'partial melt fraction', and it is important to realise this is not the same as the actual melt fraction ϕ since, as we have seen, separation of melt and compaction of the matrix ensures that the melt fraction never exceeds a few percent.

The degree of melting F is really a property of the matrix, rather than the melt, since it describes what fraction of the original rock has melted. Essentially one would like to write F as an integral of the melting rate, but since the rock compacts we have to be slightly careful in doing this. If we define F as the fraction of an initial volume of rock $\mathcal{V}(0)$ which has melted, the rate at which it later melts is $m\mathcal{V}(t)$.

In the one-dimensional steady state, and to order ϕ_0, the dimensionless compaction rate is $W_Z \approx -m/St \approx -W_0/St$, meaning that the matrix compacts at the same rate it melts. Thus $\mathcal{V}(t) = \mathcal{V}(0)(1 - F)$, and the steady state has, non-dimensionally,

$$W\frac{\partial F}{\partial z} = \frac{m}{St}(1 - F). \tag{2.211}$$

The velocity is $W \approx W_0(1 - z/St)$, so this equation integrates to give

$$F(z) = \frac{z}{St} \tag{2.212}$$

Thus, as indicated in section 2.2, the degree of melting is governed by the Stefan number, and the total degree of melting at the top of the one-dimensional column is $1/St$. With our choice of parameters the partial melting region is around 50 km deep, $St \approx 2$ and we expect around 50% of the rock to melt, which is largely consistent with other models (Ahern and Turcotte, 1979; McKenzie, 1984). (2.212) also agrees with the results of Šrámek et al. (2007), who find that the degree of melting varies

approximately linearly with depth, and predict complete melting of the rock over a depth of around 100 km.

2.5 Summary

In this chapter we have set out model equations to describe the partially molten regions of the mantle under conditions of local thermodynamic equilibrium with a pressure dependent solidus. The equations are essentially the same as those of McKenzie (1984) and Šrámek et al. (2007), the differences arising from their simplification and use.

Scaling the equations motivates neglecting adiabatic temperature changes and deviatoric stresses in the matrix, so we work with a simplified model describing melt flow and matrix compaction governed by buoyancy and effective pressure. Energy conservation determines the local melting rate required in order to sustain equilibrium, which is proportional to the rate that heat is carried upwards by the matrix and melt.

Conservation laws are applied at the boundary of the partial melting region to determine its position. An additional condition requiring the boundary itself to be in thermodynamic equilibrium requires that the pressures in solid and melt be equal there if the melt fraction is non-zero.

In one dimension, the partial melt equations can be reduced to an unusual degenerate pair of equations for ϕ and N, (2.135) and (2.136) for which steady solutions are found both numerically and using analytical approximations (figures 2.6 and 2.7). These agree in many respects with other published results: the parabolic melt profile (Ahern and Turcotte, 1979; Šrámek et al., 2007); the near-linear decrease in matrix velocity; the viscous boundary layer near the onset of melting (Fowler, 1990b; Šrámek et al., 2007); and the presence of a temperature precursor beneath the partially molten region (Ahern and Turcotte, 1979). Future work will hope to extend these to two dimensions, with lateral movement of both matrix and melt, although solving even this simplified problem in that case is by no means trivial.

The boundary-layer treatment of temperature and pressure gradients at the bottom of the partial melt region allows an expression (2.194) to be derived for the depth of onset of melting. Šrámek et al. (2007) pointed out that including the density difference $r \neq 1$ will cause some extra problems near this boundary; there will be a small region in which the lower density melt requires an infinite pressure gradient to drive it through the matrix. The same behaviour occurs in our solutions if the density

difference is included, and it seems that some form of disequilibrium melting may be required. With realistic parameters however the region over which these issues arise is very small and would, for instance, make no discernible difference to the graph of figure 2.2.

In this model, melt is assumed to solidify at the base of the lithosphere and cause a jump in temperature gradient there. The requirement that effective pressure reduces to zero means that fracturing of the matrix is quite likely and this may facilitate further transport through the crust. Heat conduction and the pressure dependence of the temperature may cause an intriguing oscillatory structure to the boundary layer there, though it seems unlikely that realistic parameter values would produce dramatic oscillations such as explored in section 2.4.3.

Chapter 3

Magma channels

3.1 Melting instability

In this chapter we consider the dynamics of open channels of magma within decompressing regions of the mantle. The channels would be surrounded by the partially molten matrix that has been considered in chapter 2, and later in this chapter we will consider the interaction between a channel and the surrounding porous flow. A channel might form either through fracturing of the matrix or through reactive instabilities to the porous flow, as discussed in chapter 1.

As motivation, and as guidance for the models that follow, we begin by considering two-dimensional perturbations in the partial melt model from chapter 2. We continue to restrict our attention to the case of an ascending column, for which the prescribed solid flow is vertical, but we now allow the column to have a second dimension y. Since the spreading of the matrix is not included it may be more appropriate to consider this second dimension as being aligned with the ridge axis rather than perpendicular to it.

Using the simplified model in (2.96)-(2.102), we again ignore the matrix stresses of size $\delta_s^2\varepsilon$ and also make an additional simplification by ignoring the temperature's dependence on the effective pressure, of size δ_s^2. The equations are therefore

$$\varepsilon\frac{\partial\phi}{\partial t} + \varepsilon\nabla\cdot(\phi\mathbf{V}) + \nabla\cdot[\phi(\mathbf{u}-\varepsilon\mathbf{V})] = m, \tag{3.1}$$

$$\nabla\cdot[\phi(\mathbf{u}-\varepsilon\mathbf{V})] + St\nabla\cdot\mathbf{V} = 0, \tag{3.2}$$

$$\phi\left(\mathbf{u}-\varepsilon\mathbf{V}\right) = \phi^2\left(\mathbf{k}+\delta^2\nabla N\right), \tag{3.3}$$

$$\phi N = -St\nabla\cdot\mathbf{V}, \tag{3.4}$$

$$m + \frac{\partial T}{\partial t} + \frac{1}{St}\phi\left(\mathbf{u}-\varepsilon\mathbf{V}\right)\cdot\nabla T + \mathbf{V}\cdot\nabla T = 0, \tag{3.5}$$

$$T = -z. \tag{3.6}$$

These represent conservation of mass (3.1), (3.2), Darcy's law (3.3), the compaction relation (3.4), energy conservation (3.5) and thermodynamic equilibrium with the pressure dependent solidus (3.6). Boundary conditions are, from (2.106) and (2.108),

$$\phi = 0, \quad \mathbf{V} = W_0\mathbf{k} \quad \text{at} \quad z = 0, \tag{3.7}$$

$$N = 0 \quad \text{at} \quad z = 1. \tag{3.8}$$

Note from (3.2) that the compressible part of the matrix flow is of order $1/St$. It is therefore useful to decompose $\mathbf{V}$ into an incompressible and an irrotational part;

$$\mathbf{V} = \nabla \wedge \mathbf{\Psi} + \frac{1}{St}\nabla\mathcal{U}, \tag{3.9}$$

and we expect the partial melt dynamics to determine the compressible part, while the incompressible part is determined externally by the larger scale matrix flow. For the solutions we look for here we have

$$\nabla \wedge \mathbf{\Psi} = W_0\mathbf{k}. \tag{3.10}$$

Using (3.6) in (3.5) directly gives the melting rate as

$$m = W_0 + \frac{1}{St}\frac{\partial \mathcal{U}}{\partial z} + \frac{1}{St}\phi^2\left(1 + \delta^2\frac{\partial N}{\partial z}\right). \tag{3.11}$$

This is important as it states that the melting rate is due to advection of heat down the solidus gradient as the material decompresses. The first term is due to heat advected by the background upwelling rate of the matrix; the second term is the correction due to compaction, which causes the vertical velocity to reduce (this term will be negative); and the third term is the heat advected by the melt flow.

In the one dimensional solutions in chapter 2, the second and third terms exactly cancel (due to mass conservation (3.2) any increase in melt flow upwards is balanced by a decrease in matrix flow) and the background upwelling of the *matrix* determines the melt rate; but in two dimensions this is not necessarily the case. This chapter essentially considers what happens when it is the last term - the heat transport due to *melt* flow - which drives the melting. The fact that this gives a melting rate proportional to flow rate, and melting inevitably increases the flow rate, allows for a positive feedback with a runaway effect.

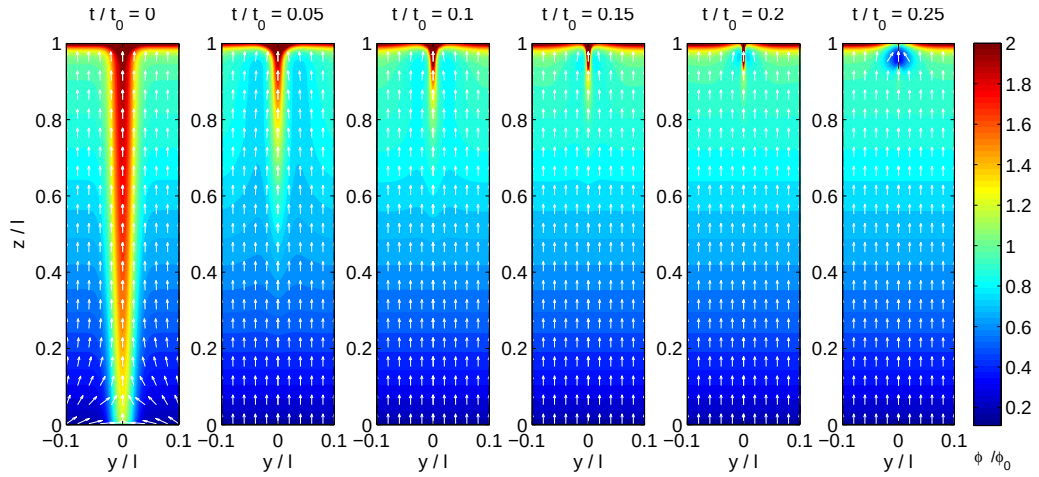

Figure 3.1: Time evolution of scaled melt fraction ϕ/ϕ_0 from an initial perturbation $\exp(-y^2/0.0005)$ to the one dimensional steady state, given by the numerical solution of (3.12)-(3.16). The parameters here are $\varepsilon = 0.02$, $\delta = 0.14$, $St = 2$, and the timescale t_0 is the advective timescale for the matrix l/V_0. White arrows show the direction of melt movement. The discretisation is smallest near the centre $y = 0$, and in the last plot shown here, some of the central cells have reached a melt fraction of 100%, at which point the model breaks down and these cells must be interpreted as an open channel. The continued evolution is then shown in figure 3.10.

With (3.9) and (3.11) the equations (3.1)-(3.4) are written in terms of ϕ, N and $\mathcal{U}$:

$$\varepsilon\frac{\partial\phi}{\partial t}+\varepsilon W_0\frac{\partial\phi}{\partial z}+\frac{\varepsilon}{St}\nabla\cdot(\phi\nabla\mathcal{U})+\nabla\cdot\left[\phi^2\left(\mathbf{k}+\delta^2\nabla N\right)\right]=W_0+\frac{1}{St}\frac{\partial\mathcal{U}}{\partial z}+\frac{1}{St}\phi^2\left(1+\delta^2\frac{\partial N}{\partial z}\right), \tag{3.12}$$

$$\nabla\cdot\left[\phi^2\left(\mathbf{k}+\delta^2\nabla N\right)\right]=\phi N, \tag{3.13}$$

$$-\nabla^2\mathcal{U}=\phi N, \tag{3.14}$$

and the boundary conditions are

$$\phi=0,\quad \frac{\partial\mathcal{U}}{\partial z}=0\quad\text{at}\quad z=0, \tag{3.15}$$

$$N=0,\quad U=0\quad\text{at}\quad z=1. \tag{3.16}$$

The one dimensional steady state solutions were given in chapter 2, and apart from in small boundary layers near $z = 0$ and $z = 1$ are given by

$$\phi\sim W_0^{1/2}z^{1/2},\quad N\sim\frac{W_0^{1/2}}{z^{1/2}},\quad \mathcal{U}\sim W_0\frac{1-z^2}{2}. \tag{3.17}$$

Figure 3.1 shows the evolution of a perturbation to this steady state, from the numerical solutions of (3.12)-(3.16). The finite volume method used to calculate these is

outlined in appendix C. The initial perturbation is Gaussian in the second dimension y and adds a maximum of 1% to the melt fraction. Initially the perturbation appears to diminish, as the matrix compacts more in regions of larger porosity. However, near the top of the partial melting region the area with larger porosity melts faster; the perturbation grows and the melt from the surroundings is focussed in towards the centre at $y = 0$. In the very centre of the perturbation the porosity grows more and more until it reaches 100%; when this happens it is clearly inappropriate to describe it as a porous medium and the current model breaks down.

Later we describe how we deal with this issue numerically, but for the moment we take this focussing mechanism, along with the possibility for fracturing or other reactive instabilities, as motivation to consider the dynamics of open channels or conduits.

The melting instability demonstrated in figure 3.1 is very similar to the reactive infiltration instability (Kelemen et al., 1995; Aharonov et al., 1995; Spiegelman et al., 2001), since it relies upon the fact that melting, or dissolution (which is essentially the same thing), occur faster in regions where there is more melt flow. In the case of reactive infiltration this is because the melt transported from below finds itself undersaturated and dissolves the matrix; in our case the ascending melt finds itself too hot and loses heat by melting the matrix. Since we consider only one-component rock, this feedback can continue until (locally) the matrix has all melted.

3.2 Channel dynamics

3.2.1 Preliminaries

We start with a 'lumped' model for flow within a planar 'crack-shaped' channel; we then consider how this follows from a fuller three dimensional description of the flow, and then go on to look at a cylindrical shaped conduit. Importantly, we are considering the channel to be embedded within a viscously deforming matrix which is constrained to be at the solidus temperature. This has three important consequences; (1) the matrix is porous and we expect the channel to be fed by melt flow from the surrounding regions through the small holes in the walls; (2) the walls can melt; and (3) the walls can deform viscously.

The last point means that these channels are not the same as conduits or cracks in an elastic medium. In that case the pressure in the channel is related to the *displacement* of the walls, whereas here it is related to the *velocity* of the walls. The best physical analogy is with Röthlisberger channels of water flowing within

viscously deforming ice, and the equations here will bare many similarities with those (Röthlisberger, 1972; Nye, 1976; see also chapter 4).

Surrounding matrix

Throughout this section we will assume that the inflow of melt through the channel walls is somehow prescribed; then in the next section we go on to calculate this by coupling the channel and the surrounding porous flow.

We also assume throughout this section that the pressure in the surrounding matrix is lithostatic

$$p_s = p_m - \rho_s g z, \tag{3.18}$$

and that its temperature T_s is constrained to the solidus

$$T_s = T_m + \Gamma(p_l - p_m). \tag{3.19}$$

Here p_m and T_m are the reference values at $z = 0$, ρ_s is the solid density, g is the gravitational acceleration and Γ is the Clapeyron slope. If the melt pressure in the channel is p_l, it is useful to work in terms of the channel effective pressure

$$N_c = p_s - p_l. \tag{3.20}$$

Although the temperature of the matrix is constrained to the solidus, we allow for the possibility that the melt within the channel (which is not in such close contact with the solid rock) can have a different (higher) temperature. Instead of the absolute temperature T_l it is helpful to work in terms of the *excess* temperature

$$\theta = T_l - T_s. \tag{3.21}$$

Viscous closure

A reduced pressure intrusion in a viscous fluid will close down due to creep. The rate at which this happens depends upon the viscosity of the fluid η_s, the pressure difference N_c, and geometry of the intrusion; in general we will write V_n to denote the velocity that the wall moves in the normal direction $\mathbf{n}$. For a cylindrical channel with radius R, Nye (1952) showed that

$$V_n = -\frac{RN_c}{2\eta_s}. \tag{3.22}$$

For other shapes, the closure rate is less straightforward. If it has a long crack-like shape, as in figure 3.2, we assume that the width h in the y direction is much less

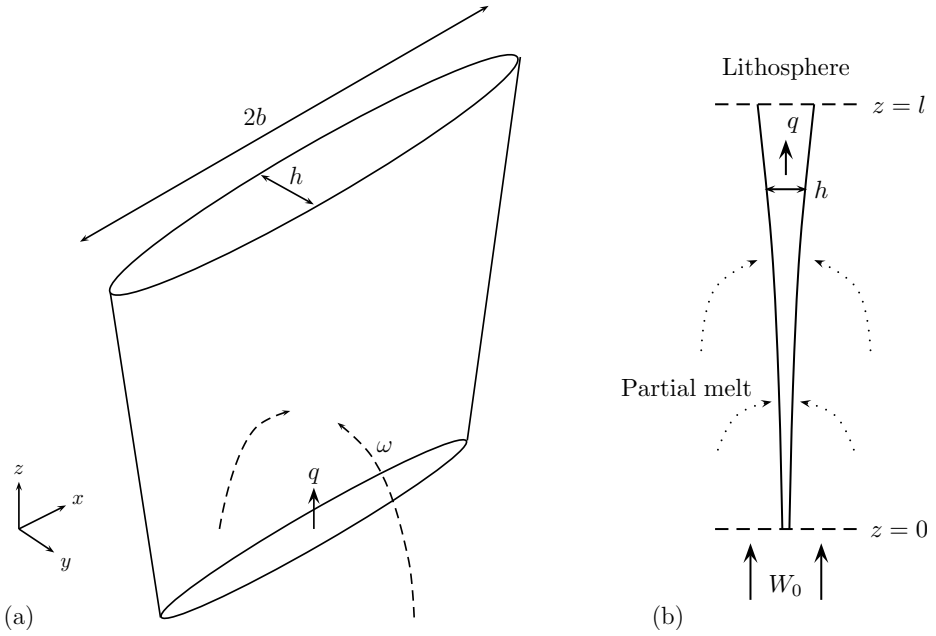

Figure 3.2: (a) Geometry of channel considered in section 3.2.2, with width h, half-breadth b, flux per unit breadth q and influx ω; (b) the two dimensional setup for a channel occupying the full depth of the partially molten region.

than the half-breadth b in the x direction, which is also much less than the length l in the (vertical) z direction. For the purposes of understanding the matrix motion the variations in the z direction are then of little importance, and the closure rate can be calculated using standard complex variable theory (Muskhelishvili, 1953). The velocity of the walls in the y direction V_y satisfies

$$\frac{\partial V_y}{\partial x} = -\frac{1}{2\pi\eta_s}\int_{-b}^{b}\left\{\frac{b^2-\xi^2}{b^2-x^2}\right\}^{1/2}\frac{N_c(\xi)}{\xi-x}\,\mathrm{d}\xi. \tag{3.23}$$

This is similar to the expression for the displacement of a crack in a linear elastic solid. If the effective pressure is constant along the breadth of the crack, it can be integrated to give

$$V_y = -\frac{(b^2-x^2)^{1/2}N_c}{2\eta_s}. \tag{3.24}$$

Notice that (3.22) and (3.24) are similar, and the difference arises from the length which multiplies N_c/η_s. For shapes between a long thin crack and a cylinder, a similar relationship should apply but one has to decide on an appropriate length scale to use.

3.2.2 Planar cracks

The crack is aligned in the vertical z direction and contains melt with density ρ_l and viscosity η_l. We ignore variations in the x direction and consider only the two

dimensional case, with melt flowing from either side into the crack of width $h(z,t)$. The Reynolds number is small (see later, (3.79)), so the flow is laminar, and the two-dimensional vertical flux $q(z,t)$ is given by the Poiseuille law

$$q = \frac{h^3}{12\eta_l}\left(\Delta\rho g + \frac{\partial N_c}{\partial z}\right). \tag{3.25}$$

Here $\Delta\rho = \rho_s - \rho_l$ is the density difference and N_c is the effective pressure (3.20), assumed constant across the width of the channel. The continuity equation is

$$\frac{\partial h}{\partial t} + \frac{\partial q}{\partial z} = \frac{m}{\rho_l} + \omega, \tag{3.26}$$

in which m (kg m^{-1} s^{-1}) is the rate of melting of the walls, and the source term ω accounts for the inflow of melt through the walls.

Melting of the walls causes the width h to grow, but closure causes it to decrease at a rate given by twice (3.24). Taking the value in the middle of the crack ($x = 0$), we have the kinematic condition

$$\frac{\partial h}{\partial t} = \frac{m}{\rho_s} - \frac{bN_c}{\eta_s}. \tag{3.27}$$

We do not yet know the melting rate however, and to calculate this we must include an energy equation; written in terms of the cross-sectionally averaged excess temperature $\overline{\theta}$ this is

$$m\left(L + c\overline{\theta}\right) + \rho_l c\omega\overline{\theta} + \rho_l ch\frac{\partial}{\partial t}\left(T_s + \overline{\theta}\right) + \rho_l cq\frac{\partial}{\partial z}\left(T_s + \overline{\theta}\right) = kh\frac{\partial^2}{\partial z^2}\left(T_s + \overline{\theta}\right) + q\left(\Delta\rho g + \frac{\partial N}{\partial z}\right). \tag{3.28}$$

The first term is the energy lost to meting the walls (L is the latent heat of melting, c is the specific heat capacity, and $c\overline{\theta}$ is the amount the melt must be heated by), the second term is the energy required to heat the inflowing melt, the rest of the left hand side is heat advection, and the terms on the right are conduction and viscous dissipation (k is the thermal conductivity). Only conduction in the vertical direction remains in this lumped model; conduction in the horizontal y direction is responsible for the melting term, since this is caused by a heat flux into the wall. The details of this energy transfer from the bulk flow into the wall are parameterized by a heat transfer equation

$$mL = \frac{\alpha k\overline{\theta}}{h}, \tag{3.29}$$

for conductive heat transfer enhanced by advection in a pipe. The constant $\alpha = 10$ will be deduced later from a fuller consideration of the melt flow.

With ω prescribed, (3.25)-(3.29) provide a closed system of equations for the flux q, the width h, the effective pressure N_c, the temperature $\overline{\theta}$, and the melt rate m, *provided* we also prescribe b. Presumably b should also satisfy its own evolution equation similar to (3.27); however it is not entirely clear what the analogue should be, and we certainly cannot hope to include it without also considering flow in the x direction. We therefore assume that b is given.

Non-dimensionalisation

Before scaling the equations it is useful to outline the expected dynamics. The melt flowing in through the walls will rise up the channel due to its buoyancy. As it rises, the temperature of the walls decreases due to decompression, and the melt finds itself at an elevated temperature; this causes a heat flux into the walls which consequently melt. A steady state will be possible when this melting balances the viscous closure in the kinematic condition (3.27).

This suggests that the dominant balances should be between flux and inflow in (3.26), and between flux and buoyancy in (3.25). The melting rate in (3.28) balances vertical advection and the energy transfer equation (3.29) then determines the required excess temperature. If the length scale is l we write $z = lz^*$, $b = b_0 b^*$, $p = p_m - p_0 p^*$, $T_s = T_m + T_0 T_s^*$, $N_c = N_{c0} N^*$, $m = m_0 m^*$, $h = h_0 h^*$, $q = q_0 q^*$, $\theta = \theta_0 \theta^*$, $\omega = \omega_0 \omega^*$, $t = t_{c0} t^*$. We choose the scales (with subscript 0) to achieve the balances

$$T_s - T_m \sim \Gamma \rho_s g z, \quad q \sim \frac{h^3 \Delta\rho g}{12\eta_l} \sim \omega z, \quad mL \sim \rho_l c \Gamma \rho_s g q \sim \frac{\alpha k \overline{\theta}}{h}, \quad \frac{m}{\rho_s} \sim \frac{b N_c}{\eta_s}. \tag{3.30}$$

Given ω_0 this gives $q_0 = \omega_0 l$, and in terms of q_0 the other scales are

$$p_0 = \rho_s g l, \tag{3.31}$$

$$T_0 = \Gamma \rho_s g l, \tag{3.32}$$

$$h_0 = \left(\frac{12\eta_l q_0}{\Delta\rho g} \right)^{1/3}, \tag{3.33}$$

$$m_0 = \frac{\rho_l c \Gamma \rho_s g}{L} q_0, \tag{3.34}$$

$$N_{c0} = \frac{\eta_s m_0}{\rho_s b_0} = \frac{\eta_s \rho_l c \Gamma g}{b_0 L} q_0, \tag{3.35}$$

$$\theta_0 = \frac{h_0 m_0 L}{\alpha k} = \frac{\rho_l c \Gamma \rho_s g}{\alpha k} \left(\frac{12\eta_l q_0}{\Delta\rho g} \right)^{1/3} q_0, \tag{3.36}$$

$$t_{c0} = \frac{\eta_s h_0}{N_{c0} b_0} = \frac{\rho_s}{\rho_l} \frac{L}{c\Gamma \rho_s g} \frac{h_0}{q_0}. \tag{3.37}$$

Scaling all the variables in this way, and then dropping the asterisks, results in the non-dimensional equations

$$q = h^3 \left(1 + \delta_c^2 \frac{\partial N_c}{\partial z}\right), \tag{3.38}$$

$$\frac{1}{r\ St} \frac{\partial h}{\partial t} + \frac{\partial q}{\partial z} = \frac{m}{St} + \omega, \tag{3.39}$$

$$\frac{\partial h}{\partial t} = m - bN_c, \tag{3.40}$$

$$m\left(1 + \frac{\mu}{St}\overline{\theta}\right) + \mu\omega\overline{\theta} + h\frac{\partial}{\partial t}\left(T_s + \mu\overline{\theta}\right) + q\frac{\partial}{\partial z}\left(T_s + \mu\overline{\theta}\right) = \frac{1}{Pe} h \frac{\partial^2}{\partial z^2}\left(T_s + \mu\overline{\theta}\right) + (r-1)\nu q\left(1 + \delta_c^2 \frac{\partial N}{\partial z}\right), \tag{3.41}$$

$$m = \frac{\overline{\theta}}{h}, \tag{3.42}$$

$$T_s = -z - \frac{r-1}{r}\delta_c^2 N_c. \tag{3.43}$$

The dimensionless parameters that have been used here are

$$r = \frac{\rho_s}{\rho_l}, \tag{3.44}$$

$$St = \frac{L}{c\Gamma\rho_s g l}, \tag{3.45}$$

$$\mu = \frac{\theta_0}{\Gamma\rho_s g l}, \tag{3.46}$$

$$Pe = \frac{\rho_l c q_0 l}{k h_0}, \tag{3.47}$$

$$\delta_c^2 = \frac{N_{c0}}{\Delta\rho g l}, \tag{3.48}$$

$$\nu = \frac{gl}{c\Gamma\rho_s g l}. \tag{3.49}$$

As in chapter 2, r is the density ratio; St is the Stefan number, which is the ratio of latent to sensible heat; μ is the ratio of excess temperature to the change in the solidus; Pe is the Péclet number; δ_c^2 is the ratio of channel effective pressure to buoyancy force; and ν is the ratio of gravitational potential energy to sensible heat.

Parameter	Value	Parameter	Value
g	$10\ \mathrm{m\ s^{-2}}$	Γ	$10^{-7}\ \mathrm{K\ Pa^{-1}}$
ρ_s	$3 \times 10^3\ \mathrm{kg\ m^{-3}}$	α	10
ρ_l	$2.5 \times 10^3\ \mathrm{kg\ m^{-3}}$	$\hat{\alpha}$	6π
c	$10^3\ \mathrm{J\ kg^{-1}\ K^{-1}}$	η_l	10 Pa s
k	$2.5\ \mathrm{J\ m^{-1}\ s^{-1}\ K^{-1}}$	η_s	10^{19} Pa s
L	$3 \times 10^5\ \mathrm{J\ kg^{-1}}$	l	50 km

Table 3.1: Values of constants used in chapter 3.

Taking a notional inflow rate $\omega_0 = 10^{-10}\ \mathrm{m\ s^{-1}}$, length $l = 50$ km and half-breadth $b_0 = 1$ km, and using the values in table 3.1 for the other parameters gives the typical values

$$q_0 \sim 5 \times 10^{-6}\ \mathrm{m^2\ s^{-1}}, \tag{3.50}$$

$$T_0 \sim 150\ \mathrm{K}, \tag{3.51}$$

$$h_0 \sim 5\ \mathrm{mm}, \tag{3.52}$$

$$m_0 \sim 1.3 \times 10^{-7}\ \mathrm{kg\ m^{-2}\ s^{-1}}, \tag{3.53}$$

$$N_{c0} \sim 0.4\ \mathrm{MPa}, \tag{3.54}$$

$$\theta_0 \sim 8 \times 10^{-6}\ \mathrm{K}, \tag{3.55}$$

$$t_{c0} \sim 1.2 \times 10^8\ \mathrm{s}, \tag{3.56}$$

for the scales, and

$$r \sim 1.2, \tag{3.57}$$

$$St \sim 2, \tag{3.58}$$

$$\mu \sim 5 \times 10^{-8}, \tag{3.59}$$

$$Pe \sim 5 \times 10^7, \tag{3.60}$$

$$\delta_c^2 \sim 0.002, \tag{3.61}$$

$$\nu \sim 3. \tag{3.62}$$

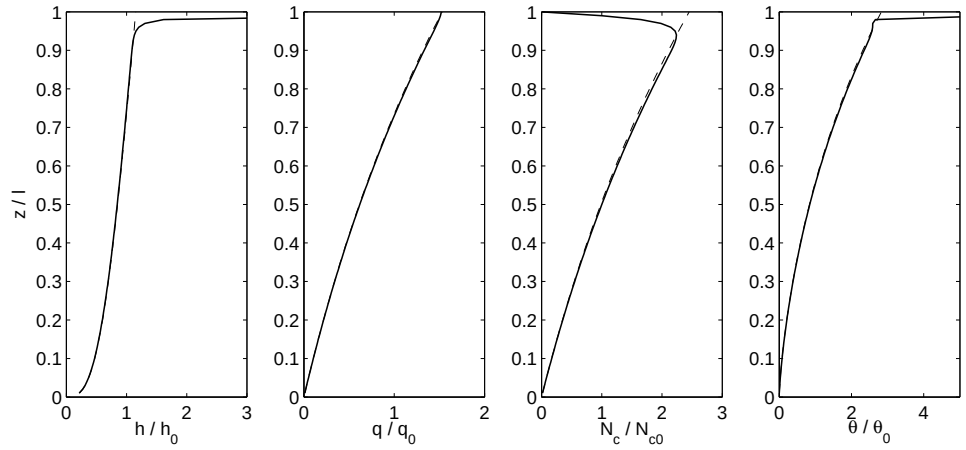

Figure 3.3: Steady state solutions for width h, flux q, effective pressure N_c and excess temperature θ, to (3.38)-(3.43) and (3.63), with $\omega = 1$ and $r = 1.2$, $St = 2$, $Pe = \infty$, $\delta_c^2 = 0.01$, $\nu = 3$ and $\mu = 0.0004$. The solid lines show the numerical solution, the dashed lines show the approximate solution given by (3.64)-(3.67).

Boundary conditions

The length scale chosen above is appropriate for a channel that occupies the full depth of the partially molten region of the mantle. The model is equally suited to shorter channels, but for our purposes here we will assume that it extends all the way from the bottom $z = 0$ to the top of the partially molten region, $z = 1$ in the scaled variables. By the 'top', we mean the base of the lithosphere; we will not say too much about what happens to the channel above that, but it may be that the melt ponds beneath the lithosphere and periodically erupts, or it may carry on continuously as a lithospheric conduit to feed a magma chamber.

At the bottom of the channel it is appropriate to prescribe zero flux $q = 0$. It is not entirely clear what the condition we should apply at the top is; in chapter 2 we suggested that the effective pressure should go to zero at the top of the partially molten region, and one possibility is that we should apply the same condition in the channel. We therefore suggest the boundary conditions

$$q = 0 \quad \text{at} \quad z = 0, \qquad N_c = 0 \quad \text{at} \quad z = 1. \tag{3.63}$$

Steady-state behaviour

$1/Pe$ and μ are very small and can for the most part be neglected. This is indicative of the fact that the vertical melt motion is far too fast for vertical conduction to have any effect, and that the temperature in the channel rises only a tiny fraction

above the temperature of the surrounding matrix. δ_c^2 is also small and means that the leading order steady solutions are very straightforward:

$$q = h^3 = \int_0^z \omega(\tilde{z}) \exp\left(\frac{(z-\tilde{z})(1+(r-1)\nu)}{St}\right) \, \mathrm{d}\tilde{z}, \tag{3.64}$$

$$m = q(1+(r-1)\nu), \tag{3.65}$$

$$N_c = \frac{m}{b}, \tag{3.66}$$

$$\overline{\theta} = hm. \tag{3.67}$$

This is shown in figure 3.3, along with the steady state numerical solution to (3.38)-(3.43) and (3.63). The only problem with this outer solution is that it does not satisfy the condition $N_c = 0$ at $z = 1$. In order to do so there must be a boundary layer in which the pressure adjusts, and from (3.38) the length scale over which this occurs is δ_c^2; the details are omitted.

Stability

There appears to be a reasonably sensible steady state solution for a crack-shaped channel given by (3.64)-(3.67). The melt flux is driven by buoyancy; melting occurs at a rate proportional to the flux, due to a combination of advection down the solidus and viscous dissipation, both of which have the effect of causing heat transfer into the channel walls. The temperature of the melt rises very little above the wall temperature.

However, the problem with such a long thin channel is that it may be unstable to perturbations in its width. Since the melting rate is proportional to the melt flux, wherever the channel is wider (and therefore transporting a larger flux) it will melt faster and grow wider. Because the closure rate depends only on the breadth b it has no compensating variation, so unusually wide regions will grow and unusually narrow regions will close down. The only possible stabilising mechanism could be heat conduction along the breadth, but it is intuitively clear that this will only have an effect over a length scale comparable to the width h.

We therefore expect that the long thin channel will be unstable, and we suggest it is likely to break up into a series of more cylindrical shaped channels. The model above becomes inappropriate, and a similar one based on a cylindrical cross-section will be more appropriate.

3.2.3 Three-dimensional flow

Before suggesting a cylindrical model, we take a step back and consider a fuller three-dimensional description of the melt flow. This satisfies the Navier-Stokes equations

$$\nabla \cdot \mathbf{u} = 0, \tag{3.68}$$

$$\rho_l \left(\frac{\partial \mathbf{u}}{\partial t} + \mathbf{u} \cdot \nabla \mathbf{u} \right) = \nabla N_c + \Delta \rho g \mathbf{k} + \eta_l \nabla^2 \mathbf{u}. \tag{3.69}$$

and the energy equation is

$$\rho_l c \left(\frac{\partial}{\partial t} + \mathbf{u} \cdot \nabla \right) (T_s + \theta) = k \nabla^2 (T_s + \theta) + \frac{\eta_l}{2} \left(\nabla \mathbf{u} + \nabla \mathbf{u}^T \right)^2. \tag{3.70}$$

If the boundary of the channel has outward pointing normal $\mathbf{n}$, tangent $\mathbf{t}$ we denote its velocity in the normal direction v_n. This is due to the competition between melting m_n and closure $-V_n$ in the normal direction.

$$v_n = \frac{m_n}{\rho_s} + V_n. \tag{3.71}$$

The boundary conditions on the melt velocity are

$$\rho_l \mathbf{u} \cdot \mathbf{n} = \rho_l v_n - m_n - \rho_l \omega_n, \tag{3.72}$$

$$\mathbf{u} \cdot \mathbf{t} = 0, \tag{3.73}$$

where ω_n is the normal inflow rate of melt through the walls.

Boundary conditions on the temperature are

$$\theta = 0, \tag{3.74}$$

$$-k \nabla \theta \cdot \mathbf{n} = m_n L. \tag{3.75}$$

(3.74) states that the temperature must be continuous, and (3.75) is a Stefan condition which conserves energy by relating the heat flux to the latent heat required for melting. In principle it should also account for temperature gradients within the surrounding porous medium, but we assume that this is all maintained at the same (solidus) temperature.

Planar channels

If the channel is planar we assume, as above, the width h in the y direction is much smaller than the half-breadth b in the x direction, and the length l in the z direction. The lengths are therefore scaled by writing $z = lz^*$, $x = b_0x^*$, $y = h_0y^*$, and we define

$$\varepsilon = \frac{h_0}{b_0} \sim 10^{-5}, \qquad \hat{\varepsilon} = \frac{b_0}{l} \sim 0.02, \tag{3.76}$$

to be the two small aspect ratios. The velocities are then scaled by writing $w = w_0w^*$, $u = \hat{\varepsilon}w_0u^*$, $v = \varepsilon\hat{\varepsilon}w_0v^*$. We choose the scalings that are consistent with those used above in (3.31)-(3.37); this means choosing w_0 so that $q_0 = w_0h_0$. With all the variable scales chosen as in (3.31)-(3.38) we additionally have

$$w_0 = \left(\frac{\Delta\rho g q_0^2}{12\eta_l}\right)^{1/3} \sim 10^{-3} \text{ m s}^{-1}, \tag{3.77}$$

and we scale the closure velocity V_n with

$$V_{n0} = \frac{m_0}{\rho_s} = \frac{\rho_l}{\rho_s}\frac{c\Gamma\rho_s g}{L}q_0 \sim 4 \times 10^{-11} \text{ m s}^{-1}. \tag{3.78}$$

The non-dimensional parameters will be as in (3.44)-(3.49), with typical values (3.57)-(3.62), with ε and $\hat{\varepsilon}$ given by (3.76) and the reduced Reynolds number given by

$$Re = \varepsilon^2\hat{\varepsilon}^2\frac{\rho_l w_0 l}{\eta_l} \sim 5 \times 10^{-10}. \tag{3.79}$$

Written in the non-dimensional variables, but dropping the asterisks, the equations (3.68)-(3.70) are

$$\frac{\partial u}{\partial x} + \frac{\partial v}{\partial y} + \frac{\partial w}{\partial z} = 0, \tag{3.80}$$

$$Re\left(\frac{1}{rSt}\frac{\partial w}{\partial t} + u\frac{\partial w}{\partial x} + v\frac{\partial w}{\partial y} + w\frac{\partial w}{\partial z}\right) = 12\left(1 + \delta_c^2\frac{\partial N}{\partial z}\right) + \varepsilon^2\frac{\partial^2 w}{\partial x^2} + \frac{\partial^2 w}{\partial y^2} + \varepsilon^2\hat{\varepsilon}^2\frac{\partial^2 w}{\partial z^2}, \tag{3.81}$$

$$\hat{\varepsilon}^2 Re\left(\frac{1}{rSt}\frac{\partial u}{\partial t} + u\frac{\partial u}{\partial x} + v\frac{\partial u}{\partial y} + w\frac{\partial u}{\partial z}\right) = 12\delta_c^2\frac{\partial N}{\partial x} + \varepsilon^2\hat{\varepsilon}^2\frac{\partial^2 u}{\partial x^2} + \hat{\varepsilon}^2\frac{\partial^2 u}{\partial y^2} + \varepsilon^2\hat{\varepsilon}^4\frac{\partial^2 u}{\partial z^2}, \tag{3.82}$$

$$\varepsilon^2\hat{\varepsilon}^2 Re\left(\frac{1}{rSt}\frac{\partial v}{\partial t} + u\frac{\partial v}{\partial x} + v\frac{\partial v}{\partial y} + w\frac{\partial v}{\partial z}\right) = 12\delta_c^2\frac{\partial N}{\partial y} + \varepsilon^4\hat{\varepsilon}^2\frac{\partial^2 v}{\partial x^2} + \varepsilon^2\hat{\varepsilon}^2\frac{\partial^2 v}{\partial y^2} + \varepsilon^4\hat{\varepsilon}^4\frac{\partial^2 v}{\partial z^2}, \tag{3.83}$$

$$\frac{1}{rSt}\frac{\partial}{\partial t}\left(T_s+\mu\theta\right)+w\frac{\partial T_s}{\partial z}+\mu\left(u\frac{\partial\theta}{\partial x}+v\frac{\partial\theta}{\partial y}+w\frac{\partial\theta}{\partial z}\right)$$
$$=\frac{1}{\alpha}\left(\varepsilon^2\frac{\partial^2\theta}{\partial x^2}+\frac{\partial^2\theta}{\partial y^2}+\varepsilon^2\hat{\varepsilon}^2\frac{\partial^2\theta}{\partial z^2}+\frac{\varepsilon^2\hat{\varepsilon}^2}{\mu}\frac{\partial^2 T_s}{\partial z^2}\right)$$
$$+\frac{(r-1)\nu}{12}\left(\left(\frac{\partial w}{\partial y}+\varepsilon^2\hat{\varepsilon}^2\frac{\partial v}{\partial z}\right)^2+\varepsilon^2\left(\frac{\partial w}{\partial x}+\hat{\varepsilon}^2\frac{\partial u}{\partial z}\right)^2+\hat{\varepsilon}^2\left(\frac{\partial u}{\partial y}+\varepsilon^2\frac{\partial v}{\partial x}\right)^2\right.$$
$$\left.+2\varepsilon^2\hat{\varepsilon}^2\left(\left(\frac{\partial u}{\partial x}\right)^2+\left(\frac{\partial v}{\partial y}\right)^2+\left(\frac{\partial w}{\partial z}\right)^2\right)\right). \quad (3.84)$$

The wall temperature is

$$T_s=-z-\frac{r-1}{r}\delta_c^2 N_c. \quad (3.85)$$

If the channel walls are at $y=\pm h(x,z,t)/2$, the boundary conditions there are

$$v_n=\frac{h_t/2}{(1+\varepsilon^2h_x^2/4+\varepsilon^2\hat{\varepsilon}^2h_z^2/4)^{1/2}}=m_n+V_n, \quad (3.86)$$

$$\left(\frac{u}{\varepsilon},v,\frac{w}{\varepsilon\hat{\varepsilon}}\right)\cdot\frac{(-\varepsilon h_x/2,1,-\varepsilon\hat{\varepsilon}h_z/2)}{(1+\varepsilon^2h_x^2/4+\varepsilon^2\hat{\varepsilon}^2h_z^2/4)^{1/2}}=\frac{1}{rSt}v_n-\frac{1}{St}m_n-\omega_n, \quad (3.87)$$

$$\left(\frac{u}{\varepsilon},v,\frac{w}{\varepsilon\hat{\varepsilon}}\right)\cdot(0,\varepsilon\hat{\varepsilon}h_z/2,1)=\left(\frac{u}{\varepsilon},v,\frac{w}{\varepsilon\hat{\varepsilon}}\right)\cdot(1,\varepsilon h_x/2,0)=0, \quad (3.88)$$

$$m_n=-\frac{1}{\alpha}(\varepsilon\theta_x,\theta_y,\varepsilon\hat{\varepsilon}\theta_z)\cdot\frac{(-\varepsilon h_x/2,1,-\varepsilon\hat{\varepsilon}h_z/2)}{(1+\varepsilon^2h_x^2/4+\varepsilon^2\hat{\varepsilon}^2h_z^2/4)^{1/2}}, \quad (3.89)$$

$$\theta=0. \quad (3.90)$$

Lubrication approximation

Since Re is small all the inertial terms can be neglected, and since ε and $\hat{\varepsilon}$ are also small the situation is hugely simplified. Neglecting terms of order Re, $\hat{\varepsilon}$ and μ, and also for simplicity ignoring the dissipative terms, the momentum and energy equations are:

$$0=12\left(1+\delta_c^2\frac{\partial N}{\partial z}\right)+\frac{\partial^2 w}{\partial y^2}+\varepsilon^2\frac{\partial^2 w}{\partial x^2}, \quad (3.91)$$

$$0=\frac{\partial N}{\partial x}, \quad (3.92)$$

$$0=\frac{\partial N}{\partial y}, \quad (3.93)$$

$$\alpha w\frac{\partial T_s}{\partial z}=\frac{\partial^2\theta}{\partial y^2}+\varepsilon^2\frac{\partial^2\theta}{\partial x^2}, \quad (3.94)$$

$$T_s=-z \quad (3.95)$$

with boundary conditions

$$w = 0 \quad \text{at} \quad y = \pm\frac{h}{2}, \tag{3.96}$$

$$\theta = 0 \quad \text{at} \quad y = \pm\frac{h}{2}. \tag{3.97}$$

From (3.92) and (3.93) the effective pressure is uniform across the channel. so that the driving pressure gradient in (3.91) is independent of x and y. Ignoring $O(\varepsilon)$ terms, the solutions for the velocity and temperature are

$$w = \overline{w}\left(\frac{3}{2} - 6\frac{y^2}{h^2}\right), \quad \overline{w} = h^2\left(1 + \delta_c^2\frac{\partial N}{\partial z}\right), \tag{3.98}$$

$$\theta = \overline{\theta}\left(\frac{25}{16} - \frac{15}{2}\frac{y^2}{h^2} + 5\frac{y^4}{h^4}\right), \quad \overline{\theta} = \frac{\alpha}{10}h^4\left(1 + \delta_c^2\frac{\partial N}{\partial z}\right). \tag{3.99}$$

The melting rate (for both walls) therefore comes from (3.89):

$$m = 2m_n = -\frac{2}{\alpha}\theta_y|_{y=\frac{h}{2}} = \frac{10}{\alpha}\frac{\overline{\theta}}{h}. \tag{3.100}$$

This motivates our choice of $\alpha = 10$, because this calculation provides the basis for the parameterized heat transfer equation (3.42). Similarly the solution for w, and the definition of the flux $q = \overline{w}h$, is what gives rise to the flow law (3.38).

Having calculated the melting rate (3.100), this feeds into the kinematic condition (3.86). Using the closure rate in (3.24) it can be written

$$\frac{\partial h}{\partial t} = m - (b^2 - x^2)^{1/2}N_c, \tag{3.101}$$

which is equivalent to (3.40). The remaining equations in the lumped model (the continuity equation (3.39) and energy equation (3.41)) can be derived by integrating (3.80) over the width with boundary conditions (3.86) and (3.87), and by integrating (3.84) with boundary conditions (3.89) and (3.90), using the solutions (3.98) and (3.99) for w and θ. The last of these in fact produces

$$\begin{aligned} m\left(1 + \frac{\mu}{St}\overline{\theta}\right) + \mu\omega\overline{\theta} + \frac{1}{r\ St}h\frac{\partial}{\partial t}\left(T_s + \mu\overline{\theta}\right) + q\frac{\partial}{\partial z}\left(T_s + \mu\overline{\theta}\right) + \frac{3}{14}\mu\frac{\partial}{\partial z}\left(q\overline{\theta}\right) \\ = \frac{1}{Pe}h\frac{\partial^2}{\partial z^2}\left(T_s + \mu\overline{\theta}\right) + (r-1)\nu q\left(1 + \delta_c^2\frac{\partial N_c}{\partial z}\right), \end{aligned} \tag{3.102}$$

which is the same as (3.20) except for the $3\mu/14$ term; this arises because of the nonlinearity of the advective term, and because $\overline{w\theta} \neq \overline{w}\overline{\theta}$. Note we have used the fact that $Pe = \alpha\mu/\varepsilon^2\hat{\varepsilon}^2$.

Stability

Using the expression for the average temperature $\overline{\theta}$ in (3.99) and the melt rate in (3.100), the kinematic condition (3.101) is approximately (ignoring δ_c^2),

$$\frac{\partial h}{\partial t} = h^3 - (b^2 - x^2)^{1/2} N_c, \tag{3.103}$$

and the channel should have the approximate steady shape

$$h_0 = (b^2 - x^2)^{1/6} N_c^{1/3}. \tag{3.104}$$

However, since $\partial h/\partial t \sim h^3$ in (3.103), this is unstable to perturbations in h. To see these, and the possible stabilising effect of heat conduction, we look at the $O(\varepsilon)$ correction to m. Expanding w and θ in (3.91) and (3.94) as

$$w(x,y,z) = w_0(x,y,z) + \varepsilon^2 w_1(x,y,z) + \ldots, \tag{3.105}$$

$$\theta(x,y,z) = \theta_0(x,y,z) + \varepsilon^2 \theta_1(x,y,z) + \ldots, \tag{3.106}$$

the solutions for w_0 and θ_0 are given by (3.98) and (3.99), and the solutions for w_1 and θ_1 are

$$w_1 = \left(1 + \delta_c^2 \frac{\partial N}{\partial z}\right) \left[h^3 \frac{\partial^2 h}{\partial x^2} + h^2 \left(\frac{\partial h}{\partial x}\right)^2\right] \left(\frac{3}{8} - \frac{3}{2}\frac{y^2}{h^2}\right), \tag{3.107}$$

$$\theta_1 = \alpha \left(1 + \delta_c^2 \frac{\partial N}{\partial z}\right) \left[h^5 \frac{\partial^2 h}{\partial x^2} \left(\frac{1}{4}\frac{y^4}{h^4} - \frac{1}{2}\frac{y^2}{h^2} + \frac{7}{64}\right) + h^4 \left(\frac{\partial h}{\partial x}\right)^2 \left(\frac{1}{4}\frac{y^4}{h^4} - \frac{9}{8}\frac{y^2}{h^2} + \frac{17}{64}\right)\right]. \tag{3.108}$$

The melting rate, from (3.89) is then

$$m = -\frac{2}{\alpha}\left(\frac{\partial \theta_0}{\partial y} + \varepsilon^2 \frac{\partial \theta_1}{\partial y} - \varepsilon^2 \frac{1}{2}\frac{\partial h}{\partial x}\frac{\partial \theta_0}{\partial x}\right)\Bigg|_{y=\frac{h}{2}} \tag{3.109}$$

$$= \left(1 + \delta_c^2 \frac{\partial N_c}{\partial z}\right)\left[h^3 + \varepsilon^2 \frac{3}{4} h^4 \frac{\partial^2 h}{\partial x^2} + \varepsilon^2 \frac{9}{4} h^3 \left(\frac{\partial h}{\partial x}\right)^2\right]. \tag{3.110}$$

The kinematic condition (3.103) is therefore

$$\frac{\partial h}{\partial t} = h^3 + \varepsilon^2 \frac{3}{4} h^4 \frac{\partial^2 h}{\partial x^2} + \varepsilon^2 \frac{9}{4} h^3 \left(\frac{\partial h}{\partial x}\right)^2 - (b^2 - x^2)^{1/2} N_c, \tag{3.111}$$

and small local perturbations of the form $e^{\sigma t + ikx}$ to the approximate steady state (3.104) have the dispersion relationship

$$\sigma = 3h_0^2 - \frac{3}{4}\varepsilon^2 h_0^4 k^2. \tag{3.112}$$

Thus perturbations with wavelength larger than $\pi\varepsilon h_0$ (i.e. $k < 2/\varepsilon h_0$) will grow unstably. This suggests that a long thin channel will be unstable to collapse into more cylindrical channels.

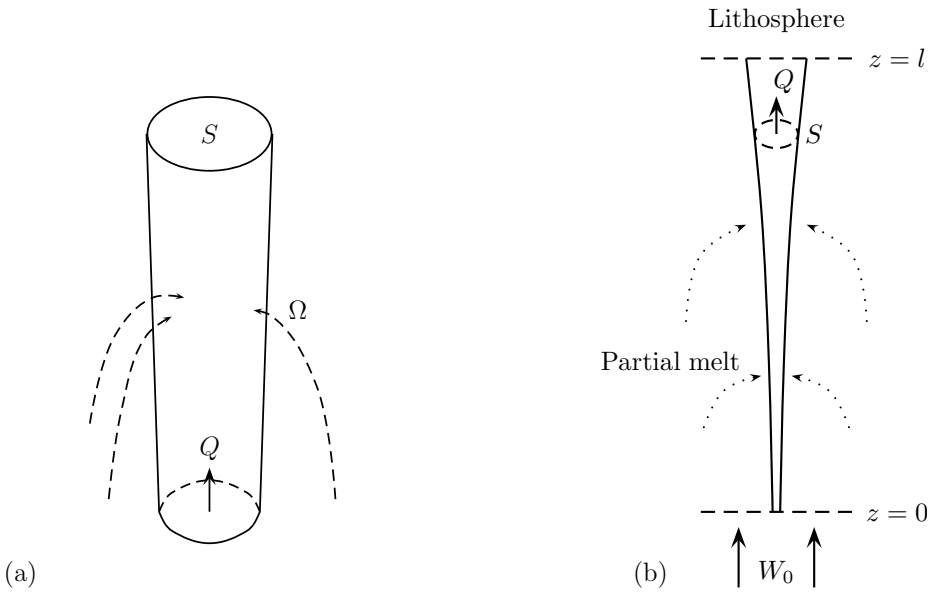

Figure 3.4: (a) Geometry of channel considered in section 3.2.4, with cross-sectional area S, flux Q and influx Ω; (b) the radial setup for a channel occupying the full depth of the partially molten region.

3.2.4 Cylindrical channels

Based on the above discussion we expect a cylindrical cross-section to be the natural shape for channels in the viscously deforming mantle. In the analogous situation of water flowing through ice it is well known, and readily observed, that channels are (at least approximately) cylindrical. We therefore pose a model analogous to that for a crack shape in section 3.2.2, (3.25)-(3.29), but with a circular cross-section. This could be derived by considering the three dimensional flow as in section 3.2.3, but it is straightforward to write down a lumped model from the outset. The main difference from before is in the closure relationship, which will require much larger effective pressures to counteract melting.

For a circular cross-sectional area S, with effective pressure N_c, the volume flux Q is given by the Poiseuille law

$$Q = \frac{S^2}{8\pi\eta_l}\left(\Delta\rho g + \frac{\partial N_c}{\partial z}\right). \tag{3.113}$$

The continuity equation is

$$\frac{\partial S}{\partial t} + \frac{\partial Q}{\partial z} = \frac{M}{\rho_l} + \Omega, \tag{3.114}$$

in which M is melting rate of the walls, and Ω is the melt source through the walls. Note M and Ω have different dimensions to m and ω used before, because they involve

melting and inflow around the whole circumference. The closure rate for a circle is given by (3.22), which means the kinematic condition for the walls is

$$\frac{\partial S}{\partial t} = \frac{M}{\rho_s} - \frac{SN_c}{\eta_s}. \tag{3.115}$$

The energy equation is

$$M\left(L + c\overline{\theta}\right) + \rho_l c\Omega\overline{\theta} + \rho_s cS\frac{\partial}{\partial t}\left(T_s + \overline{\theta}\right) + \rho_l cQ\frac{\partial}{\partial z}\left(T_s + \overline{\theta}\right) = kS\frac{\partial^2}{\partial z^2}\left(T_s + \overline{\theta}\right) + Q\left(\Delta\rho g + \frac{\partial N_c}{\partial z}\right). \tag{3.116}$$

The heat transfer equation can be calculated from the three dimensional flow as in section 3.2.3 above and gives

$$ML = \hat{\alpha}k\overline{\theta}, \tag{3.117}$$

in which the dimensionless constant $\hat{\alpha} = 6\pi$. The wall temperature T_s is given by the solidus (3.19).

Equations (3.19), (3.113)-(3.117) provide a closed system for the flux, cross-section, effective pressure, temperature and melting rate assuming Ω is prescribed. Note that if melting is ignored (so temperature must also be ignored) and $\Omega = 0$, then (3.115) gives the effective pressure, which can be substituted into (3.113) and (3.114) to give

$$Q = \frac{S^2}{8\pi\eta_l}\left(\Delta\rho g + \eta_s\frac{\partial}{\partial z}\left(\frac{1}{S}\frac{\partial Q}{\partial z}\right)\right). \tag{3.118}$$

This, in combination with the continuity equation (3.114) gives equations which have often been used to describe solitary waves on fluid conduits (Olson and Christensen, 1986; Helfrich and Whitehead, 1990; Richardson et al., 1996). In the small perturbation limit it reduces to the Korteweg de-Vries equation, with soliton solutions (Whitehead and Helfrich, 1986).

Non-dimensionalisation

As before, the variables are scaled by writing $z = lz^*$, $p = p_m + p_0 p^*$, $T_s = T_m + T_0 T_s^*$, $N_c = N_{c0}N_C^*$, $M = M_0 M^*$, $S = S_0 S^*$, $Q = Q_0 Q^*$, $\theta = \theta_0\theta^*$, $\Omega = \Omega_0\Omega^*$, $t = t_{c0}t^*$, but the appropriate choice of scales is now different. In the steady state, the size of the channel and the effective pressure adjust to balance the melting rate in (3.115). It turns out that the cross-sectional area required in order to achieve this balance is so large that the dominant balance in the flow law (3.113) is between the buoyancy and pressure gradient. In other words, the melt pressure is close to *magmastatic*

equilibrium, and viscous drag balances only a small fraction of the buoyancy force $\Delta\rho g$.

These balances motivate choosing the scales so that

$$T_s - T_m \sim \Gamma\rho_s g z, \quad Q \sim \Omega z, \quad N_c \sim \Delta\rho g z, \quad ML \sim \rho_l c\Gamma\rho_s g Q \sim \hat{\alpha}k\theta, \quad \frac{M}{\rho_s} \sim \frac{SN_c}{\eta_s}, \tag{3.119}$$

which requires taking $Q_0 = \Omega_0 l$, and

$$T_0 = \Gamma\rho_s g l \sim 150 \text{ K}, \tag{3.120}$$

$$N_{c0} = \Delta\rho g l \sim 2.5 \times 10^8 \text{ Pa}, \tag{3.121}$$

$$M_0 = \frac{\rho_l c\Gamma\rho_s g}{L} Q_0 \sim 2.5 \times 10^{-4} \text{ kg m}^{-1} \text{ s}^{-1}, \tag{3.122}$$

$$S_0 = \frac{\rho_l}{\rho_s}\frac{\eta_s}{\Delta\rho g l}\frac{c\Gamma\rho_s g}{L} Q_0 \sim 3000 \text{ m}^2, \tag{3.123}$$

$$\theta_0 = \frac{\rho_l c\Gamma\rho_s g}{\hat{\alpha}k} Q_0 \sim 1.6 \text{ K}, \tag{3.124}$$

$$t_{c0} = \frac{\eta_s}{N_{c0}} = \frac{\eta_s}{\Delta\rho g l} \sim 4 \times 10^{10} \text{ s} \approx 1000 \text{ y}, \tag{3.125}$$

in terms of Q_0 and l. The approximate values here suppose that a typical melt flux may be $Q_0 = 0.01$ m^3 s^{-1}, and the length of the channel is again taken as the full depth of the partially molten region $l = 50$ km. Note that the effective pressure, the temperature and time are now scaled differently to earlier in sections 3.2.2 and 3.2.3. Dropping the asterisks, the dimensionless equations are

$$\Lambda Q = S^2\left(1 + \frac{\partial N_c}{\partial z}\right), \tag{3.126}$$

$$\frac{1}{r\ St}\frac{\partial S}{\partial t} + \frac{\partial Q}{\partial z} = \frac{1}{St}M + \Omega, \tag{3.127}$$

$$\frac{\partial S}{\partial t} = M - SN_c, \tag{3.128}$$

$$M\left(1 + \frac{\mu}{St}\overline{\theta}\right) + \mu\Omega\overline{\theta} + \frac{1}{r\ St}S\frac{\partial}{\partial t}\left(T_s + \mu\overline{\theta}\right) + Q\frac{\partial}{\partial z}\left(T_s + \mu\overline{\theta}\right) = \frac{1}{Pe}S\frac{\partial^2}{\partial z^2}\left(T_s + \mu\overline{\theta}\right) + (r-1)\nu Q\left(1 + \frac{\partial N_c}{\partial z}\right), \tag{3.129}$$

$$M = \overline{\theta}, \tag{3.130}$$

$$T_s = -z - \frac{r-1}{r}N_c. \tag{3.131}$$

The dimensionless parameters r, St and ν are as before in (3.44)-(3.49), μ and Pe are now given by

$$\mu = \frac{\theta_0}{\Gamma \rho_s g l} \sim 0.01, \tag{3.132}$$

$$Pe = \frac{\rho_l c Q_0 l}{k S_0} \sim 1.7 \times 10^5, \tag{3.133}$$

and the new parameter Λ, which measures the ratio of viscous drag to buoyancy force, is

$$\Lambda = \frac{8\pi\eta_l}{\Delta\rho g}\frac{Q_0}{S_0^2} \sim 6 \times 10^{-11}, \tag{3.134}$$

The fact that Λ is so small means that the melt pressure in the conduit is very close to magmastatic. Λ depends on the flux as $1/Q_0$, so a much lower flux would be needed in order to make it order 1. The fact that μ is small means that the temperature difference between the melt in the conduit and the walls is small (though not quite as small as it was for the planar crack in section 3.2.2).

Boundary conditions

As in section 3.2.2 we have chosen the length of the channel to be appropriate for a channel that extends the full depth of the partially molten region. Since there is unlikely to be a reservoir of melt at the bottom of this region feeding the channel, the natural condition there is zero flux. As above, we must also apply a boundary condition at the top (i.e. the base of the lithosphere), and we say that the effective pressure must be zero there. Thus

$$Q = 0 \quad \text{at} \quad z = 0, \quad N_c = 0 \quad \text{at} \quad z = 1. \tag{3.135}$$

Since according to (3.126) the effective pressure profile is roughly magmastatic, the condition at the top sets the 'origin' for this profile, and means that the melt pressure throughout the channel is reduced from the surrounding matrix pressure.

Steady-state behaviour

Neglecting the small terms of order μ and Λ causes $\overline{\theta}$ to decouple and the channel equations (3.126)-(3.131) reduce to

$$0 = 1 + \frac{\partial N_c}{\partial z}, \tag{3.136}$$

$$\frac{1}{rSt}\frac{\partial S}{\partial t} + \frac{\partial Q}{\partial z} = \frac{1}{St}M + \Omega, \tag{3.137}$$

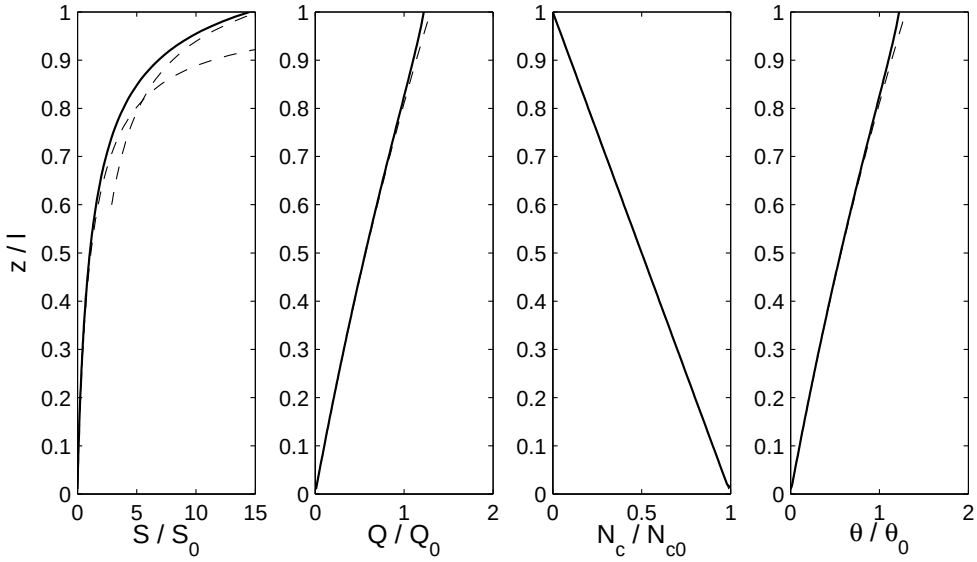

Figure 3.5: Steady state solutions to (3.126)-(3.131) and (3.135), for a constant influx $\Omega = 1$. The parameter values are $r = 1.2$, $St = 2$, $\Lambda = 5 \times 10^{-11}$, $\mu = 0.01$, $\nu = 3$. Dashed lines are the approximate solutions given by (3.140)-(3.143) and (3.150).

$$\frac{\partial S}{\partial t} = M - SN_c, \tag{3.138}$$

$$M - \frac{Q}{r} = 0 \tag{3.139}$$

These state that the melt pressure varies magmastatically, the melt flux increases due to melting of the walls and additional inflow through them, the channel opens and closes due to melting and viscous deformation, and the rate that the walls melt is given by the rate hot fluid is advected from below (i.e. down the solidus).

Taking the boundary conditions (3.135) and a prescribed inflow $\Omega(z)$, the steady-state solutions to (3.136)-(3.139) are

$$Q = \int_0^z \Omega(\tilde{z}) \exp\left(\frac{z - \tilde{z}}{rSt}\right) \, \mathrm{d}\tilde{z}, \tag{3.140}$$

$$M = \overline{\theta} = \frac{Q}{r}, \tag{3.141}$$

$$N_c = 1 - z, \tag{3.142}$$

$$S = \frac{1}{r(1-z)} \int_0^z \Omega(\bar{z}) \exp\left(\frac{z - \bar{z}}{rSt}\right) \, \mathrm{d}\bar{z}, \tag{3.143}$$

which are shown in figure 3.5.

Behaviour near $z = 1$

The steady solution (3.140)-(3.143) suggests that as the effective pressure approaches zero near $z = 1$ the cross-sectional area grows without bound, so that it is infinite at $z = 1$. This is because the closure rate goes to zero in (3.128) so melting causes the area to grow indefinitely.

This issue can be avoided if we allow the host matrix also to have a small vertical velocity, so that is, as well as the melt, is ascending. Since we are considering the channel to be embedded in the partially molten region beneath a mid-ocean ridge or hotspot, as in chapter 2, this is indeed what is happening; the rock is only partially molten *because* it is itself ascending. If the matrix is also moving, then the derivative in (3.128) should really be a material derivative, which we write as

$$\frac{\partial S}{\partial t} + \varepsilon\delta^2 W \frac{\partial S}{\partial z} = M - SN_c. \tag{3.144}$$

The small dimensionless vertical velocity is written as $\varepsilon\delta^2 W$ for reasons of later consistency (ε and δ^2 are as in chapter 2). As S grows near $z = 1$ this extra derivative becomes important; the correction to the solution there can be found by rescaling

$$z = 1 - \varepsilon^{1/2}\delta W^{1/2}\tilde{z}, \tag{3.145}$$

$$S = \frac{Q(1)}{r\varepsilon^{1/2}\delta W^{1/2}}\tilde{S}, \quad N_c = \varepsilon^{1/2}\delta W^{1/2}\tilde{N}_c, \quad Q = Q(1)\tilde{Q}, \quad M = \frac{Q(1)}{r}\tilde{M}. \tag{3.146}$$

Then the leading order steady state equations are

$$\tilde{N}_c = \tilde{z} \tag{3.147}$$

$$-\frac{\partial \tilde{S}}{\partial \tilde{z}} = \tilde{M} - \tilde{S}\tilde{N}_c, \tag{3.148}$$

$$\tilde{Q} = \tilde{M} = 1. \tag{3.149}$$

The solution for $\tilde{S}$ is

$$\tilde{S} = \int_{\tilde{z}}^{\infty} e^{(\tilde{z}^2 - \tilde{\zeta}^2)/2}\, \mathrm{d}\tilde{\zeta} = \sqrt{\frac{\pi}{2}} e^{\tilde{z}^2/2}\mathrm{erfc}(\tilde{z}/\sqrt{2}). \tag{3.150}$$

This boundary layer solution is shown in figure 3.5, and implies that the cross-sectional area at $z = 1$ tends to the finite dimensionless value $S = \sqrt{\pi/2}Q(1)/r\varepsilon^{1/2}\delta W^{1/2}$.

3.2.5 Summary

Equations (3.38)-(3.43) provide a model for a thin two-dimensional channel in which the closure rate depends on the breadth of the crack in the third dimension. Solutions for a prescribed inflow are shown in figure 3.3. The effective pressure is relatively small, so the melt flow is driven by the full buoyancy force $\Delta\rho g$.

However, we suggest that this is not an appropriate shape of channel to consider, since variations in the melting rate along the wall will cause the flow to localise into a series of cylindrical channels. Equations (3.126)-(3.131) therefore provide what we consider to be a more appropriate model for channels in the viscously deforming mantle, and the solutions to these for a prescribed inflow are shown in figure 3.5. In this case melting again happens at a rate proportional to the melt flux, but the necessary effective pressure to counteract this with closure is much larger. The melt pressure is therefore nearly magmastatic, and the melt flow is driven by only a small fraction of the full buoyancy force.

The fact that the melt pressure in the channel is very close to magmastatic means that it can be significantly reduced from the melt pressure in the pores of the surrounding matrix; in chapter 2 we saw that the pore pressure is close to the lithostatic pressure in the matrix (since δ^2 is small). There is therefore a pressure gradient towards the channel which can cause the melt from the pores to be drawn into it. This is what provides the source Ω, and we now look to calculate this by reintroducing the porous flow in the matrix.

3.3 Porous flow into a channel from partial melt

3.3.1 Radial flow

We use the simplified non-dimensional model for the partial melting region in section 3.1, (3.1)-(3.6). Using the velocity potential in (3.9), we reduced this to

$$\varepsilon\frac{\partial\phi}{\partial t}+\varepsilon W_0\frac{\partial\phi}{\partial z}+\frac{\varepsilon}{St}\nabla\cdot(\phi\nabla\mathcal{U})+\nabla\cdot\left[\phi^2\left(\mathbf{k}+\delta^2\nabla N\right)\right]=W_0+\frac{1}{St}\frac{\partial\mathcal{U}}{\partial z}+\frac{1}{St}\phi^2\left(1+\delta^2\frac{\partial N}{\partial z}\right), \tag{3.151}$$

$$\nabla\cdot\left[\phi^2\left(\mathbf{k}+\delta^2\nabla N\right)\right]=\phi N, \tag{3.152}$$

$$-\nabla^2\mathcal{U}=\phi N, \tag{3.153}$$

with

$$\phi=0,\quad \frac{\partial\mathcal{U}}{\partial z}=0\quad\text{at}\quad z=0, \tag{3.154}$$

$$N = 0, \quad U = 0 \quad \text{at} \quad z = 1. \tag{3.155}$$

It may be useful to remember that the scales for the variables in these equations are given by (2.42)-(2.47), and in particular

$$\phi_0 u_0 = \frac{r}{St} V_0, \tag{3.156}$$

$$N_0 = \delta^2 \Delta\rho g l, \tag{3.157}$$

$$t_0 = \frac{l}{V_0}. \tag{3.158}$$

It is immediately clear that the dimensionless lengthscale over which the effective pressure has an effect is the compaction length δ. This means that the pressure perturbation caused by the presence of a channel can be expected to affect a surrounding region of size δ, and it can draw in melt from this region. Given the scale for the porous melt flux (3.156) it is therefore sensible to define the scales for the radial inflow Ω_0 and channel flux Q_0 as

$$\Omega_0 = \delta^2 l \phi_0 u_0 = \frac{r}{St} \delta^2 l V_0 \sim 8 \times 10^{-7} \text{ m}^2 \text{ s}^{-1}, \tag{3.159}$$

$$Q_0 = \Omega_0 l = \frac{r}{St} \delta^2 l^2 V_0 \sim 0.04 \text{ m}^3 \text{ s}^{-1}. \tag{3.160}$$

These then define the scales for the channel variables by (3.120)-(3.125).

Boundary conditions at a channel

Now suppose that the partially molten region modelled by (3.151)-(3.155) surrounds a cylindrical channel with dimensionless radius r_c that extends the full depth $0 < z < 1$. Extra boundary conditions are required at $r = r_c$ and these must match the behaviour in the partially molten region with the behaviour in the channel; the melt pressure must be continuous, the normal velocity of the matrix must match with the closure velocity in (3.128), and the melt flow through the boundary provides the source term Ω to the channel.

Since the channel effective pressure is scaled with $\Delta\rho g l$, the boundary condition on the effective pressure in the partially molten region is

$$N = \frac{N_c}{\delta^2} \approx \frac{1 - z}{\delta^2} \quad \text{at} \quad r = r_c, \tag{3.161}$$

where this last approximation is that the channel pressure is very close to magmastatic. This is a good approximation since Λ in (3.126) is so small, and it is a welcome simplification, since it means the porous flow decouples from the precise dynamics of the channel.

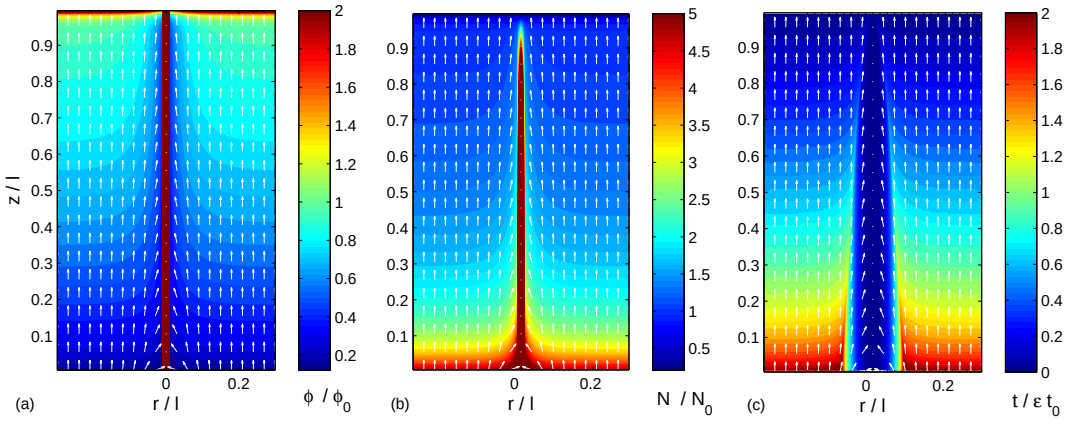

Figure 3.6: (a)-(b); Steady state solutions, for melt fraction ϕ and effective pressure N, to (3.151)-(3.155) with (3.161)-(3.163) at a channel boundary $r = r_c = 5 \times 10^{-4}$. White arrows show the direction of melt flow. The parameters are $\varepsilon = 0.01$, $\delta = 0.14$, $St = 20$. The variables shown are scaled, and any values above the maximum on the colour scale are coloured the same. The width of the channel has been exaggerated, and the melt fraction around it is very small ($< 0.5\%$). (c); Travel time for melt to be extracted from the porous flow for the same situation. White arrows show the direction of melt flow. The time is scaled with the typical advective time in the partially molten region $\varepsilon t_0 = l/u_0$. The corresponding behaviour of the channel is shown in figure 3.7.

With the scales given in (3.159), the influx to the channel is

$$\Omega = -2\pi r_c \phi^2 \frac{\partial N}{\partial r}\bigg|_{r_c}. \tag{3.162}$$

The velocity of the channel walls comes from the closure rate (3.22); written in terms of the scaled variables this is

$$2\pi r_c \mathbf{V} \cdot \mathbf{n}|_{r_c} = -\frac{\delta^2}{St^2} S N_c \approx -\frac{\delta^2}{St^2}\frac{Q}{r}, \tag{3.163}$$

where $\mathbf{n}$ is the outward normal to the walls, and the last approximation is for a steady state channel, in which the closure rate balances the melting rate due to melt flux Q.

Numerical solution

Since the channel is much narrower than the scale of the partially molten region, the dimensionless radius r_c (scaled with l) will be very small. The radius should in theory depend on the cross-sectional area S, and therefore increase with z, but for the purposes of the numerical solution we give here, we will apply the boundary condition at a fixed radius r_c which does not depend on height. The calculation is therefore not

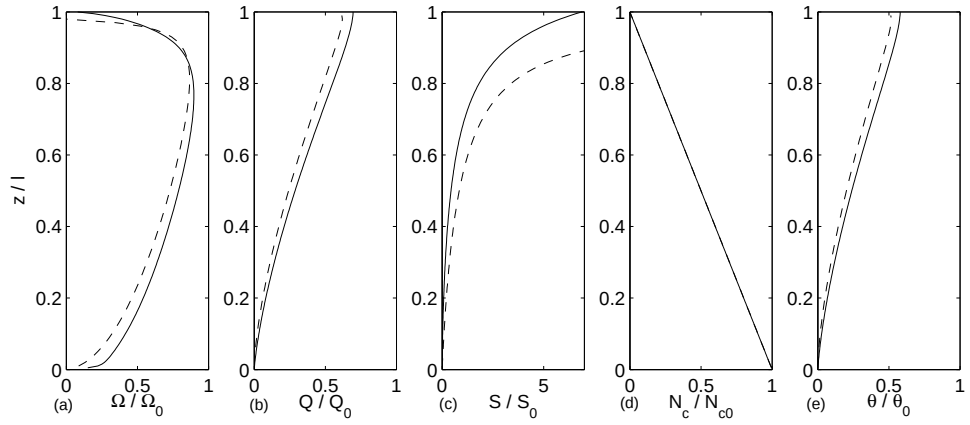

Figure 3.7: (a) Influx to channel in figure 3.6; the solid line is calculated from the numerical solution of (3.151)-(3.155) and (3.161)-(3.163), and the dashed line is the approximate analytical solution (3.192). (b)-(e) Flux, cross-sectional area, effective pressure and excess temperature for the channel at the centre of figure 3.6; solid lines are using the numerically calculated influx Ω and the numerical solution of (3.126)-(3.131) and dashed lines are using the approximate Ω and solutions (3.140)-(3.143). The parameters are $\varepsilon = 0.01$, $\delta = 0.14$, $St = 20$, $\mu = 0.01$, $r = 1$.

exact, but this is necessary because the computation is performed on a fixed grid; since r_c is small, there would not be sufficient resolution to capture its variation accurately. Further details of the discretisation used are given in appendix C. The porous region 'sees' the channel essentially as a line sink, and for the purposes of seeing how it responds to this it is sufficient to apply the boundary conditions (3.161)-(3.163) at a fixed r_c.

Figure 3.6 shows a steady state numerical solution of (3.151)-(3.155) with (3.161)-(3.163) at the channel. The calculated inflow Ω and resulting flux Q are shown in figure 3.7. The large effective pressure in the channel causes steep pressure gradients towards it, drawing the melt in. The large effective pressure also causes enhanced matrix compaction there, and results in a *decrease* in melt fraction towards the channel, which is perhaps slightly surprising. The decrease in permeability does not stop the melt getting through however, as the pressure gradients drawing it in are sufficiently high.

Approximate analytical solutions

Some straightforward analytical understanding of the flow into the channel can be seen if the Stefan number is large, corresponding to the matrix undergoing only a small degree of melting. It is found numerically that the behaviour when St is smaller is not

significantly different. The only important contribution St makes to the equations is in the melting rate on the right hand side of (3.151) and assuming St is large means we are ignoring the feedback of flow rate on melting in the partially molten region; in section 3.1 we saw that this gives a mechanism to produce a channel in the first place, but once the channel is formed this feedback is no longer important for the porous flow (though it is of course important *within* the channel).

Ignoring $1/St$ terms, and also the small advective term of order ε in (3.151), the matrix deformation described by $\mathcal{U}$ decouples and we need only solve for ϕ and N. In the steady state we have

$$\nabla \cdot [\phi^2(\mathbf{k} + \delta^2 \nabla N)] = W_0, \tag{3.164}$$

$$\nabla \cdot [\phi^2(\mathbf{k} + \delta^2 \nabla N)] = \phi N, \tag{3.165}$$

with

$$\phi = 0 \quad \text{at} \quad z = 0, \tag{3.166}$$

$$N = 0 \quad \text{at} \quad z = 1, \tag{3.167}$$

$$N = \frac{N_c}{\delta^2} \quad \text{at} \quad r = r_c. \tag{3.168}$$

The behaviour in the far field tends towards the one-dimensional solution, which, ignoring the boundary layers, is well approximated by

$$\phi = W_0 z^{1/2} \quad N = \frac{W_0^{1/2}}{z^{1/2}}. \tag{3.169}$$

Having found the solution for ϕ and N we can then calculate the inflow to the channel from (3.162).

The compaction relation (3.165) tells us that the effective pressure is inversely related to the melt fraction:

$$N = \frac{W_0}{\phi}, \tag{3.170}$$

and ϕ therefore satisfies a non-linear reaction diffusion equation (3.164). Rescaling

$$r = \delta R, \tag{3.171}$$

and taking only the leading order terms in δ, we have

$$2\phi \frac{\partial \phi}{\partial z} = W_0 + \frac{W_0}{R} \frac{\partial}{\partial R} \left(R \frac{\partial \phi}{\partial R} \right), \tag{3.172}$$

$$\phi = 0 \quad \text{at} \quad z = 0, \tag{3.173}$$

$$\phi = \delta^2 \frac{W_0}{N_c} \quad \text{at} \quad R = R_c, \tag{3.174}$$

$$\phi \to W_0^{1/2} z^{1/2} \quad \text{as} \quad R \to \infty. \tag{3.175}$$

We seek approximate solutions by writing ϕ as a perturbation from the far field solution;

$$\phi = W_0^{1/2} z^{1/2} + \psi, \tag{3.176}$$

and then approximating the nonlinear advection term

$$2\phi \frac{\partial \phi}{\partial z} \approx 2 W_0^{1/2} z^{1/2} \frac{\partial \phi}{\partial z}. \tag{3.177}$$

This is somewhat analogous to Oseen's approximation for slow flow past a sphere (Oseen, 1910; Batchelor, 1967). With the change of variable

$$\xi = W_0^{1/2} z^{1/2}, \tag{3.178}$$

the problem becomes

$$\frac{\partial \psi}{\partial \xi} = \frac{\partial^2 \psi}{\partial R^2} + \frac{1}{R} \frac{\partial \psi}{\partial R}, \tag{3.179}$$

$$\psi = 0 \quad \text{at} \quad \xi = 0, \qquad \psi \to 0 \quad \text{as} \quad R \to \infty, \tag{3.180}$$

$$\psi = \psi_c \equiv \delta^2 \frac{W_0}{N_c} - \xi, \quad \text{at} \quad R = R_c. \tag{3.181}$$

This can be solved using a Laplace transform, which gives a modified Bessel equation

$$\frac{\partial^2 \overline{\psi}}{\partial R^2} + \frac{1}{R} \frac{\partial \overline{\psi}}{\partial R} - p \overline{\psi} = 0, \tag{3.182}$$

$$\overline{\psi} \to 0 \quad \text{as} \quad R \to R_c, \tag{3.183}$$

$$\overline{\psi} = \overline{\psi}_c \quad \text{at} \quad R = R_c, \tag{3.184}$$

for which the solution is

$$\overline{\psi} = \overline{\psi}_c \frac{K_0(\sqrt{p} R)}{K_0(\sqrt{p} R_c)}. \tag{3.185}$$

Thus

$$\psi = \frac{1}{2\pi i} \int_{\gamma - i\infty}^{\gamma + i\infty} e^{p\xi} \overline{\psi}_c \frac{K_0(\sqrt{p} R)}{K_0(\sqrt{p} R_c)} \, \mathrm{d}p, \tag{3.186}$$

and the flux into the channel is given by

$$\Omega = -2\pi r_c \phi^2 \frac{\partial N}{\partial r}\bigg|_{r_c} = 2\pi R_c W_0 \frac{\partial \psi}{\partial R}\bigg|_{R_c} = W_0 R_c i \int_{\gamma - i\infty}^{\gamma + i\infty} e^{p\xi} \overline{\psi}_c \sqrt{p} \frac{K_1(\sqrt{p} R_c)}{K_0(\sqrt{p} R_c)} \, \mathrm{d}p. \tag{3.187}$$

If, as we expect, R_c is small (remember R_c is the channel radius scaled by the compaction length δl), asymptotic approximations to the Bessel functions can be used;

$$K_0(x) \sim -\ln\frac{x}{2} - \gamma, \tag{3.188}$$

$$K_1(x) \sim \frac{1}{x}, \tag{3.189}$$

($\gamma = 0.5772\ldots$ is the Euler-Mascheroni constant), so

$$\sqrt{p}\frac{K_1(\sqrt{p}R_c)}{K_0(\sqrt{p}R_c)} \sim \frac{1}{-\ln\frac{R_c}{2} - \gamma}\frac{1}{R_c}, \tag{3.190}$$

and

$$\Omega \sim -\frac{2\pi W_0 \psi_c}{-\ln\frac{R_c}{2} - \gamma}. \tag{3.191}$$

In terms of the original variables, and taking $N_c = 1 - z$, this is

$$\Omega \sim \frac{2\pi W_0^{3/2}}{-\ln\frac{R_c}{2} - \gamma}\left(z^{1/2} - \delta^2\frac{W_0^{1/2}}{1-z}\right), \tag{3.192}$$

and gives an integrated flux into the channel (scaled with Q_0 in (3.160)),

$$Q \sim \frac{4\pi}{3}\frac{W_0^{3/2}}{-\ln\frac{R_c}{2} - \gamma}\left(z^{3/2} + \frac{3}{2}\delta^2 W_0^{1/2}\ln(1-z)\right). \tag{3.193}$$

Figure 3.7 shows these approximations in comparison with the numerical calculations; remember that the approximation is not valid near the boundaries $z = 0$ and $z = 1$. The effect of having St smaller is to cause a reduction in the melting rate close to the channel (because the melt is moving sideways and therefore not carrying as much heat down the solidus gradient), and thus a slight reduction in the influx from that given by (3.192). Nevertheless (3.193) is quite a reasonable approximation for the total melt entering the channel.

3.3.2 Planar flow

Two-dimensional channels

The above has all looked at radially symmetric flow into a cylindrical channel. For two dimensional flow, such as we saw in section 3.1, a 'channel' only has flow coming in from either side. It might be thought of as extending a long way in the missing third dimension, and therefore equivalent to the wide crack-shaped channel in section 3.2.2. However, we saw there that such a shape will be unstable and will localise into

a series of cylindrical channels, or at least channels with similar dimensions in both horizontal directions, and this results in a quite different channel effective pressure.

We would nevertheless like to know how channels can form and behave in two-dimensional flow such as in section 3.1, so we must interpret these two-dimensional channels as behaving similar to the cylindrical ones above. To do this, we suggest modifying the closure relation for the crack model in section 3.2.2, from (3.27) to

$$\frac{\partial h}{\partial t} = \frac{m}{\rho_s} - \frac{hN_c}{\eta_s}. \tag{3.194}$$

The remaining equations; the Poiseuille flow law (3.25), continuity equation (3.26), energy equation (3.28) and heat transfer equation (3.29); are as before. The presence of h in the closure rate however, necessitates a different scaling which is more similar to that for the cylindrical channel. The effective pressure roughly balances buoyancy, and the width h is determined by balancing closure with melting in (3.194). In terms of $q_0 = \omega_0 l$, the new scales instead of (3.33)-(3.37) are

$$m_0 = \frac{\rho_l c \Gamma \rho_s g}{L} q_0 \sim 1.2 \times 10^{-7} \text{ kg m}^{-2} \text{ s}^{-1}, \tag{3.195}$$

$$N_{c0} = \Delta\rho g l \sim 2.5 \times 10^8 \text{ Pa}, \tag{3.196}$$

$$h_0 = \frac{\eta_s m_0}{\rho_s N_{c0}} = \frac{\rho_l}{\rho_s} \frac{\eta_s}{\Delta\rho g l} \frac{c\Gamma\rho_s g}{L} q_0 \sim 1.5 \text{ m}, \tag{3.197}$$

$$\theta_0 = \frac{h_0 m_0 L}{\alpha k} = \frac{\rho_l}{\alpha k} \frac{\rho_l}{\rho_s} \frac{\eta_s}{\Delta\rho g l} \frac{c^2\Gamma^2\rho_s^2 g^2}{L} q_0^2 \sim 2.5 \times 10^{-3} \text{ K}, \tag{3.198}$$

$$t_{c0} = \frac{\eta_s}{\Delta\rho g l} \sim 4 \times 10^{10} \text{ s}, \tag{3.199}$$

where the approximate values assume a typical flux $q_0 = 5 \times 10^{-6}$ m^2 s^{-1}. Dimensionless parameters r, St, μ, ν and Pe are then defined as in (3.44)-(3.49), and additionally

$$\lambda = \frac{12\eta_l}{\Delta\rho g} \frac{q_0}{h_0^3} = \frac{12\eta_l \Delta\rho^2 L^3 l^3}{\eta_s^3 \rho_l^3 c^3 \Gamma^3 g} \frac{1}{q_0^2} \sim 3 \times 10^{-8}. \tag{3.200}$$

The dimensionless equations are then

$$\lambda q = h^3 \left(1 + \frac{\partial N_c}{\partial z}\right), \tag{3.201}$$

$$\frac{1}{r\ St} \frac{\partial h}{\partial t} + \frac{\partial q}{\partial z} = \frac{m}{St} + \omega, \tag{3.202}$$

$$\frac{\partial h}{\partial t} = m - hN_c, \tag{3.203}$$

$$m\left(1+\frac{\mu}{St}\overline{\theta}\right)+\mu\omega\overline{\theta}+h\frac{\partial}{\partial t}\left(T_s+\mu\overline{\theta}\right)+q\frac{\partial}{\partial z}\left(T_s+\mu\overline{\theta}\right)$$
$$=\frac{1}{Pe}h\frac{\partial^2}{\partial z^2}\left(T_s+\mu\overline{\theta}\right)+(r-1)\nu q\left(1+\frac{\partial N}{\partial z}\right), \quad (3.204)$$

$$m=\frac{\overline{\theta}}{h}, \quad (3.205)$$

$$T_s=-z-\frac{r-1}{r}N_c. \quad (3.206)$$

As for the cylindrical channels in section 3.2.4, λ is very small so the effective pressure varies approximately magmastatically. μ is also small, so the melting rate is essentially proportional to flux q in (3.204), and the width h grows until the closure balances this melting in (3.203).

For the purposes of calculating the flow into the channel from the partially molten region, essentially all that matters is the pressure in the channel, since it acts as a line sink to the porous flow and it is the size of the pressure reduction that determines how much melt is drawn in. Our main conclusion from section 3.2, and above, was that the channel pressure should be approximately magmastatic, so the precise details of the channels dynamics are of little importance.

Boundary conditions at a channel

Assume now that a two-dimensional channel is surrounded on either side by the partially molten region modelled by (3.151)-(3.155). The channel is centered on $y=0$ and its walls are at $y=\pm y_c$; the flow is symmetric so we need only consider the flow for positive y. As for the cylindrical channel above, the channel width will be much smaller than the scale of the partially molten region, so the porous flow effectively 'sees' the channel as an infinitely thin line sink at $y=0$.

As for a cylindrical channel, the lengthscale over which the pressure perturbation caused by the channel will extend is the compaction length δ, which suggests choosing the size for the inflow ω_0 and channel flux q_0 as

$$\omega_0=\delta\phi_0 u_0=\frac{r\delta}{St}V_0\sim 10^{-10}\ \mathrm{m\ s^{-1}}, \quad (3.207)$$

$$q_0=\omega_0 l=\frac{r\delta}{St}V_0 l\sim 5\times 10^{-6}\ \mathrm{m^2\ s^{-1}}. \quad (3.208)$$

Continuity of the effective pressure requires

$$N=\frac{N_c}{\delta^2}\approx\frac{1-z}{\delta^2}\quad\text{at}\quad y=y_c. \quad (3.209)$$

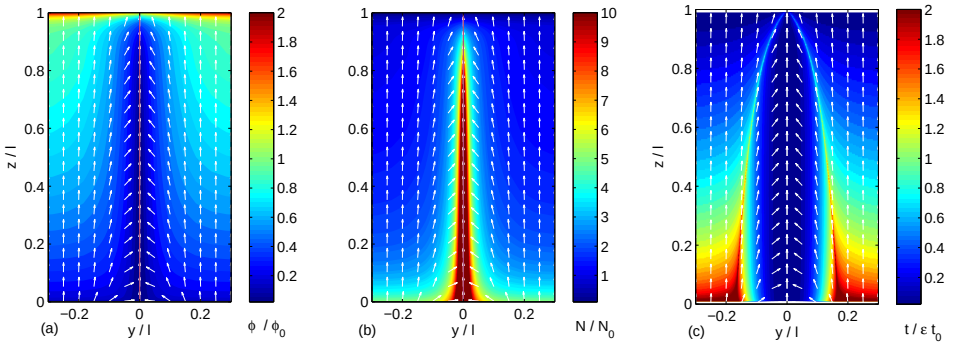

Figure 3.8: (a)-(b); Steady state solutions, for melt fraction ϕ and effective pressure N, to (3.151)-(3.155) with (3.209)-(3.211) at a channel boundary $y = \pm y_c = 5 \times 10^{-6}$. White arrows show the direction of melt flow. The parameters are $\varepsilon = 0.02$, $\delta = 0.14$, $St = 20$. The variables shown are scaled, and any values above the maximum on the colour scale are coloured the same. The melt fraction around the channel is very small ($< 0.5\%$). (c); Travel time for melt to be extracted from the porous flow for the same situation. White arrows show the direction of melt flow. The time is scaled with the typical advective time in the partially molten region $\varepsilon t_0 = l/u_0$. The corresponding behaviour of the channel is shown in figure 3.9.

The velocity of the matrix in towards the channel must match the closure rate, which means

$$2\mathbf{V} \cdot \mathbf{n}|_{y_c} = -\frac{\delta}{St^2} h N_c. \tag{3.210}$$

The influx, scaled as in (3.207), is then calculated from

$$\omega = -2\delta\phi^2 \frac{\partial N}{\partial y}\bigg|_{y_c}. \tag{3.211}$$

Numerical solution

Figure 3.8 shows a steady state numerical solution of (3.151)-(3.155) with (3.209)-(3.211) at the channel. The corresponding inflow ω and resulting flux q are shown in figure 3.9. As for a cylindrical channel, the large effective pressures near the channel cause a reduction in the melt fraction there, and the length scale over which this occurs is on the order of the compaction length δl.

Approximate analytical solutions

As in section 3.3.1 an analytical approximation for the flow into the channel can be found by taking the limit $St \to \infty$, which means ignoring the destabilising terms in

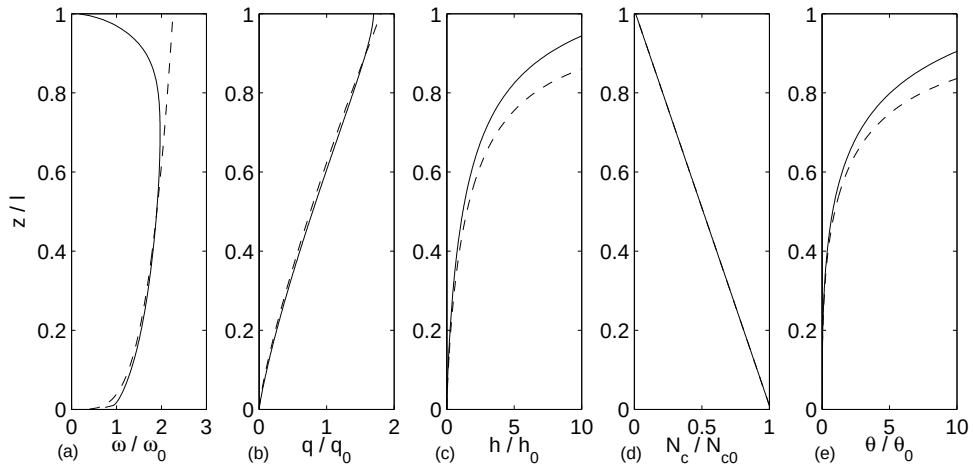

Figure 3.9: (a) Influx to channel in figure 3.8; the solid line is calculated from the numerical solution of (3.151)-(3.155) and (3.209)-(3.211), and the dashed line is the approximate analytical solution (3.220). (b)-(e) Flux, cross-sectional area, effective pressure and excess temperature for the channel at the centre of figure 3.8; solid lines are using the numerically calculated influx ω and the numerical solution of (3.201)-(3.206) and dashed lines are using the approximate ω. The parameters are $\varepsilon = 0.02$, $\delta = 0.14$, $St = 20$, $\mu = 0.01$, $r = 1$.

the porous region. Ignoring terms of order $1/St$ and ε, we have equations (3.164)-(3.167), with boundary condition

$$N = \frac{N_c}{\delta^2} \quad \text{at} \quad y = y_c, \tag{3.212}$$

at the channel. The effective pressure is therefore given by $N = W_0/\phi$, and the equation (3.164) for ϕ is approximated as in (3.177). Then, as in section 3.3.1, after rescaling

$$y = \delta Y, \tag{3.213}$$

and defining ξ and ψ as in (3.178) and (3.176), the perturbed melt fraction ψ satisfies the leading order linear problem

$$\frac{\partial \psi}{\partial \xi} = \frac{\partial^2 \psi}{\partial Y^2}, \tag{3.214}$$

$$\psi = 0 \quad \text{at} \quad \xi = 0, \qquad \psi \to 0 \quad \text{as} \quad Y \to \infty, \tag{3.215}$$

$$\psi = \psi_c \equiv \delta^2 \frac{W_0}{N_c} - \xi, \quad \text{at} \quad Y = Y_c. \tag{3.216}$$

The solution for ψ, via a Laplace transform or Green function for instance, is given by

$$\psi = \frac{1}{2\sqrt{\pi}} \int_0^\xi \psi_c(\hat{\xi}) \frac{Y - Y_c}{(\xi - \hat{\xi})^{3/2}} e^{-(Y-Y_c)^2/4(\xi-\hat{\xi})} \, \mathrm{d}\hat{\xi}. \tag{3.217}$$

The influx to the channel (3.211) can therefore be written in terms of the value of ψ there;

$$\begin{aligned}\omega &= 2W_0 \frac{\partial \psi}{\partial Y}\bigg|_{Y_c} \\ &= \lim_{Y\to Y_c} \frac{W_0}{\sqrt{\pi}} \int_0^\xi \psi_c(\xi-\hat{\xi}) \left(\frac{1}{\hat{\xi}^{3/2}} - \frac{(Y-Y_c)^2}{2\hat{\xi}^{5/2}} \right) e^{-(Y-Y_c)^2/4\hat{\xi}} \, \mathrm{d}\hat{\xi} \\ &= \frac{W_0}{\sqrt{\pi}} \left(-\frac{2}{\xi^{1/2}}\psi_c(0) - \int_0^\xi \frac{2}{\hat{\xi}^{1/2}} \frac{\partial \psi_c}{\partial \xi}(\xi-\hat{\xi}) \, \mathrm{d}\hat{\xi} \right). \end{aligned} \tag{3.218}$$

If the $O(\delta^2)$ term in (3.216) is ignored, $\psi_c = -\xi$ and the solution (3.217) can be evaluated as

$$\begin{aligned}\psi(\xi) &= -\frac{1}{2\sqrt{\pi}} \int_0^\xi (\xi-\hat{\xi}) \frac{(Y-Y_c)}{\hat{\xi}^{3/2}} e^{-(Y-Y_c)^2/4\hat{\xi}} \, \mathrm{d}\hat{\xi} \qquad (3.219) \\ &= -\left(\xi + \frac{(Y-Y_c)^2}{2} \right) \mathrm{erfc}\left(\frac{Y-Y_c}{2\xi^{1/2}} \right) + \frac{1}{\sqrt{\pi}} (Y-Y_c) \xi^{1/2} e^{-(Y-Y_c)^2/4\xi}. \end{aligned}$$

This gives the solution for the melt fraction ϕ, and the influx, scaled as in (3.207), is

$$\omega = \frac{4}{\sqrt{\pi}} W_0 \xi^{1/2} = \frac{4}{\sqrt{\pi}} W_0^{5/4} z^{1/4}. \tag{3.220}$$

The cumulative flux to enter the channel, scaled as in (3.208), is

$$q = \frac{16}{5\sqrt{\pi}} W_0^{5/4} z^{5/4}. \tag{3.221}$$

This influx is compared with the numerical calculation in figure 3.9.

3.4 Channel evolution

3.4.1 Growth of a channel

Two-dimensional flow

We now return to section 3.1 to see how the channels described in sections 3.2 and 3.3 can naturally evolve from the melting instability seen there. Figure 3.1 showed the evolution of a Gaussian perturbation to the one-dimensional steady state up until the time at which the melt fraction in some of the discretised cells reached 100%. Once this stage is reached, these cells should be interpreted as a channel, whose dynamics are governed by the non-dimensional equations (3.201)-(3.206).

The numerical simulation can be continued by no longer attempting to solve the porous flow equations (3.12)-(3.14) for the 'channelised' cells, and instead applying

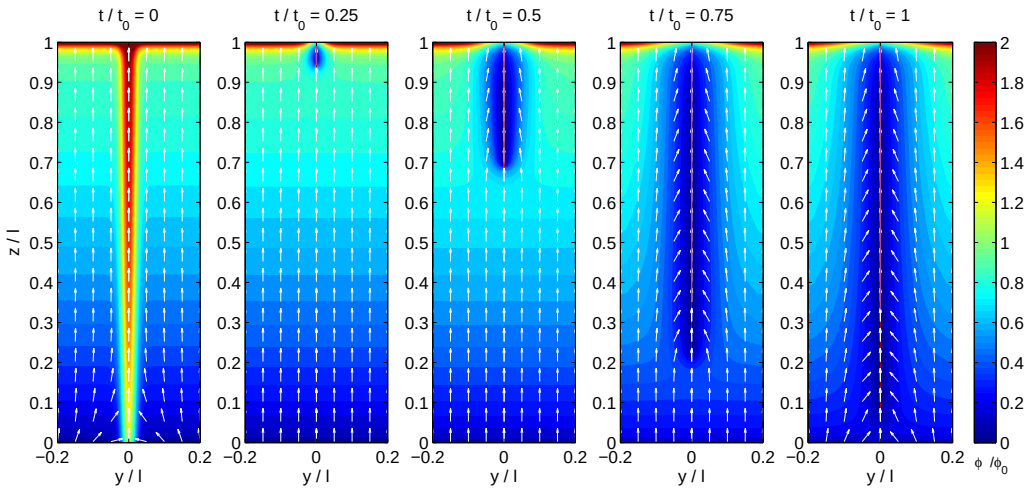

Figure 3.10: Time evolution for melt fraction ϕ (continued from figure 3.1) of an initial perturbation $\exp(-y^2/0.0005)$ to the one dimensional steady state, given by the numerical solution of (3.12)-(3.16), with parameters $\varepsilon = 0.02$, $\delta = 0.14$, $St = 2$. White arrows show the direction of melt movement. When the melt fraction in a cell reaches 100%, it is interpreted as a channel; the porous equations are no longer solved for there, and instead boundary conditions (3.209)-(3.211) are used.

boundary conditions (3.209)-(3.211) there, together with the channel behaviour satisfying (3.201)-(3.206). The resulting evolution is shown in figure 3.10. The channel that initially forms near the top of the region has a relatively high effective pressure and therefore draws in melt from the surroundings; the enhanced vertical melt flow beneath the 'tip' of the channel results in more melting there, and causes the channel to extend downwards.

In the numerical simulation, the channel does not quite reach the bottom of the partially molten region, because the vertical resolution is insufficient to capture its continued downward growth; it does however get very close. This to some extent justifies considering channels in sections 3.2 and 3.3 that extend the full depth. If an open channel is somehow formed in the partially molten region through a different mechanism, we would still expect it to extend downwards as in figure 3.10 because the melt flow drawn in from below results in excessive melting at the tip; the growth of a channel in this way seems similar to headward erosion of a gully observed during overland water flow.

Radial flow

We can easily modify the methods above to look at the growth of a cylindrical channel as in section 3.3.1. Equations (3.12)-(3.16) are solved to find a one dimen-

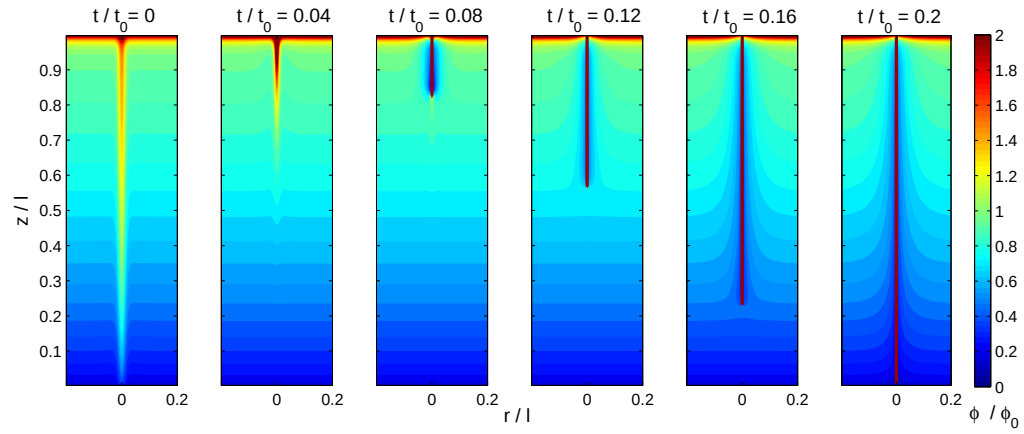

Figure 3.11: Evolution of melt fraction around a channel from a radially symmetric numerical calculation of (3.12)-(3.16), when the initial condition is the one dimensional steady state with a Gaussian shaped perturbation added. The maximum initial porosity (scaled with ϕ_0) is around 2. Parameter values are $\varepsilon = 0.01$, $\delta_c = 0.14$, $St = 2$. All variables are scaled, and any scaled melt fraction larger than 2 is shown in red. When the melt fraction reaches 100% (corresponding to the scaled ϕ reaching 200), these cells are interpreted as channels as in section 3.2 and the pressure is prescribed to be magmostatic there. The boundary conditions (3.161)-(3.163) are then used.

sional steady state; the dimensionless melt fraction is then perturbed by an amount $0.5\exp(-r^2/0.0002)$, so that the maximum perturbed melt fraction is around 1%. The resulting evolution is shown in figure 3.11, where as soon as the melt fraction reaches 100%, we adopt boundary conditions (3.161)-(3.163) at the edges of the channelised cells.

3.4.2 Channel spacing

The previous sections have shown that a channel can be expected to affect the surrounding partially molten region out to a distance on the order of the compaction length δl, and to draw in melt from a comparable region. It is therefore natural to assume that the spacing between neighbouring channels will be on the order of the compaction length. Notice however that comparing figures 3.6 and 3.8 suggests that the region affected by a cylindrical channel (with flow coming in from all directions) is actually somewhat smaller than for the strictly two-dimensional flow.

For the two-dimensional case we attempt to show how such a spacing would naturally evolve with a numerical simulation of the simplified partial melt equations (3.12)-(3.16). The initial conditions are taken as random perturbations to the one-dimensional steady state, and when the melt fraction reaches 100%, the channelised

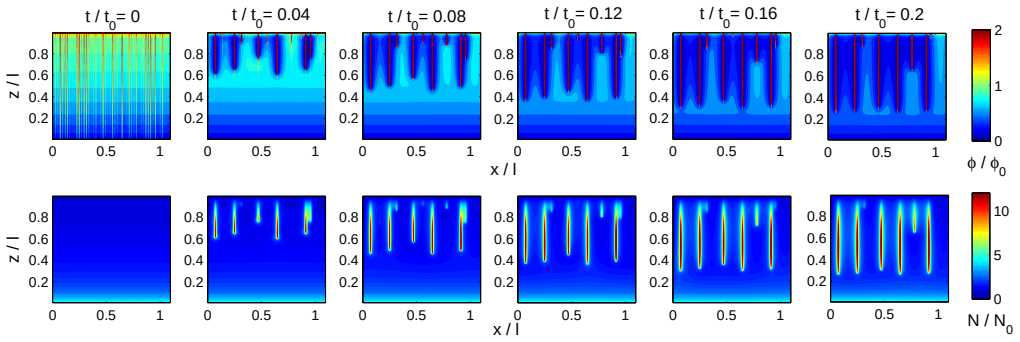

Figure 3.12: Evolution of ϕ and N in a two dimensional numerical simulation of equations (3.12)-(3.16), with an initial condition consisting of the one-dimensional steady state perturbed by random sized additions to the porosity in thin columns of cells with dimensionless width 10^{-4}. The maximum perturbed porosity (scaled with ϕ_0) is around 2. Boundary conditions in y are periodic, and the parameter values are $\varepsilon = 0.01$, $\delta_c = 0.14$, $St = 2$. All variables are scaled, and any scaled melt fraction larger than 2 is shown in red. If the melt fraction reaches 100% (corresponding to the scaled ϕ reaching 200), the equations no longer hold; such cells are interpreted as channels as in section 3.2 and the pressure is prescribed to be magmastatic there with boundary conditions (3.209)-(3.211). A characteristic spacing of channels similar to the compaction length develops, and the melt fraction between channels is very small ($< 0.5\%$). The channel growth downwards is slowing towards the end of this simulation, which is a consequence of the resolution not being high enough to pick up the continued extension; the initial growth nevertheless appears to be well resolved.

cells are replaced with boundary conditions (3.209)-(3.211).

One of the difficulties in doing this is that the resolution required to capture the localisation and growth of a channel is quite high. This is because the melt fraction in the partially molten region is typically very low, so when the melt localises it must occupy a comparatively narrow channel. It is the *local* feedback of melt flow on melting that produces the instability, so if melt flow that is concentrated over a region 1 m wide (say) in reality is spread over a numerical cell 10 m wide (say), a large part of this feedback is lost.

The simulations shown in figures 3.1 and 3.11 have one very narrow cell in the centre with decreasing resolution further away from the channel. For a general perturbation we do not *a priori* know where the channels are going to form, and in order to allow for this we choose a numerical grid that has columns of cells with different widths; very narrow columns are interspersed with wider ones. The initial perturbation then consists of adding small amounts to the melt fraction within each of the thinnest cells to act as 'seeds' for potential channels; each column is perturbed by a random amount, but with a maximum disturbed melt fraction of around 1%.

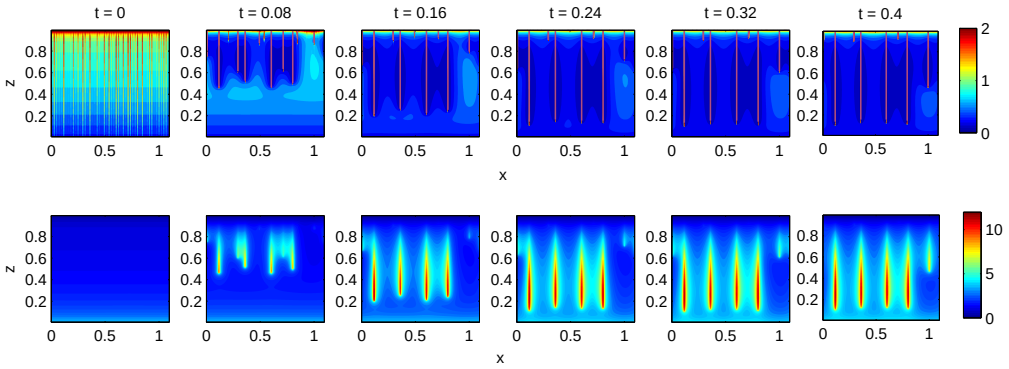

Figure 3.13: As in figure 3.13, but with $\delta = 0.22$. The characteristic spacing between adjacent channels is larger due to the greater compaction length.

The results are shown in figure 3.12. Some of the perturbations quickly disappear while others grow to form channels; as the incipient channels grow they try to draw in melt from the surrounding region, and consequently the larger channels grow at the expense of the smaller ones. This causes a typical spacing of channels to develop, comparable to the compation length δl, and the vast majority of melt from the whole region ends up being focussed sideways into one of the channels. Figure 3.13 shows a similar simulation with a larger compaction length, which shows a slightly larger spacing between channels.

3.5 Discussion

3.5.1 Instability

The models for melt flow within the partially molten region in chapter 2 and within a channel in this chapter are very similar, and are based on the same governing physics. The crucial difference is in the melting rate (3.11), which is driven by the decompression of both matrix and melt; a channel results when it is the melt flow which dominates, since this produces the positive feedback.

The instability mechanism seen in sections 3.1 and 3.4 is essentially the same as that which causes reactive infiltration on a solubility gradient (here it is the solidus gradient which causes 'melting' in order to maintain equilibrium, whereas there it is a solubility gradient which causes 'dissolution'). Here however, the local melting rate continues to increase until an open channel forms; this is because, unlike in a dissolution reaction, there is no limit to the amount of solid that can be 'eroded'.

The instability appears to be non-linear, requiring a finite perturbation in melt fraction to initiate a channel; for larger Stefan numbers (corresponding to a lesser degree of melting) a larger perturbation is needed to initiate a channel. Substantial variations in melt fraction are presumably ubiquitous in the mantle (due to heterogeneities in composition for example), and if not, then the other instability mechanisms mentioned in chapter 1 may provide them.

It is possible that the system becomes linearly unstable at smaller values of the Stefan number; however a proper linear stability analysis is not easy to perform due to difficulties in determining the vertical eigenfunction. A similar analysis has been applied to the reactive infiltration mechanism (Aharonov et al., 1995), and suggests that *uniform* flow should be linearly unstable, but this analysis is complicated when the 'background' state, against which one linearises, depends on z. Since including the melting rate (and therefore having a non-constant background state) is central to our model it is not possible to apply the same simple analysis here. Nevertheless, a *local* perturbation of (3.12)-(3.14) to the one-dimensional state $\tilde{\phi}(z)$, $\tilde{N}(z)$, of the form

$$\phi = \tilde{\phi}(z) + e^{\sigma t/\varepsilon + iky}, \tag{3.222}$$

gives a dispersion relation

$$\begin{aligned} \sigma &= \frac{\varepsilon}{St}\tilde{\phi}\tilde{N} + \frac{2}{St}\tilde{\phi}(1+\delta^2\tilde{N}') - \left(1 - \frac{\varepsilon\tilde{\phi}}{St}\right)\left(\tilde{N} + \frac{\delta^2\tilde{\phi}^2\tilde{N}''}{\tilde{\phi} + \delta^2\tilde{\phi}^2k^2}\right) \\ &\sim \frac{2\tilde{\phi}}{St} - \tilde{N}. \end{aligned} \tag{3.223}$$

This essentially compares the effects of increased melting rate and compaction rate due to a change in melt fraction, and since $\tilde{N} \sim W_0/\tilde{\phi}$, suggests instability if

$$St < \frac{2\tilde{\phi}^2}{W_0}. \tag{3.224}$$

In comparing the ideas here with work on the reactive infiltration instability (Aharonov et al., 1995; Spiegelman et al., 2001; Spiegelman and Kelemen, 2003), it is worthwhile pointing out that the situation we consider here is that in which the Damköhler number (for melting, rather than dissolution) is infinite (the Damköhler number measures the relative speed of reaction to advection). In this limit, as in (3.223) above, the most unstable linear perturbations are for large wavenumbers (Spiegelman et al., 2001). The spacing that is seen to develop in figures 3.12 and 3.13 is well into the non-linear regime.

3.5.2 Channel flux and spacing

Regardless of how they form, the amount of melt which enters a channel can be expected to be comparable to that which is produced within a compaction length; this is exactly what the scaling for Q_0 in (3.160) says, and the value for Q in (3.193) gives an improved estimate based on our suggested dynamics for the surrounding partially molten region.

The compaction length in the mantle is notoriously unknown, due to uncertainties and variability in properties such as the grain size and particularly the viscosities, which are also really dependent on temperature, pressure and composition. The values used above are rough estimates but in reality the viscosities of both melt and matrix may vary by at least an order of magnitude. Typical estimates for the compaction length range between 10 m and 10 km, with the most likely probably somewhere in the middle of this range. The flux in one channel therefore has a similarly large range of variability; in terms of the dimensional parameters it can be written, from (3.160),

$$Q_0 = \frac{r}{St}\delta^2 l^2 V_0 = \eta_s \left(\frac{a^2}{b\eta_l \Delta\rho g}\right)^{1/2} \left(\frac{\rho_s}{\rho_l}\frac{c\Gamma\rho_s g}{L}\right)^{3/2} l^{3/2} V_0^{3/2}. \tag{3.225}$$

The spacing between adjacent channels must naturally also vary in the same way; a smaller compaction length suggests more, closely-spaced, small channels, whereas a longer compaction length suggests fewer, widely-spaced, larger channels.

3.5.3 Residence times

The melt velocity in the cylindrical channel is seen from the definition of S_0 in (3.123) to be independent of the melt flux; the typical velocity is

$$w_{c0} = \frac{Q_0}{S_0} = \frac{\rho_s}{\rho_l}\frac{L}{c\Gamma\rho_s g}\frac{\Delta\rho g l}{\eta_s} \approx 100 \text{ m a}^{-1}, \tag{3.226}$$

using the values in table 3.1 (this is the same as for the two dimensional crack in section 3.3.2, though not the same as that in section 3.2.2). The flow is therefore much faster than the porous flow ($u_0 \approx 1$ m a^{-1}), but not enormous. This is because the melt pressure is close to magmastatic; the channel acts almost like a reservoir of melt, which is only slowly driven upwards. (3.226) is comparable to, and may be even faster than, what geophysical constraints suggest (Kelemen et al., 1997), but it is interesting to note from section 3.2.4 that the scaled velocity is roughly $Q/S = rN_c$ in the steady channel, and is therefore decreasing towards the top; thus (3.226) is probably an over estimate for the typical velocity.

These velocities for channel / porous flow suggest travel times for melt to ascend the depth of the partially molten region in a conduit may be only several hundred years, compared to 30 thousand years or more to rise the same distance by porous flow (these are estimates using the values in table 3.1, so must be taken with due caution). Figures 3.6 and 3.8 show the time taken for melt to be extracted from the partially molten region, either into the channel or to the top of the region. These are calculated by integrating along streamlines from each point in the partially molten region.

It is seen that melt within the accumulation zone around the channel is relatively quickly drawn in, being in the partial melting region for around 3 ky. Melt slightly further away appears to be retarded by the influence of the channel without being drawn into it, and takes longer to reach the surface than that furthest away, which is unaffected by the presence of the channel.

3.5.4 Chemical tracers

Chemical feedbacks on the dynamics of the partially molten region have been ignored in this study, but we can nevertheless consider the effect of this type of melt extraction on the concentration of tracer elements within the rocks. The different residence times for melt flow seen above can be expected to produce corresponding variations in composition. If an element has concentration c_s in the solid matrix and c_l in the melt, these will satisfy equations such as

$$\frac{\partial}{\partial t}[(1-\phi)c_s] + \nabla \cdot [(1-\phi)\mathbf{V}c_s] = \nabla \cdot [(1-\phi)D_s \nabla c_s] - \Gamma, \tag{3.227}$$

$$\frac{\partial}{\partial t}[\phi c_l] + \nabla \cdot [\phi \mathbf{u} c_l] = \nabla \cdot [\phi D_l \nabla c_l] + \Gamma, \tag{3.228}$$

where Γ is the dissolution rate from solid to melt, and D_l and D_s are diffusion coefficients.

However the simplest things to consider are idealized tracer elements, which have a constant bulk partition coefficient κ, meaning that in equilibrium the concentrations in solid and melt must be in ratio

$$\kappa = \frac{c_s}{c_l}. \tag{3.229}$$

Incompatible elements have a small bulk partition coefficient, so preferentially move into the melt from the solid. If we assume that the porous flow is in equilibrium (i.e.

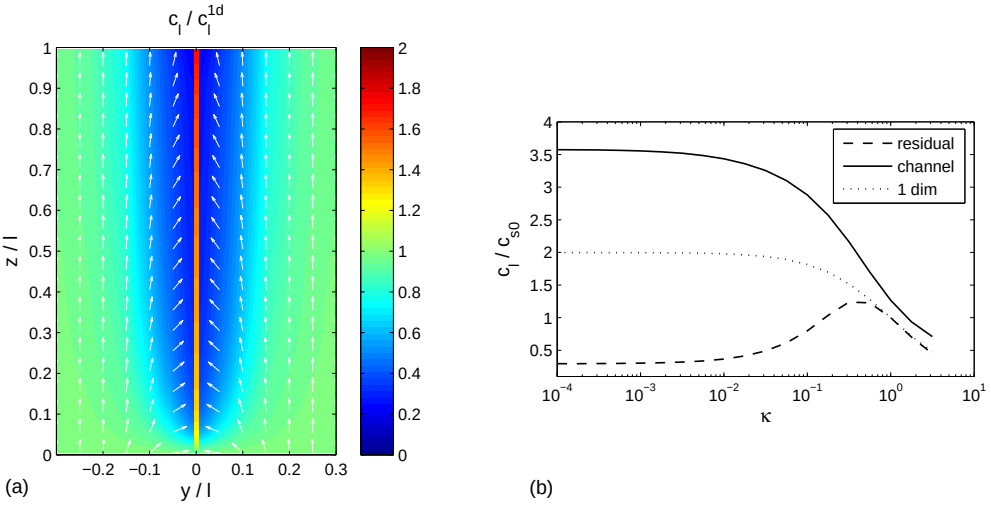

Figure 3.14: (a) Concentration of an incompatible trace element with bulk partition coefficient $\kappa = 10^{-2}$ relative to the concentration that would be expected for one dimensional equilibrium upwelling. White arrows show direction of melt movement. The width of the channel is exaggerated. Here $\delta = 0.14$, $St = 2$, $\varepsilon = 0.01$, $W_0 = 1$. (b) Concentrations of trace elements in erupted melt compared to the concentration of the parent rock for different bulk partition coefficients $\kappa = c_s/c_l$. These are calculated using (3.230) from the steady state solutions to (3.151)-(3.155) with (3.161)-(3.163) at a channel boundary $y = y_c = 5 \times 10^{-6}$, as shown in figure 3.8. The solid line shows the concentration in the melt at the top of the channel, the dashed line shows the concentration in the melt in the residual matrix close to the top of the channel, and the dotted line shows the concentration in melt at the top of a one dimensional porous column.

Γ in (3.227) and (3.228) quickly adjusts to whatever is needed to cause this) the total conservation equation is,

$$\frac{\partial}{\partial t}\left[\phi c_l + \kappa(1-\phi)c_l)\right] + \nabla \cdot \left[\phi \mathbf{u} c_l + \kappa(1-\phi)\mathbf{V} c_l\right] = 0, \tag{3.230}$$

where we have ignored diffusion (the compositional Péclet number $V_0 l/D_s$ is likely to be very large). A channel, where $\phi = 1$, is chemically isolated, since there is no local solid concentration for c_l to equilibrate with. (3.230) can be solved for the concentrations together with (3.151)-(3.155) for the melt fraction and velocities. Steady state calculations for the two dimensional case shown in figure 3.8, are summarized in figure 3.14.

The concentration in the channel is assumed to be well mixed; if on the other hand the chemical signal is preserved from when the melt entered the channel it might be expected that the more enriched melt from deeper in the mantle ascends in the centre, with the melts from shallower nearer the edges (Spiegelman and Kelemen, 2003); this

would lead to more variability than is shown in figure 3.14. It is in any case seen that the channel melt is enriched in incompatible elements with small bulk partition coefficients, whilst the melt in the surrounding residual matrix is relatively depleted.

3.5.5 Channel alignment

The channels studied here are all aligned vertically since the buoyancy force causes the melt to rise vertically. If variations in the matrix pressure due to the viscous stresses in (2.98) were included, they would introduce an extra pressure gradient in Darcy's law (2.99), which effectively realigns the buoyancy force driving melt flow. In a matrix undergoing corner flow at a spreading ridge, these additional pressure gradients will be directed towards the ridge (Spiegelman and McKenzie, 1987) so channels which form might be expected to align themselves in the same direction. They could then provide an efficient mechanism to focus flow towards the ridge axis from a wider melting area.

Intersection of two channels in a viscous medium was investigated by Ito and Martel (2002); they found that their dykes only interact over distances smaller than the compaction length, and we have seen that the channels studied here are already spaced at this distance. As seen in figure 3.12, closer channels do not want to coexist because the larger ones grow at the expense of the smaller ones by drawing in the surrounding melt. If channels are focussed together by stress gradients, however, it is possible they would be forced to intersect and thus form a coalescing network feeding a highly localised supply of melt to the ridge axis.

3.6 Summary

In this chapter we have studied equations, and straightforward steady solutions, for open conduits of melt, and have tried to make use of the well developed models for analogous Röthlisberger channels in ice. The important point that has not been made in previous such models for magma flow, is that if the temperature of the surrounding matrix is decreasing, the ascending melt loses heat to it and the resulting melting of the walls has a dominant effect in controlling the shape and size of the channel.

Long thin channels would, we suggest, be unstable to pinching off into cylindrical shapes, and the pressure gradient within such a conduit would be very close to magmastatic. It would be able to drain a surrounding region of the porous matrix on the order of the compaction length, collecting a melt flux $Q \sim 0.01$ m^3 s^{-1} $\sim$ 3×10^5 m^3 a^{-1}, with ascent velocity on the order of 100 m a^{-1}. The surrounding

residual matrix is reduced to very low melt fractions ($< 0.5\%$), and the melt from these regions is extracted into a channel in a few thousand years.

Channels might naturally evolve from an instability very similar to the reactive infiltration instability associated with the heat transport by the melt, and would have a spacing comparable to the compaction length. They could act as a very efficient method for extracting melt and offer a physically grounded mechanism for near-fractional extraction.

We do not claim that these types of channel *necessarily* exist in the mantle; but rather point out that the mechanisms to produce and maintain them are there. The models presented here are of course far too simplistic to capture everything that is going on beneath mid-ocean ridges, and it is possible that other processes are dominant. However, it is interesting to observe that channels can form naturally during decompression melting even for a single component rock.

Future work should look at modelling the melting of rocks with a more realistic composition, and determining the melting rate self-consistently. Useful references for this include Ribe (1985b) and Katz (2008), who suggest model equations to study two component systems. In the simplest form, the model (3.1)-(3.5) would have to be supplemented by two equations for the concentrations of a component in melt and matrix, together with an equilibrium constraint in place of (3.6) that prescribes the temperature as a function of depth and composition, and relates the compositions in melt and matrix. It does not yet seem clear whether the same extent of focussing seen here would be possible in such a model or not.

Part II

Subglacial water flow

Chapter 4

Introduction

4.1 Motivation and Outlook

4.1.1 Motivation

Understanding the nature of subglacial drainage networks that transport meltwater from beneath glaciers and ice sheets is important because of their effect on the basal boundary condition for the ice flow. It is increasingly observed that there are substantial changes in the ice velocity over short (diurnal/seasonal) time scales, and this is widely believed to be due to changes in the slip of the ice at its bed, which in turn are inferred to be caused by sudden changes in the hydraulic system (Kamb et al., 1985; Zwally et al., 2002; Copland et al., 2003; Joughin et al., 2008). Understanding the interaction between ice, water, and the underlying substrate is therefore of great importance in predicting the behaviour of ice masses over the coming decades, particularly in response to the warming climate.

It is well established that the water pressure in the drainage system plays a crucial role in determining how fast the ice can deform over areas of bedrock and how much sediment deformation occurs in areas where the ice is underlain by a layer of till (Bindschadler, 1983; Iken and Bindschadler, 1986; Alley et al., 1986; Bindschadler et al., 2003). The water pressure depends upon how much meltwater is being produced and how effective the drainage system is at routing it from beneath the ice (Weertman, 1972; Röthlisberger, 1972; Hubbard and Nienow, 1997). Different types of drainage system are thought to exist and these can be broadly characterised as *localised* or *distributed*. Localised systems have a low water pressure and transport water quickly; distributed systems tend to have a higher pressure and transport water more slowly. Much of the interesting observed ice dynamics are thought to result from the interaction and transition between different types of drainage system (Kamb

et al., 1985; Kamb, 1987; Meier et al., 1994; Kamb and Engelhardt, 1987; Anderson et al., 2004; Nuttall and Hodgkins, 2005).

4.1.2 Outlook

The rest of this chapter will review a simple model for ice flow, some of the standard theories for basal sliding, and some of the standard models of meltwater drainage.

In chapter 5 we model the interaction between efficient channelised and less efficient distributed flow, with the aim of better understanding when and how many channels should exist in different situations. This will be done in the context of simple generalised models of channelised and distributed drainage, and the mathematical formulation is very similar to the models in part I. We suggest there is an analogue to the compaction length, and that this determines a typical spacing between channels, set by a balance between downstream and transverse potential gradients. We also make some comparison of the results with the typical spacing of *eskers*, long sinuous ridges of sediment that are common in deglaciated regions (Shreve, 1985).

In chapter 6 we use a model for coupled distributed-channelised flow to explain *seasonal waves* on a glacier; these are annual speed-up events that propagate down the glacier during the course of the summer (Hodge, 1974). The suggestion is that these are caused by a wave in the pressure in the distributed drainage system that allows the ice to slide faster.

4.2 Ice flow

This section provides a brief introduction to modelling the flow of ice. Glacial ice is usually taken to behave as a viscous fluid which deforms according to the non-linear 'Glen' flow law

$$\dot{\varepsilon}_{ij} = A\tau^{n-1}\tau_{ij}, \tag{4.1}$$

in which $\dot{\varepsilon}_{ij}$ is the strain-rate tensor, τ_{ij} is the stress-deviator tensor, and τ is the second invariant of τ_{ij}, given by

$$2\tau^2 = \tau_{ij}\tau_{ij}. \tag{4.2}$$

A and n are parameters, and A in particular can depend quite strongly on temperature. Quite different values of the parameters have been used to best fit observed data; often n is taken to be about 3 and A about 10^{-24} Pa^{-3} s^{-1}.

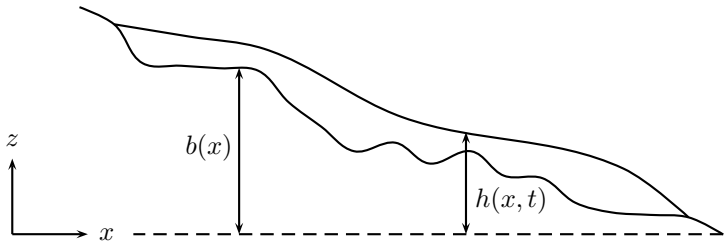

Figure 4.1: Geometry for a one-dimensional glacier.

The simplest models are for glaciers flowing in one direction as in figure 4.1. If the depth of the ice is $H(x,t)$ and ice moves in the x direction with volume flux $Q(x,t)$, the continuity equation is

$$\frac{\partial H}{\partial t} + \frac{\partial Q}{\partial x} = a, \tag{4.3}$$

where $a(x,t)$ is the *accumulation* rate, which is the net contribution of snowfall, melting and ablation.

The ice velocity in the x direction can be separated into a component $u_b(x,t)$ due to sliding over the bed $z = b(x)$, and a component $u_i(x,z,t)$ due to internal deformation of the ice. The *shallow ice approximation*, which makes use of the typically small aspect ratio between ice depth and horizontal length scale, is often used to calculate u_i, and the ice flux is then given by

$$Q = u_b H + \int_b^h u_i \, \mathrm{d}z, \tag{4.4}$$

where $h(x,t) = b(x) + H(x,t)$ is the height of the ice surface.

The dominant contribution to this ice flux depends on the relative sizes of the velocities u_b and u_i; as discussed further in the next section the sliding velocity u_b is usually assumed to depend on the shear stress at the base τ_b, but its size will also depend heavily on the nature of the bed (rough/smooth, hard/soft) and the water pressure. Two limiting cases are worth mentioning. Further details of the expressions below can be found in, for instance, Fowler and Larson (1978) or Fowler (1982); they follow from making appropriate force balances, with the rheology (4.1).

Small sliding velocity

If u_b is comparable to or smaller than u_i the dominant stress in the ice is the vertical shear stress τ_{xz}, and this allows a straightforward expression for u_i to be found, taking A as constant,

$$u_i = -\frac{2A\rho_i^n g^n}{n+1} \left(H^{n+1} - (h-z)^{n+1}\right) \left|\frac{\partial h}{\partial x}\right|^{n-1} \frac{\partial h}{\partial x}; \tag{4.5}$$

the resulting ice flux is

$$Q = u_b H - 2A\rho_i^n g^n \frac{H^{n+2}}{n+2} \left|\frac{\partial h}{\partial x}\right|^{n-1} \frac{\partial h}{\partial x}, \tag{4.6}$$

and the basal shear stress is

$$\tau_b = -\rho_i g H \frac{\partial h}{\partial x}, \tag{4.7}$$

where ρ_i is the ice density and g is the gravitational acceleration.

Large sliding velocity

If on the other hand the sliding velocity is much larger than the deformation velocity (specifically, if their ratio is less than the aspect ratio), the dominant stress in the ice is the longitudinal stress τ_{xx}. The ice flux is simply

$$Q = u_b H, \tag{4.8}$$

and the basal shear stress includes a correction for the longitudinal stresses

$$\tau_b = -\rho_i g H \frac{\partial h}{\partial x} + \frac{\partial}{\partial x}\left(2A^{-1/n} H \left|\frac{\partial u_b}{\partial x}\right|^{1/n-1} \frac{\partial u_b}{\partial x}\right). \tag{4.9}$$

4.3 Basal sliding

4.3.1 Undeformable beds

Weertman law

Classical theories for the sliding of glaciers consider ice flow over a rigid bed. These effectively treat the region near the bed as a boundary layer that provides the boundary condition for the larger scale ice flow above of the form

$$u_b = F(\tau_b) \tag{4.10}$$

There is therefore an assumption that the bed roughness is on a much smaller scale than the depth of the ice, and the sliding law can then be studied theoretically by considering ice of infinite depth subject to shear stress τ_b and speed u_b in the far field.

The first theoretical treatment was due to Weertman (1957), who suggested two mechanisms by which the ice can move over bumps in the bed. Both of these rely on the existence of a thin film of water, perhaps 1 μm thick, which can lubricate the interface between ice and bed. If the basal ice is frozen to the bed the usual no-slip condition for a viscous fluid, $u_b = 0$, applies; even at temperatures below the pressure

melting point, however, a thin film of water may exist as a result of thermodynamic pre-melting (Wettlaufer and Worster, 2006).

When a water film is present, the interface itself allows free slip, and the resistance to motion comes entirely from undulations in the bed which provide a normal force. The difference in stress between upstream and downstream of a bump enables the ice to deform over it. For very small-scale roughness however, this does not allow much movement at all, and a different mechanism known as *regelation* is more effective. This involves the ice on the upstream side of a bump melting, moving in the thin water film, and then refreezing on the downstream side. It occurs because the enhanced stress upstream of the bump lowers the melting point there (via the Clapeyron relationship), allowing the ice to melt. The energy required to do this comes from heat conduction through the bed from the downstream side, where refreezing releases latent heat.

Enhanced deformation is most effective for large obstacles and regelation for small ones; this led Weertman to suggest there is a controlling obstacle size which provides the dominant resistance to motion. Calculating the sliding rate based on this obstacle size leads to the *Weertman* sliding law,

$$u_b = R\tau_b^{(n+1)/2}, \tag{4.11}$$

where n is the exponent in Glen's flow law and R is a constant, depending on the roughness of the bed.

If the ice is treated as a Newtonian fluid, these ideas can be generalised and made more rigorous using the Fourier spectrum of the bed profile (Nye, 1969, 1970; Kamb, 1970). This gives the constant R as an integral over roughness of the bed on different scales, and the controlling obstacle size appears as a critical wavenumber.

Cavitation

The fact that the normal stress in the ice is reduced on the downstream sides of bumps presents the possibility that the ice might separate from the bed and form *cavities*. This was emphasised by Lliboutry (1968) as an important factor to consider and has since been introduced in a number of models (Iken, 1981; Lliboutry, 1987; Schoof, 2005). The presence of a cavity reduces the contact area between bed and ice and therefore reduces the resistance to motion. Since there is water at the interface, cavities will generally be water-filled, and the water pressure is therefore important in determining how much cavitiation occurs. Theoretical studies of sliding with cavitation (Iken, 1981; Fowler, 1986; Schoof, 2005) suggest the sliding law (4.10) should

be replaced by

$$u_b = F(\tau_b, N), \tag{4.12}$$

where the *effective* pressure

$$N = p_i - p_w, \tag{4.13}$$

is the difference between the hydrostatic ice pressure and the water pressure. The smaller N is, the closer the water pressure is to overburden, and the more likely the ice is to lift from the bed; thus F is expected to increase with decreasing N. The most commonly used sliding laws of the form (4.12) can be written as

$$u_b = c\tau_b^p N^{-q}, \tag{4.14}$$

in which p and q are positive constants and c is a constant depending upon the roughness of the bed (rougher beds should have smaller values of c). Typically p and q are both taken to be between 1 and 3; $p = (n+1)/2$ corresponds to Weertman's law (4.11). There is some empirical evidence for flow laws of this type (Budd et al., 1979; Bindschadler, 1983). Since c depends on the microscopic shape of the bed, it should really vary in space and may vary quite considerably; but such fine-scale details of the bed profile are usually unknown and it is often taken as a constant, chosen to produce velocities consistent with observations.

4.3.2 Deformable beds

Till

In the last twenty years or so has come the realisation that many glaciers are underlain by a layer of deformable *till*, and that the deformation of this till may provide an important and sometimes dominant contribution to the ice velocity (Boulton and Hindmarsh, 1987; Murray, 1997; Clarke, 2005). Till is unconsolidated sediment that is usually derived from erosion of the underlying bedrock by the ice. It is constantly reworked by erosion so comprises a large range of grain sizes and is usually poorly sorted. Fine grained silt and clay is mixed with larger pebbles and even larger clasts. Till is also usually wet, with water (if it is warm enough) or ice filling the pore space between grains.

Rheology of till

There has been much ongoing debate as to the rheology of till, hampered by a relative lack of field data and large uncertainties over how applicable laboratory tests are to

the real subglacial environment (Murray, 1997). There is general agreement that till possesses a Coulomb yield criterion such that it is undeformable at shear stresses τ_b less than a critical yield stress τ_c;

$$\tau_c = \tau_{c0} + N \tan \psi \tag{4.15}$$

where τ_{c0} is a constant, ψ is the friction angle, and $N = p_T - p_w$ is the effective pressure in the till (p_T is the hydrostatic overburden till pressure, which includes the overburden ice pressure p_i).

When the shear stress reaches τ_c there is some suggestion of a viscous flow law (Boulton and Hindmarsh, 1987), and some of effectively plastic deformation (Kamb, 1991; Tulaczyk et al., 2000a). If the deformation is plastic, there is infinite strain and the shear stress is $\tau_b = \tau_c$; the most widely used viscous flow law on the other hand is non-linear;

$$\dot{\varepsilon} = A_T(\tau - \tau_c)^a N^{-b}, \tag{4.16}$$

in which A_T, a and b are positive constants. The effective pressure appears again here because it has an important influence on how readily the grains can move past each other. What data are available suggest values of effective viscosity between 10^{10} and 10^{11} Pa s (Boulton and Hindmarsh, 1987; Fischer and Clarke, 2001).

Sliding

If a Coulomb-plastic till rheology is assumed there is no straightforward local boundary condition for the ice flow of the form (4.10); there is a no-slip condition over areas of the bed where $\tau_b < \tau_c$, and a known stress $\tau_b = \tau_c$ where the failure criterion is met; any additional driving stress must be taken up by the 'stuck' parts of the bed or by longitudinal or lateral stresses (Tulaczyk et al., 2000b; Schoof, 2006).

For a viscous rheology the sliding law takes essentially the same form as (4.16); assuming the sliding all results from deformation in a till layer of depth h_T in which the effecive pressure is uniform, and that τ_c is negligible, the strain rate is u_b/h_T, giving

$$u_b = h_T A_T \tau_b^a N^{-b}. \tag{4.17}$$

This has essentially the same form as (4.14), and if a combination of both till deformation and regelation processes are at work the same law can be used.

For most practical glacial applications, and for our purposes in chapter 6, (4.14) is the sliding law that is adopted, due in large part to its relative simplicity and the fact that it has at least some empirical verification.

4.4 Subglacial drainage

4.4.1 Hydraulic potential

Water at the base of the ice is derived from a combination of basal melting and transfer through the glacier from internal melting, surface melting, and precipitation. The water transport we concentrate on here is all *subglacial*, i.e. *at* the bed, though some of the ideas apply also to *englacial* transport. This water arriving from elsewhere supplies a source which varies over time (seasonally and diurnally in particular), and which can sometimes be spatially localised, as a result of crevasses and moulins.

Water flow at the bed is driven by gravity and by pressure gradients and therefore follows the gradient of a hydraulic potential

$$\phi = p_w + \rho_w g b, \tag{4.18}$$

where p_w is the water pressure, ρ_w is the water density and b is the bed elevation. Since the water pressure is typically close to the overburden ice pressure $p_i = \rho_i g(h - b)$, it is useful to write this in terms of the effective pressure, as

$$\phi = \rho_i g h + \Delta\rho g b - N, \tag{4.19}$$

where h is the surface elevation and $\Delta\rho = \rho_w - \rho_i$ is the density difference.

The direction of water flow is thus principally determined by the surface elevation, with a small correction for the bed elevation and a contribution from gradients in the effective pressure. b and h depend on the geometry of the ice rather than on any properties of the water, so it is helpful to separate the potential gradient as

$$-\nabla\phi = \boldsymbol{\Phi} + \nabla N, \qquad \boldsymbol{\Phi} = -\rho_i g \nabla h - \Delta\rho g \nabla b, \tag{4.20}$$

and $\boldsymbol{\Phi}$ can be viewed as the driving potential gradient.

4.4.2 Sheet flow

Weertman (1972) suggested that the thin water film that lubricates the ice-bed interface could be several millimetres thick and thus transport the majority of meltwater. For such a thin layer of depth h, the flow would be laminar with flux per unit width

$$q = \frac{h^3}{12\eta_w}\left(\Phi + \frac{\partial N}{\partial s}\right), \tag{4.21}$$

where η_w is the viscosity of water, s is the distance in the direction of water flow, and Φ is the gravitational potential gradient in that direction.

Walder (1982) showed, however, that such a film is likely to be unstable to collapse into a system of channels. Deeper parts of the film would transport more water and have increased frictional heating; thus the ice there melts more and the film locally grows wider, with a positive feedback ensuing. Heat conduction stabilises short wavelength disturbances (compare with section 3.2.3), but the non-linear evolution of unstable disturbances will be complicated by obstacles in the bed, movement of the ice and changes in water pressure. Several alternative modes of water flow have therefore been suggested (Hubbard and Nienow, 1997; Fountain and Walder, 1998).

4.4.3 Röthlisberger channels

Röthlisberger (1972) first proposed the theory for water flowing in open channels in the ice that are controlled by a balance between meltback (due to turbulent dissipation) and viscous closure (due to a positive effective pressure) of the ice walls. There is good and very visible evidence that tunnels of this type exist, that they transport large quantities of meltwater, and that they form branching networks stretching up glacier from the terminus (Hubbard and Nienow, 1997).

The theory has also been developed by Shreve (1972), Nye (1976) and Spring and Hutter (1982). Since we use these ideas quite extensively we outline the equations here; these are remarkably similar to the model for magma channels in section 3.2.4. Assuming a water flux Q and a cross-sectional area S, the continuity equation is

$$\frac{\partial S}{\partial t} + \frac{\partial Q}{\partial s} = \frac{m}{\rho_w} + \Omega, \tag{4.22}$$

where m is the melt rate of the walls, Ω is the source (from surrounding bed and from surface meltwater), and s is distance along the channel. The flow will be turbulent, and can be described by Manning's law

$$\rho_w g n'^2 Q^2 = S^2 R_H^{4/3} \left(\Phi + \frac{\partial N}{\partial s} \right), \tag{4.23}$$

where $R_H = S/l_w$ is the hydraulic radius, l_w is the wetted perimeter, n' is the Manning roughness coefficient and Φ is the gravitational potential gradient along the channel (4.20). Röthlisberger channels are often assumed to be semicircular (due to the fact that turbulent heat transfer should cause meltback of the ice evenly in all directions), in which case

$$FQ^2 = S^{8/3} \left(\Phi + \frac{\partial N}{\partial s} \right), \tag{4.24}$$

where F is a constant given by $F = \rho_w g n'^2 (2(\pi+2)^2/\pi)^{2/3}$. A similar relationship should hold for slightly different cross-sections provided they are similar to a semicircle.

The kinematic condition for the ice walls is written as

$$\frac{\partial S}{\partial t} = \frac{m}{\rho_i} - KSN^n, \tag{4.25}$$

where N is the effective pressure, n is the coefficient in Glen's law, and K is a constant given by $2A/n^n$ in terms of the constants in Glen's law (Nye, 1953). The first term on the right is the rate of meltback, and the second is the closure rate for ice (compare with (3.22)).

The melting rate is determined by a lumped energy equation and a heat transfer equation for turbulent flow in a pipe. These are

$$m(L + c\theta) + \rho_w c S \frac{\partial}{\partial t}(T_i + \theta) + \rho_w c Q \frac{\partial}{\partial s}(T_i + \theta) = Q\left(\Phi + \frac{\partial N}{\partial s}\right), \tag{4.26}$$

$$m(L + c\theta) = \alpha k \frac{Q^{0.8}}{S^{0.4}}\theta, \tag{4.27}$$

where T_i is the temperature of the ice, $\theta = T_w - T_i$ is the temperature difference between ice and water, c is the specific heat capacity, k is the thermal conductivity, and α is a heat exchange coefficient. Since the flow is turbulent (4.27) cannot be derived so easily as in section 3.2.3, and it is easiest to use an empirical approach; we have made use of the relationship

$$Nu = 0.023 Re^{0.8} Pr^{0.4}, \tag{4.28}$$

between the Nusselt number Nu, Reynolds number Re and Prandtl number Pr (Nye, 1976).

It turns out however that in most circumstances θ in (4.26) is very small; it is therefore essentially determined only by the heat transfer equation, which is decoupled from the remaining equations. The ice is at the melting temperature, which really depends on pressure, but we ignore this dependence and assume T_i is constant. With these simplifications (4.27) and (4.28) reduce to

$$mL = Q\left(\Phi + \frac{\partial N}{\partial s}\right), \tag{4.29}$$

which states that heat generated by turbulent dissipation goes directly into melting the walls.

In a steady state (4.24), (4.25) and (4.29) combine to give the expression

$$Q = \left(\rho_i L K F^{3/8}\right)^4 \left(\Phi + \frac{\partial N}{\partial s}\right)^{-11/2} N^{4n}, \tag{4.30}$$

for the water flux Q in terms of the effective pressure.

The effective pressure gradients are usually smaller than the driving gradient Φ, so this states that typically N should *increase* with increasing Q. This is important; larger water fluxes mean a lower water pressure, and this is thought to explain why these channels form an arborscent network - two channels competing with each other would be unstable, since water in the smaller one, at higher pressure, would leak into the larger one. How effective such leakage is is debateable however (Weertman, 1972; Lappegard et al., 2006), and interaction of a channel with the surrounding flow will be discussed further in chapter 5.

4.4.4 Linked cavities

As mentioned in section 4.3 sliding of the ice can cause cavities to form on the downstream sides of bumps in the bed. These will usually be full of water, and if there are sufficiently many of them water could be transported by flowing from one cavity to another (Lliboutry, 1968; Walder and Hallet, 1979; Kamb et al., 1985; Walder, 1986; Kamb, 1987; Humphrey, 1987; Fowler, 1987). The nature of cavity formation means that flow through such a system will generally be transverse to the ice flow, even when the overall potential gradient is in the down glacier direction. The flow paths taken by the water are therefore considerably longer and more tortuous than, for instance, for a Röthlisberger channel.

Several theoretical studies have been made of linked cavity drainage systems, and they differ in many specifics of the geometry considered; the end results are more or less the same however. Connections between cavities may either be through 'orifices' (Kamb, 1987) (simply smaller sections of the cavities themselves), 'Nye' channels incised into the bed (Walder and Hallet, 1979), mini Röthlisberger channels (Fowler, 1987) or porous flow through underlying till. In reality a combination of such mechanisms is probably most likely.

The simplest, and perhaps most useful, descriptions are based essentially on dimensional analysis and assume the flow is all through cavities, of varying size (Walder, 1986). The controls on the size of cavities come from a balance between opening, due to ice flow over bumps, and closure, due to the viscous sagging of the ice roof. For

flow over a bump of height d, the cavity area S_c opens up at a rate $u_b d$ and closes down at a rate (by analogy with (4.25)) KS_cN^n, and the balance suggests

$$S_c \propto \frac{u_b}{N^n}. \tag{4.31}$$

Flow through this area (transverse to the ice flow, and therefore $\mathbf{\Phi}$), could be described using Manning's law as above (4.24); the local hydraulic gradient $\mathcal{G}$ driving such flow is only a fraction of the overall gradient in the direction of $\mathbf{\Phi}$ because of the tortuosity of the path (Kamb, 1987). Thus

$$Q_c \propto \frac{u_b}{N^n}\mathcal{G}^{1/2}. \tag{4.32}$$

Over the whole width of the bed there will be a range of bump sizes and a range of cavity sizes; the local hydraulic gradient will therefore vary along the flow path (Kamb, 1987). Averaging over a representative width of the bed will however give relationships such as

$$h = C_1\frac{u_b}{N^n}, \tag{4.33}$$

$$q = C_2\frac{u_b}{N^n}\left(\Phi + \frac{\partial N}{\partial s}\right)^{1/2}, \tag{4.34}$$

for the average depth and volume flux per unit width in the direction of the overall potential gradient s. The constants C_1 and C_2, and the coefficients in (4.31) and (4.32), will depend on the size and frequency of bumps in the bed, the shape of the flow path, friction coefficients and other details of the fine scale geometry (Walder, 1986; Fowler, 1987).

Regardless of these, the important conclusion from (4.34) is that the effective pressure *decreases* with increasing water flux (u_b is not independent of N, but with any reasonable sliding law this conclusion is unaltered). This means there is no tendency for areas of greater flow to draw water from nearby, and it remains distributed over the bed.

The major difference between flow through these linked cavities and flow through Röthlisberger channels is that heating by turbulent dissipation is of secondary importance here, whereas it is a controlling factor in how channels operate. Turbulent heating is of course still occurring in cavity flow and can be included in the balance to derive (4.31). In the simplest description this causes the denominator in (4.31) and (4.32) to be replaced by $N^n - C_3\mathcal{G}^{3/2}$ (Walder, 1986), where the size of C_3 indicates the importance of the dissipation. If it is large enough, the size of the cavities can apparently grow without bound, which suggests the linked cavity system can become

unstable. The simple balances outlined here would then break down, the cavity would be maintained in the ice as it flows away from the bump, and the suggestion is that it then turns into a Röthisberger channel. This was invoked by Kamb (1987), who presents a somewhat more involved model for cavity formation, as the mechanism for 'surge' termination when a slowly draining system rapidly evolves to a more efficient channel system.

4.4.5 Drainage through till

The above drainage mechanisms have in mind a rigid bed; when there is a layer of till the same processes may occur, but there is possible deformation of the till to consider too. The till is also porous and will allow some water flow through it; this might be downwards into an underlying aquifer or, if the till covers impermeable bedrock, it might be along the bed in the direction of $\mathbf{\Phi}$. Darcy flow along a layer of till of depth h_T would give a volume flux per unit width

$$q = \frac{k_T h_T}{\eta_w} \left(\Phi + \frac{\partial N}{\partial s} \right), \tag{4.35}$$

in which k_T is the permeability of the till and N is the average effective pressure over the depth h_T.

Estimates of the permeability (often expressed instead as the hydraulic conductivity $\kappa_T = k_T \rho_w g / \eta_w$) vary between around 10^{-16} and 10^{-11} m^2 (Murray, 1997; Fountain and Walder, 1998). For a layer of till $h_T \sim 1$ m and a typical gravitational potential gradient for an alpine glacier $\Phi \sim 10^3$ Pa m^{-1} the flux per unit width might typically be in the range $10^{-10} - 10^{-5}$ m^2 s^{-1}, whereas typical discharges from an alpine glacier might be between 10^{-5} m^2 s^{-1} in the winter and 10^{-2} m^2 s^{-1} in the summer (Fountain and Walder, 1998). Thus drainage through the till by porous flow can evacuate only a very small percentage of the total discharge (Murray, 1997; Hubbard and Nienow, 1997; Fountain and Walder, 1998).

4.4.6 Groundwater flow

If an aquifer exists beneath the layer of till it may be more permeable and provide a more efficient route for the water. The till acts as a thin cap, but water can flow downwards at a rate

$$-w = -\frac{k_T}{\eta_w} \left(\Delta \rho_s g + \frac{\partial N}{\partial z} \right), \tag{4.36}$$

in which $\Delta \rho_s = \rho_s - \rho_w$ and ρ_s is the sediment density, and $N = p_T - p_w$ is the effective pressure in the till. The terms on the right of this equation have typical size

$10^{-9} - 10^{-4}$ m s^{-1}, so quite a reasonable discharge could be transferred down through the till into the aquifer.

Flow in the aquifer is then governed by an equivalent equation to (4.35);

$$q = \frac{k_a h_a}{\eta_w} \left(\Phi + \frac{\partial N}{\partial s} \right), \tag{4.37}$$

and if the aquifer had a depth of, say, $h_a \sim 10$ m and a permeability of $k_a \sim 10^{-10}$ m^2 (as for coarse sand, or karst limestone for instance) it might be capable of transporting fluxes up to 10^{-3} m^2 s^{-1}. It is therefore possible that groundwater flow in an underlying aquifer could, in some cases, transport significant quantities of meltwater (Flowers and Clarke, 2002; Boulton et al., 2007a).

4.4.7 Canals

If a large discharge is forced through till or through the underlying aquifer it requires large pressure gradients to do this and may cause the effective pressure to reduce to zero. When this happens the ice is essentially floating on a layer of water, and we return to the sheet flow situation discussed earlier; since this is unstable, the result is likely to be a combination of linked cavities, perhaps an uneven 'patchy' sheet (Alley, 1989), and channels.

When deformable sediment is present however, channels can be incised down into the sediment as well as up into the ice (Fowler and Walder, 1993; Walder and Fowler, 1994; Ng, 1998). The upper ice walls of the channel open and close by meltback and viscous creep, while the lower sediment walls open and close by erosion and viscous creep (assuming the sediment obeys a viscous flow law such as (4.16)). Comparing the rates of closure of ice and till, Walder and Fowler (1994) found a critical effective pressure above which ice creep is dominant and below which till creep is dominant. In the first case, channels would be roughly flat-bottomed Röthlisberger channels, and in the latter they would be roughly flat-roofed *canals* incised into the sediment.

Since the effective pressure in a Röthlisberger channel tends to be larger for steeper potential gradients (4.30), they conclude that these will be dominant when the glacier is reasonably steep, even when the bed is deformable. For very shallow potential gradients however, canals will be favoured, and unlike channels they are expected to form a braided distributed system.

A model for canals is set out by Walder and Fowler, adding sediment erosion, transport and deposition, and viscous closure of the till, to the Röthlisberger channel model above. This is somewhat more complicated, but their main results in fact

follow only from the suggestion that, since sediment erosion is important, canals will tend to have a high aspect ratio cross-section in the same way as subaerial streams over non-cohesive sediment. Their depth h will adjust to a level determined by the critical shear stress required to mobilise erosion.

For such a shallow and wide canal, an analogue of (4.22), (4.24), (4.25) and (4.29) in the steady state is

$$\frac{\partial Q}{\partial s} = \frac{m}{\rho_w} + \Omega, \tag{4.38}$$

$$\hat{F} Q^2 = S^2 h^{4/3} \left(\Phi + \frac{\partial N}{\partial s} \right), \tag{4.39}$$

$$0 = \frac{m}{\rho_s} - \frac{K}{h^2} S^2 N^n, \tag{4.40}$$

$$mL = Q \left(\Phi + \frac{\partial N}{\partial s} \right), \tag{4.41}$$

where h is the (known) depth, S is the total cross-sectional area, and $\hat{F} = \rho_w g n'^2 2^{4/3}$ is a constant. Modifications have been made to the Manning law (4.39), in which the hydraulic radius is now $\sim h$ rather than $\sim S^{1/2}$, and to the kinematic equation (4.40). This is suggested by the fact that the ice closure rate for a shallow channel with width l is

$$\frac{\partial h}{\partial t} \sim -K l N^n, \tag{4.42}$$

(compare with the closure rate for cracks in a linear viscous material discussed in section 3.2.1); multiplying by $l = S/h$ and with some assumptions about how h and l adjust gives (4.40). (4.39)-(4.41) combine to give

$$Q = \frac{h^{10/3}}{\rho_i L \hat{F}} \left(\Phi + \frac{\partial N}{\partial s} \right)^2 \frac{1}{N^n}, \tag{4.43}$$

which is quite different from the expression (4.30) for a Röthlisberger channel; the effective pressure *decreases* with increasing water flux. Neighbouring canals therefore have a tendency to equilibrate with each other, and water will remain distributed over the bed.

A fuller treatment by Ng (1998) readdressed some of these ideas, using the details of lateral sediment transport in the channel to determine the depth h and width l. This suggests a slightly different relationship to (4.43), but with N still decreasing as Q increases.

Chapter 5

The spacing of Eskers and ice sheet drainage

5.1 Introduction

The aim of this chapter is to model the interaction between efficient channel flow and the surrounding distributed flow. Evidently, a 'channelised' system cannot consist purely of channels, since by their very nature they are localised and cover only part of the bed; meltwater is being produced across the whole bed (at least where it is unfrozen) and must be transported into the channels. Water delivered to the bed from the surface may also be distributed widely over the bed (Raymond et al., 1995; Boulton et al., 2009).

Some of the issues with modelling channelised flow are in knowing where the channels will be and in determining how quickly water from elsewhere can get into them (Flowers et al., 2004; Kessler and Anderson, 2004; Lappegard et al., 2006; Boulton et al., 2009; Rempel, 2009). It clearly does not make sense to assume that all water produced at or delivered to the bed is instantly within a Röthlisberger channel, and even if it did, one would need to know how many channels the water is spread between (Flowers et al., 2004).

Moreover, it is well estabilised that the drainage system can change dramatically throughout the year (Hooke, 1989; Hubbard and Nienow, 1997; Gordon et al., 1998; Nienow et al., 1998; Willis et al., 2003); channels will open up and close down. This is particularly true of temperate alpine glaciers, and increasingly observed in high-arctic polythermal glaciers (Jansson, 1996; Copland et al., 2003) and in ice sheets (Zwally et al., 2002). Even at the height of summer melting there will usually be a region upglacier where the flow is distributed, and a transition downglacier towards a predominantly channelised system.

These are important considerations for any attempt to model meltwater drainage, which must commonly distinguish between the different types of flow. The purpose of modelling subglacial drainage is often to determine the effective pressure for a sliding law such as (4.14); it is important to know how this varies spatially over the bed, and the extent to which it is influenced by the presence of localised, low pressure channels.

We therefore hope to provide some insights into how water can transfer into a channel, and where channels can be expected to form. Section 5.2 will suggest models for distributed and channelised flow, and section 5.3 will give some of the results and conclusions that can be drawn from these.

The pattern of subglacial channels beneath ice sheets is also thought to be responsible for the position of eskers (Banerjee and McDonald, 1990; Shreve, 1985; Clark and Walder, 1994). With some assumptions concerning how the eskers are actually deposited, they can be used to infer something of the nature of the drainage systems that existed during the last ice age, and presumably still exist beneath Greenland and Antarctica. In particular the characteristic spacing of eskers at around 10 km may be indicative of the size of catchment basins for major subglacial channels (Boulton et al., 2009). This will be discussed further in section 5.4.

5.2 Model

5.2.1 Distributed flow

As has been reviewed in chapter 4, there are many different mechanisms of distributed drainage. The approach we take here is to avoid the specifics of these and describe the flow in a very generalised sense; the obvious way to do this is as an effective porous medium, and we can make use of many of the ideas used in part I. We envisage the drainage system as a porous 'sheet', characterised by an effective depth h; this can be thought of as comprising patchy films, linked cavities, Nye channels, canals, porous flow through the till, and perhaps groundwater flow. This approach is not new; Flowers and Clarke (2002; Flowers et al., 2004), for instance, describe a 'macroporous' sheet in a similar vein.

We attempt to avoid too much empiricism, and suggest a model based, at least phenomenologically, on the physical processes that are thought to be important. The intention is to make it simple and many of the finer details will inevitably have to be missed or approximated; since there is often little knowledge of such details, it is not clear this is necessarily a bad thing.

For an average depth of water h, the area flux is $\mathbf{q} = (q_x, q_y)$, and the continuity equation is

$$\frac{\partial h}{\partial t} + \nabla \cdot \mathbf{q} = \frac{m}{\rho_w} + \omega, \tag{5.1}$$

where m is the local melt rate, ρ_w is the water density, and ω is the local englacial source (most likely from surface melting), which is assumed known.

The Darcy-type flow law we suggest is

$$\mathbf{q} = \frac{k_0 h^\alpha}{\eta_w} \left(\mathbf{\Phi} + \nabla N \right), \tag{5.2}$$

where $\mathbf{\Phi}$ is the gravitational potential gradient (4.20), N is the effective pressure, η_w is the water viscosity, and $k_0 h^\alpha$ is the permeability. The value of α depends on how exactly we envisage the porous medium, but typically we can think of taking $\alpha = 3$, as for a laminar sheet of actual depth h.

To close the model we need to determine m and h. The melt rate is determined by energy conservation. Since we envisage the water being in close proximity with the ice, we assume it instantly loses any excess heat to melting and is effectively maintained at the ice (melting) temperature; this removes the need for a heat transfer equation such as (4.27) and is equivalent to the local equilibrium assumptions in chapter 2. The energy equation is therefore

$$mL + \rho_w c h \frac{\partial T_i}{\partial t} + \rho_w c \, \mathbf{q} \cdot \nabla T_i = G + \mathbf{u}_b \cdot \boldsymbol{\tau}_b + \mathbf{q} \cdot \left(\mathbf{\Phi} + \nabla N \right), \tag{5.3}$$

though we will again ignore the pressure dependence of the melting temperature, so in fact T_i is constant. L is the latent heat and c is the specific heat capacity. The source terms on the right hand side are the geothermal heat flux, the frictional heating caused by ice sliding at velocity $\mathbf{u}_b$ and shear stress $\boldsymbol{\tau}_b$ (both assumed known for our purposes here), and the frictional heating caused by the water flow.

We assume that h satisfies an evolution equation, of the form

$$\frac{\partial h}{\partial t} = W_O - W_C, \tag{5.4}$$

where W_O is the rate of opening and W_C is the rate of closure. This is very general (compare with the channel model (4.25)), and the nature of the drainage system is really determined by which processes we choose to include in W_O and W_C.

As discussed in chapter 4, opening of drainage space can be caused by a combination of:

- meltback of the ice,

- sliding of the ice over bedrock bumps or large clasts in till,
- erosion of sediments,
- dilating of till,
- uplift due to over-pressurisation;

and closure by:

- viscous creep of the ice,
- viscous creep of sediments,
- deposition of sediments,
- compaction of till.

Any of these could potentially be included in (5.4); here we choose to include only melting and ice creep:

$$W_O = \frac{m}{\rho_i}, \qquad W_C = \frac{hN}{\eta_i}. \tag{5.5}$$

The viscous closure term is chosen based on a linear ice rheology, by analogy with (4.25), and with the compaction effect in the mantle (chapter 2). η_i is the ice viscosity and ρ_i is the ice density.

From (5.5) and (5.2), and assuming the effective pressure gradient is small compared to $\Phi = |\boldsymbol{\Phi}|$, the steady state has $N \sim m\Phi^{1/\alpha}/q^{1/\alpha}$. Provided the 'background' melting rate, given by geothermal heating and frictional heating from sliding in (5.3), dominates the frictional heating from water flow, this gives an effective pressure *decreasing* with increasing water flux, as expected for a distributed system. If the frictional heating due to water flow dominates, $m \sim \Phi q$ and the situation is (more or less) as for a Röthlibserger channel; this shift in the dominant balance is the essential instability that forms channels, as discussed by Kamb (1987).

Including the frictional heating due to water flow in (5.3) should in principle allow this model to capture both distributed and channelised drainage. As a channel grows however, the idealised porous sheet is no longer a sensible description, and at some stage it would be better to model the channel as in section 4.4.3; this is outlined below.

The situation is clearly very similar to that investigated in chapter 3 for magma flow; transition from distributed to channel flow occurs when the 'unstable' contribution to melting dominates the 'passive' contribution. In the magma case these are

due to the advective derivatives of the temperature in (5.3) (or rather, (3.5)), whereas in this case they are due to geothermal and frictional heating.

5.2.2 Channelised flow

When flow localises into a channel, it is better described in terms of the volume flux Q, cross-sectional area S, and the equations for a Röthlisberger channel given in section 4.4.3. For the linear ice rheology used here, these are

$$\frac{\partial S}{\partial t} + \frac{\partial Q}{\partial s} = \frac{M}{\rho_w} + \Omega, \tag{5.6}$$

$$FQ^2 = S^{8/3}\left(\Phi + \frac{\partial N_c}{\partial s}\right), \tag{5.7}$$

$$\frac{\partial S}{\partial t} = \frac{M}{\rho_i} - \frac{SN_c}{\eta_i}, \tag{5.8}$$

$$ML = Q\left(\Phi + \frac{\partial N_c}{\partial s}\right). \tag{5.9}$$

s here is the distance along the channel, Φ is the gravitational potential gradient in that direction, M is the meltback rate (kg m^{-1} s^{-1}) and F is a constant. The *channel* effective pressure $N_c = p_i - p_w$ has the subscript to distinguish if from the effective pressure N in the distributed region (they will shortly be scaled differently).

As a reminder, these equations assume a semicircular cross section and Manning's flow law, have neglected the pressure dependence of the melting temperature and assume that the water temperature increases a negligible amount above this. In principle, the geothermal heat flux and frictional heating due to the ice flow could also be included in (5.9) as in (5.3), but the basal shear stress locally would be very small and both of these effects will be negligible in comparison to the turbulent heating.

The source term Ω could have two components; one due to water delivered directly into the channel from englacial conduits, and one due to water delivered from the surrounding distributed flow. We will assume for the rest of this chapter that the first of these is negligible; whether this is always (or ever) true is questionable, but such an additional input could quite easily be incorporated; it complicates the discussion somewhat so we neglect it for the time being.

Flow from the surrounding bed must be calculated from the porous model above. If the two sides of the channel are denoted $\mathcal{C}_+$ and $\mathcal{C}_-$, this is

$$\Omega = -\frac{k_0 h^\alpha}{\eta_w}\left(\Phi_n + \frac{\partial N}{\partial n}\right)\Bigg|_{\mathcal{C}_+} - \frac{k_0 h^\alpha}{\eta_w}\left(\Phi_n + \frac{\partial N}{\partial n}\right)\Bigg|_{\mathcal{C}_-}, \tag{5.10}$$

where $\partial/\partial n$ is the derivative in the direction normal to the channel wall, and Φ_n is the gravitational potential gradient in that direction. Since the channel will usually be aligned more or less in the direction of $\boldsymbol{\Phi}$, Φ_n will be very small.

Bridging stress

Note that we ignore the effects of any 'bridging stress' around a channel here (Weertman, 1972; Ng, 1998; Lappegard et al., 2006; Rempel, 2009). This arises in the vicinity of a low pressure channel because the average overburden pressure of the ice must be spread over the surrounding area in contact with the bed, so that the *local* normal stress of the ice on the bed is large at the edges of a channel. Since we define N in terms of the *average* overburden pressure (i.e. the hydrostatic ice pressure), the expressions for the hydraulic gradient in (5.10) are correct (unlike in Rempel (2009) for example). One could argue however that the extra bridging stress ought to appear in the numerator of the compaction rate (5.5) for the distributed flow close to the channel; but we choose to ignore this effect here.

5.2.3 Boundary conditions

The porous equations (5.1)-(5.5) can be viewed as elliptic for the effective pressure N and hyperbolic for the flux $\boldsymbol{q}$; since they are related by (5.2) this means we can expect to apply boundary conditions on either N *or* $\mathbf{q}$.

Ice sheet scale

If considering drainage over a whole catchment basin, we require $\mathbf{q} = \mathbf{0}$ at the watershed, and we require the water pressure to be atmospheric at the margin. If the ice depth falls continuously to zero at the margin this means $N = 0$ there; there are however some undesirable effects of applying such a condition, namely the unbounded growth of the drainage system according to (5.4) or (5.8). Several other effects mean this issue is avoided in practice: the finite depth of the bounding ice means the closure rates used here (which assume an 'infinite' surrounding fluid) are not quite correct; the ice may anyway have non-zero depth at the margin; or a marginal section of the channel may become open to the air so that the zero pressure condition is applied slightly up glacier from the actual margin (Evatt et al., 2006).

Based on these ideas, we treat the 'margin' as a position slightly back from the ice margin, and apply the condition

$$N = N_m \tag{5.11}$$

there, where $N_m = \rho_i g(h_m - b_m)$ is the hydrostatic ice pressure at this position.

Marginal scale

Ice sheets can be frozen to the bed in many parts and it is common for substantial meltwater to be present only in the marginal regions of the bed. Certainly it is plausible that whatever drainage is required further up glacier is accommodated by Darcy flow through sediments, and channels may only form nearer the margin where there is a greater discharge. This may be particularly true if surface melting occurs there and this additional meltwater reaches the bed.

If concentrating only on a marginal region, we apply a condition $\mathbf{q} \cdot \mathbf{n} = q_u$ at the upstream boundary, where q_u is a prescribed flux from the interior of the ice sheet.

Channel

Equivalent conditions apply for a channel, which may begin somewhere *within* the distributed flow region. At the upstream end of a channel, the condition is $Q = 0$, and at the margin

$$N_c = N_m, \tag{5.12}$$

is applied, as in (5.11).

The radius of a channel is typically very narrow compared to the scale of the distributed system; this means the porous flow effectively 'sees' the channel as a line sink, and we label the position of this line $\mathcal{C}$. Since the water pressure must be continuous, the channel provides an additional boundary condition for the porous flow;

$$N = N_c \quad \text{on} \quad \mathcal{C}. \tag{5.13}$$

Geometry

Thus far, our model applies to a general two dimensional ice sheet with surface profile $z = h(x, y)$ and bed profile $b = b(x, y)$ giving rise to gravitational potential gradient

$$\mathbf{\Phi} = -\rho_i g \nabla h - \Delta\rho g \nabla b, \tag{5.14}$$

and the simplest expression for the basal shear stress in (5.3) would be (4.7)

$$\boldsymbol{\tau}_b = -\rho_i g H \nabla h, \tag{5.15}$$

where $H = h - b$ is the ice depth.

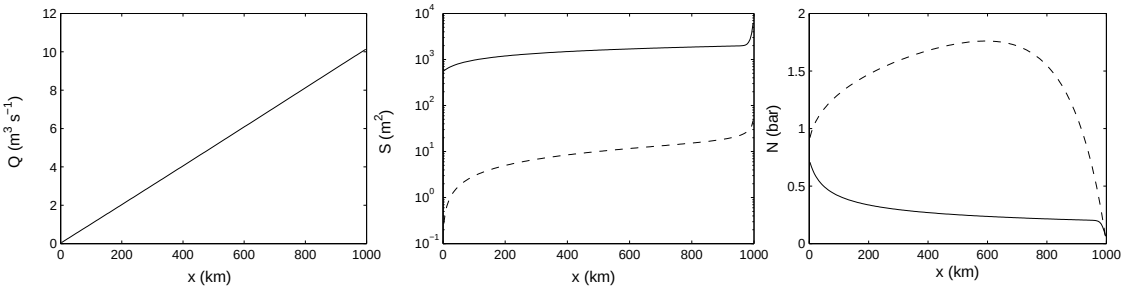

Figure 5.1: Water flux, cross-sectional area, and effective pressure for channel flow (dashed) and distributed flow (solid) down a constant potential gradient $\Phi = 10$ Pa m^{-1}. The same uniform source of water (from basal melting) is either assumed to feed straight into one large channel, or to be spread out across 10 km of the bed; the area of the distributed system is the total cross-sectional area over these 10 km. The effective pressure is zero at the ice sheet margin $x = 1000$ km.

Our results will all consider a one-dimensional ice sheet profile for which $\boldsymbol{\Phi}$ is aligned only in the x direction. We consider two different situations; firstly the whole length of a large ice sheet, when we label $x = 0$ the watershed and $x = l$ the margin, and secondly only a marginal region, when we label $x = 0$ at the upstream boundary and $x = l$ the margin.

In the first case the length scale may be of the order $l \sim 1000$ km and the ice depth may change on the order of 1 km, suggesting a typical scale for the potential gradient $\Phi_0 \sim 10$ Pa m^{-1}. An ice sheet will tend to be relatively flat on its interior however, and most of the elevation change is near the margin; thus $\Phi \sim 1$ Pa m^{-1} may be reasonable in the interior, and $\Phi \sim 100$ Pa m^{-1} nearer the margin. In the second case we therefore suggest $\Phi_0 \sim 100$ Pa m^{-1} over a length scale of, say, $l \sim 100$ km.

The model also requires prescription of geothermal heat flux G, sliding velocity $\mathbf{u}_b$, and englacial source ω. We will assume G and ω are constant (independent of space and time), and for simplicity we also take the product $\mathbf{u}_b \cdot \boldsymbol{\tau}_b$ to be constant. This is unlikely to be true in practice, but is a reasonable simplification to make for the purposes of this study; we are thereby ignoring seasonal variations and any possible feedbacks of the hydrology on the ice dynamics (as might produce ice streams, for instance).

As an illustration of the difference between the distributed and channel flow, figure 5.1 shows the cross-sectional area and effective pressure when drainage is purely by one or other of these flows; a uniform source of water is either assumed to be delivered straight into a channel or spread over a 10 km width of the bed. The effective pressure is larger for a channel, and the cross-sectional area is much smaller, meaning a larger

Parameter	Value	Parameter	Value
ρ_w	1000 kg m^{-3}	η_w	10^{-3} Pa s
ρ_i	900 kg m^{-3}	η_i	10^{13} Pa s
g	10 m s^{-2}	G	0.06 W m^{-2}
L	3×10^5 J kg^{-1}	u_b	10^{-6} m s^{-1}
n'	0.1 m$^{-1/3}$ s	k_0	10^{-5}
F	650 kg m$^{-8/3}$	α	3

Table 5.1: Values of physical parameters used in chapter 5.

average velocity.

5.2.4 Non-dimensionalisation

Scales are chosen based on a typical water flux q_0 in the distributed system and Q_0 in the channel. The size of these discharges depend on the amount of meltwater supplied to the bed, and the size of Q_0 is also determined by the size of the channel's 'catchment area'; this will be discussed shortly.

We assume a length scale l and a potential gradient scale Φ_0. Then for the porous flow equations (5.1)-(5.5), scales are chosen as

$$m_0 = \frac{G + \mathbf{u}_b \cdot \boldsymbol{\tau}_b}{L}, \tag{5.16}$$

$$W_{O0} = \frac{m_0}{\rho_i}, \tag{5.17}$$

$$h_0 = \left(\frac{\eta_w}{k_0 \Phi_0}\right)^{1/\alpha} q_0^{1/\alpha}, \tag{5.18}$$

$$N_0 = \eta_i W_{O0} \left(\frac{k_0 \Phi_0}{\eta_w}\right)^{1/\alpha} q_0^{-1/\alpha}, \tag{5.19}$$

$$t_0 = \frac{\rho_i \eta_i}{\rho_w N_0}. \tag{5.20}$$

For the channel equations (5.6)-(5.9), we choose

$$\Omega_0 = \frac{Q_0}{l}, \tag{5.21}$$

$$M_0 = \frac{Q_0 \Phi_0}{L}, \tag{5.22}$$

$$S_0 = \frac{F^{3/8}}{\Phi^{3/8}} Q_0^{3/4}, \tag{5.23}$$

$$N_{c0} = \frac{\eta_i \Phi_0^{11/8}}{\rho_i L F^{3/8}} Q_0^{1/4}, \tag{5.24}$$

Variable	Units	Ice sheet scale	Marginal scale
l	km	1000	100
Φ_0	Pa m^{-1}	10	100
τ_{b0}	Pa	10^4	10^5
q_0	m^2 s^{-1}	2×10^{-4}	2×10^{-4}
m_0	kg m^{-2} s^{-1}	2×10^{-7}	5×10^{-7}
W_{O0}	m s^{-1}	2×10^{-10}	6×10^{-10}
h_0	m	0.13	0.06
N_0	Pa	0.2×10^5	1×10^5
t_0	s	5×10^8	1×10^8
Q_0	m^3 s^{-1}	2	9
M_0	kg m^{-1} s^{-1}	3×10^{-4}	7×10^{-4}
S_0	m^2	16	2.2
N_{c0}	Pa	2×10^5	3.3×10^6

Table 5.2: Values of model scales, taking $q_0 = 2 \times 10^{-4}$ m^2 s^{-1}, and $Q_0 = 2$ m^3 s^{-1} in the first case, $Q_0 = 9$ m^3 s^{-1} in the second, as suggested by (5.40).

In the dimensionless variables, the equations in the distributed system are

$$\beta r \frac{\partial h}{\partial t} + \nabla \cdot \mathbf{q} = \beta m + \gamma \omega, \tag{5.25}$$

$$\mathbf{q} = h^\alpha \left(\mathbf{\Phi} + \delta^2 \nabla N \right), \tag{5.26}$$

$$\frac{\partial h}{\partial t} = W_O - hN, \tag{5.27}$$

$$m = 1 + \frac{\varepsilon}{\beta} \mathbf{q} \cdot \left(\mathbf{\Phi} + \delta^2 \nabla N \right), \tag{5.28}$$

$$W_O = m. \tag{5.29}$$

The five dimensionless parameters are

$$r = \frac{\rho_w}{\rho_i}, \tag{5.30}$$

$$\beta = \frac{m_0 l}{\rho_w q_0}, \tag{5.31}$$

$$\gamma = \frac{\omega_0 l}{q_0}, \tag{5.32}$$

$$\delta^2 = \frac{N_0}{\Phi_0 l}, \tag{5.33}$$

$$\varepsilon = \frac{\Phi_0 l}{\rho_w L}. \tag{5.34}$$

Parameter	Ice sheet scale	Marginal scale
r	1.1	1.1
ε	0.03	0.03
δ_c^2	0.02	0.3
δ^2	0.002	0.01
β	1	0.2
γ	0	0

Table 5.3: Typical dimensionless parameter values for the scales shown in table 5.2.

These represent the density ratio; the contribution of basal melting to total discharge; the contribution of the englacial source to total discharge; the ratio of effective pressure to the gravitational potential; and the ratio of potential energy to latent heat.

If most of the water is derived from basal melting it is appropriate to *choose* q_0 to make $\beta = 1$, or if most is derived from surface melting, to choose $\gamma = 1$.

The dimensionless equations for a channel are

$$\frac{\varepsilon r^2 \delta^2}{\delta_c^2}\frac{\partial S}{\partial t} + \frac{\partial Q}{\partial s} = \varepsilon M + \Omega, \tag{5.35}$$

$$Q^2 = S^{8/3}\left(\Phi + \delta_c^2 \frac{\partial N_c}{\partial s}\right), \tag{5.36}$$

$$\frac{r\delta^2}{\delta_c^2}\frac{\partial S}{\partial t} = M - SN_c, \tag{5.37}$$

$$M = Q\left(\Phi + \delta_c^2 \frac{\partial N_c}{\partial s}\right), \tag{5.38}$$

in which the additional dimensionless parameter is

$$\delta_c^2 = \frac{N_{c0}}{\Phi_0 l}, \tag{5.39}$$

which represents the ratio of channel effective pressure to the gravitational potential.

Typical values of the physical parameters are given in table 5.1. The resulting values for the variable scales and the dimensionless parameters, for the two different cases of ice sheet scale and marginal scale, are shown in tables 5.2 and 5.3.

As the channel effective pressure is typically larger than the effective pressure in the porous flow, it will draw in the surrounding water. Since channel effective pressure increases with discharge, this will increase the effective pressure there even more; thus the amount which makes its way into the channel is only limited by how large an area of the surrounding bed it is able to draw from. This depends on the efficiency of the distributed system at redirecting the water supply, and is determined by the size of the parameter δ^2.

Inspection of (5.25) and (5.26) shows that the dimensionless length scale over which the pressure variation caused by the channel is felt is δ. This is therefore the width for the catchment area of a channel; it is equivalent to the compaction length in chapter 3.

It is therefore sensible to define the scale for the discharge in the channel as

$$Q_0 = \delta l q_0. \tag{5.40}$$

The dimensionless boundary conditions are

$$q_x = 0 \quad \text{or} \quad q_x = q_u \quad \text{at} \quad x = 0, \tag{5.41}$$

$$N = N_m, \quad N_c = \frac{\delta^2}{\delta_c^2} N_m \quad \text{at} \quad x = 1, \tag{5.42}$$

and for a channel along $\mathcal{C}$,

$$N = \frac{\delta_c^2}{\delta^2} N_c \quad \text{on} \quad \mathcal{C}. \tag{5.43}$$

The influx to a channel (with Q_0 chosen as in (5.40)) is given by

$$\Omega = -\delta h^\alpha \frac{\partial N}{\partial n}\bigg|_{\mathcal{C}_+} - \delta h^\alpha \frac{\partial N}{\partial n}\bigg|_{\mathcal{C}_-}. \tag{5.44}$$

5.3 Results

5.3.1 Numerical calculations for a fixed channel

Initially we prescribe the location of one channel and examine its interaction with the surrounding distributed system in a steady state. If the ice sheet has a one-dimensional surface and bed profile, the channel will be aligned in the same direction. The channel is therefore chosen to lie along $y = 0$ with its head at x_c and mouth at the margin $x = 1$. Far away, as $y \to \infty$, the flow tends toward a one-dimensional flow through the distributed system.

The equations to be solved are (5.25)-(5.29) for the porous flow, with boundary conditions (5.41), (5.42) and (5.43) on $y = 0$, $x > x_c$; and with the channel effective pressure N_c determined from equations (5.35)-(5.38) and (5.42), coupled back to the porous flow through the influx (5.44). The numerical method is briefly outlined in appendix C.

We concentrate on a marginal region, with a constant discharge q_u supplied at $x = 0$, and assume there is no surface melt reaching the bed, $\gamma = 0$. β is taken to be 0.2, so melt production within the region contributes a reasonably small part of the overall

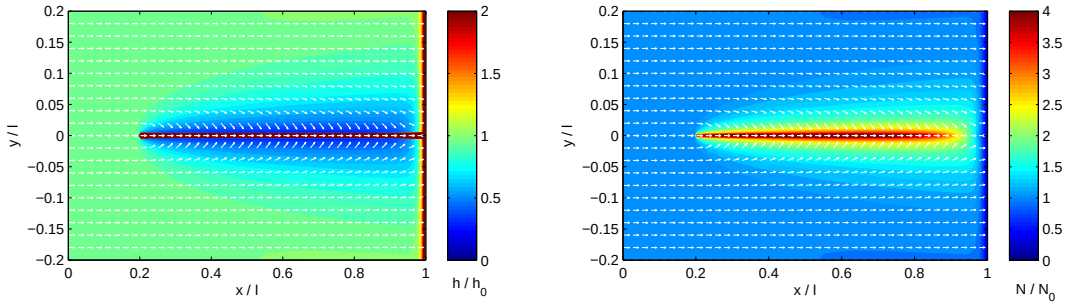

Figure 5.2: Steady state solution to equations (5.25)-(5.29) with $\delta^2 = 0.02$, $\beta = 0.2$, $r = 1.1$, $\varepsilon = 0$. $\mathbf{\Phi} = (\Phi, 0) = (1, 0)$ is constant. The boundary condition at $x = 0$ is $q_u = 0.9$, since this is supposed to represent the margin region of an ice sheet, with a supply of melt from the interior. White arrows show the direction of water movement. At $x = 1$ the effective pressure is prescribed to be $N_m = 0.2$. A channel is prescribed to begin at $y = 0$, $x = 0.2$, and the pressure within this (5.43) is calculated from the rate of inflow (5.44) and the steady state channel equations (5.35)-(5.38), with $r = 1.1$, $\varepsilon = 0$, $\delta_c^2 = 0.1$.

discharge. We also make the simplification $\varepsilon = 0$, which means neglecting the (small) destabilising contribution of viscous heating in the distributed system. To keep things simple, the driving potential gradient is constant, $\Phi = 1$ non-dimensionally.

Figure 5.2 shows the steady state solution for the distributed system, and figure 5.3 shows the corresponding solution for the channel. We see that the large effective pressure in the channel influences the surrounding porous system over a length scale comparable to δ. The water in this region is drawn inwards, but the compacting nature of the porous system means that near to the channel its depth *decreases* - it is squeezed nearly closed by the increasing effective pressure. Despite the permeability decreasing in this way, the large effective pressure gradients are sufficient to push the water through, and the channel is able to capture most of the nearby water. It is worth noticing however that these steep pressure gradients mean the large effective pressures are confined to a narrow region close to the channel, and the pressure over most of the neighbouring distributed system is much less strongly influenced.

The influx to the channel in this case is greatest near its head, since there is already quite a large quantity of water present in the distributed system from further upstream, and the low pressure in the incipient channel quickly draws it in. Notice though that the region upstream of the channel in figure 5.2 appears almost unaffected; the length scale over which the pressure reduction is felt in the x-direction is, from (5.26), δ^2, which is too small to be clearly visible here.

In terms of the physical variables, the channel here is 80 km long, draws water

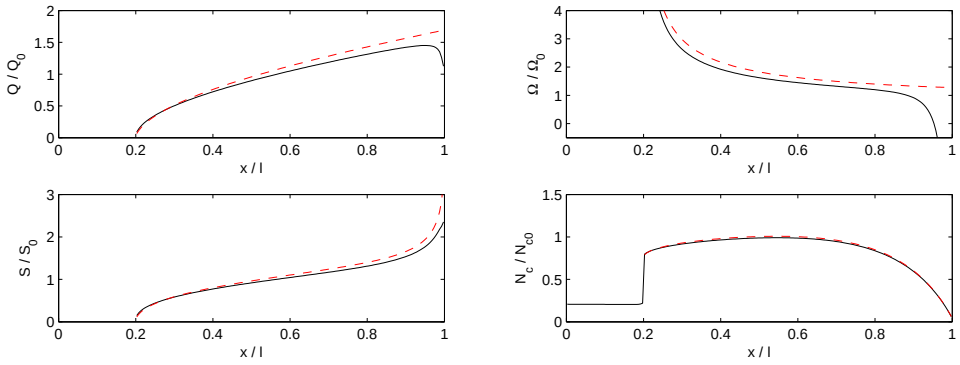

Figure 5.3: Solutions for the channel in figure (5.2). The dashed lines show the analytical approximation for the influx and flux from (5.63) and (5.65). Note that the water goes back out into the surrounding bed very near to the margin because the effective pressure there seems to be larger than it is in the channel. The scale for the flux here is $Q_0 = \delta q_0 l \sim 9$ m^3 s^{-1}.

from a region approximately 10 km wide, and collects a discharge of around 10 m^3 s^{-1}. The effective pressure within the channel is around 30 bar, compared to around 1 bar in the distributed system.

5.3.2 Approximation for flow into a channel

In this section, we make some approximations in order study the coupling between channel and porous flow analytically; these are similar to those made in section 3.3. We are looking at steady states of equations (5.25)-(5.29), (5.35)-(5.38) and conditions (5.41)-(5.44). To make progress we study the case $\varepsilon = 0$ (neglecting viscous heating), and note that δ^2 and δ_c^2 may both be small.

Specifically, since δ_c^2/δ^2 is the ratio of the size of effective pressures in channel and porous flow, we could assume asymptotically that $\delta^2 \ll \delta_c^2 \ll 1$. These are singular approximations however, and it may also be the case that δ_c^2 is not all that small; at least initially, we make no assumptions on the size of δ_c^2.

In this case the channel satisfies

$$Q = \int_{x_c}^{x} \Omega \, \mathrm{d}x, \qquad N_c = \left(\Phi + \delta_c^2 \frac{\partial N_c}{\partial x}\right)^{11/8} Q^{1/4}, \tag{5.45}$$

with the boundary condition $N_c = \delta^2 N_m/\delta_c^2$ at $x = 1$.

The distributed flow has $W_O = m = 1$ and

$$\nabla \cdot \left[h^\alpha \left(\mathbf{\Phi} + \delta^2 \nabla N\right)\right] = \beta m + \gamma \omega, \tag{5.46}$$

$$W_O = hN, \tag{5.47}$$

with the conditions $N = N_m$ at $x = 1$ and $q_x = h^\alpha \left(\Phi + \delta^2 \partial N/\partial x\right) = q_u$ at $x = 0$. The coupling conditions are

$$N\big|_{y=0} = \frac{\delta_c^2}{\delta^2} N_c, \qquad \Omega = -2\delta h^\alpha \frac{\partial N}{\partial y}\bigg|_{y=0}, \quad \text{for} \quad x > x_c, \tag{5.48}$$

where we assume symmetry so that the inflow from both sides of the channel is the same.

Far-field one-dimensional solution

We denote the one-dimensional solution (i.e. if the channel were not there) as $q_\infty(x)$, $h_\infty(x)$, $N_\infty(x)$, defined by

$$q_\infty = q_u + \int_0^x \beta m + \gamma\omega \, \mathrm{d}x, \qquad h_\infty = \frac{W_O}{N_\infty}, \tag{5.49}$$

and N_∞ given by the solution to

$$\frac{q_\infty N_\infty^\alpha}{W_O^\alpha} = \Phi + \delta^2 \frac{\partial N_\infty}{\partial x}, \qquad N_\infty = N_m \quad \text{at} \quad x = 1. \tag{5.50}$$

If we assume the source terms provide a uniform supply of meltwater $\beta = 1$, $\gamma = 0$, then since δ^2 is small, these are (except in a small boundary region near $x = 1$)

$$q_\infty(x) = q_u + \beta x, \qquad h_\infty(x) = \frac{q_\infty(x)^{1/\alpha}}{\Phi(x)^{1/\alpha}}, \qquad N_\infty(x) = W_O \frac{\Phi(x)^{1/\alpha}}{q_\infty(x)^{1/\alpha}}. \tag{5.51}$$

Approximate solution near channel

From (5.47) the effective pressure varies inversely with the depth of the distributed system $N = W_O/h$, leaving one equation for the depth,

$$\frac{\partial}{\partial x}\left(h^\alpha \Phi\right) - \delta^2 W_O \nabla \cdot \left(h^{\alpha-2} \nabla h\right) = \beta. \tag{5.52}$$

To calculate the influx to the channel we rescale the transverse coordinate y. Writing

$$y = \delta Y, \tag{5.53}$$

and taking only the leading order terms in δ^2, (5.52) can be written as

$$\frac{\alpha}{\alpha - 1} h\Phi \frac{\partial}{\partial x}\left(h^{\alpha-1}\Phi^{1-1/\alpha}\right) = \beta\Phi^{1-1/\alpha} + \frac{W_O}{\alpha - 1}\frac{\partial^2}{\partial Y^2}\left(h^{\alpha-1}\Phi^{1-1/\alpha}\right). \tag{5.54}$$

This motivates defining a new variable,

$$\psi = h^{\alpha-1}\Phi^{1-1/\alpha} - h_\infty^{\alpha-1}\Phi^{1-1/\alpha}, \tag{5.55}$$

as a proxy for the depth of the distributed system relative to the one-dimensional state. To make useful further progress we must then *approximate* the advective term on the left hand side by

$$h(x,Y)\Phi(x) \approx h_\infty(x)\Phi(x), \tag{5.56}$$

(compare with section 3.3 and Oseen's approximation), and then define a distorted length variable,

$$\xi = \int_0^x \frac{W_O}{\alpha h_\infty(\hat{x})\Phi(\hat{x})}\,\mathrm{d}\hat{x}. \tag{5.57}$$

The problem is then simply

$$\frac{\partial\psi}{\partial\xi} = \frac{\partial^2\psi}{\partial Y^2}, \tag{5.58}$$

$$\psi = 0 \quad \text{at} \quad \xi = 0, \qquad \psi \to 0 \quad \text{as} \quad Y \to \infty, \tag{5.59}$$

$$\psi = \psi_c(\xi) \equiv \left(\frac{\delta^2 W_O}{\delta_c^2 N_c}\right)^{\alpha-1}\Phi^{1-1/\alpha} - h_\infty^{\alpha-1}\Phi^{1-1/\alpha} \quad \text{on} \quad Y = 0, \quad \xi > \xi_c, \tag{5.60}$$

where ξ_c is the position of the head of the channel. This last boundary condition (5.60) couples it to the problem for N_c, (5.45), with the influx given by (5.48):

$$\Omega = \frac{2W_O}{\alpha-1}\frac{1}{\Phi^{1-1/\alpha}}\frac{\partial\psi}{\partial Y}\bigg|_{Y=0}. \tag{5.61}$$

The solution to (5.58)-(5.60) gives

$$\Omega = -\frac{2W_O}{\alpha-1}\frac{1}{\sqrt{\pi}}\frac{1}{\Phi^{1-1/\alpha}}\left[\frac{\psi_c(\xi_c)}{(\xi-\xi_c)^{1/2}} + \int_0^{\xi-\xi_c}\frac{1}{\hat{\xi}^{1/2}}\frac{\partial\psi_c}{\partial\xi}(\xi-\hat{\xi})\,\mathrm{d}\hat{\xi}\right], \tag{5.62}$$

which must be solved in conjunction with (5.45) and (5.60). It forms a messy integro-differential system for ψ_c, or equivalently N_c.

Limit of large channel effective pressure: $\delta^2 \ll \delta_c^2$

We can make some further progress if we now make use of the limit $\delta^2 \ll \delta_c^2$. In this case ψ_c becomes independent of the channel effective pressure, effectively decoupling the porous flow from the channel flow; the distributed system 'sees' the channel as a sink with infinite effective pressure, and its depth squeezes to zero there. The influx in this case can be written

$$\Omega = \frac{2W_O}{\alpha-1}\frac{1}{\sqrt{\pi}}\frac{1}{\Phi(\xi)^{1-1/\alpha}}\left[\frac{q_\infty(\xi_c)^{1-1/\alpha}}{(\xi-\xi_c)^{1/2}} + \beta\frac{\alpha-1}{W_O}\int_0^{\xi-\xi_c}\frac{\Phi(\xi-\hat{\xi})^{1-1/\alpha}}{\hat{\xi}^{1/2}}\,\mathrm{d}\hat{\xi}\right], \tag{5.63}$$

using the one-dimensional solution (5.51), for which it is helpful to note

$$h_\infty(\xi)^{\alpha-1}\Phi(\xi)^{1-1/\alpha} = q_\infty(\xi)^{1-1/\alpha} = q_u^{1-1/\alpha} + \beta\frac{\alpha-1}{W_O}\int_0^\xi \Phi^{1-1/\alpha}\,\mathrm{d}\xi. \tag{5.64}$$

From (5.45), this gives

$$Q(\xi) = \int_{\xi_c}^{\xi} \frac{2\alpha}{\alpha-1}\frac{q_\infty(\xi')^{1/\alpha}}{\sqrt{\pi}}\left[\frac{q_\infty(\xi_c)^{1-1/\alpha}}{(\xi'-\xi_c)^{1/2}} + \beta\frac{\alpha-1}{W_0}\int_0^{\xi'-\xi_c}\frac{\Phi(\xi'-\hat{\xi})^{1-1/\alpha}}{\hat{\xi}^{1/2}}\,\mathrm{d}\hat{\xi}\right]\,\mathrm{d}\xi', \tag{5.65}$$

and then, if $\delta_c^2 \ll 1$,

$$N_c = Q^{1/4}\Phi^{11/8}. \tag{5.66}$$

Note the first terms in (5.63) and (5.65) give the influx due to the discharge in the distributed system already present from upstream of the channel, and the second terms give the influx due to the continued supply of meltwater to the distributed system along the length of the channel.

Thus we have found expressions for the influx to the channel and the effective pressure there; these are shown in figure 5.3, where they are compared to the numerical calculations. The behaviour of the distributed flow also follows from the solution for ψ.

Pressure at channel head

Notice from (5.65) that the discharge in the channel increases from zero at ξ_c (x_c) as $(\xi-\xi_c)^{1/2}$, and the effective pressure from (5.66) similarly increases from zero with infinite gradient. This means that neglecting the $O(\delta^2/\delta_c^2)$ term in ψ_c, (5.60), and neglecting the derivative of N_c in (5.45) are apparently both singular approximations. If we include the derivative in (5.45) however, we find that N_c in fact tends to a finite non-zero value at ξ_c.

To see this we note from (5.62) that, quite generally, provided $\partial\psi_c/\partial\xi = o((\xi-\xi_c)^{-1})$ near the channel head ξ_c, the influx there is approximately

$$\begin{aligned}\Omega &\sim -\frac{2W_O}{\alpha-1}\frac{1}{\sqrt{\pi}}\frac{1}{\Phi(\xi_c)^{1-1/\alpha}}\frac{\psi_c(\xi_c)}{(\xi-\xi_c)^{1/2}} \\ &\sim -\frac{2}{\alpha-1}\frac{1}{\sqrt{\pi}}\left(\frac{\alpha W_O q_\infty(x_c)^{1/\alpha}}{\Phi(x_c)^{1-1/\alpha}}\right)^{1/2}\frac{\psi_c(x_c)}{(x-x_c)^{1/2}}.\end{aligned} \tag{5.67}$$

We can therefore write the channel flux near its head as [1]

$$Q = A(x - x_c)^{1/2}, \qquad A(x_c) = -\frac{4}{\alpha - 1}\frac{1}{\sqrt{\pi}}\left(\frac{\alpha W_O q_\infty(x_c)^{1/\alpha}}{\Phi(x_c)^{1-1/\alpha}}\right)^{1/2}\psi_c(x_c). \tag{5.68}$$

This form for the flux near x_c motivates scaling

$$x = x_c + \delta_c^{16/7}\Phi(x_c)^{3/7}A^{2/7}\tilde{x}, \qquad N_c = \delta_c^{2/7}\Phi(x_c)^{10/7}A^{2/7}\tilde{N}_c, \tag{5.69}$$

in order to bring the derivative of N_c into (5.45). This equation then becomes

$$\frac{\partial \tilde{N}_c}{\partial \tilde{x}} = \frac{\tilde{N}_c^{8/11}}{\tilde{x}^{1/11}} - 1, \tag{5.70}$$

which must be solved with the matching behaviour $\tilde{N}_c \sim \tilde{x}^{1/8}$ as $\tilde{x} \to \infty$ (We have assumed here that Φ is roughly constant on the scale $x \sim \delta_c^{16/7}$). There is a unique initial value $\tilde{N}_c(x_c)$ for which the solution correctly matches with this, and it can be calculated numerically; $\tilde{N}_c(x_c) \equiv \Psi \approx 0.962$. Hence, rather than tending to zero at the head of the channel, the effective pressure has limiting value

$$N_c(x_c) = \delta_c^{2/7}\Psi\Phi(x_c)^{10/7}A(x_c)^{2/7}. \tag{5.71}$$

Provided A is sufficiently large (i.e. provided there is a sufficiently large flow into the channel), this value is large enough that $\delta^2 W_O/\delta_c^2 N_c$ can be consistently neglected in $\psi_c(x_c)$, which is therefore simply $-q_\infty(x_c)^{1-1/\alpha}$.

5.3.3 Channel extent

We have found an approximation to the influx (5.63), assuming the position of the channel is known. The question then arises whether we could choose any position for the start of the channel x_c, or whether something else selects it. If the $\delta^2 W_O/\delta_c^2 N_c$ term in (5.60) is neglected, there is apparently no constraint in choosing x_c and one could for instance choose $x_c = 0$, at the watershed.

Physically, we envisage that a channel will grow headward into the glacier by melting (or 'thermal erosion') of the ice near its head, but that this process will at some stage be limited by the supply of water from the surroundings. It is easiest to see this from the approximation for the channel pressure at its head (5.71); as the

[1] Note that this expression for the influx to the channel head comes from the solution of the diffusion equation (5.58), meaning that the porous flow upstream of the channel head is completely unaffected. Locally however, the effective pressure gradient in (5.46) causes diffusion in the ξ direction too, so the flow upstream should really be affected by the channel's presence. In appendix B we show that this does not affect the calculation of Ω.

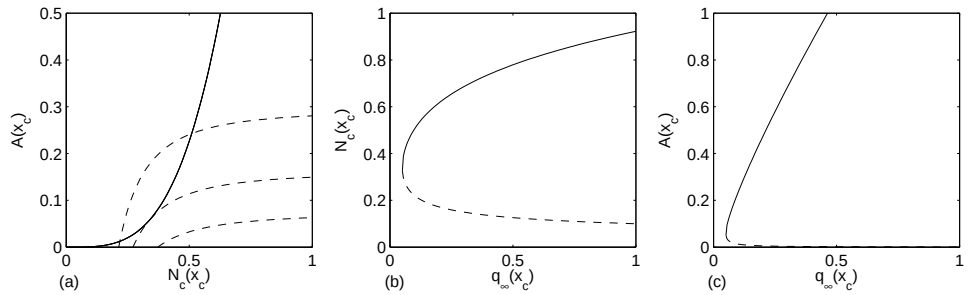

Figure 5.4: (a), Equations (5.71) (solid) and (5.72) (dashed) for 3 different values of q_∞, giving two, one or no solutions; (b), (c), solutions for $N_c(x_c)$ and $A(x_c)$.

size of the influx A gets smaller, the effective pressure gets smaller, and there will be a point at which this effective pressure becomes insufficient to draw in any water.

We therefore suggest that the head of the channel will evolve so that, in the steady state, it is located as far up-glacier as allows for a viable channel solution. By a 'viable' solution we mean one in which the pressure in the channel is sufficiently lower than the pressure in the distributed system to draw in the required influx to sustain it at that pressure. In order to determine this it is clearly necessary to include the N_c dependence in ψ_c, since otherwise the porous flow is always 'seeing' the channel as having infinite effective pressure. The expression for the influx (5.68) is therefore $Q = A(x - x_c)^{1/2}$, with

$$A(x_c) = \frac{4}{\alpha - 1}\frac{1}{\sqrt{\pi}}\left(\frac{\alpha W_O q_\infty(x_c)^{1/\alpha}}{\Phi(x_c)^{1-1/\alpha}}\right)^{1/2}\left[q_\infty(x_c)^{1-1/\alpha} - \left(\frac{\delta^2 W_O}{\delta_c^2}\right)^{\alpha-1}\frac{\Phi(x_c)^{1-1/\alpha}}{N_c(x_c)^{\alpha-1}}\right]. \tag{5.72}$$

The influx is now coupled to the channel effective pressure, which is itself coupled to the influx through (5.71). For a *given* channel head location x_c, it is therefore necessary to solve (5.71) and (5.72) simultaneously for $N_c(x_c)$ and $A(x_c)$. That only some channel locations are viable then becomes evident from the fact that there is not always a solution. The two equations are written more neatly as

$$A(x_c) = a - b/N_c(x_c)^{\alpha-1}, \qquad A(x_c) = cN(x_c)^{7/2}, \tag{5.73}$$

in which a, b and c depend on x_c through $q_\infty(x_c)$ and $\Phi(x_c)$. These two curves clearly intersect, and a solution is therefore possible, if c is small enough; see figure 5.4. After a little algebra, the condition for there to be a solution can be written

$$q_\infty(x_c) > q_*, \tag{5.74}$$

where the critical flux $q_*(x_c)$ depends on the hydraulic gradient:

$$q_*(x_c) = \left[\left(\frac{8}{7}\right)^{\frac{7}{\alpha-1}} \left(\frac{2\alpha+5}{8}\right)^{\frac{2\alpha+5}{\alpha-1}} \frac{\pi W_O^6}{\alpha \Psi^7} \frac{\delta^{14}}{\delta_c^{16}}\right]^{\alpha/(2\alpha+6)} \frac{1}{\Phi(x_c)^{(9\alpha-6)/(2\alpha+6)}}. \qquad (5.75)$$

For a given x_c, if $q_\infty(x_c)$ is smaller than $q_*(x_c)$ there is no solution, meaning that the amount of water in the distributed system is so small that, were a channel to exist there, there would be insufficient influx to keep the water pressure low enough to sustain it. If $q_\infty(x_c)$ is larger than the critical value, there are two roots, suggesting there may be two possible steady states; one with a larger influx, and larger effective pressure, than the other. In this case, we anticipate that the state with the lower influx would be unstable since, supposing the effective pressure were to increase slightly, this would cause the influx to increase too, which would in turn lead to a larger increase in the effective pressure. For a given x_c we would expect the stable state to be given by the larger of the two solutions to (5.73).

We are really interested in how far up the glacier the channel could possibly extend however, so want to know what is the smallest value of x_c for which there is a solution; this is given by the position for which $q_\infty = q_*$. It will be noticed that for most reasonable cases, q_∞ will be increasing with distance along the glacier and, since the surface slope tends to increase towards the margin, q_* will be decreasing. A channel can therefore begin at the position where the discharge first exceeds the critical level q_*.

This is an algebraically messy criterion, but it essentially says that the discharge must be sufficient that it can provide just enough turbulent heating to keep a channel open against viscous closure.

The actual growth of the channel is of course not a steady-state process, and to study it would require including the dissipative heating in (5.28). Indeed it is evident from the approximate solutions in the previous section that the flux $\mathbf{q}$ is apparently infinite near x_c in that case, so neglecting the $O(\varepsilon)$ heating term in (5.28) is wrong. The dissipative heating *is* however included in the channel equations (5.35)-(5.38), so if the disharge is sufficient to cause enough melting to counteract viscous closure this manifests itself in a viable solution for the channel. When the channel has extended as far as it can, neglecting the dissipative heating in the distributed flow is therefore not such a bad approximation, since we know already that it would not be sufficient to create and sustain a longer channel.

Linear stability of porous flow

We briefly compare the criterion above for channel formation with the linear stability of the porous sheet flow. This is governed by equations (5.25)-(5.29), which combine to give

$$\frac{\partial h}{\partial t} = 1 + \frac{\varepsilon}{\beta} h^\alpha |\mathbf{\Phi} + \delta^2 \nabla N|^2 - hN, \tag{5.76}$$

$$\nabla \cdot [h^\alpha (\mathbf{\Phi} + \delta^2 \nabla N)] = \beta r h N - \beta(r-1) - \varepsilon(r-1) h^\alpha |\mathbf{\Phi} + \delta^2 \nabla N|^2 + \gamma\omega. \tag{5.77}$$

The steady one dimensional solutions are denoted q_∞, h_∞, N_∞, as in section 5.3.2 (though note we are now including the turbulent heating), and a perturbation to the effective depth $h = h_\infty + h'$ will satisfy [2]

$$\frac{h_\infty}{h'} \frac{\partial h'}{\partial t} = -1 + (\alpha - 1) \frac{\varepsilon}{\beta} q_\infty \left(\Phi + \delta^2 \frac{\partial N_\infty}{\partial x} \right). \tag{5.79}$$

Instability will therefore occur if (ignoring the small effective pressure gradient),

$$q_\infty > \frac{\beta}{(\alpha - 1)\varepsilon} \frac{1}{\Phi}. \tag{5.80}$$

Since β is typically order 1 and ε is small, this critical flux is quite large, and the instability criterion is unlikely to be met anywhere.

This can be compared with q_* in (5.75), which is typically much smaller ($\delta \ll \delta_c$) and *is* likely to be reached; our channel forming criterion is therefore much more easily satisfied than the linear instability of the porous flow suggests. It should be noted that the critical flux q_* gives the necessary distributed flux to feed into a channel, and we have not shown that it would be sufficient to *create* a channel directly from uniform flow. Our argument is rather that a channel will *extend* up glacier (by headward melting) as far as this critical flux is exceeded; the actual initiation of the channel would occur near the margin.

[2] Note (5.79) assumes there is no change in the effective pressure; if a perturbation $N = N_\infty + N'$ is also allowed, and we assume h' and N' are both proportional to e^{iky}, we find

$$\frac{h_\infty}{h'} \frac{\partial h'}{\partial t} = \frac{1}{\beta r + \delta^2 h_\infty^{\alpha-1} k^2} \left[\varepsilon h_\infty^\alpha \left(\Phi + \delta^2 \frac{\partial N_\infty}{\partial x} \right)^2 - (\alpha - 1)\beta - (\alpha - 1)\gamma\omega \right.$$
$$\left. + (\alpha - 1) h_\infty^\alpha \frac{\partial}{\partial x} \left(\Phi + \delta^2 \frac{\partial N_\infty}{\partial x} \right) + \delta^2 h_\infty^{\alpha-1} k^2 \left((\alpha - 1) \frac{\varepsilon}{\beta} h_\infty^\alpha \left(\Phi + \delta^2 \frac{\partial N_\infty}{\partial x} \right)^2 - 1 \right) \right]. \tag{5.78}$$

For most sensible parameter values the largest growth rates are for large k, in which case the pressure perturbation is negligible and the growth rate is given by (5.79).

5.3.4 Spacing and extent of channels

Our main conclusion, which comes directly from the model setup, is that a channel can be expected to influence the surrounding distributed flow over a length scale comparable to its *compaction* length δ. The obvious implication is that adjacent channels might be expected to be spaced at a similar distance. Closer inspection of the approximate solutions in section 5.3.2, in particular of (5.58), shows that the transverse length scale over which a channel has an effect is $Y \sim \xi^{1/2}$, where ξ is the distorted length of the channel. Since $\xi \sim W_O l_c / q_\infty^{1/\alpha} \Phi^{1-1/\alpha}$ (from (5.57)) if l_c is the dimensionless length of the channel, this means the dimensionless spacing is

$$y \sim \delta \left(\frac{W_O l_c}{q_\infty^{1/\alpha} \Phi^{1-1/\alpha}} \right)^{1/2}, \tag{5.81}$$

where the variables should be taken as averages over the length of the channel. Note these are all dimensionless quantities - the terms in the brackets simply give a correction to the spacing due to the fact that their values over the length of the channel may not necessarily be the same as the values chosen for the scales in the definition of δ, (5.33); the corresponding dimensional spacing is given below in (5.82).

This suggests that channels of a given length will be more widely spaced if:

- the potential gradient is smaller,
- the rate of opening of the distributed system is faster, or
- the permeability of the distributed system is larger (causing δ^2 to be larger).

The second conclusion concerns how favourable channel transport is, and therefore how far up-glacier channels will extend. From (5.75), the following factors tend to make channels more favourable:

- the potential gradient is larger,
- the rate of opening of the distributed system is slower, or
- the permeability of the distributed system is smaller.

Thus, the same properties that make channelised drainage start further up-glacier tend to make the channels more closely spaced; both are associated with inefficiency of the distributed system. This is slightly complicated by the fact that the longer channels, other things being equal, would tend to be spaced further apart (5.81).

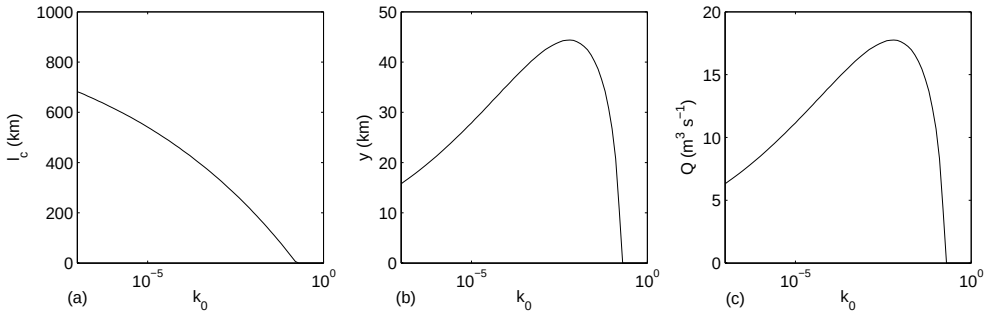

Figure 5.5: (a) Extent of channels, (b) spacing of channels, and (c) channel discharge, for varying permeability constant k_0, in an ice sheet of length $l = 1000$ km, depth $h_0 = 1$ km, with surface $h/h_0 = 1 - x^4/l^4$. The dimensionless potential gradient is therefore $\Phi = 4x^3$, and the other parameters are as given in table 5.1. The water flux is assumed to increase linearly with distance from the ice divide, up to $q_0 = 2 \times 10^{-4}$ m^2 s^{-1} at the margin. l_c is calculated from the criterion (5.74), y from (5.81), and $Q = yq_0$. Note that if the permeability is too large, channels are not favoured anywhere and the drainage all occurs through the porous system. If the permeability is small, channels are favoured, but they are spaced close together and each channel has a low flux in it.

Figure 5.5 shows how the length, spacing and discharge in channels depends on the permeability of the porous system, for an ice sheet of shape $h = 1 - x^4$, with discharge increasing linearly from the ice divide at $x = 0$. It is seen that channels extend further up the glacier as the permeability is decreased, since the porous system becomes very inefficient at transporting any water. If the permeability is small however, the width over which the channel draws in water is smaller, so the spacing is also smaller. If the permeability becomes too large, channels are never favoured and a purely distributed flow occurs to the edge of the ice sheet.

5.3.5 Ice sheet drainage

Based on the previous discussions, this section considers what form drainage takes on the scale of an ice sheet. Given a one dimensional ice sheet profile, and prescribed source of meltwater, we know what the discharge q_∞ would be if drainage were all distributed. We can use the condition (5.74) to determine where a channel can be expected to start, and then calculate the spacing from a neighbouring channel (5.81) using the average of Φ over the length of the channel. We suggest this determines the size of the 'catchment area' for that channel, and therefore solve the model equations (5.25)-(5.29) on a region with twice this width, using Neumann boundary conditions at the sides to replicate the effect of a watershed.

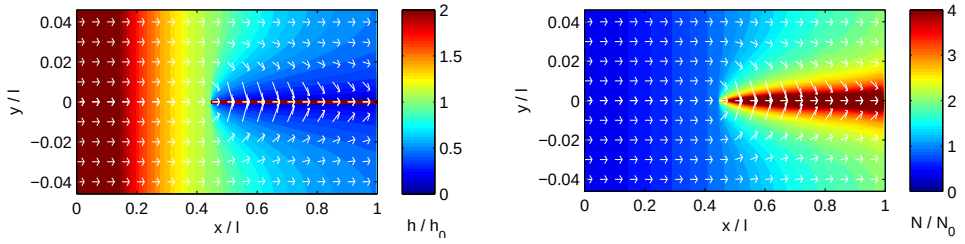

Figure 5.6: Depth of drainage system and effective pressure surrounding a channel from steady state solution of (5.25)-(5.29), (5.43), (5.44) and (5.35)-(5.38), with parameters $\delta^2 = 0.005$, $\delta_c^2 = 0.05$, $\beta = 1$, $\gamma = 0$, $r = 1.1$, $\alpha = 3$, $\varepsilon = 0$, $N_m = 0.2$. The potential gradient is $\Phi = 4x^3$, corresponding to an ice sheet with surface $h = 1 - x^4$, and the melting rate is constant $m = 1$ everywhere, with zero flux at $x = 0$. The boundary conditions in y are no flux at the watershed. The discharge in the channel is shown in figure 5.7. The partition of discharge and effective pressures is shown in figure 5.8.

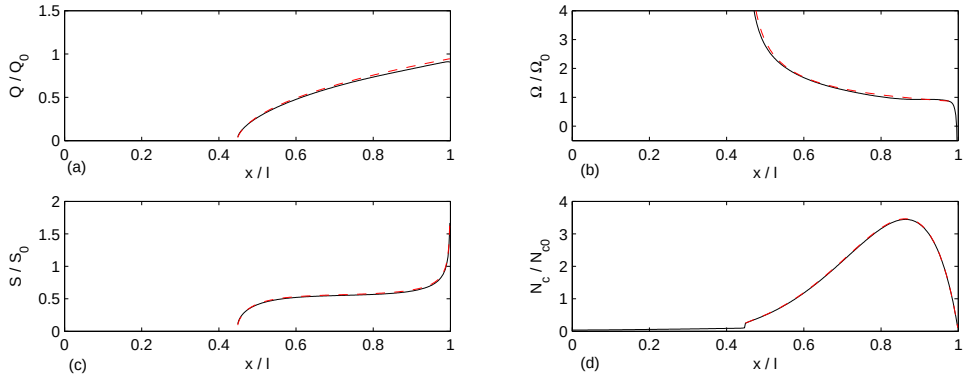

Figure 5.7: (a) Flux, (b) influx, (c) cross-sectional area and (d) effective pressure in the channel shown in figure 5.6. Dashed lines show the analytical approximations given by (5.63), (5.65) and the resulting solutions of (5.45).

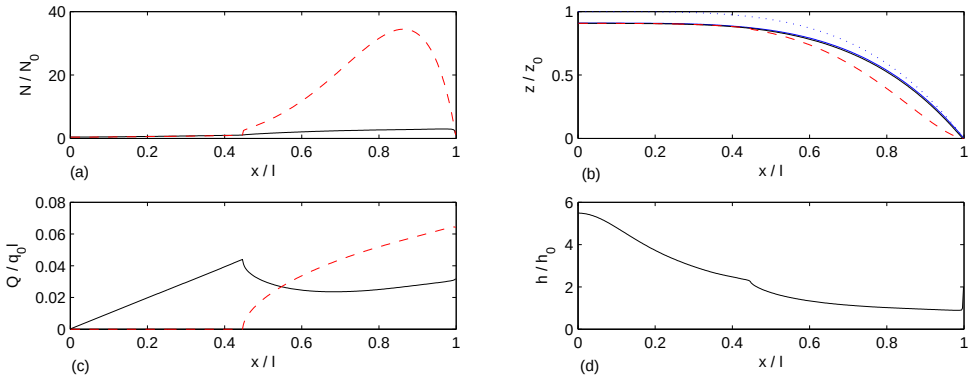

Figure 5.8: (a) Average effective pressure (solid) across the catchment basin shown in figure 5.6 and effective pressure in the channel (dashed), as a function of distance down glacier. (b) Piezometric surfaces equivalent to the effective pressure shown in (a); blue dotted is the ice surface, blue solid is the water level if $p_w = p_i$ at the bed, black solid is the average water level across the basin, and red dashed is the water level in the channel. (c) Total down-glacier discharge in basin carried by porous system (solid) and channel (dashed). (d) Average drainage system depth across basin.

Figures 5.6 and 5.7 show steady state results for an ice sheet spreading from an ice divide at $x = 0$, with ice surface $h = 1 - x^4$. This is taken as a rough approximation for a typical profile, at least in the sense that it is flat in the interior and steepens towards the margin. Geothermal heating occurs at a constant rate, and results in discharge increasing linearly with x. The position of the channel head x_c is found from (5.74) and then equations (5.25)-(5.29) are solved for the steady state together with (5.43), (5.44) and (5.35)-(5.38).

Figure 5.8 shows some of the properties of the drainage system as a function of distance down glacier, averaged over the width of the basin. The most important are the discharge carried by the channel and porous flow respectively, the effective pressure in the channel, and how this relates to the average effective pressure. Note that although the effective pressure in the channel is much larger than in the porous flow, it drops off quite quickly away from it so that the increase in the *average* effective pressure due to the presence of the channel is not perhaps as large as one might expect. The profile of effective pressure and drainage system depth *across* the basin are shown in figure 5.9.

One caveat however is that the size of the catchment area (over which this average is taken) has been chosen to be twice the compaction length (5.81); it is not clear that the catchment area should be *exactly* this size - it may be somewhat smaller, in which case the average pressure will be more influenced by the channel.

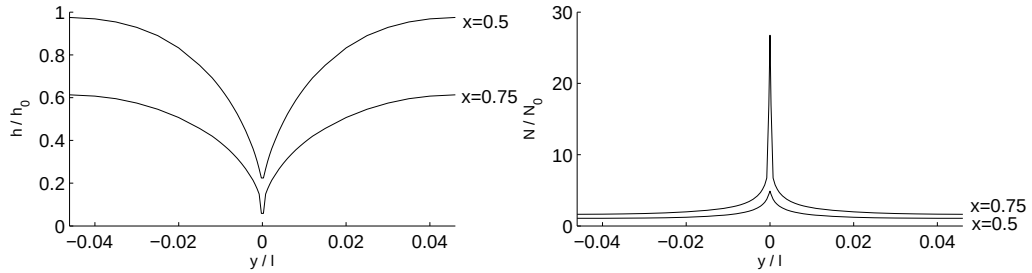

Figure 5.9: Profiles of drainage system depth and effective pressure as a function of the across-stream coordinate at two downstream locations, $x = 0.5$ and $x = 0.75$, in figure 5.6.

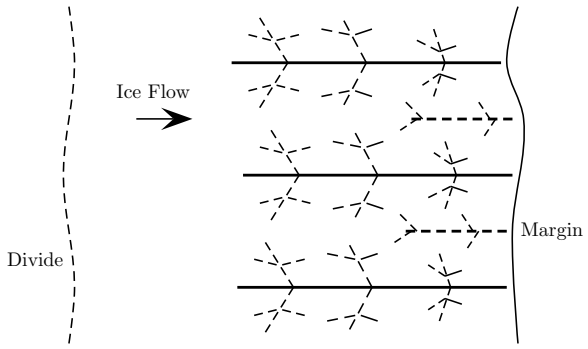

Figure 5.10: Schematic of the possible structure of a channel network, with progressively smaller branches breaking off a main artery, formed by secondary and tertiary instabilities of flow into the main channel. Near the margin, larger quantities of meltwater and a steeper potential gradient reduce the size of the catchment basins so that smaller channels open up in between. Only the larger main channels aligned with the ice flow (shown as solid lines) can be expected to exist in the same location for a long time and to form eskers.

5.3.6 Secondary instabilities

The critical condition on the water flux for channels to form, (5.74), can be generalised for water flow in the direction of an arbitrary potential gradient $\mathbf{\Phi} + \nabla N$. That is, if the flux through the distributed system q is larger than q_* (based on the local hydraulic gradient), then a channel is possible. Close to a major channel for instance, the potential gradient is aligned in towards the channel, and the resulting inflow of water will usually be sufficient to satisfy the critical condition. This suggests a secondary instability in which the flow into a main channel also evolves into channels, whose spacing will be given by a local equivalent of the compaction length (5.81). The flow into these channels may also be subject to instability, so that the resulting drainage pattern would be a branching network, similar to that shown in figure 5.10.

The spacing between main channels (5.81) also depends on the background discharge q_∞. Typically this increases quite significantly towards the margin, and the hydraulic gradient due to the surface slope also becomes much larger there; both these factors suggest a closer spacing of channels close to the margin, so it is quite likely that new shorter channels may form between two adjacent channels from further upstream. This makes some intuitive sense, and is in agreement with the observations and results of Boulton et al. (2009).

The presence of tributaries will allow for more efficient transfer of water into the major channels than has been calculated above. It also means that the larger effective pressures in the channel will be felt further out over the bed, so that the average pressure is much more influenced by the channel than is suggested in figures 5.8 and 5.9.

5.4 Eskers

5.4.1 Field observations

Eskers are long sinuous ridges of stratified sediment that are common in deglaciated regions of North America and Northern Europe (Prest et al., 1968). They have heights ranging up to about 30 m, widths on the order $10 - 100$ m, and can stretch for up to hundreds of kilometres (Flint, 1930; Brennand, 2000).

The term esker, deriving from the Gaelic *eiscir* meaning ridge, has been used to describe many different such landforms, some of which comprise a single well-defined ridge and others that are multi-crested and braided (Warren and Ashley, 1994; Huddart and Bennett, 1997; Brennand, 2000). They are all generally thought to be formed as a result of sediment deposition in subglacial and proglacial (near the margin) meltwater streams; large, elongate eskers have been interpreted as casts of major subglacial channels, and therefore represent a 'fossilised' image of the drainage system (Banerjee and McDonald, 1990; Shreve, 1985; Clark and Walder, 1994).

There has been some debate over how to interpret such fossils however, since it is not clear whether they were deposited widely at a similar time, or whether it was a more gradual process as the ice sheet retreated. There is some suggestion they could form almost instantaneously during large floods (Shaw, 1994), but most are thought to have formed in what is described as a 'time-transgressive' fashion, meaning that they build up slowly over time with most deposition occurring near to the ice margin (Brennand, 2000). In this case the observed pattern of eskers is not quite a 'snapshot' of the drainage system, but rather an evolution in space and time.

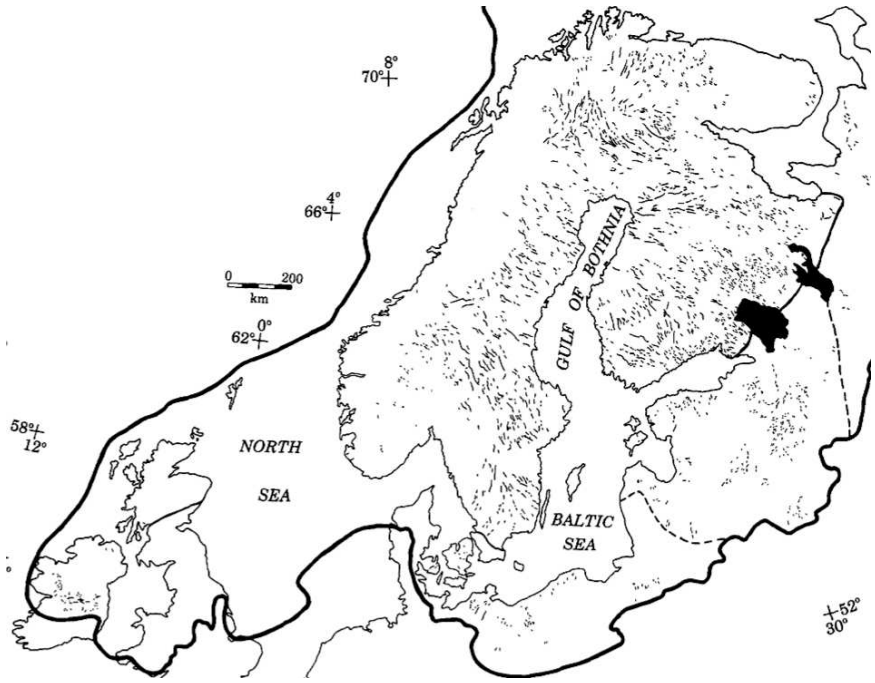

Figure 5.11: Distribution of eskers deposited beneath the Fennoscandian ice sheet, with margin shown by the thick solid line. Reproduced from Clark and Walder (1994).

The size of eskers is typically larger than would be feasible for the cross-section of a channel, and suggests they form through a gradual build up of sediment on the channel floor, with the overlying channel moving upwards into the ice. The esker building process would stop either when the ice retreats or when the sediment builds up so much that the water favours another route and the channel shifts to a different location.

Shreve (1985) has carefully mapped the positions of eskers in Maine and compared them with the expected flow paths for meltwater based on reconstructions of the retreating ice sheet. This provides quite convincing evidence that they form in subglacial tunnels, and it is further suggested that the local size and sedimentology of the esker reflects the hydraulic potential gradient; where the gradient was steeper the ridge is narrow and sharp crested, where it was shallower it is wider and may be multi-crested.

Many eskers do not have such a neat well-defined ridge structure however, with significant braiding and widenings. Segmented ridges, interrupted by 'beads', are thought to indicate sequential (perhaps annual) deposition in outwash fans or deltas near the ice sheet margin as it retreats (most esker-forming tunnels are thought to flow into a proglacial lake) (Warren and Ashley, 1994; Brennand, 2000). Other features

often referred to as eskers are thought to form parallel to former ice margins (rather than perpendicular as would be the case for deposition in a subglacial tunnel); the distinction between these and other forms of terminal moraine is somewhat loose (Warren and Ashley, 1994; Owen, 1997). They may form through deposition and erosion in proglacial lakes, supraglacial meltwater channels, and outwash fans over stagnating ice and ice-cored moraines (Huddart and Bennett, 1997; Brennand, 2000; Russell et al., 2001).

5.4.2 Model implications

The eskers we are concerned with are those that form perpendicular to the former ice margin, and based on the above observations we assume that these represent the casts of the subglacial drainage channels.

The view of time-transgressive formation outlined above requires esker-forming channels to be stable over many years, perhaps centuries, of ice sheet retreat, and suggests that only the largest dominant arteries in a drainage network will produce them. Channels that close down over the winter due to the lack of surface-derived meltwater are unlikely to keep reopening in the same location, so it is usually thought that esker-forming channels must be open year-round. The actual erosion and deposition may occur predominantly during periods of higher discharge (Boulton et al., 2009), but the *location* of the stable channels will be determined by the drainage system required for the lower year-round discharge.

It also seems unlikely that channels misaligned with the ice flow could have produced significant eskers because as the ice slides it would alter the course of such channels and erode most sediment deposits.

These considerations suggest that only the major channels aligned in the direction of the ice flow are those likely to produce eskers (see figure 5.10) and, since the position of these channels varies little, the time-transgressive deposition reflects a stable drainage network that existed for a long time. In particular, the spacing between eskers should follow from the spacing between adjacent major channels (5.81), which is written dimensionally as

$$y \approx \left(\frac{\eta_i W_O k_0^{1/\alpha} l}{\eta_w^{1/\alpha} q_0^{1/\alpha} \Phi^{1-1/\alpha}} \right)^{1/2} . \tag{5.82}$$

This is expected to be around 10 km, which is in rough agreement with the observed $8 - 25$ km spacing (Boulton et al., 2009).

The conclusions in section 5.3.4 concerning whether channels exist and what their spacing will be follow directly over to the existence and spacing of eskers; this means eskers are more likely, and will be more closely spaced, where

- the potential gradient is higher,
- the distributed system is less efficient,
- the meltwater discharge is larger.

These implications, and our reasons for them, are very similar to those recently put forward by Boulton et al. (2007a,b, 2009). They suggested that drainage occurs by a combination of groundwater flow and esker-forming channels, and that the spacing adjusts to ensure that the water pressure between adjacent channels is less than the overburden ice pressure. If the spacing between two channels were too large, the pressure at the 'interfluve' between them would rise to the overburden pressure and, they suggest, local uplift of the ice would create a new channel. Channelised drainage would therefore begin when the down-glacier water flux becomes too large for the groundwater system to accommodate without becoming over-pressurised.

Boulton et al. suggest the channel spacing increases with the transmissivity of the groundwater aquifer, and decreases with increasing discharge in the down-glacier direction. This agrees with our own results, the transmissivity being identifiable with the permeability of the more general distributed flow.

The main difference with our own work is the criteria for forming channels; whereas in Boulton et al.'s work a channel forms where the effective pressure reaches zero, we instead require that the discharge reaches a critical level (5.75) at which the heat generated by turbulent water flow is sufficient to keep a channel open against the larger effective pressure and ice closure rate.

5.5 Summary

We have presented a very general model for distributed drainage as an effective porous medium, making the analogy with the compacting partially molten mantle in chapter 2. We have included geothermal and frictional heating, and viscous closure of the ice, as processes that influence the size of the drainage system, but it is hopefully clear that other processes could be parameterised and included in a straightforward way.

Channels are modelled as line sinks within the distributed system, whose strength depends upon the water pressure; unlike in chapter 3 when we knew in advance

that the pressure would be nearly magmastatic, it must be calculated using the Röthlisberger equations. There is a compaction length analogous to that in the mantle, estimated to be around 10 km, and we suggest that adjacent channels will be spaced at around this distance from one another; this is a similar, though slightly different, criterion from that given by Boulton et al. (2009). The spacing is consistent with the observed patterns of eskers.

The permeability of the distributed flow close to a channel is decreased due to large effective pressures squeezing the pore space, so steep pressure gradients are required to draw water in. The average pressure over the width of the drainage basin may be only mildly affected by the presence of the channel, and this may have important implications for sliding laws that incorporate a dependence on effective pressure. Secondary instabilities of the lateral flow into a channel may however spread the channel's influence over a larger area.

Our model bears some similarity to the work of Rempel (2008, 2009), who studies seepage flows through a layer of till in the vicinity of a channel, though he includes rather different effects, focussing on the possibility for a partially frozen fringe within the till. Melting and freezing of the fringe are related to temperature and effective pressure and when the effective pressure near a channel is large this can produce a thick frozen fringe that acts to reduce the permeability there. Thus, for a different reason, it is again found that steep pressure gradients are needed close to a channel to draw water into it. If bridging stresses were included, they would presumably also have a similar effect.

We have suggested that channels that form initially close to the margin will grow headward into the glacier, and that in the steady state they should begin where the background discharge in the distributed system reaches a critical value q_* (5.75). This suggests that channel flow is more favourable when the surface slope is larger and when the distributed system is less permeable.

It should be pointed out that this work has looked only at a steady state drainage system and ignored the potentially large variations that occur during summer melting. The formation of eskers suggests that at least some of the drainage system retains its structure over many years, and that is the part we have here been concerned with, but it is likely that other parts are constantly evolving.

The model posed here could be used to examine non-steady states, but there are some issues over how to deal with the changing length of a channel. Unlike in chapter 3 there is no upper bound to the 'porosity' here, so, as the depth of the drainage system grows near the head of the channel (due to the turbulent heating in (5.28)),

it is not clear when to switch from the distributed to channel equations. Since ε is also small, it would require very high resolution close to the head of the channel to accurately capture the unstable growth numerically, and we have not attempted to perform such time-dependent calculations.

Chapter 6

Seasonal waves on glaciers

6.1 Introduction

Waves on glaciers have been observed for over 100 years. The theory of *kinematic* waves has been well developed by Weertman (1958) and Nye (1960), and can account for observed bulges in the surface of the ice that travel downglacier at around five times the ice velocity.

An altogether different type of wave, however, is a perturbation in the ice velocity itself. Such waves, termed *Druckwellen*, were apparently well known on the Hintereisferner at the begninning of the last century, travelling between 20 and 150 times as fast as the ice itself (Blümcke and Finsterwalder, 1905; Deeley and Parr, 1914). This type of wave on the Hintereisferner was also documented in the 1950s (Schimpp, 1958; Finsterwalder, 1961), and perhaps the best example is seen on Nisqually glacier, in the detailed velocity measurements made by Hodge (1974). These waves appear to be associated with annual speed-up of the glacier and have therefore been described as *seasonal waves*. Unfortunately, more recent and widespread observations of them are lacking and, perhaps because of this, they have received little attention. This chapter will explore a simple explanation for these waves as being due to kinematic waves in the subglacial drainage system.

Nisqually glacier

Our main aim is to reproduce some of the qualitative features of Hodge's measurments, which are summarized in figures 6.1 and 6.2. Nisqually glacier, on Mount Rainier in Washington, is a temperate valley glacier about 5 km long, and the surface velocity of the 3 km ablation area was measured for a two year period. There were large increases in the velocity during the summer at all points in the ablation area. The timing of the peak velocity during the summer and the minimum velocity during

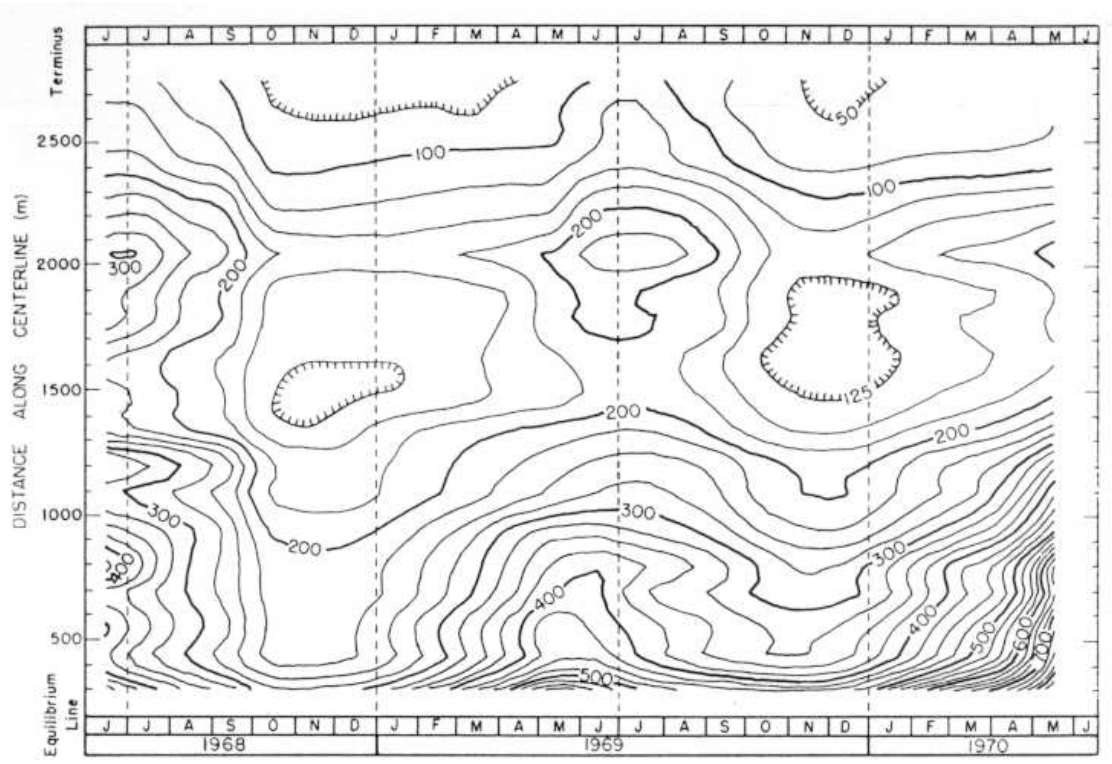

Figure 6.1: Measured surface speed of Nisqually Glacier, Mt. Rainier, Washington, as a function of distance and time. Contour interval is 25 mm d^{-1}. Reproduced from Hodge (1974).

the winter is about 1 month later towards the terminus than near the equilibrium line, and this progressive shift represents the seasonal wave that Hodge estimates to be travelling at around 20 km y^{-1}. There is no associated surface elevation change, and the presumption is that the large seasonal velocity variations, and consequently the seasonal wave, are due to changes in the slip of the glacier at its bed.

Variations in sliding and hydrology

Changes in the slip of a glacier due to hydraulic forcing are well known, both on temperate (with unfrozen bed) and polythermal (with partly frozen bed) glaciers (Brzozowski and Hooke, 1981; Hooke et al., 83; Jansson, 1996; Copland et al., 2003; Nuttall and Hodgkins, 2005). However, the velocity changes occurring during the seasonal wave in figure 6.1 appear to be distinct from so-called 'spring events' (Meier et al., 1994; Willis, 1995; Harper et al., 2002; Anderson et al., 2004; MacGregor et al., 2005) or 'mini-surges' (Kamb and Engelhardt, 1987), when a period of fast sliding accompanied by high borehole water pressures occurs during the spring, and after

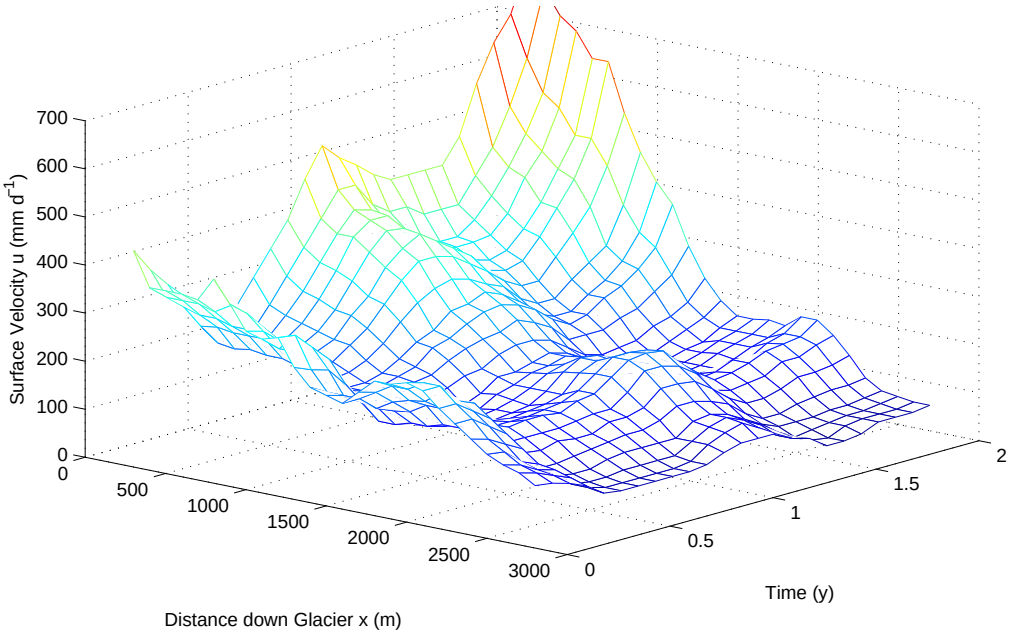

Figure 6.2: A surface representation of figure 6.1, with surface velocity as a function of distance and time.

which sliding velocities reduce to a more steady summer value (Iken and Bindschadler, 1986; Mair et al., 2001; Willis et al., 2003). These are often correlated with 'hydraulic events' associated with a transition in drainage system structure. They have been observed to travel rapidly either up or down glacier. Unlike these, however, the seasonal wave we consider is a longer-lived feature involving the passage of a mid-season maximum.

A variety of field experiments have been used to infer that beneath many temperate and polythermal glaciers, there is a constantly evolving drainage system (Hooke, 1989; Hock and Hooke, 1993; Hubbard and Nienow, 1997; Gordon et al., 1998; Nienow et al., 1998). The general picture, if it is possible to draw one amongst the peculiarities of every glacier, is that during the winter when there is little if any meltwater reaching the bed, drainage occurs through an inefficient distributed system. As meltwater starts to penetrate to the bed during the spring, the water pressure builds up and in many cases the system is unable to accommodate the additional water, reorganising itself into a more efficient channelized system. As water quantities drop during the autumn, the channelized system shuts down, or partially shuts down, and there is a return to slow distributed flow.

In trying to understand how the flow of meltwater can produce the seasonal wave in figure 6.1 we would also like to relate this to these other types of behaviour - both

hydrological and dynamical - that are observed on other glaciers. Whilst it is pretty clear that water pressures influence sliding velocities, we would like to use these ideas to understand and predict the temporal and spatial changes that one might expect to see.

6.2 Glacier waves

6.2.1 Kinematic waves

The simplest model for one-dimensional ice flow was outlined in chapter 4; the basal shear stress is given approximately by (4.7), there is a sliding law of the form (4.12), the continuity equation is (4.3) and the ice flux (4.8). Since seasonal variations in velocity are for the most part thought to represent changes in sliding, we will treat the case in which this dominates internal deformation.

For a valley glacier the surface slope is often roughly constant, so by scaling the shear stress and sliding velocity according to

$$\tau_b \sim -\rho_i g H \frac{\partial h}{\partial x}, \qquad u_b \sim F(\tau_b, N), \tag{6.1}$$

an approximate dimensionless model is

$$\frac{\partial H}{\partial t} + \frac{\partial (u_b H)}{\partial x} = a, \tag{6.2}$$

$$u_b = F(\tau_b, N), \tag{6.3}$$

$$\tau_b = H. \tag{6.4}$$

For a fixed N this is a non-linear wave equation for H; if a is independent of time there is a steady state, and perturbations to this state will travel with characteristic speed

$$v = F(H, N) + F_{\tau_b}(H, N)H. \tag{6.5}$$

If the sliding law is $u_b \sim \tau_b^m$, for instance, this gives $v = (m+1)u_s$, where $u_s = u_b$ is the surface speed. This is the essence of the standard kinematic wave theory (Lighthill and Whitham, 1955; Nye, 1960; Fowler, 1982; Weertman and Birchfield, 1983), and internal deformation of the ice can also be easily included. Waves are expected to move at $3-5$ times the surface speed, and bulges moving at such speeds have been observed (Lliboutry, 1958; Weertman, 1958; Finsterwalder, 1959). According to (6.2)-(6.3) shocks will naturally develop as the wave propagates, and the effects of the changing surface slope or longitudinal stresses on τ_b (4.9) must be included to determine the shock structure (Nye, 1960; Fowler and Larson, 1980; Fowler, 1982).

6.2.2 Seasonal waves

The kinematic theory gives wave speeds much too low to explain seasonal waves. Fowler (1982) offered the only previous explanation for these by suggesting an alternative sliding law. This was based on early observations that cavitation at the bed can significantly increase sliding velocities, suggesting a form for F that increases slowly up to a critical velocity u_c, but much faster when this velocity is exceeded and cavitation occurs. Fowler explores the effects of such a sliding law in detail, but the explanation for the seasonal wave is really no different from the kinematic theory above; since F is a steep function of H the depth is roughly constant H_c, but the small perturbations to this give rise to large variations in velocity so that (6.2) becomes approximately

$$\frac{\partial u_b}{\partial t} + F_{\tau_b}(H_c, N)H_c\frac{\partial u_b}{\partial x} = F_{\tau_b}(H_c, N)a. \tag{6.6}$$

The wave speed is still (6.5) in the limit of large F_{τ_b}, so to explain seasonal waves this would require the form of F to be hugely different from the usual $F \sim \tau_b^m$. Such an explanation would also require an accompanying wave in the depth, albeit of small amplitude, that has not been observed.

6.2.3 Drainage system waves

The alternative explanation that we explore below is that a seasonal wave has little to do with the continuity equation (6.2), and is rather driven by a kinematic wave in the drainage system. Over a seasonal timescale (6.2) requires $H \approx$ constant, so the variations in velocity come entirely from variations in N in the sliding law (6.3).

As reviewed in chapter 4, N depends on the nature of the drainage system and the amount of water present. In the simplest case, when the effective pressure gradients are dominated by the driving gravitational potential gradient, N is just a local function of the discharge Q,

$$N = N(Q). \tag{6.7}$$

Variations in N follow from variations in Q, which satisfy a kinematic wave equation of the form

$$\frac{\partial S}{\partial t} + \frac{\partial Q}{\partial x} = M, \tag{6.8}$$

where $S = S(Q)$ is the cross-sectional area of the drainage system and $M(x, t)$ is the meltwater source (from basal melting and, more importantly in a temperate glacier, from surface melting).

Variations in the supply of meltwater over the course of the year will cause kinematic waves in the discharge Q that travel down glacier at speed $1/S'(Q)$, i.e. at the average water speed in the drainage system. For example, if $S'(Q) = \alpha$ is taken as constant, $Q = 0$ at $x = 0$, and M is sinusoidal;

$$M(x,t) = M_0(1 + \cos\omega t), \tag{6.9}$$

then

$$Q = M_0 x + \frac{2M_0}{\alpha\omega}\cos\omega\left(t - \frac{\alpha}{2}x\right)\sin\omega\left(\frac{\alpha}{2}x\right). \tag{6.10}$$

There is a corresponding wave in the effective pressure (6.7), and consequently in the sliding velocity (6.3). It is clear that the maxima and minima in the discharge, and therefore the ice velocity, propagate down glacier at speed $2/\alpha$.

Distributed drainage

We make use of the relationships (4.33) and (4.34) for linked cavities, but since all we are really interested in is the form of the relationships $S(Q)$ and $N(Q)$, these can be taken as representing any other form of distributed system. In order to keep the ideas as simple as possible we make the (large) simplification of ignoring the effective pressure gradient in the hydraulic potential. Adopting the sliding law (4.14), this gives the relationships

$$S = \frac{C_1}{C_2\Phi^{1/2}}Q, \tag{6.11}$$

$$N = \left(WC_2\Phi^{1/2}c\tau_b^p\right)^{1/(n+q)}Q^{-1/(n+q)}, \tag{6.12}$$

in which W is the glacier width, Φ is the down-glacier gravitational potential gradient, and C_1 and C_2 are constants depending on roughness.

Clearly $S'(Q) > 0$, so waves in the discharge travel downstream, and since $N'(Q) < 0$, peaks in the discharge correspond to minima of the effective pressure and peaks in the sliding velocity. The largest ice velocities should therefore be in the summer when there is the largest discharge. The velocity variations resulting from a sinusoidal meltwater input are shown in figure 6.3.

Channelised drainage

If drainage all occurs through a Röthlisberger channel, the relationships between cross-sectional area, discharge and pressure come from (4.24) and (4.30):

$$S = \left(\frac{F}{\Phi}\right)^{3/8}Q^{3/4}, \tag{6.13}$$

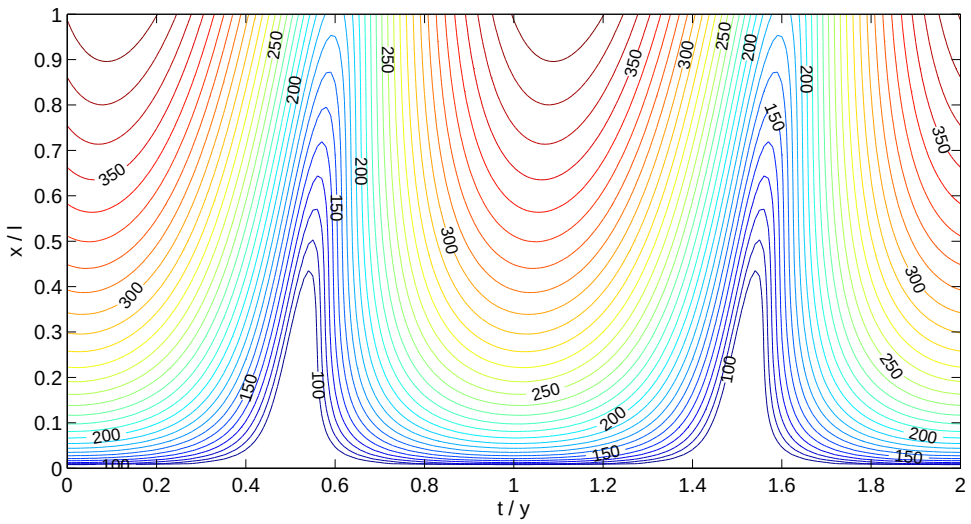

Figure 6.3: Sliding velocity variations driven by changes in water pressure in a linked cavity system, as given by (6.8), (6.11), (6.12) and (4.14), with $C_1/C_2\Phi^{1/2} = 0.2$ y. Contour interval is 10 mm d^{-1}.

$$N = \left(\frac{\Phi^{11/8}}{\rho_i L K F^{3/8}}\right)^{1/n} Q^{1/4n}. \tag{6.14}$$

$S'(Q)$ is again positive, but since $N'(Q)$ is now positive, maxima in the discharge correspond to minima in the ice velocity. The peak sliding velocities should therefore occur in the winter, which is certainly not what is observed in figure 6.1.

Another issue with channelised drainage, already discussed in chapter 5, is that the regions of the bed away from the channel must still accommodate meltwater, and since the channel flow is so efficient, its cross-sectional area is probably small compared to the area of the surrounding cavities. (6.13) may not be a very appropriate choice for S in this case and it may be better to take S as the area of the cavities (4.33), as determined by the effective pressure (6.14);

$$S = W C_1 c \tau_b^p \left(\frac{\Phi^{11/8}}{\rho_i L K F^{3/8}}\right)^{-(n+q)/n} Q^{-(n+q)/4n}. \tag{6.15}$$

$S'(Q)$ would then be negative, and waves can be expected to propagate upstream. The velocity variations resulting from a sinusoidal meltwater input in this case are shown in figure 6.4.

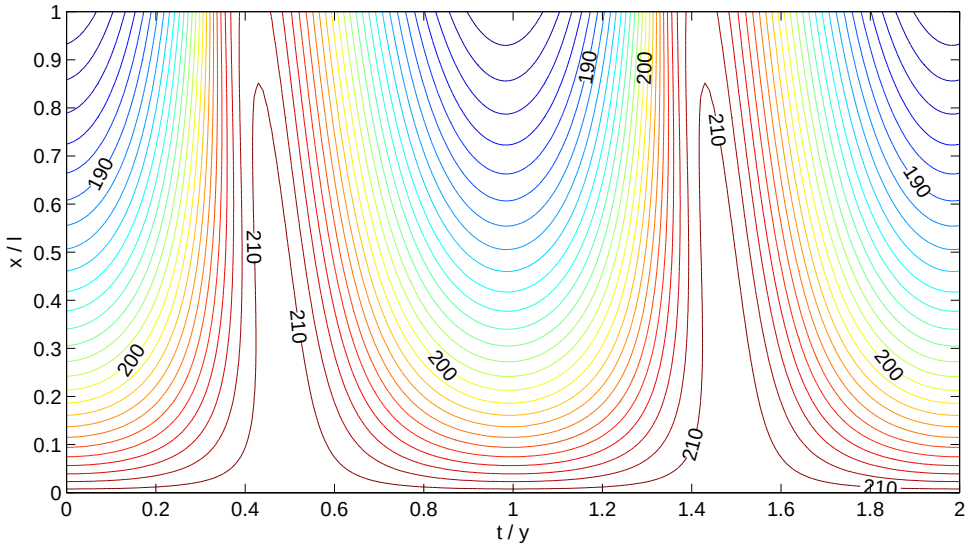

Figure 6.4: Sliding velocity variations driven by changes in water pressure in a channel system, as given by (6.8), (6.14), (6.15) and (4.14). Contour interval is 1 mm d^{-1}.

6.3 Coupled drainage

6.3.1 Model

Comparing figures 6.3 and 6.4 with figure 6.1 shows that different aspects of the two drainage systems give apparently realistic behaviour. The distributed system produces a downstream travelling wave with a peak in the summer, but has velocity increasing with distance downglacier; the channelised system produces an upstream travelling wave with a peak in the winter, but has velocity decreasing with distance downglacier, as in figure 6.1.

This, together with the substantial field evidence that drainage system transitions are important, motivates considering a coupled model in which we treat the two systems as operating in parallel. The situation envisaged is of a largely cavity covered bed interstected by a branching network of channels. Water will be assumed to reach the bed distributed across the whole glacier; it moves slowly downglacier through the linked cavities but preferentially moves into the channel system if the water pressure there is lower.

Unlike in chapter 5, we describe this all in a lumped fashion, using only the total discharge in the cavities $Q(x,t)$ and the channels $Q_c(x,t)$ as variables. Transfer between the two systems is parameterised as a function of the average effective pressures $N(x,t)$ and $N_c(x,t)$, and is denoted $L(N,N_C)$. Chapter 5 has given some insights into

how this leakage could be chosen, but the simplest assumption is that it is directly proportional to the pressure difference;

$$L = k(N_c - N). \tag{6.16}$$

The constant k describes how easily water moves out of the cavity system and can be roughly estimated from the rate of flow down a potential gradient through a cavity system, with the width of the glacier W used as a suitable length scale. For a gravitational slope Φ_0, the total discharge would be $Q = kW^2\Phi_0$, and if Q can be measured or inferred this can be rearranged to estimate k; taking $Q \sim 1$ m^3 s^{-1}, $W = 1$ km and $\Phi_0 = 10^3$ Pa m^{-1} gives $k = 10^{-9}$ m^2 s^{-1} Pa^{-1}.

We now have two continuity equations,

$$\frac{\partial S}{\partial t} + \frac{\partial Q}{\partial x} = M - L(N, N_c), \tag{6.17}$$

$$\frac{\partial S_c}{\partial t} + \frac{\partial Q_c}{\partial x} = M_c + L(N, N_c), \tag{6.18}$$

for the distributed and channelised systems respectively. These are complemented by the algebraic expressions (6.11), (6.12), (6.13) and (6.14) for the cross-sectional areas and effective pressures.

Separate meltwater inputs have been included to the two systems, but in most of what follows we will take $M_c = 0$ and assume that all meltwater reaches the bed in the distributed system, as in chapter 5. The channels at the bed are considered as very localised structures so that the vast majority of the bed area is covered by cavities and it is therefore natural to suppose that the majority of the melt might enter this system (Raymond et al., 1995). It is also common that water routed from the glacier surface through crevasses and moulins may collect together englacially so that by the time it reaches the bed it is already in an efficient conduit which feeds straight into the subglacial network. Such water routing can easily be catered for by including non-zero M_c, but turns out to have relatively little effect on our results.

The ice velocity is given by the sliding law (4.14) in terms of the effective pressure N:

$$u_b = \frac{c\tau_b^p}{N^q}. \tag{6.19}$$

The choice to use the cavity pressure rather than the channel pressure is due to the fact that cavities cover the majority of the bed, and indeed it is the presence of the cavities that influences the sliding rate. We saw in chapter 5 that the *average* effective pressure may be little affected by the presence of a channel.

6.3.2 Non-dimensionalisation

The basic situation we consider is that of a model parallel slab glacier, with uniform depth and surface slope. The basal shear stress τ_b and gravitational potential gradient Φ can then be taken as constant. This simplification is made to elucidate the ideas without the extra complications of spatial and temporal changes in shear stress. Although idealistic, it may in fact be a reasonable approximation to make for the case of Nisqually glacier, which is about as uniform as one could hope for a real glacier, and where in any case there is no obvious correlation between sliding velocity and shear stress (Meier, 1968; Hodge, 1974).

The equations are made non-dimensional in the standard way. Based on a length scale l, a potential gradient Φ_0, shear stress τ_0, and a melt rate M_0 (externally prescribed by the glacier's climate and topography), we choose scales

$$Q_0 = Q_{c0} = M_0 l, \tag{6.20}$$

$$S_0 = \frac{C_1}{C_2 \Phi_0^{1/2}} Q_0, \tag{6.21}$$

$$S_{c0} = \left(\frac{F}{\Phi_0} \right)^{3/8} Q_0^{3/4}, \tag{6.22}$$

$$N_0 = \left(W C_2 \Phi_0^{1/2} k \tau_0^p \right)^{1/(n+q)} Q_0^{-1/(n+q)}, \tag{6.23}$$

$$N_{c0} = \left(\frac{\Phi_0^{11/8}}{\rho_i L K F^{3/8}} \right)^{1/n} Q_0^{1/4n}, \tag{6.24}$$

and take the timescale $t_0 = 1$ y.

The dimensionless equations are then

$$\alpha \frac{\partial S}{\partial t} + \frac{\partial Q}{\partial x} = M - \kappa(N_c - \gamma N), \tag{6.25}$$

$$\alpha_c \frac{\partial S_c}{\partial t} + \frac{\partial Q_c}{\partial x} = M_c + \kappa(N_c - \gamma N), \tag{6.26}$$

$$S = Q, \qquad S_c = Q_c^{3/4}, \tag{6.27}$$

$$N = Q^{-1/(n+q)}, \qquad N_c = Q_c^{1/4n}, \tag{6.28}$$

and the four dimensionless parameters are[1]

$$\alpha = \frac{l}{t_0} \frac{C_1}{C_2 \Phi_0^{1/2}}, \tag{6.29}$$

[1]Note there is a typographical error in Hewitt and Fowler (2008b), where l in these definitions appears as 1. If comparing with that work note also that the notation used here is slightly different; to be more consistent with the rest of this thesis, the subscript c refers to channels, while no subscript refers to cavities.

Constant	Value	Constant	Value
n	3	τ_0	10^5 Pa
p	4	Φ_0	10^3 Pa m^{-1}
q	1	F	650 kg m$^{-8/3}$
c	2×10^{-20} m s^{-1} Pa^{-3}	ρ_w	1000 kg m^{-3}
C_1	5×10^{22} Pa^3 s	ρ_i	900 kg m^{-3}
C_2	3×10^{18} Pa$^{5/2}$ m$^{3/2}$	L	3×10^5 J kg^{-1}
W	1 km	K	3×10^{-24} Pa^{-3} s^{-1}
A	10^{-23} Pa^{-3} s^{-1}	k	10^{-9} m^2 s^{-1} Pa^{-1}

Table 6.1: Values of constants used in chapter 6.

$$\alpha_c = \frac{l}{t_0}\left(\frac{F}{\Phi_0}\right)^{3/8} Q_0^{-1/4}, \tag{6.30}$$

$$\gamma = \frac{N_0}{N_{c0}}. \tag{6.31}$$

$$\kappa = \frac{kN_{c0}}{M_0}, \tag{6.32}$$

These represent, respectively, the advective timescales in years for distributed and channel drainage, the ratio of typical effective pressures in a distributed system to those in a channel system, and a 'connectedness' parameter which describes how easily water transfers between them (cf. Flowers et al., 2004).

The various constants in (6.11), (6.12), (6.13) and (6.14) depend on a number of uncertain parameters, particularly the Manning's roughness coefficient, the roughness of the bed, and the tortuosity and connectedness of flow paths in the linked cavities. The suitable values given in table 6.1 may be considered as representative of reasonable choices for these parameters, but in fact it may be more appropriate to consider the resulting non-dimensional parameters α, α_c, γ and κ as the adjustable ones since their physical meaning is also clear.

Using the values in table 6.1, and $l = 10$ km, $M_0 = 10^{-4}$ m^2 s^{-1}, gives

$$Q_0 = 1 \text{ m}^3 \text{ s}^{-1}, \tag{6.33}$$

$$S_0 = 500 \text{ m}^2, \tag{6.34}$$

$$S_{c0} = 0.9 \text{ m}^2, \tag{6.35}$$

$$N_0 = 0.6 \text{ MPa}, \tag{6.36}$$

$$N_{c0} = 1 \text{ MPa}, \tag{6.37}$$

and

$$\alpha = 0.2, \tag{6.38}$$

$$\alpha_c = 3 \times 10^{-4}, \tag{6.39}$$

$$\gamma = 0.6, \tag{6.40}$$

$$\kappa = 10. \tag{6.41}$$

A comment on the relevant timescales is in order. α_c gives the timescale for transport in channels in years and is, as expected, small. However when considering transient water flow in a channel the limiting timescale is likely to be the time for the channel area to adjust (as in (4.25)), which is somewhat longer than the advective timescale. Transient response of a channel is therefore very different to the steady state behaviour (Clarke, 2003). We will ignore the diurnal changes in meltwater input and consider only the longer term average which, we assume, varies sufficiently slowly that the channel can be considered to be in steady state. However, the extra hidden timescale for adjustment of the channel means we should be wary of the importance attached to the value of α_c.

6.3.3 Boundary conditions

We would like to solve (6.25)-(6.28) on $0 < x < 1$, $x = 0$ being the glacier head and $x = 1$ being the terminus. The natural boundary condition to apply is $Q = Q_c = 0$ at $x = 0$, but the corresponding pressures according to (6.28) are unrealistic. In fact these relationships are incorrect as Q goes to zero, since as this happens the effective pressure gradients become large and the singular approximations we make in ignoring them break down.

To see this, note from (4.34) and (4.30) that the $N - Q$ relationships (6.28) are more accurately

$$N = \frac{1}{Q^{1/(n+q)}} \left(1 + \delta^2 \frac{\partial N}{\partial x}\right)^{1/2(n+q)}, \tag{6.42}$$

$$N_c = Q_c^{1/4n} \left(1 + \delta_c^2 \frac{\partial N_c}{\partial x}\right)^{11/8n}, \tag{6.43}$$

where $\delta^2 = N_0/\Phi_0 l$ and $\delta_c^2 = N_{c0}/\Phi_0 l$ are the ratios of effective pressures to gravitational potential. By rescaling the equations it is straightforward to show that if Q or Q_c go to zero linearly as $x \to 0$, the limiting values of N or N_c are

$$N = \delta^{-2/(n+q+1)} Q'^{-1/(n+q+1)} \Psi, \qquad N_c = \delta_c^{2/(4n-1)} Q_c'^{1/(4n-1)} \Psi_c, \tag{6.44}$$

in which Ψ and Ψ_c are the initial values of the solutions to

$$1 + \frac{\partial \hat{N}}{\partial \hat{x}} = \hat{N}^{2(n+q)} \hat{x}^2, \qquad 1 + \frac{\partial \hat{N}_c}{\partial \hat{x}} = \frac{\hat{N}_c^{8n/11}}{\hat{x}^{2/11}}, \tag{6.45}$$

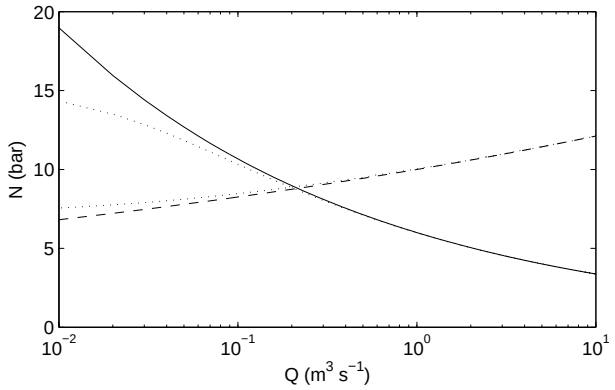

Figure 6.5: Effective pressure in cavities (solid) and channels (dashed), as given by (6.12) and (6.14). The dotted lines show an example of the modification to these approximations when the flux Q is small and the effective pressure gradients are important; these are solutions of (6.45).

respectively, which match with $\hat{N} \sim \hat{x}^{-1/(n+q)}$ and $\hat{N}_c \sim \hat{x}^{1/4n}$ as $\hat{x} \to \infty$. Ψ and Ψ_c must be found numerically, and when $n = 3$, $q = 1$, they are $\Psi \approx 1.45$, $\Psi_c \approx 0.86$.

It is typically found however that even the initial values (6.44) have $N_c < N$, so that the water pressure in a channel is higher than in the cavities. Thus water would flow out of a channel; this is indicative of the fact that channels will not tend to exist when the discharge is too small (see chapter 5). There are two methods of dealing with this: in section 6.4.4 we allow a region of only distributed drainage in the upper part of the glacier, with a transition downstream to the coupled system; for the moment however, we simply restrict our attention to a region sufficiently far down the glacier that both drainage systems operate. For this to be the case the water pressure in the channel must be lower than in the cavities (Clarke, 1996); the simplest criterion is that $N_c > N$ for the same discharge Q, which requires the critical dimensionless discharge (see figure 6.5)

$$Q_E = \gamma^{4n(n+q)/(5n+q)}. \tag{6.46}$$

Bearing this discussion in mind, we therefore begin by treating the origin $x = 0$ as a position slightly down glacier from the head, and prescribe

$$Q = Q_c = Q_E \quad \text{at} \quad x = 0. \tag{6.47}$$

For the same reason concerning the neglected effective pressure gradients, we do not attempt to apply a condition at the terminus, as in chapter 5. In reality there will be a boundary region in which the pressure adjusts to become atmospheric.

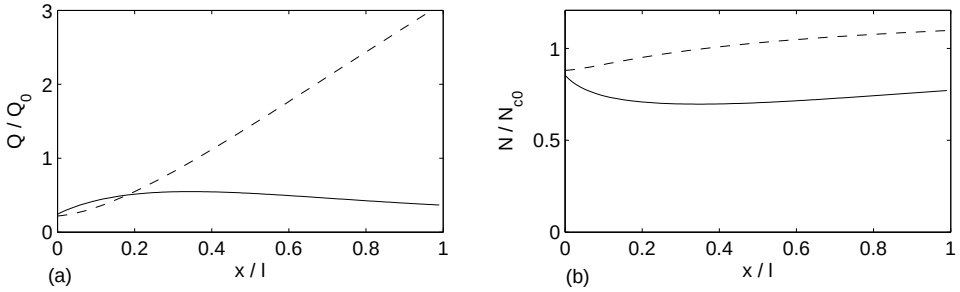

Figure 6.6: (a) Discharge carried by cavities (solid) and channels (dashed) as a function of distance downglacier when $M = 3$, $M_c = 0$. This is the steady state solution of (6.25)-(6.28) and (6.47); (b) Effective pressure in cavities (solid) and channels (dashed).

6.4 Results and discussion

6.4.1 Numerical results

Equations (6.25)-(6.28) together with (6.47) are solved using an upwinding forward difference scheme. Figure 6.6 shows the water flux through the two drainage systems in the steady state when $M = 3$ is constant, and shows the increasing fraction of the total discharge carried by the channels.

To investigate seasonal changes the melt supply is again taken to be sinusoidal. Figure 6.7 shows a contour plot of the spatial and temporal variations in the sliding velocity resulting from the varying cavity pressure according to (6.19). There is a peak at some distance downglacier from the head where the largest water flux is carried by the distributed system, resulting in the smallest values of effective pressure. Further down the glacier, the water is carried more and more by the channel system that acts to increase the effective pressure and therefore reduce the sliding velocity.

6.4.2 Linearised solutions

Though the equations are straightforward and easily solved numerically, in this section we briefly consider a linear version which provides some insight to the waves that are produced in figure 6.7. As mentioned earlier, the dimensionless timescale α_c for the channels may be irrelevant in practice as the kinematic opening or closing takes longer, but in any case it is very small so we set $\alpha_c = 0$ here.

Then linearising the equations (6.25)-(6.28) about the value $Q = Q_C = Q_E$ (6.47), we have

$$\alpha \frac{\partial Q}{\partial t} + \frac{\partial Q}{\partial x} = M - AQ_c - BQ, \tag{6.48}$$

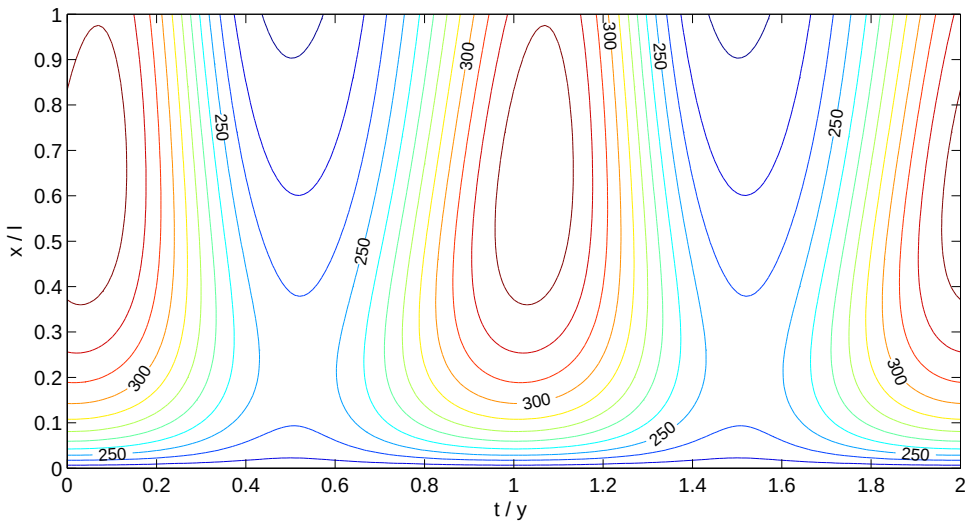

Figure 6.7: Sliding velocity variations due to changing meltwater conditions at the bed, taken from the solution of (6.25)-(6.28) and (6.47), using the sliding law (6.19). Melt input is $M = 1 + 2\,(1 + \cos 2\pi t)$. Contour interval is 10 mm d^{-1}.

$$\frac{\partial Q_c}{\partial x} = AQ_c + BQ, \tag{6.49}$$

where

$$A = \kappa N_c'(Q_E), \qquad B = -\kappa N'(Q_E), \tag{6.50}$$

and boundary conditions are

$$Q = Q_c = 0, \quad \text{at} \quad x = 0. \tag{6.51}$$

General solution

The two equations are hyperbolic, with characteristics given by $\sigma = x - t/\alpha$ and $\tau = t/\alpha$. Rewriting in terms of these two variables, and eliminating Q_c, we have

$$\frac{\partial^2 Q}{\partial\sigma\partial\tau} - Q\frac{\partial Q}{\partial\tau} + B\frac{\partial Q}{\partial\sigma} = -AM + \frac{\partial M}{\partial\sigma}, \tag{6.52}$$

with

$$Q = 0, \quad \frac{\partial Q}{\partial\tau} + BQ = M \quad \text{on} \quad \sigma + \tau = 0. \tag{6.53}$$

This is a version of the *telegraph* equation, which can be written in canonical form with the substitution

$$Q = e^{A\sigma - B\tau}\phi, \tag{6.54}$$

giving

$$\frac{\partial^2\phi}{\partial\sigma\partial\tau} + AB\phi = \left(\frac{\partial M}{\partial\sigma} - AM\right) e^{-(A\sigma - B\tau)}, \tag{6.55}$$

with

$$\phi = 0, \quad \frac{\partial \phi}{\partial \sigma} = M e^{-(A\sigma - B\tau)} \quad \text{on} \quad \sigma + \tau = 0. \tag{6.56}$$

One can write down an explicit solution to this equation using a Riemann representation. This involves solving for the adjoint operator $R(\sigma, \tau.\Sigma, T)$ that satisfies

$$\frac{\partial^2 R}{\partial \sigma \partial \tau} + AB\, R = 0, \qquad R = 1 \quad \text{on} \quad \sigma = \Sigma \quad \text{and} \quad \tau = T, \tag{6.57}$$

with the similarity solution

$$R = J_0 \left(2\sqrt{AB(\Sigma - \sigma)(T - \tau)} \right), \tag{6.58}$$

in which J_0 is the Bessel function of order 0 (Ockendon et al., 2003). The Riemann representation for the solution $Q(\Sigma, T)$ is therefore

$$\begin{aligned} Q(\Sigma, T) \;=\; & \int_{-\Sigma}^{T} \int_{-\tau}^{\Sigma} J_0 \left(2\sqrt{AB(\Sigma - \sigma)(T - \tau)} \right) \left(\frac{\partial M}{\partial \sigma} - AM \right) e^{A(\Sigma - \sigma) - B(T - \tau)} \, \mathrm{d}\sigma \, \mathrm{d}\tau \\ & + \int_{-\Sigma}^{T} J_0 \left(2\sqrt{AB(\Sigma + \tau)(T - \tau)} \right) M e^{A(\Sigma + \tau) - B(T - \tau)} \, \mathrm{d}\tau. \end{aligned} \tag{6.59}$$

Wave-like solutions

Although this gives the solution for arbitrary input $M(x, t)$ it does not make the behaviour of the solution particularly clear. Since we are interested in the waves generated by a varying input, it is more instructive to consider taking $M(t) = e^{i\omega t}$ and looking directly for time-harmonic solutions to (6.48) and (6.49). In terms of Q this is

$$\frac{\partial^2 Q}{\partial^2 x} + \alpha \frac{\partial^2 Q}{\partial x \partial t} - \alpha A \frac{\partial Q}{\partial t} - (A - B) \frac{\partial Q}{\partial x} = -A e^{i\omega t}, \tag{6.60}$$

with

$$Q = 0, \quad \frac{\partial Q}{\partial x} = e^{i\omega t} \quad \text{at} \quad x = 0, \tag{6.61}$$

which has the particular solution $Q = e^{i\omega t}/i\omega\alpha$. There are wave-like homogeneous solutions of the form

$$Q \propto e^{i\omega t + ikx}, \tag{6.62}$$

with the complex wavenumbers

$$k_{\pm} = \underbrace{-\frac{\omega\alpha}{2} - \frac{A - B}{2} i}_{u} \pm \underbrace{\left\{ \left(\frac{\omega\alpha}{2} + \frac{A - B}{2} i \right)^2 - A\omega\alpha i \right\}^{1/2}}_{v}. \tag{6.63}$$

The required combination of solutions to satisfy (6.61) is

$$Q = \frac{e^{i\omega t}}{i\omega\alpha(k_+ - k_-)}\left[(k_+ - k_-) - (k_+ + \omega\alpha)e^{ik_-x} + (k_- + \omega\alpha)e^{ik_+x}\right], \tag{6.64}$$

which can be viewed as a superposition of three waves with different speeds; ∞, $-\omega/\Re e\, k_-$ and $-\omega/\Re e\, k_+$; and decay rates; 0, $\Im m\, k_-$ and $\Im m\, k_+$.

It is straightforward[2] to deduce that the second wave speed is always positive and the third is always negative, and that the second decay rate is always positive but the third always negative. There is therefore a forwards travelling wave that dies out with distance down the glacier, and a backwards travelling wave that grows; this corresponds to the transfer of the majority of water from cavity to channel system and effectively a transition from the situation in figure 6.3 to that in figure 6.4. If $A \gg B$ or $A \ll B$, which loosely means cavities or channels are favoured respectively, the downstream wave has speed $\sim 1/\alpha$, whilst the upstream wave has speed $\sim -\infty$.

The linear solutions suggest that the effect of a sinusoidally varying input is as follows. Initially, for small x, the forward travelling 'cavity' wave always dominates, and it is easy to find that the maximum value of Q occurs where

$$\tan\omega t \approx \frac{\omega\alpha x}{2}, \tag{6.67}$$

so that the maximum propagates downglacier with speed $2/\alpha$, as in (6.10). The effect of the coupled drainage system is then to reduce this speed with distance down the glacier as the backward travelling 'channel' wave takes over. This behaviour is evident in the numerical solution in figure 6.7.

6.4.3 Seasonal waves

One of our main aims is to reproduce some of the qualitative features of figure 6.1, which we now attempt to do. In particular we look to explain the seasonal wave (that is, the downstream shift in the timing of velocity minima and maxima), and the

[2]From the definition of $v = v_R + v_I i$ in (6.63), the real and imaginary parts satisfy $v_I = -(A + B)\omega\alpha/4v_R$ and

$$v_R^2 - \frac{(A+B)^2\omega^2\alpha^2}{16v_R^2} = \frac{\omega^2\alpha^2}{4} - \frac{(A-B)^2}{4}. \tag{6.65}$$

This function of v_R is increasing and by substituting in $v_R = \omega\alpha/2$ and $v_R = \omega\alpha(A+B)/2|A-B|$ we find bounds on v_R, and hence v_I, in terms of the real imaginary parts of $u = u_R + u_I i$:

$$-u_R < v_R < -u_R\left|\frac{A+B}{A-B}\right|, \qquad |u_I| < -v_I < |u_I|\left|\frac{A+B}{A-B}\right|. \tag{6.66}$$

general decrease in sliding velocity with distance down the ablation area. The internal deformation velocity of the ice was calculated by Hodge, based on measurements of depth and surface slope, and it can generally account for only a small component of the surface velocity. The one feature of figure 6.1 that may be caused by internal deformation is the small peak in velocities at around 2000 m, which can be attributed to deeper ice and a steeper slope in this region.

We have already seen the possibility for the forward propagating velocity maxima in figure 6.3, but it is seen there that modeled sliding velocities increase all the way to the terminus as the water pressure increases. The observed velocity decrease, which must result through (4.14) from an *increase* in effective pressure, is exactly what occurs in the lower half of the glacier in figure 6.7, which we therefore suggest corresponds to the ablation area in figure 6.1.

Taking $x = 0$ to be the position of the equilibrium line and $x = 1$ the terminus, so concentrating only on the ablation area, (6.25)-(6.28) are solved again with the boundary condition at $x = 0$ now describing the flux of meltwater arriving there from upglacier. This is likely to be non-zero and seasonally varying, so we take a sinusoidal variation, in phase with the varying meltwater input. To aid comparison with figure 6.1, the resulting sliding velocity according to (6.19) is added to the constant deformation velocity, which is calculated using (4.5) and Hodge's measured depth and surface slope. A contour plot of the surface velocity is shown in figure 6.8; the knobbly look is due to slight non-uniformities in the deformation velocity, which, in particular, explains the peak two-thirds of the way down the region.

Several comments can be made on figure 6.8 and how it compares with figure 6.1. The first is that it demonstrates seasonal velocity changes, with a speed up at all points during the summer when there is maximum melt entering the cavities. The second is that the timing of the peak velocity does move progressively later in the year with distance downglacier. This is the result of the slow passage of water through the cavity system meaning that build-up of cavity pressure occurs later further down glacier. Thirdly, the velocity is generally decreasing toward the terminus, the reason for this being that less of the meltwater drains through cavities lower down and the cavity pressure is consequently lower there.

6.4.4 Seasonal drainage transition

One feature of figure 6.8 in particular does not agree so well with figure 6.1, and that is the apparent 'backward' propagation of the velocity minimum during the winter, of which there is no evidence in figure 6.1. This is a result of the capture property of the

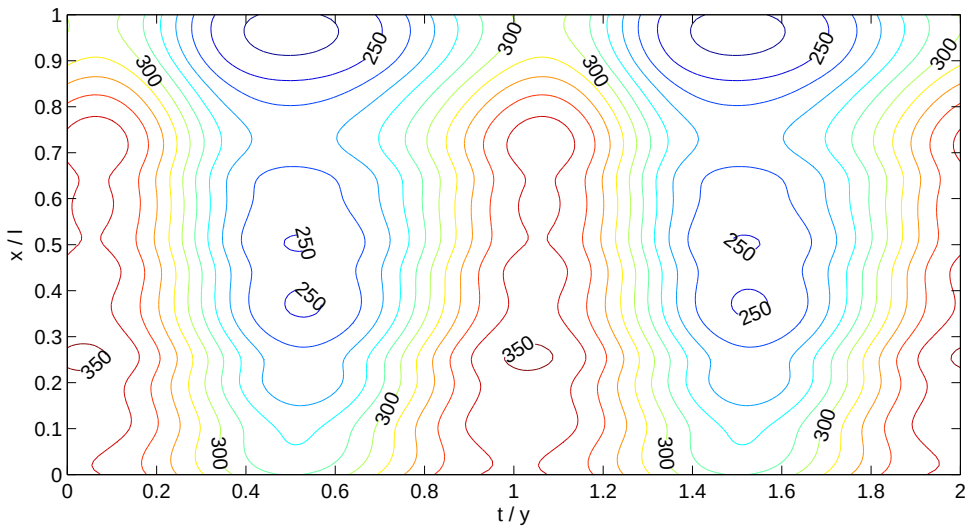

Figure 6.8: Contour plot of surface velocity variations in the ablation area; the sum of internal motion (4.5) calculated using measured shear stress, and sliding motion (6.19) based on modelled subglacial water pressures from (6.25)-(6.28), with $M = 1 + 1.5\cos 2\pi t$, and $Q = Q_c = 0.5 + 0.25\cos 2\pi t$ at $x = 0$. Contour interval is 10 mm d^{-1}.

channels which means that if there is insufficient replenishment of the cavities, the channels suck water out from them, and the situation becomes effectively like that in figure 6.4. This points towards the probably faulty assumption that both drainage systems stay open throughout the year.

Our model captures some aspects of the transition in the sense that channels become larger and carry a larger fraction of the meltwater during the summer, but actual shut down of the channels during the winter does not occur. As commented earlier (and at length in chapter 5), there is a critical discharge required to enable channel drainage to occur and we have assumed that this is exceeded throughout the year, at least in the region we are looking at. The critical value given in (6.47), based on the condition that water pressures in the channel must be lower than cavities for the same discharge, is indeed small, but this value may be misleading. For such a channel to exist, the water flux must be localised in one place, and such localisation may not occur until there is a significantly larger discharge in the distributed system. A more appropriate criterion for channel initiation is therefore

$$Q > Q_*, \tag{6.68}$$

where the value of Q_* will be glacier specific. Microscopic analysis of the unstable transition from cavities to channels (Walder, 1986; Kamb, 1987) suggests transition

should occur if the cavity pressure is large enough or equivalently, given (6.27), the cavity discharge is high enough. Field evidence that the transition occurs with the retreating snowline (Nienow et al., 1998) or during periods of warm weather (Anderson et al., 2004) when there is a substantial increase in meltwater production agree with this assertion.

Given the discussion in chapter 5, a sensible value for Q_* would seem to be q_*W, where W is the glacier width and q_* is the critical distributed discharge (5.75).

To include the transition in our model is relatively straightforward. The glacier is divided into two parts, the upper part in which drainage occurs by cavities only, and the lower part in which both types of drainage occur as above. Thus we have

$$\alpha\frac{\partial S}{\partial t}+\frac{\partial Q}{\partial x}=M, \quad \text{for} \quad 0<x<x_T(t), \tag{6.69}$$

where x_T is the position of the transition where $Q=Q_*$, and (6.25)-(6.26) still hold in $x_T<x<1$. The boundary condition at $x=0$ is $Q=0$, and again in order to ensure that $N_c>N$ when the channel starts (but without resorting to the delicate details of the channel head as in chapter 5), we suppose that there is always a small 'fictional' flux Q_{c*} in the channels before they begin, chosen as

$$Q_{c*}=\gamma^{4n}Q_*^{-4n/(n+q)}. \tag{6.70}$$

so that $N_c(Q_{c*})=N(Q_*)$. The larger the critical discharge, the lower this vestigial flux Q_{c*}.

Model calculations are made with the melt variation in M again taken to be sinusoidal. Somewhat arbitrarily we take $Q_*=1.5$, to ensure that channels close down everywhere during the winter minimum. The resulting pattern of sliding velocity changes is calculated and shown in figure 6.9. Also shown in figure 6.10(a) are the velocities at 4 different positions on the glacier, showing that the seasonal variations are very different depending on position.

Figure 6.9 now looks rather different to Hodge's observations. The top part of the glacier $x<x_T$, in which drainage occurs by linked cavities, suggests that the velocity should increase with distance from the head as the greater water flux requires a higher water pressure. Since this region encompasses the whole length of the glacier during the winter the velocity increases all the way to the terminus. Just as in figure 6.3, the slow passage of water during this time produces a seasonal wave in the minimum velocity. In the lower half of the glacier the transition to channel drainage during the spring has the initial effect of reducing the water pressure so that the sliding velocity reduces, before the large meltwater influx to the cavities in the middle of the melting

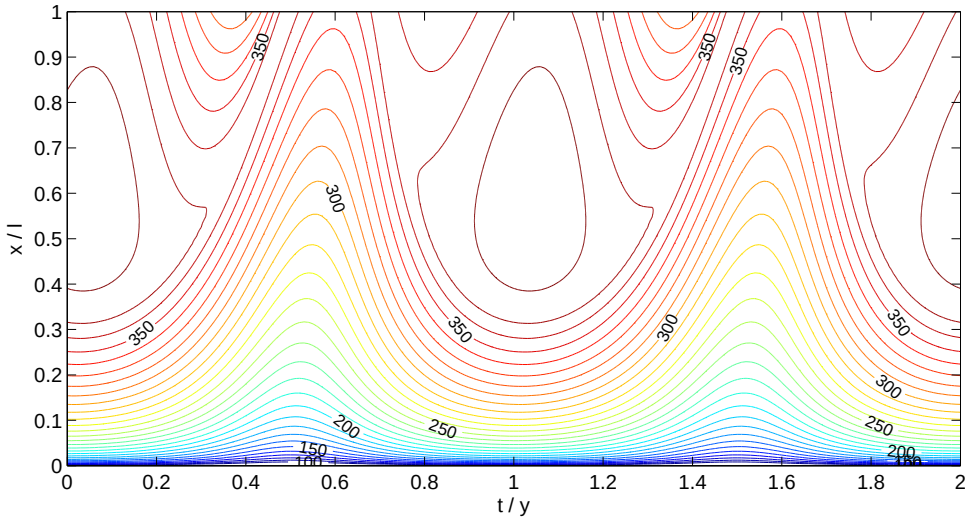

Figure 6.9: Sliding velocity variations with a transition in drainage from linked cavities to a combined system occurring when the cavity discharge reaches $Q_* = 1.5$. The position of the transition is roughly equivalent to the 350 mm d^{-1} contour. Velocities are given by the solutions of (6.69), (6.25)-(6.28) and (6.19), with meltwater input $M = 1 + 2\,(1 + \cos 2\pi t)$.

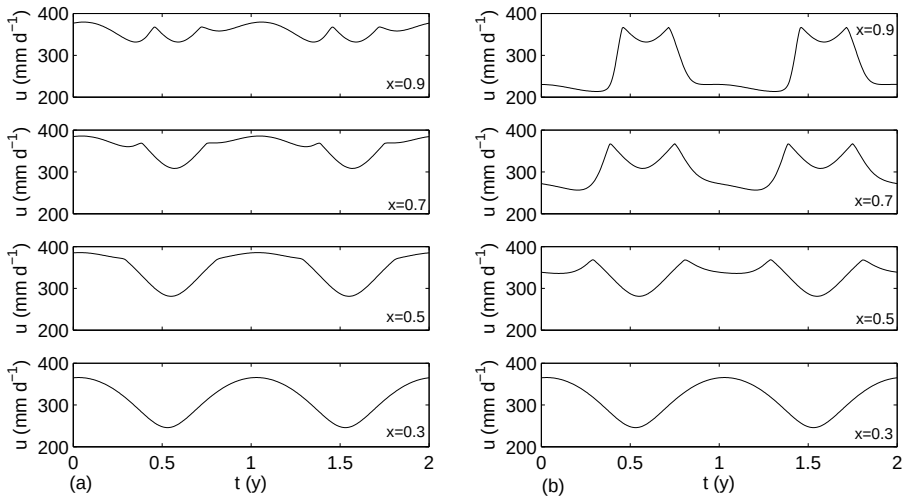

Figure 6.10: (a) Sliding velocity profiles over two years at 4 points along the glacier, with velocities calculated as in figure 6.9. x labels are a fraction of the total length from the glacier head. (b) The same as in (a), but with $\kappa = 20$ rather than 10.

season has the effect of again overpressurising the cavities so that there is another peak in the sliding velocity in mid-summer that again propagates downglacier as a seasonal wave.

This mid-season peak turns out to be heavily dependent on the connectivity parameter κ. If κ is increased, even by a factor of 2, so that water drains more quickly into the channels once they are developed, the situation is very different and is shown in figure 6.10(b). At the top of the glacier the picture is similar to figure 6.10(a), but lower down in the ablation region the channel drainage in the summer has the effect of reducing water pressures so much that the summer sliding velocity is lower than in winter. There are then sharp velocity peaks during the transition periods in spring and autumn that are quite clearly seen to propagate up and down glacier respectively. The spring speed-up is very similar to that which has been reproduced by Kessler and Anderson (2004) using a similar conceptual drainage model.

It would appear that the same mechanism of meltwater conservation in a coupled drainage system can, depending upon the glacier specific parameter values, produce either a peak sliding velocty in mid summer that propagates slowly as a seasonal wave, or more sharp velocity peaks in the spring and autumn associated with the transition in drainage structure.

6.4.5 Model sensitivity

There is a certain degree of uncertainty in the values of the parameters in this model, and indeed the exact applicability of the sliding and drainage theories. We have made similar calculations to those above with a range of values for the four non-dimensional parameters, and a range of alternative power laws in the drainage relations (6.27) and (6.28). These have quite predictable effects on the results.

Changing the timescale parameters α and α_c alters the delay in water travelling down glacier and therefore alters the 'tilt' seen in the contour plots, changing the speed of the seasonal wave. Increasing γ has a similar effect to decreasing κ since both reduce the tendency for water to move from the cavity system to the channel system. Changing κ has the most notable and interesting effect on the results; as discussed above, even a small increase causes water to move quickly so as to equalise the pressures (figure 6.10). In this case there is no seasonal wave in the maximum velocity because the water moves too quickly through the channels.

Altering the power law relationships between pressure and discharge has little qualitative effect on the results, provided of course the effective pressure still increases with discharge in the channels and decreases in the cavities.

Meltwater input to channels

The inclusion of meltwater directly into the channels has also been investigated. Since the channels very effectively route out all the water that enters them, this does not make a great difference to the results. What effect it does have is to increase the effective pressure in the channels and therefore make them even more efficient at capturing the water from the cavities.

Coupling

The coupling between the drainage systems used here is the straightforward linear dependence on the pressure difference (6.16), and more complicated choices are possible. The model in chapter 5 would suggest that it ought to depend instead on the difference between *reciprocal* powers of the effective pressure (due essentially to the pressure causing compaction and influencing the permeability of the distributed system). We could, for instance, take

$$L = k\left(\frac{1}{N} - \frac{1}{N_c}\right). \tag{6.71}$$

Besides this, as mentioned briefly in chapter 5, there is evidence for 'stress-bridges' along the edges of the channel, which may effectively seal it off from the distributed system (Weertman, 1972; Lappegard et al., 2006). In this case, hydraulic communication between the systems would be restricted to periods of high pressure when the stress bridge can be overcome, and these will usually be associated with periods of enhanced melting and runoff (Lappegard et al., 2006).

Such non-linear coupling of the drainage system inherently involves short timescale (diurnal) adjustments of the drainage structures that are not resolved in this model. In our context of smooth seasonally varying melting we are interested in the longer term average connection and must therefore choose an appropriate form for L to *represent* the actual physical processes.

The same model scenarios have been considered with alternative couplings such as (6.71), and they yield results with some difference but without altering the general properties of the seasonal wave and seasonal transitions. We refrain from further experimenting with alternative forms for L since the conclusions are essentially the same and without a more detailed description of the short-term behaviour during transient high-pressure periods, it would detract from the simplicity of the ideas to hypothesise the 'correct' form for L.

6.5 A fuller model

6.5.1 Model equations

The above models are very simple, and the emphasis was on the mechanism to produce seasonal variations, and particularly seasonal waves, in the ice velocity. As noted in Hewitt and Fowler (2008b), a fuller treatment should include the effects of longitudinal stress on the ice flow, and of effective pressure gradients on the water flow.

Longitudinal stress

To include the first of these, the basal shear stress in the sliding law (4.14) can be better approximated using the horizontal force balance (4.9), which is written in a dimensionless form as

$$0 = -H\frac{\partial h}{\partial x} - N^{q/p}|u_b|^{1/p-1}u_b + 2\frac{\partial}{\partial x}\left(\nu H\left|\frac{\partial u_b}{\partial x}\right|^{1/p-1}\frac{\partial u_b}{\partial x}\right). \tag{6.72}$$

The term in brackets is the longitudinal stress τ_{xx}, which is of dimensionless size

$$\nu = \frac{A^{-1/n}u_{b0}^{1/n}}{\rho_i g h_0 l^{1/n}}. \tag{6.73}$$

The variables have been scaled using lengthscale l, depth scale H_0, height scale h_0, and

$$\tau_0 = \frac{\rho_i g H_0 h_0}{l}, \tag{6.74}$$

$$u_{b0} = c\tau_0^p N_0^{-q}, \tag{6.75}$$

where N_0 is the scale for the effective pressure. Typical values $l \sim 10$ km, $H_0 \sim 100$ m, $h_0 \sim 1$ km, and those in table 6.1, give $\tau_0 \sim 10^5$ Pa, $u_{b0} \sim 10^{-6}$ m, and

$$\nu \sim 0.003. \tag{6.76}$$

ν is small, so (6.72) states that u_b depends approximately only on the local driving stress (the first term, as before), but if this suggests large gradients in u_b, the longitudinal stress will act to smooth these out.

Effective pressure gradients

A fuller version of the drainage model in section 6.3.1 is written, using the non-dimensionalisation of section 6.3.2, as

$$\alpha\frac{\partial S}{\partial t} + \frac{\partial Q}{\partial x} = M - \kappa(N_c - \gamma N), \tag{6.77}$$

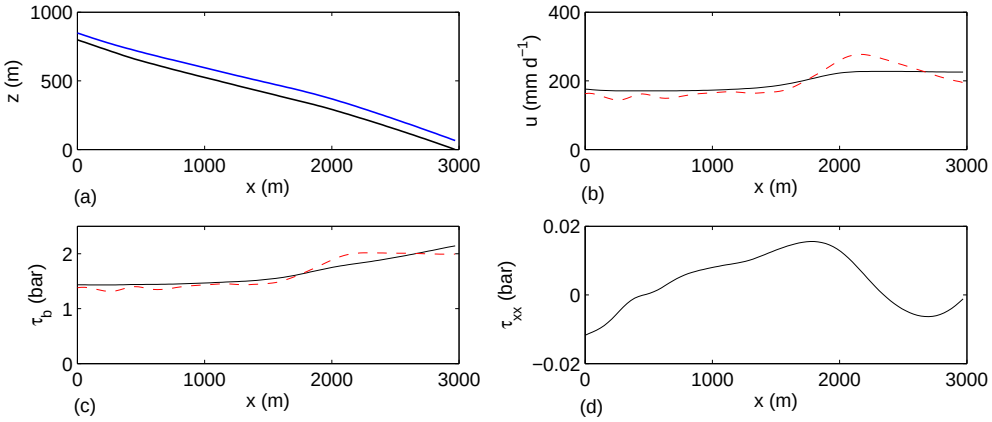

Figure 6.11: (a) Bed and surface profile of Nisqually glacier, as inferred from Hodge's measurements (Hodge, 1974); (b) Ice velocity calculated from the solution of (6.72) and (6.77)-(6.81) as shown in figure 6.13, with $\nu = 0.02$ (solid), or using the local sliding law (dashed); (c) Basal shear stress (solid) as calculated from (6.72), and driving stress (dashed); (d) Longitudinal stress as calculated from (6.72).

$$\alpha_c \frac{\partial S_c}{\partial t} + \frac{\partial Q_c}{\partial x} = M_c + \kappa(N_c - \gamma N), \tag{6.78}$$

$$Q^2 = S^2 \left(\Phi + \delta^2 \frac{\partial N}{\partial x} \right), \qquad Q_c^2 = S_c^{8/3} \left(\Phi + \delta_c^2 \frac{\partial N_c}{\partial x} \right), \tag{6.79}$$

$$Q = \frac{1}{N^{n+q}} \left(\Phi + \delta^2 \frac{\partial N}{\partial x} \right)^{1/2}, \qquad Q_c = N^{4n} \left(\Phi + \delta_c^2 \frac{\partial N_c}{\partial x} \right)^{-11/2}, \tag{6.80}$$

with the gravitational potential gradient, scaled with $\Phi_0 = \rho_i g h_0 / l$, given by

$$\Phi = -\frac{\partial h}{\partial x} - (r-1)\frac{\partial b}{\partial x}, \qquad h = b + \mu H. \tag{6.81}$$

The additional dimensionless parameters are

$$\delta^2 = \frac{N_0}{\Phi_0 l}, \qquad \delta_c^2 = \frac{N_{c0}}{\Phi_0 l}, \qquad \mu = \frac{H_0}{h_0}, \qquad r = \frac{\rho_w}{\rho_i}, \tag{6.82}$$

(note $\gamma = \delta^2/\delta_c^2$ is the ratio of effective pressure scales). (6.77) and (6.78) are the continuity equations, (6.79) are the turbulent flow laws, and (6.80) are expressions of the kinematic balance between opening and closing (these still assume that each drainage system instantly adjusts to its steady behaviour for a given discharge).

Boundary conditions

(6.77)-(6.81), together with (6.72), provide a more general model for a rapidly sliding glacier with two component drainage system, and can be solved numerically for a

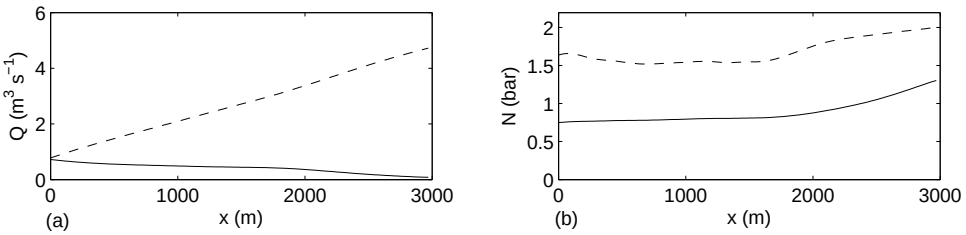

Figure 6.12: (a) Discharge in cavities (solid) and channels (dashed) from the solution of (6.77)-(6.81) as shown in figure 6.13; (b) Corresponding effective pressures.

given bed b, ice depth H, and meltwater supplies M and M_c. Both the drainage and the ice flow problems are now elliptic, requiring additional boundary conditions. We expect to prescribe Q and Q_c at $x = 0$, and N and N_c at the snout $x = 1$, where the pressure must be atmospheric. If H goes to 0 at the end points, no boundary conditions are required for (6.72) since the diffusive stresses are degenerate; if H does not go to 0 however, we might expect to prescribe an ice flux $u_b H$ at $x = 0$ and zero stress $\tau_{xx} = 0$ at $x = 1$.

6.5.2 Nisqually glacier

Hodge (1974) measured the ice depth and surface slope of the ablation region of Nisqually glacier and this profile is shown in figure 6.11(a). Using these, and the size of the observed velocities, we estimate an appropriate value of ν to be around 0.02.

Figures 6.11, 6.12 and 6.13 show an example of the solutions to (6.72) and (6.77)-(6.81), using the inferred bed and surface profile, and imposing a sinusoidal meltwater input M as before. $x = 0$ here corresponds to the equilibrium line, at which Hodge's measurements started; a constant ice flux is prescribed there. The effective pressure gradients have still been ignored here, though it is possible to include them. The dimensionless parameters used correspond to the length scale $l = 3$ km, height $h_0 = 300$ m, depth $H_0 = 100$ m, and discharge $Q_0 = 1$ m^3 s^{-1}, with the other scales following from previous definitions.

Figure 6.12 shows a snapshot of the drainage system properties, and figure 6.11(b)-(d) shows the ice velocity and stress that results. The velocity is compared with that given by the 'local' sliding law (i.e. if $\nu = 0$), and the basal shear stress is compared with the driving stress; it is seen that the longitudinal stresses play quite an important role in smoothing out the variations in velocity downstream.

This will naturally have the effect of damping seasonal waves, as can be seen also in figure 6.13, where the down glacier delay in the timing of the velocity maximum,

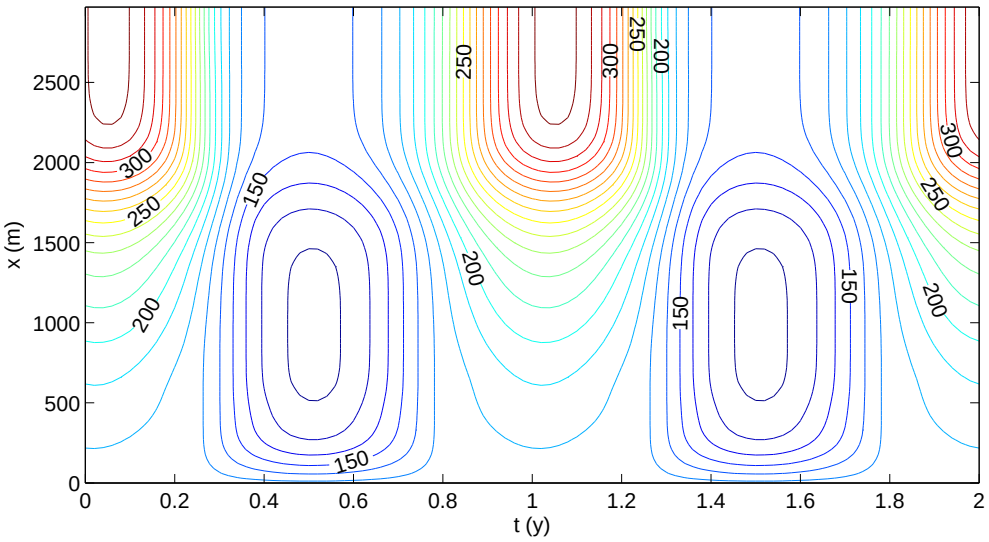

Figure 6.13: Sliding velocity u_b from the solution of (6.72) and (6.77)-(6.81), using the geometry in figure 6.11(a), with $\nu = 0.02$, $\alpha = 0.2$, $\alpha_c = 0$, $\kappa = 5$, $\gamma = 0.6$, $\delta^2 = \delta_c^2 = 0$, $\mu = 0.3$, $r = 1.1$, $n = 3$, $p = 4$, $q = 1$, and with seasonally varying meltwater supply $M = 1+2(1+\cos 2\pi t)$, $M_c = 0$, and $Q = Q_c = 0.5+0.25(1+\cos 2\pi t)$ at $x = 0$. Contour interval is 10 mm d^{-1}.

though present, is less obvious. Note that figure 6.13 looks very little like figure 6.1 although it is calculated using the measured glacier geometry; this is because, as has been found previously (Meier, 1968; Hodge, 1974), the velocity does not depend on stress in the expected way. These calculations are not therefore intended to reproduce figure 6.1 - they are more for interest, to see what the model would predict. Presumably there are lateral stresses from the sides of the glacier, combined with non-uniform roughness of the bed, that could better account for the observed velocity profile.

6.5.3 A model glacier

To illustrate the effect of the effective pressure gradients and the longitudinal stresses over the whole length of a glacier, we adopt a 'typical' valley glacier profile with parabolic depth profile, and constant bed slope. In the dimensionless variables this is $H = 1 - (1 - 2x)^2$ and $b = 1 - x$, and it is shown in figure 6.14(a).

Figures 6.14(b)-(d), 6.15 and 6.16 show examples of the solutions to (6.72) and (6.77)-(6.81) for this case. As in section 6.3 we take $Q = Q_c = Q_E$ at $x = 0$ and, since the water pressure is atmospheric and the ice depth goes to zero at the snout $x = 1$, we take $N = N_c = 0$ there. The solutions are shown in terms of dimensional variables

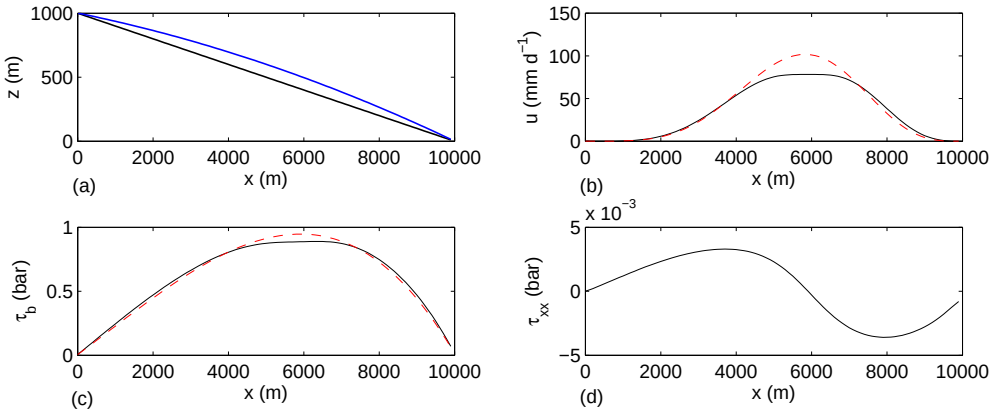

Figure 6.14: (a) Elevation of bed $b = 1 - x$, non-dimensionally, and glacier depth $H = 1 - (1 - 2x)^2$; (b) Velocity calculated from solution to (6.72) and (6.77)-(6.81) (solid) as shown in figure 6.16, or using the local sliding law (dashed); (c) Basal shear stress (solid) as calculated from (6.72), and driving stress (dashed); (d) Longitudinal stress as calculated from (6.72).

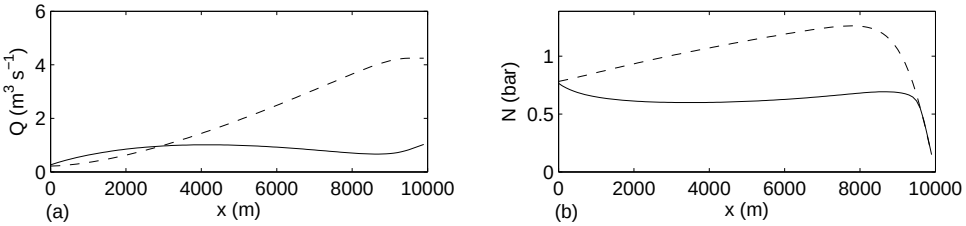

Figure 6.15: (a) Discharge through cavities (solid) and channels (dashed) from the solution to (6.77)-(6.81) as shown in figure 6.16; (b) Corresponding effective pressures; note the boundary layers near $x = 1$, where these are prescribed to be 0.

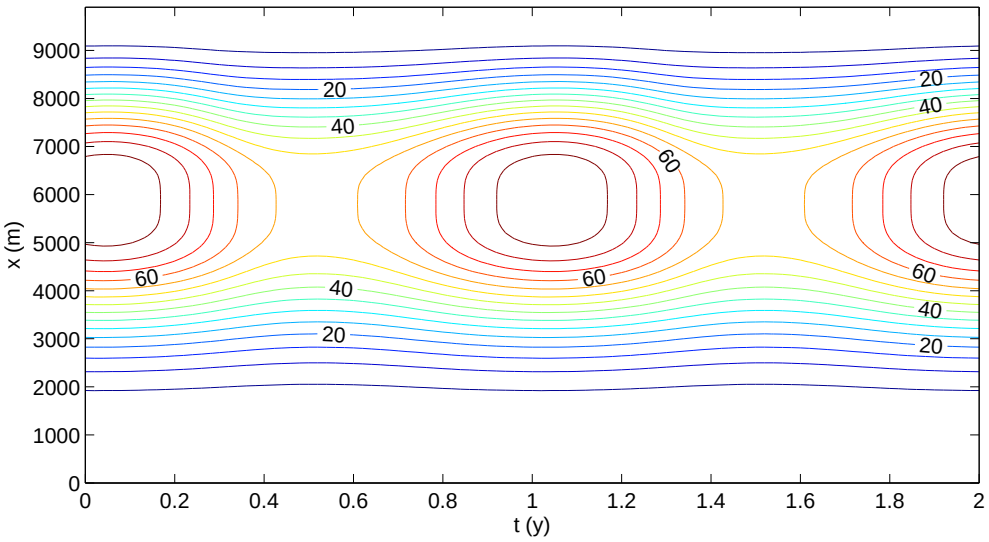

Figure 6.16: Sliding velocity u_b from the solution of (6.72) and (6.77)-(6.78) for a glacier with dimensionless shape $H = 1-(1-2x)^2$ on slope $b = 1-x$, with $\nu = 0.003$, $\alpha = 0.2$, $\alpha_c = 0$, $\kappa = 10$, $\gamma = 0.6$, $\delta^2 = 0.06$, $\delta_c^2 = 0.1$, $\mu = 0.1$, $r = 1.1$, $n = 3$, $p = 4$, $q = 1$, and with seasonally varying meltwater supply $M = 1+2(1+\cos 2\pi t)$, $M_c = 0$, and boundary conditions $Q = Q_c = Q_E$ at $x = 0$, $N = N_c = 0$ at $x = 1$. Contour interval is 5 mm d^{-1}.

using the typical values in table 6.1, with length $l = 10$ km, height $h_0 = 1$ km, and depth $H_0 = 100$ m. The meltwater supply is $M = 1 + 2(1 + \cos 2\pi t)$ cm^2 s^{-1}.

Figure 6.14(b)-(d) shows a typical profile of the velocity, and the corresponding basal shear stress and longitudinal stress. As expected the flow is extensional over the upper part and compressional over the lower part. The peak velocity at the deepest point is smoothed out from that predicted by the local sliding law. Figure 6.15 shows a typical profile of discharge carried by cavities and channels and the corresponding effective pressure. There is a boundary region corresponding to the size of δ^2 and δ_c^2 over which the pressure adjusts to the atmospheric condition at the snout; this does not have much effect on the ice velocity (figure 6.14(b)), since the driving stress there is so small.

The effect of the seasonally varying meltwater supply is seen in figure 6.16; the ice speeds up at all points during the summer when melt production is highest. There is a slight delay in the timing of the maximum with distance down glacier, though it is not particularly noticeable.

6.6 Summary

Seasonal waves manifest themselves in the progressive shift of a maximum or minimum down the glacier. We have shown that kinematic waves in a slow distributed drainage system are a possible cause of this type of wave, as shown in figure 6.8. This represents our best attempt at reproducing the seasonal variations observed by Hodge. A slow drainage system, which is poorly connected to any faster channelised system, is necessary to produce the waves; otherwise the presence of the channels effectively damps the seasonal peaks in the effective pressure, and can lead to an apparent backward wave in which the pressure peak occurs earlier further downstream. To produce the estimated speed on Nisqually glacier requires an advective timescale for drainage of around 1 month.

Including longitudinal stress couples the ice velocity along the length of the glacier and therefore acts to damp seasonal waves; it does not damp them entirely however, only smoothing out relatively large gradients in the velocity that result from non-uniform surface slopes and driving stress. Using the measured surface and depth profiles on Nisqually glacier gives a very poor match with the observed velocity profile, and we must assume that aspects we have not included here, such as the effects of the valley sides, play an important role in explaining this.

If a seasonal shut down of the channels is accounted for, the peak sliding velocity may either occur during mid-summer, when water quantities are largest, or during the spring transition, in which case it can lead to an upglacier propagation of the velocity peak, accompanying the upglacier growth of the channel system.

This chapter has assumed throughout that each drainage system is separately in a steady state, so that the simple relationships between flux, cross-sectional area, and effective pressure apply. A more detailed understanding of the seasonal transition, particularly the differences between opening up and closing down of the channelised system, must involve consideration of the channel, and possibly cavity, *dynamics*.

Conclusions

The reader is referred back to the summaries at the end of chapters 2, 3, 5 and 6 for a slightly more detailed overview of their contents. Here, we provide a brief summary of the conclusions, and pointers towards further work.

Magma migration

Chapter 2 focussed on deriving a simple model for decompression melting, and particularly for melting of a one-dimensional upwelling column beneath a mid-ocean ridge. By ignoring compositional effects, this may be seen as a large simplification of the real mantle, but the intention was to keep the model equations simple enough to gain analytical understanding whilst still being consistent in the application of conservation laws.

Treating the boundaries of the partially molten region as 'free' allowed us to determine their location by conserving energy flux across them; the results showed that the depth at which melting starts is typically very close to the depth at which the adiabatic geotherm (in the absence of melting) would intersect the pressure-dependent solidus, and justifies treating this boundary as known when considering the dynamics of the partially molten region.

The position of the upper boundary of the partial melting region can similarly be determined if it is assumed that all melt solidifies there; this is evidently wrong, but some additional assumption (or better, prediction) of what does happen to the melt there would be required to say anything else. The temperature dependence of the mantle viscosity must also play a role in determining the location of, and the dynamics near, the base of the lithosphere and crust. We do not intend to make any firm conclusions about what happens there, and note that further study of the coupling between flow in the partially molten region and transport in the lithosphere would be welcome. Chapters 2 and 3 have to some extent assumed that whatever coupling occurs has little effect on the dynamics further down, but it is not obvious

that this is necessarily true. Episodic eruptions from a magma chamber might, for instance, trigger changes lower in the partially molten region.

When imposing an upper boundary on the partial melting region, it was necessary to have a condition on the effective pressure there, and the argument in section 2.1.4 suggests that thermodynamic equilibrium of the boundary would require $N = 0$ there. Again, whether this would be true if one made other assumptions about the connection with melt flow into a magma chamber or lithospheric conduit is not clear. For the one-dimensional solutions in chapter 2, the effect of this condition is confined to a thin boundary layer (figure 2.2). Although we investigated some exotic properties of this boundary layer in section 2.4, it would be wrong to read too much into them; the conclusion we should take is rather that consistently determining the melting rate from an energy equation may have some interesting effects.

Chapter 3 focussed on the observation that, when the solidus is simply pressure-dependent, the melting rate is determined by the rate heat is released from upwelling material, both matrix and melt. This was shown to cause sufficiently large perturbations from a one-dimensional steady state to localise into open channels, drawing melt from a surrounding region comparable to the compaction length. Localisation of this sort is essentially the same as reactive infiltration in soluble materials, and the main result we want to emphasise is simply that the same thing can occur if the rock were just single component.

Even if cracks form through 'fracturing' in the partially molten region, the heat transport by melt flowing up such a fracture would cause melting of the walls, and we have shown that it is important to account for this melting, just as it is for water channels in ice. We suggested that a planar channel would be unstable to non-uniform melting and would evolve into a more cylindrical shape. The resistance to flow in such a conduit would be very small and the pressure gradient within it would therefore be close to magmastatic. Melt velocities on the order of 100 m y^{-1} were predicted, which is broadly consistent with inferences from geochemistry. The size of a conduit would be determined by the compaction length, since it would efficiently draw in most of the melt generated in a surrounding region of that size.

Again, there is uncertainty over the appropriate pressure condition to apply at the top of a conduit (the base of the lithosphere), and future work should look at coupling a supply of melt from the asthenosphere with transport through a dike in the lithosphere or into a magma chamber, which might allow for different possibilities.

Further work should therefore include:

- Extending solutions in chapter 2 to two dimensions, with matrix motion appropriate for a spreading ridge in the second dimension. The solution method for determining the boundaries of the partially molten region would have to be different from that used here, since we scaled the equations using its unknown depth, which would then be space dependent. A method such as the enthalpy method used by Katz (2008) offers more promise. Since melt will naturally be drawn towards the ridge axis, it would probably be necessary to readdress the assumption that all melt solidifies at the base of the lithosphere, perhaps allowing some of it to escape into a magma chamber at the ridge axis.

- Investigating the relationship between melt transport in the asthenosphere and in the lithosphere. This would give further insights as to whether the boundary conditions we have used are appropriate, and how much the partial melting region is influenced by what is happening nearer the surface.

- Considering the influence of more thermodynamic components. A significant simplification we made was to ignore compositional effects, which undoubtedly have an influence on the fluid dynamics. This will make the models less tractable analytically, but the insights learned from this work would hopefully be of benefit in guiding them. Especially, it would be interesting to see how reactive instabilities develop if the melting rate is determined consistently with a pressure and composition dependent solidus.

Subglacial water flow

Chapter 5 presented a generalised model for distributed flow beneath ice, and examined the interaction with a Röthlisberger channel. This was largely motivated by the models in part I, and the observation that the nature of the fluid flow there is remarkably similar to that believed to occur beneath ice sheets.

Distributed flow was described as an effective porous medium and the volume of pore space was suggested to evolve according to opening and closure rates that are due to melting of the ice and compaction due to the overburden pressure. This leads to steady state relationships between discharge and pressure that are typical of idealised distributed drainage structures such as cavities and canals.

Röthlisberger channels act as line sinks to the porous flow, since the effective pressure is larger there; there is a compaction length that determines the distance

over which the distributed system accommodates the pressure perturbation. This suggests a spacing between channels that is similar, though slightly different, to those proposed by Boulton et al. (2009) and Rempel (2009), who concentrate on different physical processes. For typical values beneath an ice sheet, we predicted spacing between major channels to be on the order of 10 km, and this compares well with the spacing of eskers.

Compaction of the drainage space causes a reduction in permeability close to a channel and means that large effective pressures are confined to a region very close to it; the *average* effective pressure may be significantly less than that in the channel.

We suggested that channels that form initially near the margin would extend backwards up the glacier due to frictional heating of the water flow into their head, and that this would continue until the rate of supply of water from the surroundings is insufficient to keep it open against viscous closure. This suggests a critical discharge (5.75) in the distributed flow, dependent on the hydraulic potential gradient, above which a channel would be possible.

We have considered only steady state drainage, with a constant supply of water from geothermal and frictional heating. Extensions to this work could examine time dependent water supply, and the actual growth and shut down of a channel. This will require more sophisticated numerical techniques for the flow in the vicinity of a channel, but the current model is sufficiently simple that this ought to be possible.

More practically, it is hoped that the ideas given here, particularly concerning the spacing between channels and the criterion for where channels can begin, can be helpful in building appropriate *average* descriptions of water flow that are required for large-scale ice sheet models. In this case one cannot hope to resolve either the channel or the flow field around a channel, but must instead parameterise the nature of the water flow.

Chapter 6 formed a slight aside, but gives an example of how the nature of subglacial drainage can affect ice flow. It is a very simple illustration of how the ideas from chapter 5 might be useful in practice. We suggested that observed waves in the ice velocity during the course of a summer may be caused by water flow through a slowly draining distributed system and an accompanying wave in the water pressure.

Coupling to a faster flowing Röthlisberger channel can moderate the speed of the wave and depending upon the efficiency of the connection between the two types of drainage, can result in lower or higher ice velocities in the summer. If channels are caused to shut down when discharge is too low (as suggested in chapter 5), the

transition to and from channelised drainage during the spring and autumn can cause peaks in the ice velocity then, which travel up or down glacier as the channel network extends or shrinks; this is also in line with some field observations.

Despite accounting for a seasonally varying supply of meltwater, the work in chapter 6 has still assumed that the drainage systems' dynamics are in a steady state. Future work should account for the time-evolution of the individual drainage systems; if water supply varies sufficiently smoothly the results here would hold, but it is frequently observed that dramatic changes occur when water supply varies abruptly, and how the short time-scale variations affect the drainage structures is therefore of great interest. This is true of the models in both chapter 5 and chapter 6, and will be important in building predictive models of events such as lake drainage in Antarctica (Wingham et al., 2006) or the impact of crevasse opening in Greenland (Zwally et al., 2002; Das et al., 2008).

It is hoped that the analogues drawn between melt drainage subglacially and in the mantle have been helpful. Both situations involve a lot of complex behaviour, and the models we have used are very simplistic, which perhaps overemphasises the similarities; nevertheless, it is useful to notice how melt flow has been modelled by different fluid dynamical communities, and to point towards future avenues for research.

Appendix A

Solution to Ricatti equation

To find the solution to (2.144) or (2.169), first note that by rescaling $\hat{z} \sim W_0^{1/3}$, $\hat{N} \sim W_0^{1/3}$ in the first case, or $z \sim \delta^{4/3} W_0^{1/3}$, $N \sim \delta^{-2/3} W_0^{1/3}$ in the second, these are both equivalent to solving:

$$N_z = zN^2 - 1, \quad N = 0 \quad \text{at} \quad z = z_1, \tag{A.1}$$

with $z_1 = \infty$ in the first case, or $z_1 = 1/\delta^{4/3} W_0^{1/3}$ in the second. The solution can be found by writing

$$N = -\frac{1}{z}\frac{v_z}{v}, \tag{A.2}$$

and rewriting the equation in terms of v:

$$v_{zz} - \frac{1}{z} v_z - zv = 0, \quad v_z = 0 \quad \text{at} \quad z = z_1. \tag{A.3}$$

Then changing variables

$$v = zy, \quad z = (3/2)^{2/3} x^{2/3}, \tag{A.4}$$

this equation becomes

$$x^2 y_{xx} + x y_x - \left(x^2 + (2/3)^2\right) y = 0, \tag{A.5}$$

which is a modified Bessel equation. The solutions are $I_{2/3}(x)$ and $K_{2/3}(x)$, where $I_{2/3}(x) \to \infty$ as $x \to \infty$ and $K_{2/3}(x) \to \infty$ as $x \to 0$. The solution for v is therefore

$$v = z\left[A I_{2/3}\left(2z^{3/2}/3\right) + B K_{2/3}\left(2z^{3/2}/3\right)\right], \tag{A.6}$$

for constants A and B. Using the facts that

$$I'_{2/3}(x) = I_{-1/3}(x) - \frac{2}{3x} I_{2/3}(x), \quad K'_{2/3}(x) = -K_{1/3}(x) - \frac{2}{3x} K_{2/3}(x), \tag{A.7}$$

gives

$$v_z = z^{3/2}\left[AI_{-1/3}\left(2z^{3/2}/3\right) - BK_{1/3}\left(2z^{3/2}/3\right)\right]. \tag{A.8}$$

Using the boundary condition this allows the ratio A/B to be determined and we find eventually that the solution for N is

$$N = \frac{1}{z^{1/2}} \frac{I_{-1/3}\left(2z_1^{3/2}/3\right) K_{1/3}\left(2z^{3/2}/3\right) - K_{1/3}\left(2z_1^{3/2}/3\right) I_{-1/3}\left(2z^{3/2}/3\right)}{I_{-1/3}\left(2z_1^{3/2}/3\right) K_{2/3}\left(2z^{3/2}/3\right) + K_{1/3}\left(2z_1^{3/2}/3\right) I_{2/3}\left(2z^{3/2}/3\right)}. \tag{A.9}$$

If the boundary condition is at $z_1 = \infty$, this simplifies to

$$N = \frac{1}{z^{1/2}} \frac{K_{1/3}\left(2z^{3/2}/3\right)}{K_{2/3}\left(2z^{3/2}/3\right)}. \tag{A.10}$$

Appendix B

Influx to head of channel

Here we use the Wiener-Hopf technique to calculate the steady state influx to the head of a channel in chapter 5 including the effective pressure gradients in the downstream direction. We scale (5.52) close to the head of the channel $x = x_c$, $y = 0$ by writing

$$x = x_c + \delta^2 \hat{x}, \qquad y = \delta^2 \hat{y}, \tag{B.1}$$

and assume Φ is constant on the scale $x \sim \delta^2$ to find leading order equation

$$\frac{\alpha}{\alpha - 1} h \Phi(x_c) \frac{\partial}{\partial \hat{x}} h^{\alpha - 1} = \frac{W_O}{\alpha - 1} \left(\frac{\partial^2}{\partial \hat{x}^2} h^{\alpha - 1} + \frac{\partial^2}{\partial \hat{y}^2} h^{\alpha - 1} \right). \tag{B.2}$$

Then approximate $h = h_\infty(x_c)$ in the advective term, and define new variables again by

$$\hat{x} = \frac{W_O}{\alpha h_\infty(x_c) \Phi(x_c)} \xi, \qquad \hat{y} = \frac{W_O}{\alpha h_\infty(x_c) \Phi(x_c)} \eta, \tag{B.3}$$

$$h^{\alpha - 1} = h_\infty^{\alpha - 1} + \frac{\psi}{\Phi(x_c)^{1 - 1/\alpha}}. \tag{B.4}$$

The problem for ψ is then

$$\frac{\partial \psi}{\partial \xi} = \frac{\partial^2 \psi}{\partial \xi^2} + \frac{\partial^2 \psi}{\partial \eta^2}, \tag{B.5}$$

$$\psi \to 0 \quad \text{at} \quad \eta \to \infty, \tag{B.6}$$

$$\frac{\partial \psi}{\partial \eta} = 0 \quad \text{at} \quad \eta = 0, \quad \xi < 0, \tag{B.7}$$

$$\psi = \psi_c \equiv \left(\frac{\delta^2 W_O}{\delta_c^2 N_c} \right)^{\alpha - 1} \Phi(x_c)^{1 - 1/\alpha} - h_\infty(x_c)^{\alpha - 1} \Phi(x_c)^{1 - 1/\alpha} \quad \text{at} \quad \eta = 0, \quad \xi > 0. \tag{B.8}$$

To use the Wiener Hopf technique, define two Fourier transforms as

$$\hat{\psi}_+(k, \eta) = \int_0^\infty \psi(\xi, \eta) e^{ik\xi} \, \mathrm{d}\xi, \qquad \hat{\psi}_-(k, \eta) = \int_{-\infty}^0 \psi(\xi, \eta) e^{ik\xi} \, \mathrm{d}\xi, \tag{B.9}$$

which are analytic in upper and lower half planes respectively. The transformed problem for $\hat{\psi} = \hat{\psi}_- + \hat{\psi}_+$ then becomes

$$\left(k^2 - ik\right)\hat{\psi} = \hat{\psi}_{\eta\eta}, \tag{B.10}$$

$$\hat{\psi}(k,\eta) \to 0 \quad \text{as} \quad \eta \to \infty, \tag{B.11}$$

$$\hat{\psi}_\eta(k,0) = \hat{\psi}_{\eta+}(k,0), \tag{B.12}$$

$$\hat{\psi}(k,0) = \hat{\psi}_c(k) + \hat{\psi}_-(k,0), \tag{B.13}$$

where $\hat{\psi}_-(k,0)$ and $\hat{\psi}_{\eta+}(k,0)$ are as yet unknown. The solution satisfying the boundary conditions is

$$\hat{\psi} = A(k)e^{-(k^2-ik)^{1/2}\eta}, \tag{B.14}$$

where

$$A(k) = \frac{\hat{\psi}_{\eta+}(k,0)}{(k^2-ik)^{1/2}} = \hat{\psi}_c(k) + \hat{\psi}_-(k,0). \tag{B.15}$$

Here $(k^2-ik)^{1/2}$ is defined with branch cuts along the imaginary axis $(-\infty i, 0]$ and $[i, \infty i)$ (i.e. $(k-i)^{1/2} = |k-i|^{1/2}e^{i\theta_1/2}$ with $\theta_1 = \arg(k-i) \in [-3\pi/2, \pi/2]$, and $k^{1/2} = |k|^{1/2}e^{i\theta_2/2}$ with $\theta_2 = \arg k \in [-\pi/2, 3\pi/2]$).

Multiplying by $(k-i)^{1/2}$, we can define two unknown functions

$$\Psi_+(k) = \frac{\hat{\psi}_{\eta+}(k,0)}{k^{1/2}}, \qquad \Psi_-(k) = (k-i)^{1/2}\hat{\psi}_-(k,0) \tag{B.16}$$

to write the boundary conditions (B.15) in the form

$$\Psi_+(k) - \Psi_-(k) = (k-i)^{1/2}\hat{\psi}_c(k). \tag{B.17}$$

By construction Ψ_+ and Ψ_- are analytic in upper and lower half planes respectively, so this constitutes a Riemann-Hilbert problem. Once solved, the solution for $\hat{\psi}$ is given by

$$\hat{\psi} = \frac{\Psi_+(k)}{(k-i)^{1/2}}e^{-(k^2-ik)^{1/2}\eta}, \tag{B.18}$$

and the flux into $\eta = 0$ is given by

$$\frac{\partial\psi}{\partial\eta}(\xi,0) = -\frac{1}{2\pi}\int_{-\infty}^{\infty} k^{1/2}\Psi_+(k)e^{-ik\xi}\,\mathrm{d}k. \tag{B.19}$$

We expect $\hat{\psi}_c(k)$ to have a pole at $k=0$ (in the lower half plane) which is determined by the behaviour of ψ_c at infinity; assuming it is bounded, $\hat{\psi}_c(k) \sim 1/k$, and assuming this is the only pole we can therefore satisfy (B.17) by writing

$$(k-i)^{1/2}\hat{\psi}_c(k) = \underbrace{(-i)^{1/2}\hat{\psi}_c(k)}_{\Psi_+} \quad + \quad \underbrace{(k-i)^{1/2}\hat{\psi}_c(k) - (-i)^{1/2}\hat{\psi}_c(k)}_{-\Psi_-}, \tag{B.20}$$

in order to remove the singularity at 0 from Ψ_-.

Thus

$$\begin{aligned}\frac{\partial\psi}{\partial\eta}(\xi,0) &= -\frac{(-i)^{1/2}}{2\pi}\int_{-\infty}^{\infty} k^{1/2}\hat{\psi}_c(k)e^{-ik\xi}\,\mathrm{d}k, \\ &= -\frac{1}{\sqrt{\pi}}\left[\frac{\psi_c(0)}{\xi^{1/2}} + \int_0^{\xi}\frac{1}{\xi'^{1/2}}\frac{\partial\psi_c}{\partial\xi}(\xi-\xi')\,\mathrm{d}\xi\right]. \qquad \text{(B.21)}\end{aligned}$$

This is exactly the same as the solution when there is no diffusion in the ξ direction, and it yields the expression (5.67) for the influx close to the channel head.

Appendix C

Numerical methods

Chapter 3

Porous flow equations

Here we briefly describe the discretisation used to solve equations (3.12)-(3.14), in the two-dimensional case. A fixed grid of rectangular cells is constructed as shown in figure C.1, with cells centered at points (y_j, z_i), and with sides of length Δy_j and Δz_i. Values of melt fraction ϕ_{ij}, effective pressure N_{ij} and velocity potential $\mathcal{U}_{ij}$ are calculated for each cell, while fluxes $q_{y\ ij}$ and velocities V_{ij} are calculated for the right sides of each cell, and $q_{z\ ij}$ and W_{ij} for the upper sides. At each time step, (3.13) is solved for N_{ij} using the current values of ϕ_{ij}, then (3.14) is solved for $\mathcal{U}_{ij}$. These are used to calculate the compaction rate and the melting rate in (3.12) explicitly, and this equation advances ϕ_{ij} for the next time step.

To do this, (3.13) is discretised as

$$\phi_{ij} N_{ij} \Delta z_i \Delta y_j = (q_{y\ ij} - q_{y\ ij-1})\Delta z_i + (q_{z\ ij} - q_{z\ i-1j})\Delta y_j, \tag{C.1}$$

in which the fluxes are calculated as, for example,

$$q_{z\ ij} = \frac{(\Delta z_i + \Delta z_{i+1})\phi_{ij}^2 \phi_{i+1j}^2}{\phi_{ij}^2 \Delta z_{i+1} + \phi_{i+1j}^2 \Delta z_i} \left(1 + \delta^2 \frac{2(N_{i+1j} - N_{ij})}{\Delta z_i + \Delta z_{i+1}}\right). \tag{C.2}$$

The term at the front of this expression is the geometric mean of the permeabilities in cells i and $i+1$. (C.1) and (C.2) provide a linear system for N_{ij}, in which the boundary conditions for ϕ and N in (3.15)-(3.16) are easily implemented.

Having solved for N_{ij}, (3.14) is discretised as

$$(W_{ij} - W_{i-1j})\Delta y_j + (V_{ij} - V_{i-1j})\Delta z_i = -\frac{1}{St}\phi_{ij} N_{ij} \Delta z_i \Delta y_j, \tag{C.3}$$

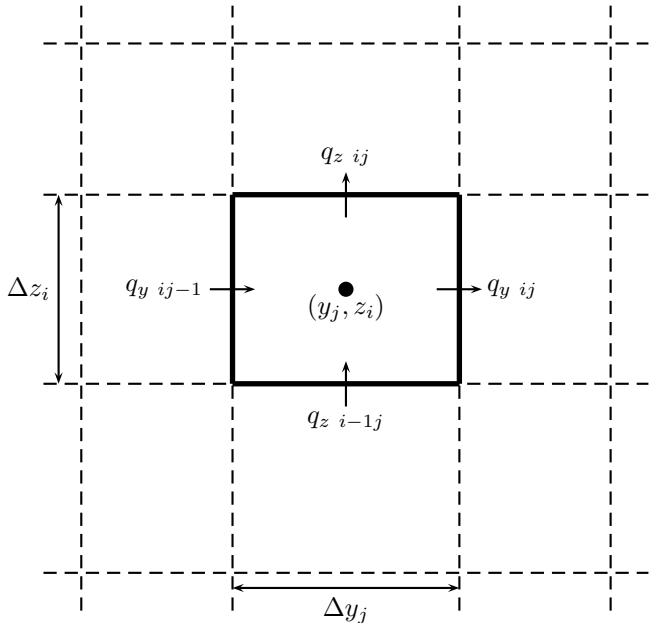

Figure C.1: Grid cells used in discretisation of porous flow equations, with fluxes assigned to the right and upper sides of each cell.

with velocities given by

$$W_{ij} = W_0 + \frac{1}{St}\frac{2(\mathcal{U}_{i+1j} - \mathcal{U}_{ij})}{\Delta z_i + \Delta z_{i+1}}, \qquad V_{ij} = \frac{1}{St}\frac{2(\mathcal{U}_{ij+1} - \mathcal{U}_{ij})}{\Delta y_j + \Delta y_{j+1}}. \tag{C.4}$$

This provides a linear system for $\mathcal{U}_{ij}$. Having calculated N_{ij} and $\mathcal{U}_{ij}$, the fluxes (C.2) and velocities (C.4) are known, and are used to calculate the melt rate using the average across each cell;

$$m_{ij} = \frac{W_{ij} + W_{i-1j}}{2} + \frac{1}{St}\frac{q_{z\ ij} + q_{z\ i-1j}}{2}. \tag{C.5}$$

(3.12) is then discretised as

$$\varepsilon\frac{\phi_{ij}^k - \phi_{ij}^{k-1}}{\Delta t}\Delta z_i \Delta y_j + \varepsilon(\phi_{ij+1}^k V_{ij}^{k-1} - \phi_{ij}^k V_{ij-1}^{k-1})\Delta z_i + \varepsilon(\phi_{ij}^k W_{ij}^{k-1} - \phi_{i-1j}^k W_{i-1j}^{k-1})\Delta y_j = (m_{ij}^{k-1} - \phi_{ij}^{k-1} N_{ij}^{k-1})\Delta z_i \Delta y_j, \tag{C.6}$$

in which the superscripts refer to the time step.

Initial conditions for the iterations are typically taken as the approximate solution $\phi = W_0^{1/2} z^{1/2}$, which is then allowed to evolve to the one-dimensional steady state before adding perturbations in the y direction.

Boundary conditions for a channel

When the melt fraction ϕ_{ij} reaches 100%, we no longer attempt to solve for N_{ij} in those cells. Instead we *apply* a channel pressure $N_{ij} = N_c/\delta^2$ (from (3.209)) in the discretisation (C.1)-(C.2). Since we are interested in the steady-state, and the channel time scale is much smaller than the time scale for the porous flow, we take the good approximation $N_c = 1 - z_i$ (from (3.209)), and therefore avoid solving for the channel dynamics at the same time. Having found N_{ij}, the flux into the channel from the neighbouring cells is known, and the channel equations can then be solved independently. Instead of (C.3), for the channel cells we then apply the condition $V_{ij} - V_{ij-1} = \delta Q/St^2$ (from (3.210)) when calculating $\mathcal{U}_{ij}$. (C.6) is then solved only for the non-channel cells.

When calculating the flow around a single channel, we typically calculate the solution on only one side. In this case, reflective conditions on the fluxes are applied with, for instance, $q_{ij-1} = -q_{ij}$ at the left hand edge. Higher resolution is generally desired close to the channel, so the width of the cells Δy_j is chosen to provide this, with thin cells near $y = 0$ and increasingly wider cells out to a far-field boundary, at which Neumann conditions are usually applied.

Radial coordinates

When written in the finite volume formulation used here, the extension of the discretisation to radial coordinates is relatively straightforward; the area elements $\Delta z_i \Delta y_j$ become volume elements $2\pi r_j \Delta z_i \Delta r_j$ and the 'faces' Δz_i and Δy_j become $2\pi(r_j \pm \Delta r_j/2)\Delta z_i$ and $2\pi r_j \Delta r_j$. The expressions for the central cell at $r = 0$ must be adjusted appropriately.

Chapter 5

Equations (5.25)-(5.29) are solved in essentially the same way as that outlined above. They are written more succinctly as

$$m = 1 + \frac{\varepsilon}{\beta}\mathbf{q} \cdot (\mathbf{\Phi} + \delta^2 \nabla N), \tag{C.7}$$

$$\nabla \cdot [h^\alpha (\mathbf{\Phi} + \delta^2 \nabla N)] = \beta r h N - \beta(r-1)m + \gamma\omega, \tag{C.8}$$

$$\frac{\partial h}{\partial t} = m - hN. \tag{C.9}$$

A fixed grid is set up as in figure C.1 above, with values h_{ij}, N_{ij} and m_{ij} being calculated for each cell, and values of $\mathbf{\Phi}_{ij}$ (given) and fluxes $q_{x\ ij}$ and $q_{y\ ij}$ assigned to

the upper and right sides of each cell. m_{ij} is calculated explicitly from (C.7) using the average flux and potential gradient across the cell. The discretised version of (C.8) (as in (C.1)-(C.2) above) is solved as a linear system for N_{ij}, and (C.9) is used to step forward h_{ij} explicitly.

To include a channel, the 'channelised' cells at $y = 0$, $x > x_c$ are assigned a pressure N_c which must be chosen in order to satisfy the channel equations (5.35)-(5.38). Since the time scale for these equations is shorter than that for the porous flow, the steady-state solution for the channel is found (for a given Ω) by solving the discretised system of non-linear equations using a Newton method.

At each time step, therefore, (C.8) is first solved for N_{ij} by prescribing the values of N_c from the previous time step; the resulting influx to the channel Ω is then used to calculate new values for N_c from the steady-state channel equations, and (C.8) is then solved again for N_{ij}, using the updated N_c.

Initial conditions for these iterations are chosen using the analytical approximations given in section 5.3.2; it is especially important to have a good initial guess for N_c. In chapter 5 we are concerned only with steady-state solutions, so these are then allowed to evolve towards the steady state.

Most of the calculations shown here have taken $\varepsilon = 0$, which means ignoring the turbulent heating by water flow in the distributed system. If ε is taken to be non-zero, it can cause runaway growth due to a large melting rate at the head of the channel. Provided the discretisation is sufficiently coarse, this is not resolved numerically; if a fine enough resolution is used however, the depth h in the cell next to the head of the channel will grow hugely, and at some stage the channel should be extended to include it. It is not clear when to do this, and we have not attempted to perform such calculations here; the necessary resolution to capture the growth of the channel is large, and useful further work would make use of a moving mesh in order to do this accurately.

Bibliography

Aharonov, E., Whitehead, J. A., Kelemen, P. B., and Spiegelman, M. (1995). Channeling instability of upwelling melt in the mantle. *J. Geophys. Res.*, 100:20433–20450.

Ahern, J. L. and Turcotte, D. L. (1979). Magma migration beneath an ocean ridge. *Earth Plan. Sci. Lett.*, 45:115–122.

Alley, R. B. (1989). Water-pressure coupling of sliding and bed deformation: I. Water system. *J. Glaciol.*, 35:108–118.

Alley, R. B., Blankenship, D. D., Bentley, C. R., and T., R. S. (1986). Deformation of till beneath ice stream B, West Antarctica. *Nature*, 322:57–59.

Anderson, R. S., Anderson, S. P., MacGregor, K. R., Waddington, E. D., O'Neel, S., Riihimaki, C. A., and Loso, M. G. (2004). Strong feedbacks between hydrology and sliding of a small alpine glacier. *J. Geophy. Res.*, 109.

Asimow, P. D. and Stolper, E. M. (1999). Steady-state mantle-melt interactions in one dimension: I. Equilibrium transport and melt focusing. *J. Petrol.*, 40:475–494.

Banerjee, I. and McDonald, B. C. (1990). Nature of esker sedimentation. In Jopling, A. V. and McDonald, B. C., editors, *Glaciofluvial and Glaciolacustrine Sedimentation*, volume 23, pages 132–154. SEPM Special Publication.

Batchelor, G. K. (1967). *An Introduction to Fluid Mechanics*. Cambridge University Press.

Bercovici, D., Ricard, Y., and Schubert, G. (2001). A two-phase model for compaction and damage. 1. general thoery. *J. Geophys. Res.*, 106:8887–8906.

Bindschadler, R. (1983). The importance of pressurized subglacial water in separation and sliding at the glacier bed. *J. Glaciol.*, 28:239–265.

Bindschadler, R. A., King, M. A., Alley, R. B., Anandakrishnan, S., and Padman, L. (2003). Tidally controlled stick-slip discharge of a West Antarctic ice stream. *Science*, 301:1087–1089.

Blümcke and Finsterwalder, S. (1905). Zeitliche änderungen in der Geschwindigkeit der Gletscherbewegung. *Sitzungsber. d. mat. phys. Klasse d. k. Bayer. Akad. d. Wissensch.*, 35:129.

Boulton, G. S., Hagdorn, M., Maillot, P. B., and Zatsepin, S. (2009). Drainage beneath ice sheets: Groundwater-channel coupling, and the origin of esker systems from former ice sheets. *Quat. Sci. Rev.*, 28:621–638.

Boulton, G. S. and Hindmarsh, R. C. A. (1987). Sediment deformation beneath glaciers: rheology and geological consequences. *J. Geophys. Res.*, 92:9059–9082.

Boulton, G. S., Lunn, R., Vidstrand, P., and Zatsepin, S. (2007a). Subglacial drainage by groundwater-channel coupling, and the origin of esker systems: Part I - glaciological observations. *Quat. Sci. Rev.*, 26:1067–1090.

Boulton, G. S., Lunn, R., Vidstrand, P., and Zatsepin, S. (2007b). Subglacial drainage by groundwater-channel coupling, and the origin of esker systems: Part II - theory and simulation of a modern system. *Quat. Sci. Rev.*, 26:1091–1105.

Brennand, T. A. (2000). Deglacial meltwater drainage and glaciodynamics: inferences from Laurentide eskers, Canada. *Geomorphology*, 32:263–293.

Bruce, P. M. and Huppert, H. E. (1989). Thermal control of basaltic fissure eruptions. *Nature*, 342:665–667.

Brzozowski, J. and Hooke, R. L. (1981). Seasonal variations in surface velocity of the lower part of Storglaciären, Kebnekaise, Sweden. *Geografiska Annaler.*, 63:233–240.

Buck, W. R. and Su, W. (1989). Focused mantle upwelling below mid-ocean ridges due to feedback between viscosity and melting. *Geophys. Res. Lett.*, 16:641–644.

Budd, W. F., Keage, P. L., and Blundy, N. A. (1979). Empirical studies of ice sliding. *J. Glaciol.*, 23:157–170.

Clark, P. U. and Walder, J. S. (1994). Subglacial drainage, eskers, and deforming beds beneath the Laurentide and Eurasian ice sheets. *Geol. Soc. Am. Bull.*, 106:304–314.

Clarke, G. K. C. (1996). Lumped-element analysis of subglacial hydraulic circuits. *J. Geophys. Res.*, 101:17547–17559.

Clarke, G. K. C. (2003). Hydraulics of subglacial outburst floods: new insights from the Spring-Hutter formulation. *J. Glaciol.*, 49:299–313.

Clarke, G. K. C. (2005). Subglacial processes. *Annu. Rev. Earth Planet. Sci.*, 33:247–276.

Copland, L., Sharp, M. J., and Nienow, P. W. (2003). Links between short-term velocity variations and the subglacial hydrology of a predominantly cold polythermal glacier. *J. Glaciol.*, 49:337–348.

Das, S. B., Joughin, I., Behn, M., Howat, I. M., King, M. A., Lizarralde, D., and Bhatia, M. P. (2008). Fracture propagation to the base of the Greenland ice sheet during supraglacial lake drainage. *Science*, 320:778–781.

Deeley, R. M. and Parr, P. H. (1914). On the Hintereis Glacier. *Phil. Mag.*, 27:153.

Drew, D. A. (1983). Mathematical modeling of two-phase flow. *Ann. Rev. Fluid Mech.*, 15:261–291.

Evatt, G. W., Fowler, A. C., Clark, C. D., and Hulton, N. R. J. (2006). Subglacial floods beneath ice sheets. *Phil. Trans. R. Soc. A*, 364:1769–1794.

Finsterwalder, R. (1959). Chamonix glaciers. *J. Glaciol.*, 3:547–548. Letter.

Finsterwalder, R. (1961). Der Haushalt des Hintereisferners (Ötztal). *J. Glaciol.*, pages 1159–1160.

Fischer, U. H. and Clarke, G. K. C. (2001). Review of subglacial hydro-mechanical coupling: Trapridge Glacier, Yukon Territory, Canada. *Quat. Int.*, 86:29–43.

Flint, R. (1930). The Origin of the Irish "Eskers". *Geographical Review*, 20:615–630.

Flowers, G., Clarke, G. K. C., Björnsson, H., and Pálsson, F. (2004). A coupled sheet-conduit mechanism for jökulhlaup propagation. *Geophy. Res. Lett.*, 31.

Flowers, G. E. and Clarke, G. K. C. (2002). A multicomponent coupled model of glacier hydrology 1. theory and synthetic examples. *J. Geophys. Res.*, 107.

Fountain, A. G. and Walder, J. S. (1998). Water flow through temperate glaciers. *Rev. Geophys.*, 36:299–328.

Fowler, A. C. (1982). Waves on glaciers. *J. Fluid Mech.*, 120:283–321.

Fowler, A. C. (1985). A mathematical model of magma transport in the asthenosphere. *Geophys. Astrophys. Fluid Dynamics*, 33:63–96.

Fowler, A. C. (1986). A sliding law for glaciers of constant viscosity in the presence of subglacial cavitation. *Proc. R. Soc. Lond. A*, 407:147–170.

Fowler, A. C. (1987). Sliding with cavity formation. *J. Glaciol.*, 33:255–267.

Fowler, A. C. (1989). Generation and creep of magma in the earth. *SIAM J. Appl. Math.*, 49:231–245.

Fowler, A. C. (1990a). A compaction model for melt transport in the earth's asthenosphere. Part 1. The basic model. In Ryan, M., editor, *Magma transport and storage*. John Wiley & sons Ltd., London.

Fowler, A. C. (1990b). A compaction model for melt transport in the earth's asthenosphere. Part 2. Applications. In Ryan, M., editor, *Magma transport and storage*. John Wiley & sons Ltd., London.

Fowler, A. C. and Larson, D. A. (1978). On the flow of polythermal glaciers I. Model and preliminary analysis. *Proc. R. Soc. Lond. A*, 363:217–242.

Fowler, A. C. and Larson, D. A. (1980). On the flow of polythermal glaciers II. Surface wave analysis. *Proc. Roy. Soc. London Ser. A*, 370:155–171.

Fowler, A. C. and Walder, J. S. (1993). Creep closure of channels in deforming subglacial till. *Proc. R. Soc. A*, 441:17–31.

Gordon, S., Sharp, M., Hubbard, B., Smart, C., Ketterling, B., and Willis, I. (1998). Seasonal reorganization of subglacial drainage inferred from measurements in boreholes. *Hydrological Processes*, 12:105–133.

Harper, J. T., Humphrey, N. F., and Greenwood, M. C. (2002). Basal conditions and glacier motion during the winter/spring transition, Worthington Glacier, Alaska, USA. *J. Glaciol.*, 4:42–50.

Helfrich, K. R. and Whitehead, J. A. (1990). Solitary waves on conduits of buoyant fluid in a more viscous fluid. *Geophys. Astophys. Fluid Dynamics*, 51:35–52.

Hewitt, I. J. and Fowler, A. C. (2008a). Partial melting in an upwelling mantle column. *Proc. Roy. Soc. A*, 464:2467–2491.

Hewitt, I. J. and Fowler, A. C. (2008b). Seasonal waves on glaciers. *Hydrol. Process.*, 22:3919–3930.

Hewitt, I. J. and Fowler, A. C. (2009). Melt channelization in ascending mantle. *J. Geophys. Res.*, 114.

Hock, R. and Hooke, R. L. (1993). Evolution of the internal drainage system in the lower part of the ablation area of Storglaciären, Sweden. *Geol. Soc. Am. Bull.*, 105:537–546.

Hodge, S. M. (1974). Variations in the sliding of a temperate glacier. *J. Glaciol.*, 13:349–369.

Hooke, R. L. (1989). Englacial and subglacial hydrology: A qualitative review. *Arctic and Alpine Research*, 21:221–233.

Hooke, R. L., Brzozowski, J., and Bronge, C. (83). Seasonal variations in surface velocity, Storglaciären, Sweden. *Geografiska Annaler.*, 65:263–277.

Hubbard, B. and Nienow, P. (1997). Alpine subglacial hydrology. *Quaternary Scienc Reviews*, 16:939–955.

Huddart, D. and Bennett, M. R. (1997). The Carstairs Kames (Lanarkshire, Scotland): morphology, sedimentology and formation. *J. Quat. Sci.*, 12:467–484.

Humphrey, N. F. (1987). Coupling between water pressure and basal sliding in a linked-cavity hydraulic system. In *The Physical Basis of Ice Sheet Modelling*, pages 105–119, Wallingford, UK. International Association of Hydrological Sciences.

Huppert, H. E. and Bruce, P. M. (1990). Solidification and melting along dykes by the laminar flow of basaltic magma. In Ryan, M. P., editor, *Magma Transport and Storage*, pages 87–101. John Wiley & Sons, Chichester, England.

Iken, A. (1981). The effect of the subglacial water pressure on the sliding velocity of a glacier in an idealized numerical model. *J. Glaciol.*, 27:407–421.

Iken, A. and Bindschadler, R. A. (1986). Combined measurements of subglacial water pressure and surface velocity of Findelengletscher, Switzerland: conclusions about drainage system and sliding mechanism. *J. Glaciol.*, 32:101–119.

Ito, G. and Martel, S. J. (2002). Focusing of magma in the upper mantle through dike interaction. *J. Geophys. Res.*, 107:2223.

Iwamori, H. (1993). A model for disequilibrium mantle melting incorporating melt transport by porous and channel flows. *Nature*, 366:734–737.

Jansson, P. (1996). Dynamics and hydrology of a small polythermal valley glacier. *Geografiska Annaler.*, 78:171–180.

Johnson, K. T. M., Dick, H. J. B., and Shimizu, N. (1990). Melting in the oceanic upper mantle: an ion microprobe study of diopsides in abyssal peridotites. *J. Geophys. Res.*, 95:2661–2678.

Joughin, I., Das, S. B., King, M. A., Smith, B. E., Howat, I. M., and Moon, T. (2008). Seasonal speedup along the Western flank of the Greenland ice sheet. *Science*, 320:781–783.

Kamb, B. (1961). The thermodynamic theory of non-hydrostatically stressed solids. *J. Geophys. Res.*, 66:259–271.

Kamb, B. (1970). Sliding motion of glaciers: Theory and observation. *Rev. Geophys.*, 8:673–728.

Kamb, B. (1987). Glacier surge mechanism based on linked cavity configuration of the basal water system. *J. Geophys. Res.*, 92:9083–9100.

Kamb, B. (1991). Rheological nonlinearity and flow instability in the deforming bed mechanism of ice stream motion. *J. Geophys. Res.*, 96:16585–16595.

Kamb, B. and Engelhardt, H. (1987). Waves of accelerated motion in a glacier approaching surge: The mini-surges of Variegated Glacier, Alaska, U.S.A. *J. Glaciol.*, 33:27–46.

Kamb, B., Raymond, W. D., Harrison, W. D., Engelhardt, H., Echelmeyer, K. A., Humphrey, N., Brugman, M. M., and Pfeffer, T. (1985). Glacier surge mechanism: 1982-1983 surge of Variegated Glacier, Alaska. *Science*, 227:469–479.

Katz, R. F. (2008). Magma dynamics with the enthalpy method: Benchmark solutions and magmatic focusing at mid-ocean ridges. *J. Petrol.*, 49:2099–2121.

Katz, R. F., Spiegelman, M., and Holtzman, B. (2006). The dynmics of melt and shear localization in partially molten aggregates. *Nature*, 442:676–679.

Kelemen, P. B., Hirth, G., Shimizu, N., Spiegelman, M., and Dick, H. J. B. (1997). A review of melt migration processes in the adiabatically upwelling mantle beneath oceanic spreading ridges. *Phil. Trans. R. Soc. Lond. A*, 355:283–318.

Kelemen, P. B., Whitehead, J. A., Aharonov, E., and Jordahl, K. A. (1995). Experiments on flow focusing in soluble porous media, with applications to melt extraction from the mantle. *J. Geophys. Res.*, 100:475–496.

Kessler, M. A. and Anderson, R. S. (2004). Testing a numerical glacial hydrological model using spring speed-up events and outburst floods. *Geophys. Res. Lett.*, 31.

Lappegard, G., Kohler, J., Jackson, M., and Hagen, J. O. (2006). Characteristics of subglacial drainage systems deduced from load-cell measurements. *J. Glaciol.*, 52:137–148.

Lighthill, M. J. and Whitham, G. B. (1955). On kinematic waves. *Proc. Roy. Soc. London Ser. A*, 229:281–345.

Lister, J. R. and Kerr, R. C. (1991). Fluid-mechanical models of crack propagation and their application to magma transport in dykes. *J. Geophys. Res.*, 96:10049–10077.

Lliboutry, L. (1958). La dynamique de la Mer de Glace et la vague de 1891-95 d'apres les mesures de Joseph Vallot. *IASH*, 46:125–138.

Lliboutry, L. (1968). General theory of subglacial cavitation and sliding of temperate glaciers. *J. Glaciol.*, 7:21–58.

Lliboutry, L. (1987). Realistic, yet simple bottom boundry conditions for glaciers and ice sheets. *J. Geophys. Res.*, 92:9101–9109.

Maaloe, S. (2003). Melt dynamics of a partially molten mantle with randomly oriented veins. *J. Petrol.*, 44:1193–1210.

MacGregor, K. R., Riihimaki, C. A., and Anderson, R. S. (2005). Spatial and temporal evolution of rapid sliding on bench glacier, Alaska, USA. *J. Glaciol.*, 51:49–63.

Mair, D., Nienow, P., Willis, I. C., and Sharp, M. J. (2001). Spatial patterns of glacier motion during a high-velocity event: Haut Glacier d'Arolla, Switzerland. *J. Glaciol.*, 47:9–20.

McKenzie, D. (1984). The generation and compaction of partially molten rock. *J. Petrol.*, 25:713–765.

McKenzie, D. (1985). The extraction of magma from the crust and mantle. *Earth. Plan. Sci. Lett.*, 74:81–91.

Meier, M., Lundstrom, S., Stone, D., Kamb, B., Engelhardt, H., Humphrey, N., Dunlap, W. W., Fahnestock, M., Krimmel, R. M., and Walters, R. (1994). Mechanical and hydrologic basis for the rapid motion of a large tidewater glacier. 1. Observations. *J. Geophys. Res.*, 99:15219–15229.

Meier, M. F. (1968). Calculations of slip of Nisqually Glacier on its bed: no simple relation of sliding velocity to shear stress. In *Union de Géodésie et Géophysique Internationale. Association Internationale d'Hydrologie Scientific. Assemblée générale de Berne, 25 Sept. - 7 Oct. 1967. Rapports et discussions.*, pages 49–57.

Murray, T. (1997). Assessing the paradigm shift: deformable glacier beds. *Quat. Sci. Rev.*, 16:995–1016.

Muskhelishvili, N. I. (1953). *Some basic problems of the mathematical theory of elasticity.* P. Noordhoff, Groningen.

Ng, F. (1998). *Mathematical modelling of subglacial floods.* PhD thesis, University of Oxford.

Nicolas, A. (1986). A melt extraction model based on structural studies in mantle peridotites. *J. Petrol.*, 27:999–1022.

Nienow, P., Sharp, M., and Willis, I. (1998). Seasonal changes in the morphology of the subglacial drainage system, Haut Glacier d'Arolla, Switzerland. *Earth Surf. Process. Landforms*, 23:825–843.

Nuttall, A. and Hodgkins, R. (2005). Temporal variations in the flow velocity at Finsterwalderbreen, a Svalbard surge-type glacier. *Ann. Glaciol.*, 42:71–76.

Nye, J. F. (1952). The mechanics of glacier flow. *J. Glaciol.*, 2:82–93.

Nye, J. F. (1953). The flow law of ice from measurements in glacier tunnels, laboratory experiments and the Jungfraufirn borehole experiment. *R. Soc. London, Ser. A*, 219:477–489.

Nye, J. F. (1960). The response of glaciers and ice-sheets to seasonal and climatic changes. *Proc. R. Soc. Lond. A*, 256:559–584.

Nye, J. F. (1969). A calculation on the sliding of ice over a wavy surface using a Newtonian viscous approximation. *Proc. Roy. Soc. Lond. A*, 311:445–467.

Nye, J. F. (1970). Glacier sliding without cavitiation in a linear viscous approximation. *Proc. R. Soc. Lond. A*, 315:381–403.

Nye, J. F. (1976). Water flow in glaciers: Jökulhlaups, tunnels and veins. *J. Glaciol.*, 17:181–207.

Ockendon, J. R., Howison, S. D., Lacey, A. A., and Movchan, A. B. (2003). *Applied Partial Differential Equations*. Oxford University Press, Oxford.

O'Hara, M. J. (1965). Primary magmas and the origin of basalts. *Soct. J. Geol.*, 1:19–40.

Olson, P. and Christensen, U. (1986). Solitary wave propagation in a fluid conduit within a viscous matrix. *J. Geophys. Res.*, 91:6367–6374.

Ortoleva, P., Chadam, J., Merino, E., and Sen, A. (1987a). Geochemical self-organisation, I, Reaction-transport feedbacks. *Am. J. Sci.*, 287:979–1007.

Ortoleva, P., Merino, E., Moore, C., and Chadam, J. (1987b). Geochemical self-organisation, II, The reaction-infiltration instability. *Am. J. Sci.*, 287:1008–1040.

Oseen, C. W. (1910). Ober die Stokes'sche Formel, und 0ber eine verwandte Aufgabe in der Hydrodynamik. *Ark. Math. Astronom. Fys.*, 6(29).

Owen, G. (1997). Origin of an esker-like ridge - erosion or channel-fill? Sedimentology of the Monington 'Esker' in Southwest Wales. *Quat. Sci. Rev.*, 16:675–684.

Prest, V. K., Grant, D. R., and Rampton, V. N. (1968). Glacial map of canada.

Raymond, C. F., Benedict, R. J., Harrison, W. D., Echelmeyer, K. A., and Sturm, M. (1995). Hydrological discharges and motion of Fels and Black Rapids Glaciers, Alaska, USA: implications for the structure of their drainage systems. *J. Glaciol.*, 41:290–304.

Rempel, A. W. (2008). A theory for ice-till interactions and sediment entrainment beneath glaciers. *J. Geophys. Res.*, 113.

Rempel, A. W. (2009). Effective stress profiles and seepage flows beneath glaciers and ice sheets. *J. Glaciol.*, 55:431–443.

Ribe, N. M. (1985a). The deformation and compaction of partial molten zones. *Geophys. J. R. Astron. Soc.*, 83:487–501.

Ribe, N. M. (1985b). The generation and composition of partial melts in the earth's mantle. *Earth Plan. Sci. Lett.*, 73:361–376.

Richardson, C. N. (1998). Melt flow in a variable viscosity matrix. *Geophys. Res. Lett.*, 25:1099–1102.

Richardson, C. N., Lister, J. R., and McKenzie, D. (1996). Melt conduits in a viscous porous matrix. *J. Geophys. Res.*, 101:20423–20432.

Roper, S. M. and Lister, J. R. (2005). Buoyancy-driven crack propagation from an over-pressured source. *J. Fluid. Mech.*, 536:79–98.

Röthlisberger, H. (1972). Water pressure in intra- and subglacial channels. *J. Glaciol.*, 11:177–203.

Russell, A. J., Knudsen, Ó., Fay, H., Marren, P. M., Heinz, J., and Tronicke, J. (2001). Morphology and sedimentology of a giant supraglacial, ice-walled, jökulhlaup channel, Skeidarárjökull, Iceland: implications for esker genesis. *Global and Planetary Change*, 28:193–216.

Schimpp, O. (1958). Der Eishaushalt am Hintereisferner in den Jahren 1952-53 und 1953-54. *Union Géodésique et Géophysique Internationale. Association Internationale d'Hydrologie Scientifique. Assemblée générale de Toronto, 3-14 Sept. 1957.*, 4:301–314.

Schoof, C. (2005). The effect of cavitation on glacier sliding. *Proc. R. Soc. A*, 461:609–627.

Schoof, C. (2006). Variational methods for glacier flow over plastic till. *J. Fluid. Mech.*, 555:299–320.

Scott, D. R. and Stevenson, D. J. (1984). Magma Solitons. *Geophys. Res. Lett.*, 11:1161–1164.

Scott, D. R. and Stevenson, D. J. (1986). Magma ascent by porous flow. *J. Geophys. Res.*, 91:9283–9296.

Scott, D. R. and Stevenson, D. J. (1989). A self-consistent model of melting, magma migration and buoyancy-driven circulation beneath mid-ocean ridges. *J. Geophys. Res.*, 94:2973–2988.

Scott, D. R., Stevenson, D. J., and Whitehead, J. A. (1986). Observations of solitary waves in a viscously deformable pipe. *Nature*, 319:759–761.

Shaw, J. (1994). A qualitative view of sub-ice-sheet landscape evolution. *Progress in Physical Geography*, 18:159–184.

Shreve, R. L. (1972). Movement of water in glaciers. *J. Glaciol.*, 11:205–214.

Shreve, R. L. (1985). Ekser characteristics in terms of glacier physics, Katahdin esker system, Maine. *Geol. Soc. Am. Bull.*, 96:639–646.

Sleep, N. (1988). Tapping of melt by veins and dikes. *J. Geophys. Res.*, 93:10255–10272.

Sparks, D. W. and Parmentier, E. M. (1991). Melt extraction from the mantle beneath spreading centers. *Earth. Plan. Sci. Lett.*, 105:368–377.

Spence, D. A., Sharp, P. W., and Turcotte, D. L. (1987). Buoyancy-driven crack propagationn: a mechanism for magma migration. *J. Fluid. Mech.*, 174:135–153.

Spiegelman, M. (1993a). Flow in deformable porous media. Part 1 Simple analysis. *J. Fluid Mech.*, 247:17–38.

Spiegelman, M. (1993b). Physics of melt extraction: Theory, Implications and Applications. *Phil. Trans. Phys. Sci. Eng.*, 342:23–41.

Spiegelman, M. (2003). Linear analysis of melt band formation by simple shear. *Geochem. Geophys. Geosys.*, 4.

Spiegelman, M. and Kelemen, P. B. (2003). Extreme chemical variability as a consequence of channelized melt transport. *Geochem. Geophys. Geosys.*

Spiegelman, M., Kelemen, P. B., and Aharonov, E. (2001). Causes and consequences of flow organisation during melt transport: The reaction infiltration instability in compactible media. *J. Geophys. Res.*, 106:2061–2078.

Spiegelman, M. and Kenyon, P. (1992). The requirements for chemical disequilibrium during magma migration. *Earth Planet. Sci. Lett.*, 109:611–620.

Spiegelman, M. and McKenzie, D. (1987). Simple 2-D models for melt extraction at mid-ocean ridges and island arcs. *Earth. Plan. Sci. Lett.*, 83:137–152.

Spring, U. and Hutter, K. (1982). Conduit flow of a fluid through its solid phase and its application to intraglacial channel flow. *Int. J. Eng. Sci.*, 20:327–363.

Šrámek, O., Ricard, Y., and Bercovici, D. (2007). Simultaneous melting and compaction in deformable two-phase media. *Geophys. J. Int.*, 168:964–982.

Stevenson, D. J. (1989). Spontaneous small-scale melt segregation in partial melts undergoing deformation. *Geophys. Res. Lett.*, 16:1067–1070.

Stevenson, D. J. and Scott, D. R. (1991). Mechanics of fluid-rock systems. *Ann. Rev. Fluid Mech.*, 23:305–339.

Tulaczyk, S., Kamb, W. B., and Engelhardt, H. F. (2000a). Basal mechanics of Ice Stream B, West Antarctica. 1. till mechanics. *J. Geophys. Res.*, 105:463–481.

Tulaczyk, S., Kamb, W. B., and Engelhardt, H. F. (2000b). Basal mechanics of Ice Stream B, West Antarctica. 2. undrained plastic bed model. *J. Geophys. Res.*, 105:483–494.

Turcotte, D. L. and Ahern, J. L. (1978). A porous flow model for magma migration in the asthenosphere. *J. Geophys. Res.*, 83:767–772.

Walder, J. S. (1982). Stability of sheet flow of water beneath temperate glaciers and implications for glacier surging. *J. Glaciol.*, 28:273–293.

Walder, J. S. (1986). Hydraulics of subglacial cavities. *J. Glaciol.*, 32:439–445.

Walder, J. S. and Fowler, A. C. (1994). Channelized subglacial drainage over a deformable bed. *J. Glaciol.*, 40:3–15.

Walder, J. S. and Hallet, B. (1979). Geometry of former subglacial water channels and cavities. *J. Glaciol.*, 23:335–346.

Warren, W. P. and Ashley, G. M. (1994). Origins of the ice-contact stratified ridges (eskers) of Ireland. *J. Sedimentary Res.*, A64:433–449.

Weertman, J. (1957). On the sliding of glaciers. *J. Glaciol.*, 3:33–38.

Weertman, J. (1958). Travelling waves on glaciers. *IASH*, 47:162–168.

Weertman, J. (1972). General theory of water flow at the base of a glacier or ice sheet. *Reviews of Geophysics and Space Physics*, 10:287–333.

Weertman, J. and Birchfield, G. E. (1983). Basal water film, basal water pressure, and velocity of travelling waves on glaciers. *J. Glaciol.*, 29:20–27.

Wettlaufer, J. S. and Worster, M. G. (2006). Premelting dynamics. *Annu. Rev. Fluid Mech.*, 38:427–452.

Whitehead, J. A. and Helfrich, K. R. (1986). The Korteweg-de Vries equation from laboratory conduit and magma migration equations. *Geophys. Res. Lett.*, 13:545–546.

Willis, I. C. (1995). Interannual variations in glacier motion - a review. *Prog. Phys. Geog.*, 19:61–106.

Willis, I. C., Mair, D., Hubbard, B., Nienow, P., Fischer, U. H., and Hubbard, A. (2003). Seasonal variations in ice deformation and basal motion across the tongue of Haut Glacier d'Arolla, Switzerland. *Ann. Glaciol.*, 36:157–167.

Wingham, D. J., Siegert, M. J., Shepherd, A., and Muir, A. S. (2006). Rapid discharge connects Antarctic subglacial lakes. *Nature*, 440:1033–1036.

Zwally, H. J., Abdalati, W., Herring, T., Larson, K., Saba, J., and Steffen, K. (2002). Surface melt-induced acceleration of Greenland ice-sheet flow. *Science*, 297:218–222.